

Università degli Studi di Salerno

Dipartimento di Chimica e Biologia "Adolfo Zambelli"



Development of Iron-Based Catalysts
for the
Coupling of Carbon Dioxide with Epoxides

Tesi di Dottorato in Chimica - XXX Ciclo

A.A. 2016/2017

Candidato: Francesco Della Monica

Tutor: Prof. Carmine Capacchione

Co-Tutor: Prof. Alfonso Grassi

Coordinatore: Prof. Gaetano Guerra

A Veronica

Table of Contents

Summary	10
List of abbreviations	12
1 Introduction.....	14
1.1 The carbon dioxide concern.....	14
1.2 Reaction of CO ₂ with epoxides	16
1.3 Catalytic systems for cyclic organic carbonates formation	17
1.4 Catalytic systems for polycarbonates formation	21
1.4.1 Bicomponent systems	21
1.4.2 Bimetallic systems	23
1.5 Iron based catalytic systems.....	25
1.6 Motivation of the thesis	30
1.7 References	32
2 Bis-thioether-triphenolate iron(III) complexes	35
2.1 Synthesis and characterization	35
2.2 Catalytic activity	38
2.3 Scope of the catalyst.....	42
2.4 Theoretical calculations.....	45
2.5 Conclusions.....	48
2.6 Experimental Part.....	50
General considerations.....	50
Synthesis of the pro-ligand 2,2'-(((5-(tert-butyl)-2-hydroxy-1,3-phenylene)bis(methylene))bis (sulfanediy))-bis(2,4-di-(α,α' -dimethylbenzyl)phenol) L2 (Scheme 2).....	51
Synthesis of the pro-ligand 2,2'-(((5-(tert-butyl)-2-hydroxy-1,3-phenylene)bis(methylene))bis (sulfanediy))-bisphenol L3 (Scheme 2)	54
Synthesis of the pro-ligand 2,6-[(3,5-Dichloro-2-hydroxyphenyl)thio]-4-tert-butylphenol L4 (Scheme 2)	57

Synthesis of the pro-ligand 2,6-[[3,5-dimethyl-2-hydroxyphenyl]thio]-4-chlorophenol L5 (Scheme 2).....	60
Synthesis of the pro-ligand 2,6-[[3,5-dimethyl-2-hydroxyphenyl]thio]-4-tert-butylphenol L6 (Scheme 2)	63
Synthesis of the iron(III) complex 2 (Scheme 2)	66
Synthesis of the iron(III) complex 3 (Scheme 2)	66
Synthesis of the iron(III) complex 4 (Scheme 2)	66
Synthesis of the iron(III) complex 5 (Scheme 2)	67
Synthesis of the iron(III) complex 6 (Scheme 2)	67
ESI-MS Characterization	68
FT-IR characterization	70
UV-Vis characterization	83
Crystallographic data of the Iron(III) complex 6	86
Typical procedure for CO ₂ /epoxide coupling to cyclic carbonates catalyzed by 6/TBAB	88
Catalytic tests	89
2.7 References	90
3 [OSSO]-type Iron(III) complexes	91
3.1 Synthesis and characterization	91
3.2 Cyclic organic carbonate formation.....	94
3.3 Co-polymerization of CO ₂ with cyclohexene oxide	99
3.4 Kinetic study	103
3.4.1 Propylene carbonate formation	103
3.4.2 Poly(cyclohexene carbonate) formation.....	108
3.5 Conclusions.....	111
3.6 Experimental Part.....	112
General considerations.....	112
Synthesis of the [OSSO]-type ligand L7 (Scheme 5)	112
Synthesis of the iron(III) complex 7 (Scheme 4)	115

Synthesis of the iron(III) complex 8 (Scheme 4)	115
Synthesis of the iron(III) complex 9 (Scheme 4)	115
Synthesis of the iron(III) complex 10 (Scheme 4)	116
ESI-MS Characterization	116
Effective magnetic moment measurements in solution	118
FT-IR analysis.....	120
Crystallographic data of the Iron(III) complex 8.....	126
Catalytic tests	128
Gel permeation chromatography characterization	131
Thermal analysis.....	133
Kinetic experiments for PC formation promoted by 10/TBAB .	134
Reaction order with respect to [10].....	134
Reaction order with respect to [TBAB]	135
Reaction order with respect to [PO].....	136
Reaction order with respect to P(CO ₂)	137
Eyring plot.....	138
Kinetic experiments for PCHC formation promoted by 8/TBAC	139
Reaction order with respect to [8].....	139
Reaction order with respect to [TBAC]	140
Reaction order with respect to [CHO].....	141
Reaction order with respect to P(CO ₂)	142
Eyring plot.....	143
3.7 References	144
4 Thioether-phenolate Fe(II) and Fe(III) complexes	146
4.1 Synthesis and characterization	146
4.2 Catalytic activity	149
4.3 Conclusions.....	153

4.4 Experimental section.....	154
General considerations.....	154
Synthesis of the pro-ligand 4- <i>tert</i> -butyl-2,6-((2,6-dimethyl)thiophenyl)-phenol L11 (Scheme 7)	155
Synthesis of the pro-ligand 4- <i>tert</i> -butyl-2,6-((2,6-dichloro)thiophenyl)-phenol L12 (Scheme 7)	157
Synthesis of the pro-ligand 4- <i>tetr</i> -butyl-2,6-((2,4,6-tri- <i>iso</i> -propyl)thiophenyl)-phenol L13 (Scheme 7)	159
Synthesis of the iron(II) complex 11 (Scheme 9)	161
Synthesis of the iron(II) complex 12 (Scheme 9)	161
Synthesis of the iron(II) complex 13 (Scheme 9)	161
Synthesis of the iron(III) complex 14 (Scheme 9)	161
Synthesis of the iron(III) complex 15 (Scheme 9)	162
Synthesis of the iron(III) complex 16 (Scheme 9)	162
Catalytic tests	165
4.5 References.....	166

5 The particular case of glycidol in the coupling reaction with CO₂ 167

5.1 Glycerol carbonate	167
5.2 Cycloaddition of CO ₂ to glycidol.....	168
5.3 Conclusions.....	178
5.4 Experimenta section.....	180
Computational details	180
Chemical shift versus glycidol concentration analysis	182
General procedure for CO ₂ /glycidol coupling to glycerol carbonate.....	184
General procedure for CO ₂ /propylene oxide coupling to propylene carbonate.....	184
Typical procedure for CO ₂ /epoxide coupling to the corresponding cyclic carbonate.....	184

Typical procedure for CO ₂ /epoxide coupling to the corresponding cyclic carbonate at low pressure	185
List of ¹ H MNR data for the cyclic organic carbonate products	186
5.5 References	188
Acknowledgements	192

Summary

Beside the environmental and energetic issues, carbon dioxide can be considered as a resource. Many chemical transformations based on CO₂ as C-1 building block have been developed. The coupling reaction of epoxides with CO₂ is one of the most attractive.

An overview on the state of the art for metal-mediated process is provided in the **Introduction**. Particular emphasis is given to the iron-based systems.

The preparation of bimetallic Fe(III) complexes based on polydentate bis-thioether tri-phenolate ligands is reported in **chapter 2**. Their use in the cycloaddition of CO₂ to both terminal and internal epoxides leads to the selective formation of COCs, with the highest activity reported for an Fe-based system. The DFT investigation of the reaction mechanism is also described.

In the **chapter 3**, the synthesis of a new group of mononuclear [OSSO]-type Fe(III) complexes is described. The selective formation of both cyclic organic carbonates and poly(cyclohexene carbonate) was accomplished under very mild reaction conditions. Kinetic investigations were conducted for the production of propylene carbonate and poly(cyclohexene carbonate).

The influence of the nuclearity and of the oxidation state of the metal centre on the catalytic activity were further investigated by comparing the catalytic performances of Fe(II) and Fe(III) complexes, supported by three new bis-thioether phenolate ligands. The results are described in the **chapter 4**.

In the **chapter 5**, the peculiar behaviour of the hydroxyl containing epoxide 2,3-epoxy-propanol (glycidol) in the reaction with CO₂ was investigated. The key role of the hydrogen bond in the activation of the epoxide ring was highlighted, also by means of DFT investigations. Glycidol in combination with a co-catalyst, was also used as an organocatalytic system for the cycloaddition of CO₂ to other epoxides.

List of abbreviations

APC: aliphatic polycarbonate

BPA-PC: bisphenol-A polycarbonate

BDI: β -diiminate

BPA: bisphenol-A

CHO: cyclohexene oxide

CHC: cyclohexene carbonate

COC: cyclic organic carbonate

DMAP: 4-dimethylamino pyridine

DFT: density functional theory

ee: enantiomeric excess

EO: ethylene oxide

EC: ethylene carbonate

EPC: epichlorhydrin

HO: 1,2-hexene oxide

PEC-*co*-PEO: poly(ethylene carbonate)-*co*-poly(ethylene oxide)

[PPN]Br: bis(triphenylphospine)iminium bromide

[PPN]Cl: bis(triphenylphospine)iminium chloride

[PPN]I: bis(triphenylphospine)iminium iodide

[PPN]N₃: bis(triphenylphospine)iminium azide

PC: propylene carbonate

PCHC: poly(cyclohexene carbonate)

PO: propylene oxide

SO: styrene oxide

TBAB: tetrabutylammonium bromide

TBAC: tetrabutylammonium chloride

TBAI: tetrabutylammonium iodide

TOF: turnover frequency

TON: turnover number

1 Introduction

1.1 The carbon dioxide concern

The existence of the global warming related to the greenhouse effect, and its dependence from the inflation of the greenhouse gases in the atmosphere, is by now an unquestionable fact. Carbon dioxide (CO₂) is considered to be the major responsible for the climate change on the planet Earth. The CO₂ concentration in the atmosphere recently overcome the limit of 400 ppm, respect to 278 ppm of the preindustrial period (Figure 1).¹

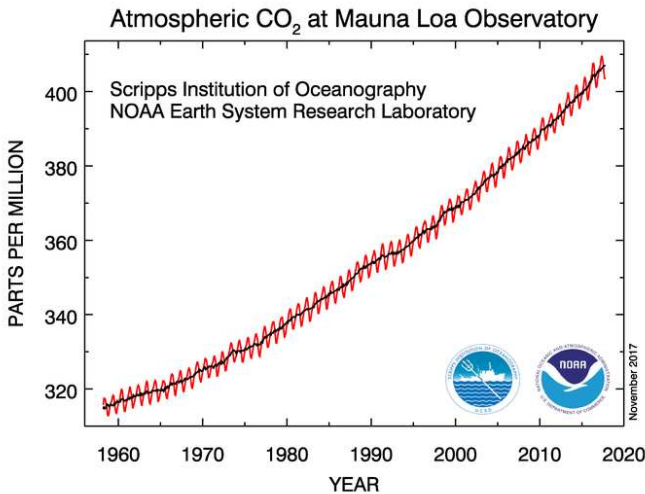


Figure 1 Mole fraction of CO₂ in dry air (red) and seasonally corrected data (black) at Mauna Loa site.¹

The main origin of the exceeding CO₂ in the atmosphere is the use of carbon-based fossil fuels for human activities. Indeed, fossil fuels represent the great part of the energy sources actually employed (around 80%), envisaging that the CO₂ concentration will further increase in the future, at least in short-medium term. With the ambitious aspiration to solve this global issue, 196 countries agreed to a global pact, named the *Paris Agreement*, during the *United Nations Climate Change Conference* in December 2015.² The main target of this agreement is to hold the temperature increase below 2 °C above the preindustrial level, and to lower the concentration of greenhouses gases in the atmosphere.

On the basis of the facts described above, it is a common attitude to look at CO₂ with concern. However, beside the environmental and energetic issues, CO₂ can be considered as a resource, useful for technological applications and chemical transformations.³ Actually, CO₂ is an inert and easy to handle gas, commonly employed for fire extinguisher and in food industry. In the supercritical form it finds applications as solvent for reactions and extractions.

More challenging is the utilization of CO₂ in chemical reactions for the production of useful products. Indeed, because of its thermodynamic stability ($\Delta G^\circ = -396 \text{ kJ/mol}$) and kinetic inertness, the use of high energy compounds or catalysts is required for any CO₂ transformation. However many applications of carbon dioxide have been investigated so far (Figure 2).⁴

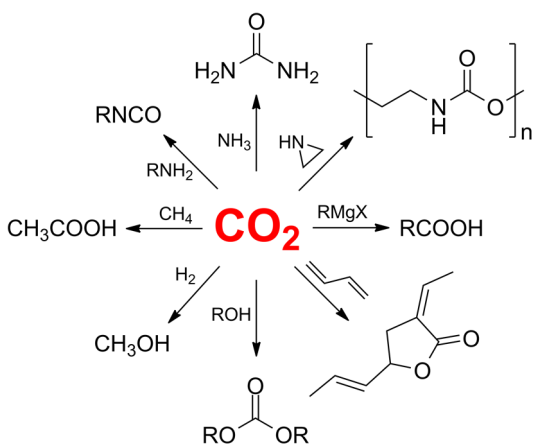


Figure 2 Some possible applications of CO₂ as reactant.

Before to replace an existing industrial process with a CO₂-based one, some requirements have to be satisfied. In details:

- ◇ The overall CO₂ emission in the new process must be reduced
- ◇ The energy and/or mass consumption must be lower with respect to the on-stream process
- ◇ Safer and eco-friendly working conditions must be employed
- ◇ Economic viability must be ensured.

Nevertheless several processes based on CO₂ utilization are applied at industrial level (e.g. production of urea, methanol, cyclic organic carbonates and polymers).

1.2 Reaction of CO₂ with epoxides

The reaction between CO₂ and epoxides attracted the attention of the scientific community, mainly during the last decade. It totally responds to the atom economy principle, trapping all CO₂ employed during the process. From this reaction it is possible to obtain two products: cyclic organic carbonates (COCs) and aliphatic polycarbonate (APC) (Figure 3).

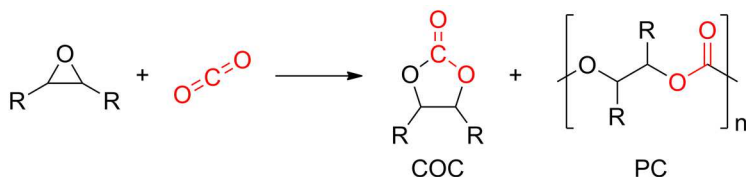
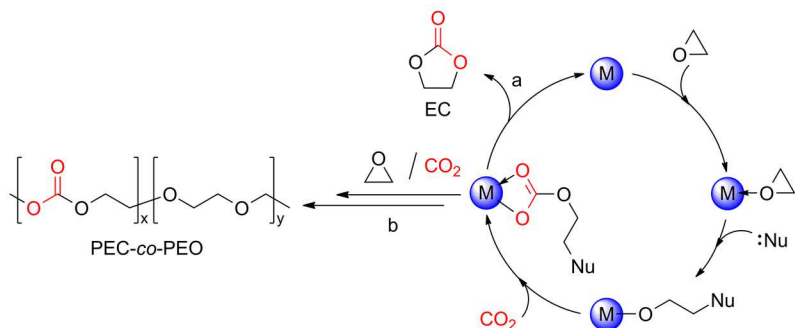


Figure 3 Reaction of CO₂ with epoxide forming cyclic organic carbonate (COC) and polycarbonate PC.

The COCs are non-toxic and poorly flammable, with high dipole moments and boiling points. They find application as aprotic solvents and electrolytes for lithium ion batteries. In addition, they can serve as intermediates for the production of polyurethanes, herbicides and plasticizers. The aliphatic polycarbonates became attractive because of the possibility to use them in substitution of the known bisphenol-A polycarbonate (BPA-PC). Indeed the BPA, released after the hydrolysis of the polymer, was found to act as endocrine disruptor, while the hydrolysis of aliphatic PC brings to the formation of non-toxic diols.⁵ Thanks to their very good properties, such as: high transparency, lightness, strength, processability and electrical insulation, polycarbonates are a class of polymeric material with many applications in the electronics, automotive, glazing etc.

In the design of an efficient CO₂/epoxides reaction process, the use of an appropriate catalytic system plays a key role. Indeed, for the uncatalyzed process, high energy barriers have been found, resulting in a sluggish reaction. For example, the energy barrier for the uncatalyzed formation of propylene carbonate (PC) was calculated by DFT and found to be as high as 58 kcal·mol⁻¹.⁶ At present, despite the number of organocatalysts is growing in the last period,⁷ the most efficient systems for this reaction are based on metal complexes, often in combination with a suitable co-catalyst.⁸

The general reaction mechanism for the metal mediated reaction of CO₂ with ethylene oxide (EO) is depicted in Scheme 1.



Scheme 1 Metal-mediated coupling of CO₂ with ethylene carbonate (EC).

The reaction pathway starts with the coordination of the epoxy ring to the Lewis acidic metal centre. The activated epoxide undergoes to the nucleophilic attack from a nucleophile present in the reaction medium, deriving from the co-catalyst or the metal catalyst, with the resulting opening of the ring. The insertion of CO₂ into the metal-oxygen bond of the alcoholate intermediate, generates a new metal-carbonate species. At this stage, the reaction can follow two different pathways: in the case the back-biting reaction is the predominant process, the ring-closing of the five-membered carbonate occurs, with formation of the ethylene carbonate EC (Scheme 1a); if the alternate insertion of the epoxide with CO₂ takes place, polycarbonate is formed. However, in the case in which the consecutive insertion of epoxide molecules is possible, a polycarbonate-co-polyether (PEC-co-PEO) polymer is obtained (Scheme 1b).

1.3 Catalytic systems for cyclic organic carbonates formation

A large number of metal based complexes for the production of cyclic organic carbonates from CO₂ and epoxides was reported in literature.⁸ As a matter of fact, the most active and selective are based on aluminium, zinc and magnesium bearing salen, porphyrin or nitrogen containing ligands. A non-exhaustive description of the most active and selective catalytic systems is reported in this paragraph.

In 2007, a dinuclear aluminium salen complex with a μ -oxo-bridge was reported by North *et al.* (Figure 4).⁹ In this case the synthesis of COCs was accomplished at 25 °C, with a catalyst loading of 2.5 mol%.

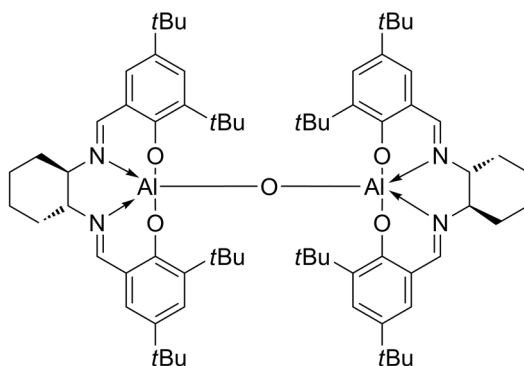


Figure 4 Dinuclear Al(salen) complex reported by North.⁹

This system is more active when compared with the monometallic analogue. Such enhancement was ascribed to the presence of two close metal centres, leading to the simultaneous activation of CO₂ and the epoxide.¹⁰ A Zn(salophen) complex was soon later reported by Kleij *et al.*, in which the steric hindrance of the substituents prevents the dimerization of the compound (Figure 5).¹¹

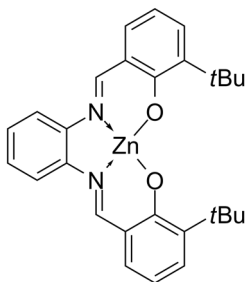


Figure 5 Mononuclear Zn(salophen) complex reported by Kleij.¹¹

In this case the constrained planar geometry of the ligand induced an enhanced Lewis acidity in the metal centre, and the complex is active under mild reaction conditions; however the reaction was confined to the use of terminal epoxides as the substrate. The effect of the nuclearity on the catalytic activity was also explored by Ema

and co-workers in the case of porphyrin-based catalysts containing one, two or three Mg centres (Figure 6).¹²

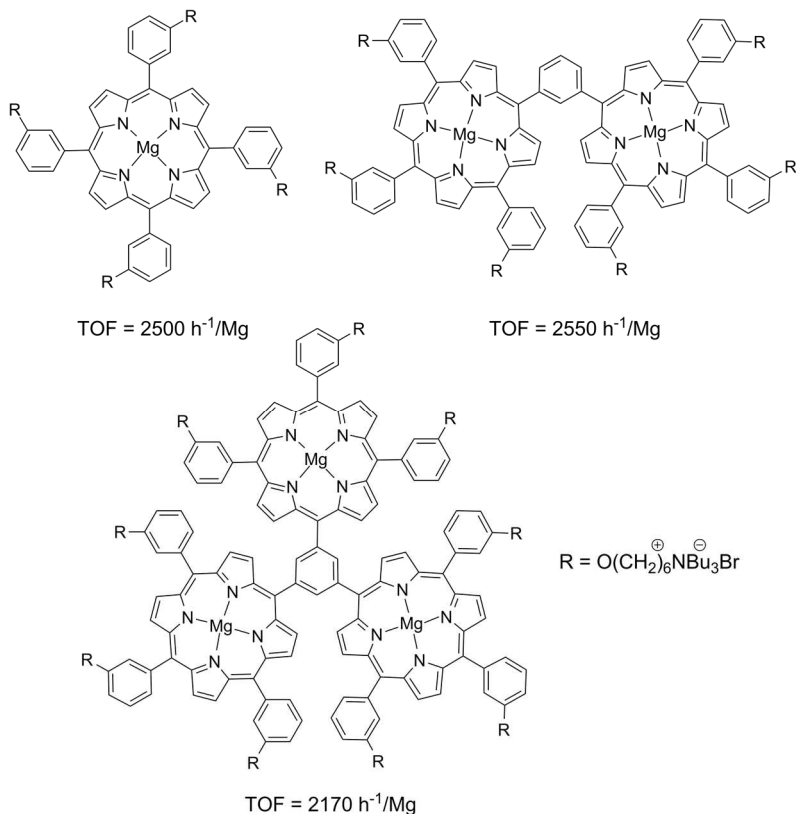


Figure 6 Porphyrin bifunctional Mg catalysts reported by Ema.¹²

The conversion of 1,2-hexene oxide (HO) into the corresponding carbonate was performed under the same reaction conditions, namely 120 °C and 17 bar of CO₂ pressure. As a matter of fact the catalytic activity is higher in the case of the trinuclear complex, if calculated on a molar basis. However, taking into account the number of metal centre per catalyst molecule, the activity was found to be almost the same in all the cases. This finding suggests that, for this system, each catalytic site operate independently from the others.^{7,12c} One of the most relevant examples is the amino(tri-phenolate) aluminium complex reported by Kleij *et al.* in 2003 for the selective production of highly functional COCs (Figure 7).¹³ This

compound, in combination with bis(triphenylphosphine)iminium iodide ([PPN]I) or bromide ([PPN]Br), resulted to be a very effective catalytic system for the synthesis of COCs with very high activity (TOF = 36000 h⁻¹ in the case of HO as the substrate at 90 °C and 10 bar of CO₂ pressure).

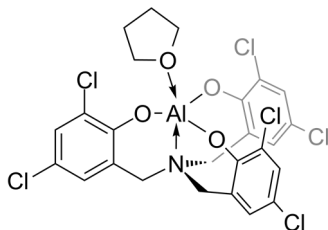


Figure 7 Amino(tri-phenolate) Al complex reported by Kleij.¹³

The application of a series of Cr(salophen) complexes in the formation of COCs under ambient temperature and pressure was described by North and co-workers in 2016 (Figure 8).¹⁴

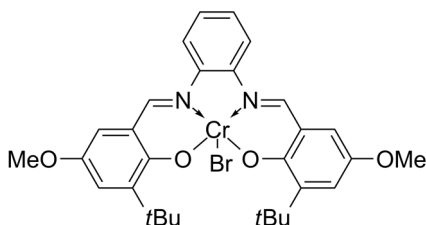


Figure 8 Chromium salophen complex reported by North.¹⁴

Although this system was found to be able to promote the cycloaddition of CO₂ to a variety of epoxides under very mild reaction conditions, the catalytic activity is not astonishing (highest TOF = 6 h⁻¹ in the case of styrene oxide), especially considering that the loading of Cr(III) in the reaction is of 2.5 mol%. Remarkably, the reaction with cyclohexene oxide (CHO) was not completely selective, leading to a mixture of the cyclic and the polymeric products. Very recently a new heteroscorpionate lanthanum complex was reported by Otero *et al* (Figure 9).¹⁵ In combination with one equivalent of tetrabutylammonium bromide (TBAB), and using styrene oxide (SO) as the substrate, an initial TOF of 15000 h⁻¹ was recorded at 110 °C. The reaction of a wide range of substrate was performed under relatively mild reaction conditions (70 °C, 10 bar of CO₂ pressure).

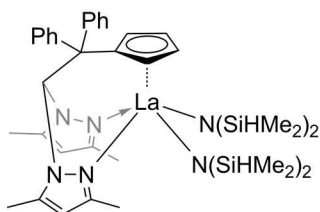


Figure 9 Heteroscorpionate La complex reported by Otero.¹⁵

In all cases the selective formation of the cyclic product was observed. Remarkably, several examples of bio-based cyclic carbonates were obtained.

1.4 Catalytic systems for polycarbonates formation

The co-polymerization of carbon dioxide with epoxides was reported for the first time by Inoue *et al.* when, in 1969, they combined $ZnEt_2$ with water to obtain polymeric product from CO_2 and propylene oxide.¹⁶ From that moment up to now, many homogeneous catalysts for the production of aliphatic polycarbonates have been developed, especially during the last twenty years. In addition to zinc, typical efficient catalysts are based on metals such as: magnesium, aluminium, cobalt and chrome. These developments have been extensively reviewed.¹⁷ As reported by Williams *et al.*,¹⁸ two general classes of homogeneous catalyst can be identified:

- a) *bicomponent systems*, including metal(III) complexes (e.g. Co, Cr, Al) in combination with a co-catalyst (e.g. [PPN]Cl, DMAP).
- b) *bimetallic systems*, including metal(II/III) complexes (e.g. Zn, Mg, Co, Cr), in which the two metals are chelated by a tethered mononucleating ligand or by a macrocyclic dinucleating ligand.

In the next paragraphs, a selection of some of the most representative example is collected.

1.4.1 Bicomponent systems

The bicomponent catalytic systems are generally used in combination with an exogenous co-catalyst, typically a bis(triphenylphosphine)iminium ([PPN]X) or a tetrabutylammonium halide (TBAX). One of the first example was the aluminium porphyrin complex reported in 1978 by Inoue.¹⁹ In this case the controlled co-

polymerization of CO₂ with PO, at room temperature and low pressure, was accomplished.

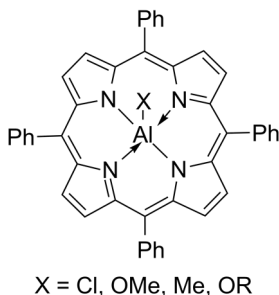


Figure 10 Aluminium porphyrin complexes reported by Inoue.¹⁹

Subsequently, several studies were conducted on the influence of the metal centre and porphyrin substitution, especially from Rieger and co-workers.²⁰ From these investigations emerges that the Cr(III) porphyrin complexes, containing electron-withdrawing groups, are the most active among all the combinations investigated. Salen ligand based complexes represent one of the most effective system for the co-polymerization reaction, in particular those of Co(III) and Cr(III) Figure 11.

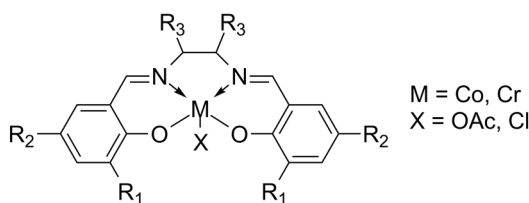


Figure 11 Example of Co(III) and Cr(III) salen complexes.

Many examples have been reported during the last decade, especially from Darensbourg, Rieger, Coates and Nozaki. In particular Nozaki *et al.* reported in 2006 the first example of bifunctional catalyst (Figure 12a).²¹ In this case, the presence of a piperidinium moiety on the salen ligand renders the use of an exogenous co-catalyst superfluous, reaching high selectivity toward the formation of polycarbonate from terminal epoxides, with a TOF = 250 h⁻¹ at room temperature. Further modifications on the salen ligands have been made later by Lee *et al.* with the introduction of flexible arms binding ammonium halide groups (Figure 12b).²² This

type of bifunctional complex was reported to be very active in the copolymerization of CO₂ with PO (TOF = 26000 h⁻¹), even at a very high monomer/catalyst ratio (25000/1).

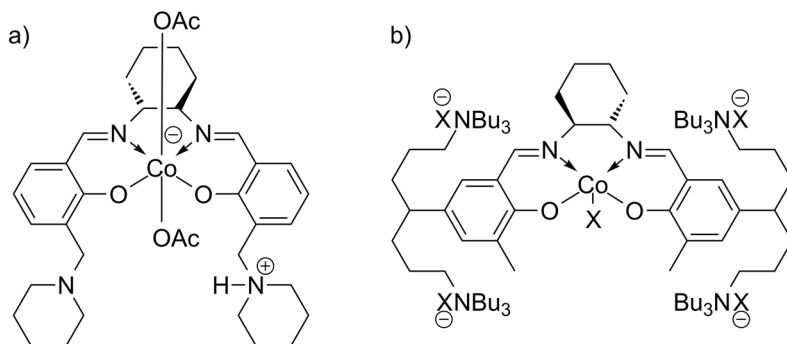


Figure 12 Bifunctional catalysts reported by Nozaki (a)²¹ and Lee (b)²².

1.4.2 Bimetallic systems

A seminal work was reported by Coates in 1998, describing the use of a β -diiminato (BDI) Zn complex as an efficient single-component catalyst for the co-polymerization of cyclohexene oxide with CO₂.²³ Subsequent mechanistic investigation conducted by varying the bulkiness of the substituents on the ligand (Figure 13), revealed the fundamental role of a bimetallic mechanism in the determination of the catalytic activity. Indeed the highest activity (TOF = 730 h⁻¹) was observed in the case of a “loosely associated” dimer existing under the co-polymerization reaction conditions.²⁴

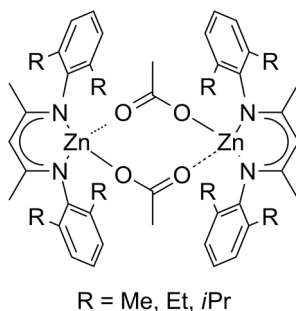


Figure 13 BDI-Zn complexes reported by Coates.²⁴

Successively, Lee and co-workers, reported the use of dinuclear bis(anilido-aldimine)Zn complexes as efficient catalysts for the co-

polymerization of CHO and CO₂ with TOF as high as 200 h⁻¹.²⁵ The catalytic activity was depending on the electron-withdrawing properties of the ligand (Figure 14).²⁶

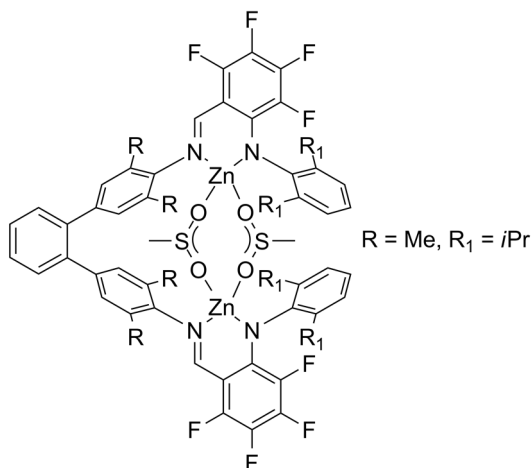


Figure 14 Bis(anilido-aldimine)Zn complex reported by Lee.²⁶

Indeed the Zn-Zn distance was shorter in the case of the fluorinated compound, and the TOF was increased up to 2860 h⁻¹. At the same time, as a drawback, the selectivity in carbonate linkages diminished with respect to the non-fluorinated system. More recently, the research group of Rieger, succeeded in tethering two β-diiminate moieties into one ligand, with outstanding results (Figure 15).²⁷



Figure 15 Highly active dinuclear zinc complex reported by Rieger.²⁷

The TOF for the production of poly(cyclohexene carbonate) (PCHC) reached the value 155000 h⁻¹, at 100 °C and 30 bar of CO₂ pressure, with molecular weights around 300000 Da. Williams and co-workers investigated the properties of Zn and Mg bimetallic complexes as well, based on a reduced Robson-type ligand (Figure 16).²⁸ The di-

zinc catalyst (Figure 16a) was one of the first examples to show promising activity under atmospheric (1 bar) pressure of CO₂ (TOF = 25 h⁻¹ at 100 °C).

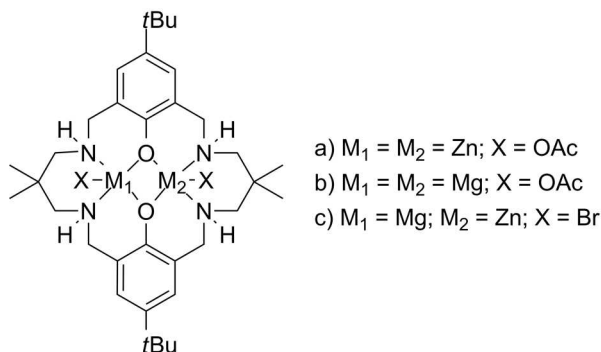


Figure 16 Bimetallic Zn and Mg complexes reported by Williams.²⁸

The substitution of zinc with magnesium (Figure 16b) increased both the catalytic activity (165 h⁻¹) and chemoselectivity toward the polycarbonate formation (>99%). However bimodal molecular weights distributions were obtained. Finally, the catalytic performances of an heterobimetallic Zn/Mg complex were investigated (Figure 16c). With respect to the corresponding homometallic complexes, an enhancement in catalytic activity was observed. Indeed the heterobimetallic Zn/Mg catalyst alone showed a TOF about five times the one recorded using an equimolar mixture of Zn and Mg homometallic complexes (34 and 7 h⁻¹ respectively), with very narrow monomodal distributions of the molecular weights (1.03 < \bar{M}_w/\bar{M}_n < 1.14).

1.5 Iron based catalytic systems

The catalytic systems described in the previous paragraphs are all based on metals such as Zn, Mg, Al, Co and Cr. All these metals have risen health and/or environment concerns. Moreover most of them have also been recently defined as endangered elements, *i.e.* an element that will be not available anymore at an affordable price in the next future.²⁹ Beside to these metals, an ideal candidate for the development of environmental and economic sustainable catalytic systems seems to be iron; indeed, it is the most abundant metal on the Earth crust (after aluminium) rendering this element a cost-effective alternative to other more precious metals. Moreover,

many iron compounds are assimilated into biological systems, and a relatively low toxicity was observed for many iron based compounds. These aspects have to be taken into accounts carefully during the improvement of processes for the pharmaceutical and food industries. On the bases of these considerations, the development of iron catalytic systems for transformations in organic chemistry impressively increased during the last twenty years. Different books and reviews have been dedicated to this argument.³⁰ Nevertheless, the amount of iron-based catalytic systems for the coupling reaction of carbon dioxide with epoxide is still limited. The first example of an iron-based complex capable to promote the reaction between CO₂ and epoxide was reported in 2000 by He *et al.*³¹ In this study, the authors investigated the use of different metallo-phthalocyanine, combined with tributylamine as the co-catalyst, for the formation of cyclic carbonates from terminal epoxides.

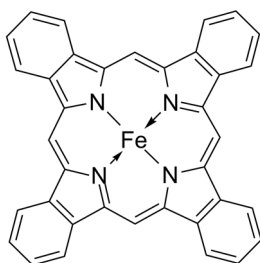


Figure 17 Fe(II) phthalocyanine complex reported by He.³¹

The Fe(II)-phthalocyanine complex (Figure 17) resulted one of the less active, however it is able to promote the selective formation of the cyclic carbonate from ethylene oxide (EO) and epichlorhydrin (EPC) at 140 °C, with a TOF of 130 and 1800 h⁻¹ respectively.

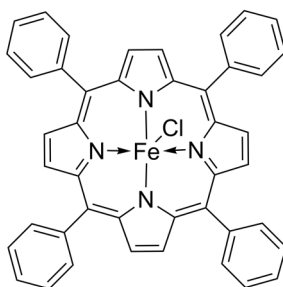


Figure 18 Fe(III) porphyrin complex reported by Jing.³²

The use of another macrocyclic ligand, such as porphyrin, was then described by Jing and co-workers.³² Also in this case the activity of several metal-porphyrin complexes was compared, in the presence of phenyltrimethylammonium tribromide (PTAT) as the co-catalyst. While the Fe(III) based catalyst (Figure 18) resulted one of the less efficient, the formation of propylene carbonate was accomplished at 25 °C and 7 bar of CO₂ pressure, with a TOF of 30 h⁻¹. In 2011 Rieger reported the synthesis and characterization of a tetraamine-Fe(II) complex and its use as a single component catalyst for the selective production of PC (Figure 19).³³

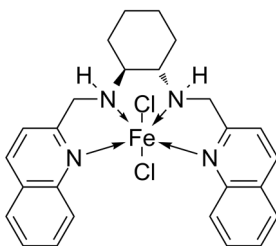


Figure 19 Tetraamine Fe(II) complex reported by Rieger.³³

Indeed, the complex used in this study was capable to promote the reaction of CO₂ with PO, at 100 °C and 15 bar of CO₂ pressure, even in the absence of any co-catalyst, with a TOF of 40 h⁻¹. A kinetic study was also performed by the authors to better understand the role of the metal centre during the reaction. The reaction pathway was found to follow a bimetallic mechanism, and the dissociation of a chlorine atom from an iron centre was postulated to explain the activation of the epoxy ring.

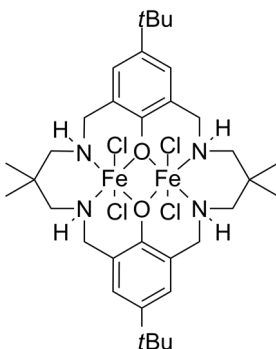


Figure 20 Bimetallic Fe(III) complex reported by Williams.³⁴

In the same year, Williams *et al.* described the synthesis of a dinuclear Fe(III) complex based on a reduced Robson-type ligand (Figure 20), analogous to the Zn based one previously reported.³⁴ When employed as a single component catalyst for the reaction of CHO with CO₂, this complex produced PCHC with high selectivity and activity (TOF = 107 h⁻¹) at 80 °C. When [PPN]Cl was used as co-catalyst, under similar conditions, the TOF reduced to 9 h⁻¹, however an inversion in the chemoselectivity was observed. Indeed the *cis* form of cyclohexene carbonate (*cis*-CHC) was obtained as the only product. Notably, it was the first example of an Fe based catalyst able to produce both the cyclic and polymeric product, depending on the reaction conditions. Another example of dinuclear Fe(III) complex, bearing an amino-triphenolate ligand, was reported by Kleij *et al* (Figure 21).³⁵

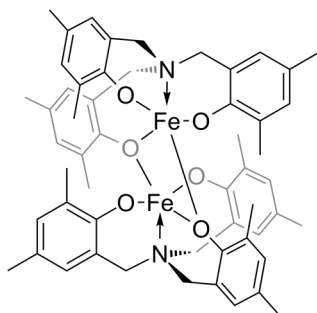


Figure 21 Dimeric amino-triphenolate Fe(III) complex reported by Kleij.³⁵

Despite the dimeric nature of the native complex, it was found to break into two monometallic portions, with each metal centre chelated by one ligand molecule and a Lewis base (pyridine or propylene oxide) saturating the coordination sphere. Using this complex in combination with tetrabutylammonium iodide (TBAI) as the co-catalyst, a broad number of both terminal and internal epoxide were selectively converted into the corresponding cyclic carbonate. Although reaction were conducted mainly at 25 °C, the catalytic activity was not very high (TOF = 5 h⁻¹ using HO as the substrate). The application of an analogous mononuclear Fe(III) complex, for the selective production of PCHC was described by Kleij and Pescarmona (Figure 21).³⁶ Actually, the monomeric complex produces PCHC with high activity (TOF=200 h⁻¹) when activated by a suitable co-catalyst such as [PPN]Cl.

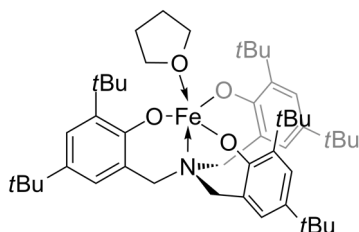


Figure 22 Fe(III) amino-triphenolate complex reported by Pescarmona.³⁶

However the reaction must be conducted in supercritical CO₂ in order to obtain high degree of selectivity, and molecular weights higher than 10 kDa are difficult to obtain. A breakthrough was marked in 2013, when Nozaki and co-workers communicated the use of a dinuclear oxo-bridged iron corrole complex for the co-polymerization of CO₂, not only with CHO, but also with terminal epoxides (Figure 23).³⁷

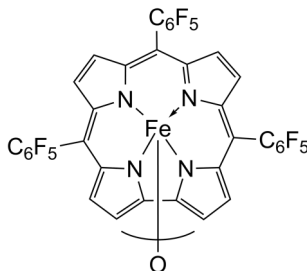


Figure 23 Iron(IV) corrole dinuclear complex reported by Nozaki.³⁷

Indeed, using [PPN]Cl as the co-catalyst, the co-polymerization of CO₂ with PO was accomplished. The catalytic activity was depending from the [PPN]Cl/Fe molar ratio, with the highest activity observed using an equimolar mixture at 80 °C and 20 bar of CO₂ pressure (TOF = 1300 h⁻¹). As a drawback, increasing the catalytic activity increases the amount of polyether fraction in the co-polymer up to 90%. Remarkably the co-polymerization of CO₂ with glycidyl phenyl ether (GPE) was also performed. In this case an isotactic enriched crystalline polymer was obtained, with a melting point of 180 °C.

It was against this background that, in 2015, the research group of Capacchione described the synthesis and characterization of the new air-stable bimetallic Fe(III) complex **1**, supported by a new trianionic pentadentate bis-thioether-tri-phenolate ligand.³⁸ In contrast to what was observed in the case of the dimeric amino-

triphenolate Fe(III) complexes reported by Kleij (Figure 21), the bimetallic structure of complex **1** was preserved in solution even after the addition of a large excess of epichlorohydrin or pyridine. On this basis the structure reported in Figure 24, with phenolate oxygen bridges, was proposed.

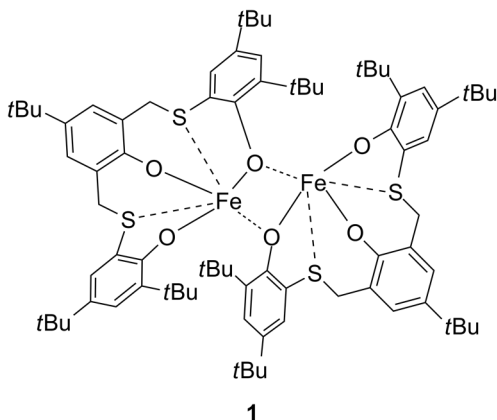


Figure 24 Bis-thioether tri-phenolate dinuclear Fe(III) complex **1** reported by Capacchione.³⁸

When activated by TBAB, the complex **1** resulted a very effective catalyst for the selective production of COCs from both terminal and internal epoxides, under relatively mild reaction conditions (100 °C, 20 bar CO₂ pressure, 0.025 mol% catalyst loading). In particular PC was obtained with a TOF of 580 h⁻¹, that was the highest activity reported for an iron based complex at that time. The catalyst was also found to be highly stereoselective. Indeed, starting from CHO, *cis*-CHC was exclusively obtained, while using the enantiomerically enriched (*R*)-styrene oxide (*ee* = 94%) as the substrate a good degree of stereoretention was observed (*ee* = 74%).

1.6 Motivation of the thesis

All the catalytic systems reported in the previous paragraphs are based on nitrogen containing ligands. Differently, in the complex **1** neutral donor sulphur atoms are present in the coordination sphere of the Fe(III) centres. The beneficial role on the catalytic activity of metal based catalysts attributed to the existence of soft sulphur atoms in the ligand structure was already observed. In particular in the case of Group 4 metals based catalysts for the polymerization of

olefins, via poly-insertion mechanism,³⁹ and cyclic esters, via coordination-insertion mechanism,⁴⁰ actually demonstrating that the sulphur atoms can play a dual role in the determination of the catalytic activity: on one hand the Lewis acidity of the catalytic centre can be modulated, on the other the decoordination of an hemi-labile neutral donor generates a vacant site on the metal. Both the effects facilitate the coordination of the substrate to the catalytic active species, enhancing the catalytic activity. On the basis of this considerations, one may argue that the introduction of the neutral soft donor sulphur atoms in the coordination sphere of iron is the responsible of the promising catalytic performances, observed for catalyst **1**, in the coupling reaction of CO₂ with epoxides. This result pushed for a deeper investigation of the use of iron based catalytic systems in this reaction.

Starting from the bimetallic thioether-triphenolate complex **1**, a number of questions arise:

- ◇ Do the steric hindrance or electronic properties of the ligand influence the catalytic activity?
- ◇ Does the mechanism involve one or two metal centres?
- ◇ Is the bimetallic nature of the complex essential to obtain highly active catalysts?
- ◇ What is the relationship between the catalyst structure and the selectivity of the reaction?

To give an answer to all these questions is essential to open the possibility to design very active and selective catalytic systems. It is the aim of this thesis to disclose this possibility, investigating the application of sulphur containing ligand based iron complexes, starting from the encouraging results obtained in the case of the complex **1**.

1.7 References

- ¹ Trends in Atmospheric Carbon Dioxide; www.esrl.noaa.gov/gmd/ccgg/trends/full.html, ESRL (accessed November 2017).
- ² <http://unfccc.int/resource/docs/2015/cop21/eng/l09r01.pdf>
- ³ *Carbon Dioxide as Chemical Feedstock*, ed. Aresta M., WILEY-VCH Verlag GmbH & Co. KGaA, Weinheim, **2010**.
- ⁴ a) Sakakura T., Choi J.-C., Yasuda H., *Chem. Rev.*, **2007**, *107*, 2365-2387. b) Cokoja M., Bruckmeier C., Rieger B., Herrmann W. A., Kühn F. E., *Angew. Chem. Int. Ed.*, **2011**, *50*, 8510-8537. c) Aresta M., Dibenedetto A., Angelini A., *Chem. Rev.*, **2014**, *114*, 1709-1742.
- ⁵ a) Morin N., Arp H.P.H., Hale S.E., *Environ. Sci. Technol.*, **2015**, *49*, 7675-7683. b) *MSC unanimously agrees that Bisphenol A is an endocrine disruptor*, European Chemical Agency ECHA, <https://echa.europa.eu/> (accessed November 2017).
- ⁶ Sun, H.; Zhang, D. J., *Phys. Chem. A*, **2007**, *111*, 8036-8043.
- ⁷ G. Fiorani, W. Guo, A. W. Kleij, *Green Chem.*, **2015**, *17*, 1375-1389.
- ⁸ Martín C., Fiorani G., Kleij A. W., *ACS Catal.*, **2015**, *5*, 1353-1370.
- ⁹ a) Meléndez, J.; North, M.; Pasquale, R., *Eur. J. Inorg. Chem.*, **2007**, 3323-3326. b) North, M.; Pasquale, R., *Angew. Chem., Int. Ed.*, **2009**, *48*, 2946-2948. c) Clegg, W.; Harrington, R. W.; North, M.; Pasquale, R., *Chem. Eur. J.*, **2010**, *16*, 6828-6843.
- ¹⁰ North, M.; Pasquale, R., *Angew. Chem. Int. Ed.*, **2009**, *48*, 2946-2948.
- ¹¹ a) Decortes, A.; Martinez Belmonte, M.; Benet-Buchholz, J.; Kleij, A. W., *Chem. Commun.*, **2010**, *46*, 4580-4582. b) Decortes, A.; Kleij, A. W., *ChemCatChem*, **2011**, *3*, 831-834.
- ¹² a) Ema, T.; Miyazaki, Y.; Koyama, S.; Yano, Y.; Sakai, T., *Chem. Commun.*, **2012**, *48*, 4489-4491. b) Ema, T.; Miyazaki, Y.; Shimonishi, J.; Maeda, C.; Hasegawa, J.-Y. *J. Am. Chem. Soc.*, **2014**, *136*, 15270-15279. c) Maeda, C.; Taniguchi, T.; Ogawa, K.; Ema, T., *Angew. Chem., Int. Ed.*, **2015**, *54*, 134-138.
- ¹³ a) Whiteoak, C. J., Kielland, N., Laserna, V., Escudero-Adán, E. C., Martin, E., Kleij, A. W., *J. Am. Chem. Soc.*, **2013**, *135*, 1228-1231. b) Whiteoak, C. J., Kielland, N., Laserna, V., Castro-Gómez, F., Martin, E., Escudero-Adán, E. C., Bo, C., Kleij, A. W., *Chem. Eur. J.*, **2014**, *20*, 2264-2275.
- ¹⁴ Castro-Osma J. A., Lamb K. J., North M., *ACS Catal.* **2016**, *6*, 5012-5025.

- ¹⁵ Martinez, J., Fernandez-Baeza, J., Sanchez-Barba, L. F., Castro-Osma, J. A., Lara-Sanchez, A., Otero, A., *ChemSusChem*, **2017**, *10*, 2886-2890.
- ¹⁶ Inoue, S., Koinuma, H., Tsuruta T., *Makromol. Chem.* **1969**, *130*, 210.
- ¹⁷ a) Darensbourg D. J., *Chem. Rev.*, **2007**, *107*, 2388-2410. b) Yeung A. D., Darensbourg D. J., *Polym. Chem.*, **2014**, *5*, 3949-3962. c) Darensbourg D. J., Wilson S. J., *Green Chemistry*, **2012**, *14*, 2665-2671. d) Kember M. R., Buchard A., Williams C. K., *Chem. Commun.*, **2011**, *47*, 141-163. e) Lu X-B, Ren W-M, Wu G-P., *Acc. Chem. Res.*, **2012**, *45*, 1721-1735. f) Klaus S., Lehenmeier M. W., Anderson C. E., Rieger B., *Coord. Chem. Rev.*, **2011**, *255*, 1460-1479. g) Coates G. W., Moore D. R., *Angew. Chem. Int. Ed.*, **2004**, *43*, 6618-6639.
- ¹⁸ Trott G., Saini P. K., Williams C. K., *Phil. Trans. R. Soc. A*, **2016**, *374*: 20150085.
- ¹⁹ Takeda N, Inoue S., *Macromol. Chem. Phys.*, **1978**, *179*, 1377-1381.
- ²⁰ a) Anderson C. E., Vagin S. I., Xia W., Jin H., Rieger B., *Macromolecules*, **2012**, *45*, 6840-6849. b) Xia W., Salmeia K. A., Vagin S. I., Rieger B., *Chem. Eur. J.*, **2015**, *21*, 4384-4390.
- ²¹ Nakano K., Kamada T., Nozaki K., *Angew. Chem. Int. Ed.*, **2006**, *45*, 7274-7277.
- ²² Sujith S., Min J. K., Seong J. E., Na S. J., Lee B. Y., *Angew. Chem. Int. Ed.*, **2008**, *47*, 7306-7309.
- ²³ Cheng M., Lobkovsky E. B., Coates G. W., *J. Am. Chem. Soc.*, **1998**, *120*, 11018-11019.
- ²⁴ Moore D. R., Cheng M., Lobkovsky E. B., Coates G. W., *J. Am. Chem. Soc.*, **2003**, *125*, 11911-11924.
- ²⁵ Lee B. Y., Kwon H. Y., Lee S. Y., Na S. J., Han S-I, Yun H., Lee H., Park Y-W., *J. Am. Chem. Soc.*, **2005**, *127*, 3031-3037.
- ²⁶ Bok T., Yun H., Lee B. Y., *Inorg. Chem.*, **2006**, *45*, 4228-4237.
- ²⁷ Kissling S., Lehenmeier M. W., Altenbuchner P. T., Kronast A., Reiter M., Deglmann P., Seemann U. B., Rieger B., *Chem. Commun.*, **2015**, *51*, 4579-4582.
- ²⁸ a) Kember M. R., Knight P. D., Reung P. T. R., Williams C. K., *Angew. Chem. Int. Ed.*, **2009**, *48*, 931-933. b) Kember M. R., Williams C. K., *J. Am. Chem. Soc.*, **2012**, *134*, 15676-15679. c) Garden J. A., Prabhjot K. S., Williams C. K., *J. Am. Chem. Soc.*, **2015**, *137*, 15078-15081.
- ²⁹ a) *Element Recovery and Sustainability RSC Green Chemistry series*, vol. 22, Ed.: Hunt A. J., RSC Publishing, Cambridge, **2013**. b) Izatt R. M., Izatt S. R., Bruening R. L., Izatt N. E., Moyer B. A., *Chem. Soc. Rev.*, **2014**, *43*, 2451-2475.

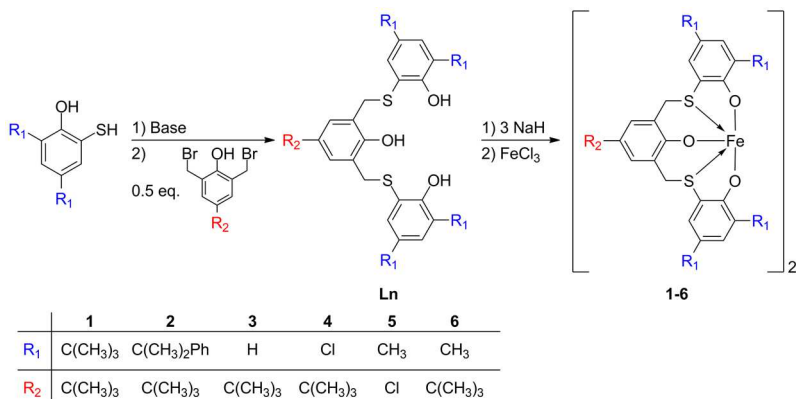
- ³⁰ a) *Iron Catalysis in Organic Chemistry*, ed. Plietker, B., Wiley-VCH: Weinheim, Germany, **2008**. b) *Iron Catalysis*, ed. Plietker, B., Springer-Verlag Berlin, Heidelberg, **2011**. c) *Iron Catalysis II*, ed. Bauer, E., Springer-Verlag Berlin, Heidelberg, **2015**. d) Bauer I., Knölker H.-J., *Chem. Rev.*, **2015**, *115*, 3170-3387. e) Fürstner A., *ACS Cent. Sci.*, **2016**, *2*, 778-789.
- ³¹ Ji D., Lu X., He R., *Applied Catalysis A: General*, **2000**, *203*, 329-333.
- ³² Jin L., Jing H., Chang T., Bu X., Wang L., Liu Z., *Applied Catalysis A: General*, **2007**, *261*, 262-266.
- ³³ Dengler J. E., Lehenmeier M. W., Klaus S., Anderson C. E., Herdtweck E., Rieger B., *Eur. J. Inorg. Chem.*, **2011**, 336-343.
- ³⁴ Buchard A., Kember M. R., Sandeman K. G., Williams C. K., *Chem. Commun.*, **2011**, *47*, 212-214.
- ³⁵ Whiteoak C. J., Martin E., Martínez Belmonte M., Benet-Buchholz J., Kleij A. W., *Adv. Synth. Catal.*, **2012**, *354*, 469-476.
- ³⁶ Taherimehr M., Al-Amsyar S. M., Whiteoak C. J., Kleij A. W., Pescarmona P. P., *Green Chem.*, **2013**, *15*, 3083-3090.
- ³⁷ Nakano K., Kobayashi K., Ohkawara T., Imoto H., Nozaki K., *J. Am. Chem. Soc.*, **2013**, *135*, 8456-8459.
- ³⁸ Buonerba A., De Nisi A., Grassi A., Milione S., Capacchione C.,* Vagin S. and Rieger B., *Catal. Sci. Technol.*, **2015**, *5*, 118-123.
- ³⁹ Capacchione C., Proto A., Ebeling H., Mülhaupt R., Möller K., Spaniol T. P., J. Okuda, *J. Am. Chem. Soc.*, **2003**, *125*, 4964-4965.
- ⁴⁰ Della Monica F., Luciano E., Roviello G., Grassi A., Milione S., Capacchione C., *Macromolecules*, **2014**, *47*, 2830-2841.

2 Bis-thioether-triphenolate iron(III) complexes

In this chapter the synthesis and full characterization of a number of bis-thioether-triphenolate ligands and of the corresponding iron(III) complexes are reported. The application of these compounds as catalyst for chemo- and stereo-selective production of cyclic organic carbonates (COCs) from carbon dioxide and epoxides is described. Insights on the role of the metal centre in the reaction mechanism are given by means of DFT investigation.

2.1 Synthesis and characterization

Motivated by the encouraging results obtained in the cycloaddition of CO₂ to epoxides promoted by the bimetallic thioether-triphenolate Fe(III) complex **1** (see paragraph 1.6) we decided to investigate the catalyst structure-reactivity relationship for this class of compounds. For this purpose, five new bis-thioether-triphenolate ligands (**L2-L6**) were synthesised using the same or modified procedure of ligand **L1** (Scheme 2).⁴¹



Scheme 2. Synthesis of the pro-ligands **L1-L6** and of the reciprocal bimetallic Fe(III) complex **1-6**.

Complexes **2-6**, were obtained by reaction of an equimolar amount of FeCl₃ with the sodium salt of the corresponding pro-ligand in THF, resulting from the reaction of the ligand precursor with 3 equivalents of sodium hydride. More in detail, the bulkiness of the substituent in the R₁ positions was both increased (**L2**) and reduced (**L3**, **L6**), and electron withdrawing chlorine atoms were alternately introduced in positions R₁ and R₂ (**L4**, **L5**).

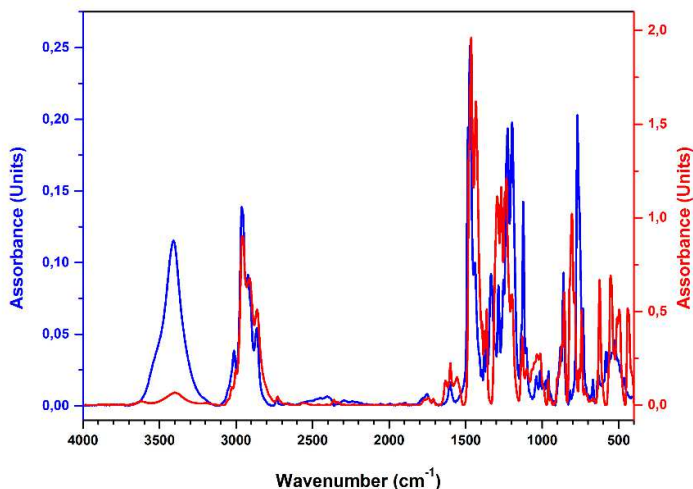


Figure 25 Comparison of the FT-IR spectra of the pro-ligand **L6** (blue curve) and of the iron(III) complex **6** (red curve).

The new ligands were purified by recrystallization or by column chromatography and fully characterized by NMR, elemental analysis, MS, and FT-IR experiments (see the experimental section). All the products were recovered in good yields (from 78 to 97%), as deep-blue powders. The formation of the desired products was confirmed by elemental analysis. In addition, in the FT-IR spectra of the complexes, the disappearance of the hydroxyl group vibration at about 3400 cm^{-1} is evident. The comparison of the FT-IR spectra of complex **6** and the corresponding pro-ligand **L6** is shown in Figure 25 as an example. The shift of the vibration bands relative to the alkyl-sulphide moiety is also observed, indicating the coordination of the sulphur atoms to the iron centre (see FT-IR Characterization). The formation of dimeric structures was supported by the ESI-MS analysis (see ESI-MS Characterization). Indeed the effective magnetic moments (μ_{eff}), determined by means of the Evans method in deuterated toluene at $30\text{ }^{\circ}\text{C}$, are comparable with the calculated value for two isolated high spin (HS) iron(III) centers ($8.37\text{ }\mu\text{B}$). Moreover the magnetic moments measured in the solid state with a magnetic balance, using the Faraday method, are in accordance with the values obtained in solution (Table 1). This finding confirms that the complexes adopt a dinuclear structure both in solution and in solid state.

Table 1 List of the effective magnetic moments (μ_{eff}) in solution and in solid state for Iron(III) complexes **1-6**.

Complex	μ_{eff} (μB)	
	Solution ^a	Solid State ^b
1	8.10 \pm 0.03	7.0 \pm 0.7
2	7.34 \pm 0.02	7.6 \pm 0.8
3	7.20 \pm 0.02	6.7 \pm 0.7
4	7.16 \pm 0.02	6.9 \pm 0.7
5	6.34 \pm 0.02	7.1 \pm 0.7
6	7.63 \pm 0.03	7.2 \pm 0.7

a) Determined with the NMR Evans method at 30 °C in Tol-d8; b) Determined with the Faraday method at 25 °C using a magnetic susceptibility balance.

In the case of the methyl substituted complex **6**, single crystals suitable for x-ray diffraction analysis were grown from a saturated acetonitrile solution.

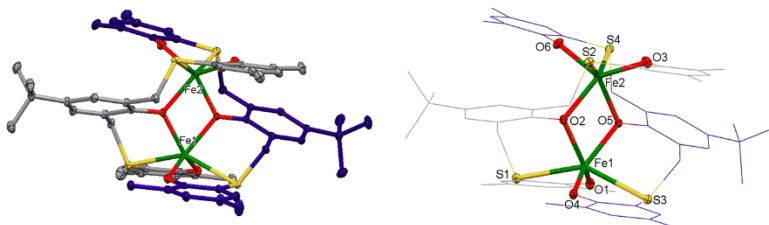


Figure 26 Molecular structure of complex **6**. On the left the structure is shown for the sake of clarity with the C atoms of one of the two ligands represented in violet colour (hydrogen atoms have been omitted). Selected bond lengths (\AA): Fe(1)···Fe(2) 3.331; Fe(1)-O(1) 1.8894(14); Fe(1)-O(4) 1.9030(13) Fe(1)-O(5) 2.0314(13); Fe(1)-O(2) 2.0384(14); Fe(1)-S(1) 2.6102(5); Fe(1)-S(3) 2.6466(5); Fe(2)-O(6) 1.8943(14); Fe(2)-O(3) 1.8994(15); Fe(2)-O(5) 2.0345(13); Fe(2)-O(2) 2.0514(14); Fe(2)-S(2) 2.5914(5); Fe(2)-S(4) 2.6585(5). On the right the coordination geometry of the two iron (III) centres is highlighted.

The molecular structure of **6** is shown in Figure 26. As hypothesized on the basis of the results described above, the compound is bimetallic in nature. It is important to underline that each ligand binds both the iron atoms, with the central phenolate moiety bridging the metal centres, probably to relieve the steric strain of the ligand. The

molecule adopts an idealized D_2 symmetry with one axis being coincident with the Fe-Fe vector. Each iron(III) in the dimeric complex exhibits a six-coordinated $[O_4S_2]$ environment generated by four phenoxo oxygen and two sulphur atoms. The Fe-O(bridging) bond lengths in **6** are longer than the Fe-O(non-bridging) ones. These Fe-O distances are slightly longer, for example, than the corresponding ones found in an iron(III) thioalix[4]arene complex.⁴² The Fe-S interactions are rather weak and fall in the range 2.5914–2.6585(5) Å whereas the Fe–Fe distance of 3.331 Å indicates that no bonding interactions are present.

2.2 Catalytic activity

All the complexes **1-6** were tested in the coupling reaction of carbon dioxide with (\pm)-propylene oxide (PO) (Table 2).

Table 2 Propylene carbonate formation promoted by Fe(III) complex **1-6**.

Entry ^a	Catalyst	Conversion ^{b,c}	TOF ^d
		mol%	h ⁻¹
1	1	16.8	672
2	2	20.1	804
3	3	16.9	676
4	4	30.2	1208
5	5	43.3	1732
6	6	46.0	1840
7 ^e	-	traces	-

a) Reaction conditions: PO = 5 mL, $7.15 \cdot 10^{-2}$ mol; Catalyst = $1.79 \cdot 10^{-5}$ mol (0.025 mol%); TBAB = $3.57 \cdot 10^{-5}$ mol (0.05 mol%); PO/TBAB/Catalyst = 4000/2/1; T = 100 °C; P(CO₂) = 2.0 MPa; reaction time = 1 h. b) Determined by ¹H NMR using mesitylene as internal standard. c) The selectivity toward the formation of PC was always found to be >99%. d) Turnover frequency ($\text{mol}_{\text{PC}} \cdot \text{mol}_{\text{Catalyst}}^{-1} \cdot \text{reaction time}^{-1}$). e) Control experiment in the absence of the iron catalyst.

Under the reaction conditions previously reported for the complex **1**, (0.025 mol% of catalyst; 0.05 mol% of TBAB; 100 °C; 20 bar of CO₂ pressure) all the complexes showed good activity, with the best performance recorded in the case of the methyl substituted complex **6**, that is about three times more efficient than **1** (compare entries 1 and 6, Table 2). This finding suggests that the less bulky the R₁ substituents are, the highest the activity. However the complex **3**, with no substituents in the R₁ positions, exhibits the same activity of **1** (compare entries 1 and 3, Table 2), and both are less active than the complex **2** with the bulky cumyl substituents (entry 2, Table 2). To solve this apparent contradiction, a deeper investigation was conducted performing other catalytic tests using complexes **1-3** and **6** in the temperature range from 80 °C to 140 °C (Figure 27).

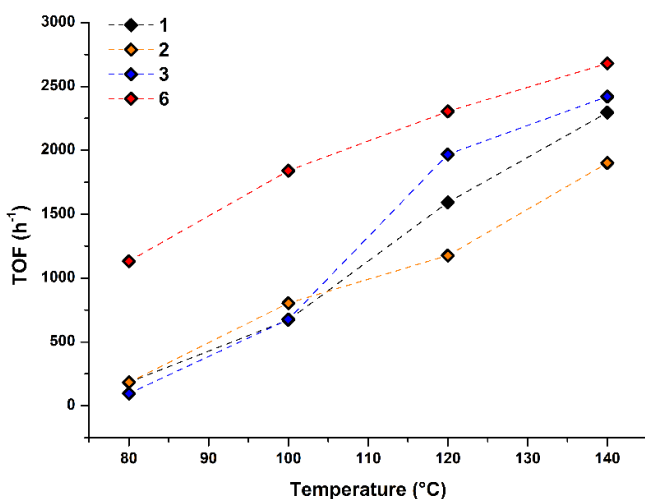


Figure 27 TOF of the iron(III) complexes **1**, **2**, **3** and **6** as a function of the reaction temperature (entries S1-16 Table S 3).

An increase of the activity by increasing the temperature was observed for all the tested catalysts, where the complex **6** is the most active in the whole range. In particular at 140 °C the activity varies in the order **6** > **3** > **1** > **2**, showing that a less encumbered metal centre is more accessible to the substrate. Notably at lower temperature (80-100 °C) the catalytic performances of the catalyst **3** are sensibly lower compared to the more sterically demanding catalysts. This discrepancy is probably due to the lower solubility of the complex **3**

in the reaction medium. On the basis of the results described above, the cycloaddition of CO₂ to (±)-PO, in the presence of 0.025 mol% of **6** under neat condition at 120 °C, was selected as benchmark reaction for the optimization of the reaction parameters. A screening of several commonly employed co-catalysts, namely dimethylaminopyridine (DMAP), bis(triphenylphosphine)iminium chloride ([PPN]Cl) or quaternary ammonium salts such as tetrabutylammonium chloride (TBAC), iodide (TBAI) and bromide (TBAB) in 1:1 molar ratio with respect to iron (0.05 mol%) was performed (Figure 28; entries S15 and S17-22, Table S 3).

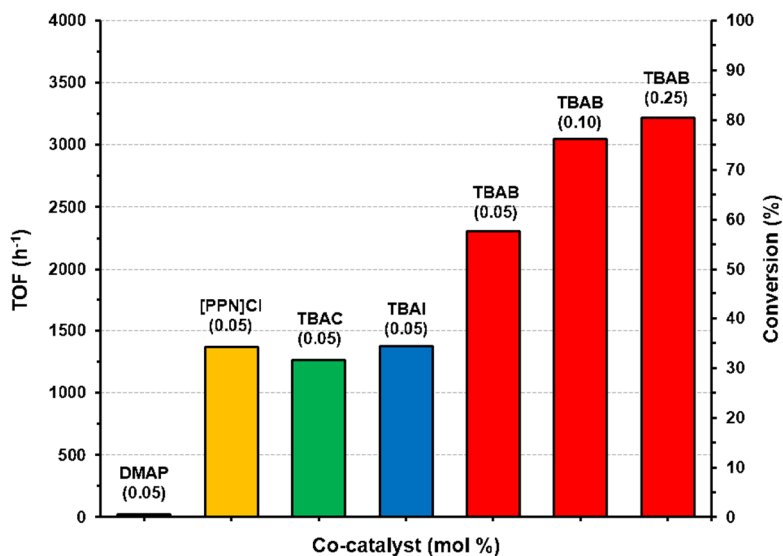


Figure 28 Effect of the co-catalyst type and loading on the catalytic activity of **6** in PO/CO₂ coupling (entries S15 and S17-22, Table S 3).

When the co-catalyst is a neutral Lewis base, such as DMAP, poor activity was recorded comparable to that of the co-catalyst alone. When the co-catalyst is a halide salt the activity increases up to 2300 h⁻¹ in the case of TBAB, demonstrating that the presence of a nucleophilic anion is essential for the activation of the catalyst. Notably increasing the TBAB loading up to 0.25 mol% the catalytic activity was significantly improved to 3300 h⁻¹, reaching a conversion of 82%. A control experiment conducted in the presence of TBAB alone resulted in low conversion (10%, entry S22, Table S 3), highlighting the synergism between the two components of the

catalytic system. The effect of the pressure of CO₂ was also investigated (entries S22 and S24–25, Table S 3). By reducing the pressure from 20 to 5 bar the activity does not drop dramatically, whereas by increasing the pressure to 40 bar an activity enhancement from 3300 to 4000 h⁻¹ was observed, reaching complete and selective conversion of PO to PC in only 1 hour.

Table 3 Propylene carbonate and hexene carbonate formation promoted by Fe(III) complex **1-6** under optimised conditions.

Reaction scheme: Epoxide + CO₂ $\xrightarrow[\text{TBAB}]{\text{1-6}}$ Carbonate

Entry ^a	Catalyst	R	Conversion ^{b,c}	TOF ^d
			mol%	h ⁻¹
1	1	Me	43.0	4300
2	2	Me	35.5	3550
3	3	Me	40.4	4040
4	4	Me	36.3	3630
5	5	Me	50.0	4990
6	6	Me	52.0	5200
7 ^e	-	Me	5	-
8	1	<i>n</i> Bu	45.7	2290
9	2	<i>n</i> Bu	17.9	900
10	3	<i>n</i> Bu	43.1	2160
11	4	<i>n</i> Bu	35.0	1750
12	5	<i>n</i> Bu	67.8	3390
13	6	<i>n</i> Bu	68.9	3450

a) Reaction conditions: T = 120 °C; reaction time = 1 h. For R = Me: PO = 5 mL, 7.15 · 10⁻² mol; Catalyst = 1.43 · 10⁻⁵ mol (0.01 mol%); TBAB = 1.43 · 10⁻⁴ mol (0.1 mol%); P(CO₂) = 2.0 MPa. For R = *n*Bu: HO = 8.6 mL, 7.15 · 10⁻² mol; Complex = 1.43 · 10⁻⁵ mol; TBAB = 1.43 · 10⁻⁴ mol; P(CO₂) = 40 bar. b) Determined by ¹H NMR using mesitylene as internal standard. c) The selectivity toward the formation of PC was always found to be >99%. d) Turnover frequency (mol_{Carbonate} · mol_{Catalyst}⁻¹ · reaction time⁻¹). e) Control experiment in the absence of the iron catalyst.

Encouraged from these good results, the catalyst loading was reduced from 0.025 to 0.01 mol% to compare the catalytic activity of catalysts **1-6** in the formation of PC. The results are listed in Table 3. The methyl substituted complex **6** was found to be the most efficient, with a TOF equal to 5200 h⁻¹ (entry 6, Table 3). To the best of our knowledge this is the highest activity reported so far for an iron based catalytic system in the formation of propylene carbonate from carbon dioxide and propylene oxide. The substantial lower activity exhibited by complexes **1** and **2**, bearing sterically demanding groups on the R₁ positions, confirms that the catalytic activity is strongly influenced by the bulkiness of the substituents on the lateral phenol rings. It is worth noting that complex **5** also proved to be highly active, reaching conversion near to that of **6** (compare entries 5 and 6, Table 3), suggesting that the electronic effect of the substituent R₂ does not play an essential role in the determination of the catalytic performance. On the other hand, in the case of complex **4** the introduction of chlorine atoms in the R₁ positions, has a deleterious effect on the catalytic activity (compare entries 4 and 6, Table 3). To further evaluate the role of the steric demand around the catalytic site on the catalytic performance, the coupling of CO₂ with a bulkier terminal epoxide such as the 1,2-epoxyhexane (HO) was performed (entries 8-13, Table 3). Both **5** and **6** exhibit again the highest activities (respectively 3390 and 3450 h⁻¹), with differences in the order of the experimental error (entries 12 and 13, Table 3). Notably, the longer alkyl chain on the epoxide ring exalts differences in the activity due to the steric hindrance of the substituents in the R₁ positions, with complex **2** displaying a considerably lower activity (entry 9, Table 3). The less sterically demanding complex **3** shows lower activity compared to **6** due to solubility issues in the reaction medium as previously described.

2.3 Scope of the catalyst

In order to investigate the applicability of the catalytic system **6**/TBAB to a wider range of substrates, we performed the coupling reaction of carbon dioxide with a series of mono-, di-substituted and internal epoxides. The results summarized in Chart 1 clearly show that the presence of an electron withdrawing substituent in the substrate, such as a chlorine atom in epichlorohydrin, has a positive effect with a TOF of 7000 h⁻¹.

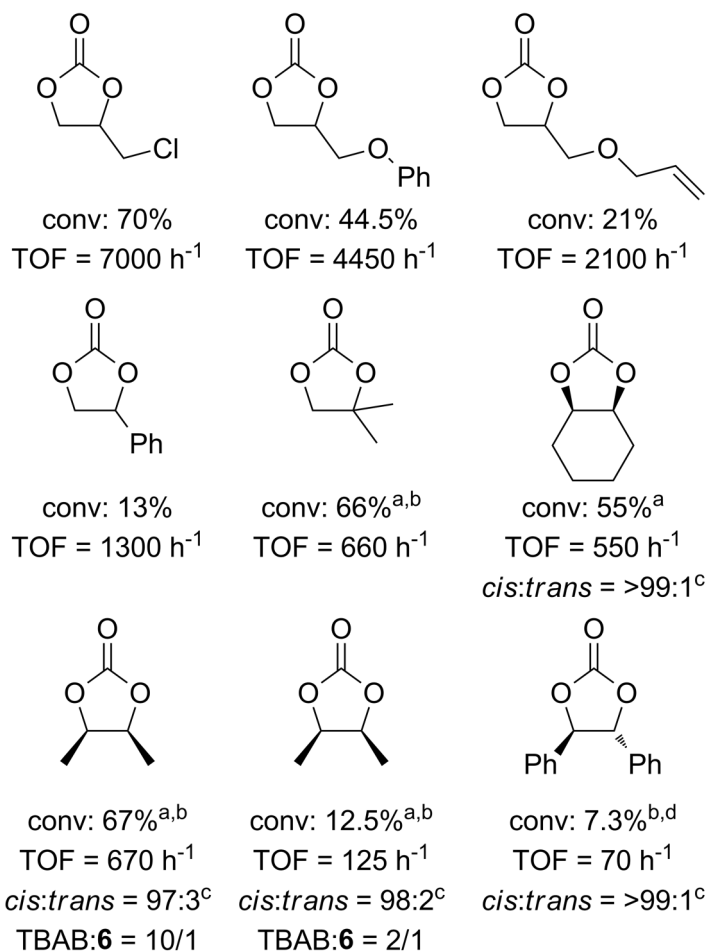
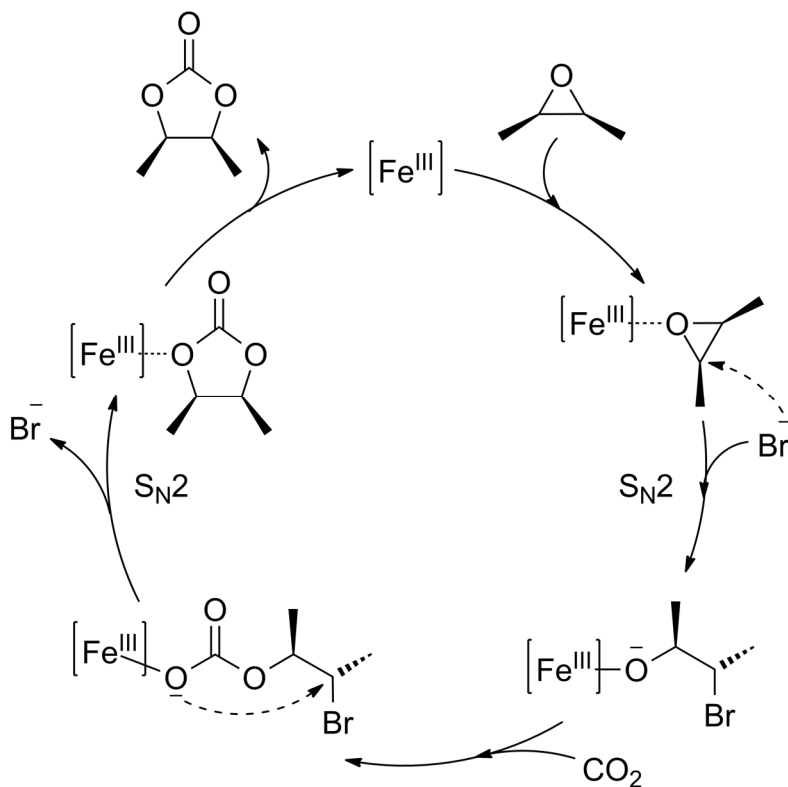


Chart 1 Cyclic organic carbonates formation promoted by Fe(III) complex **6**. Reaction conditions: epoxide = $7.15 \cdot 10^{-2}$ mol; **6** = $1.43 \cdot 10^{-5}$ mol (0.01 mol%); TBAB = $1.43 \cdot 10^{-4}$ mol (0.1 mol%); T = 120 °C; P(CO₂) = 20 bar; reaction time = 1 h. Conversion determined by ¹H NMR using mesitylene as internal standard. a) Epoxide = 1.0 mL. b) P(CO₂) = 40 bar. c) determined by ¹H NMR. d) Stilbene oxide = 1.0 g, MEK = 2 mL.

Conversely, the presence of an electron-releasing group, such as a phenoxy or a phenyl group results in an attenuation of the reactivity. Notably the more challenging substrate isobutylene oxide (1,1-dimethyloxirane) was converted in good yield to the corresponding carbonate. Moreover the *cis* form of 1,2-dimethyloxirane was converted to the corresponding carbonate not only in good yield but also with a high degree of configuration retention. Intriguingly,

complex **6** in combination with TBAB retains the configuration of the starting substrate regardless to the co-catalyst/catalyst molar ratio indicating that the attack of the bromide anion to the epoxide ring proceeds selectively via two consecutive inversions of configuration (S_N2) on the same stereocentre and that, differently to what was reported for other iron(III)-based catalysts,⁴³ this mechanism is not dependent on the bromide concentration (see Scheme 3).



Scheme 3 Proposed mechanism for the retention of stereochemical configuration in the production of *cis*-4,5-dimethyl-1,3-dioxolan-2-one from *cis*-2,3-epoxybutane and CO₂ promoted by catalyst **6** in the presence of TBAB.

A complete stereoretention was also observed in the case of *trans*-stilbene oxide and the exclusive formation of *cis*-cyclohexene carbonate (*cis*-CHC) also supports the proposed reaction mechanism. In fact, the thermodynamically disfavoured formation of *cis*-CHC should necessarily arise from a mechanism involving a double inversion of the starting CHO configuration.⁴⁴

2.4 Theoretical calculations

Deeper insights into the reaction pathway were obtained by performing DFT on the reaction mechanism for the cycloaddition of CO₂ to PO catalysed by complex **6** in the presence of TBAB. The complete energy profile is reported in Figure 29 (for clarity, we refer to the two Fe(III) centres in **6** as Fe₁ and Fe₂).

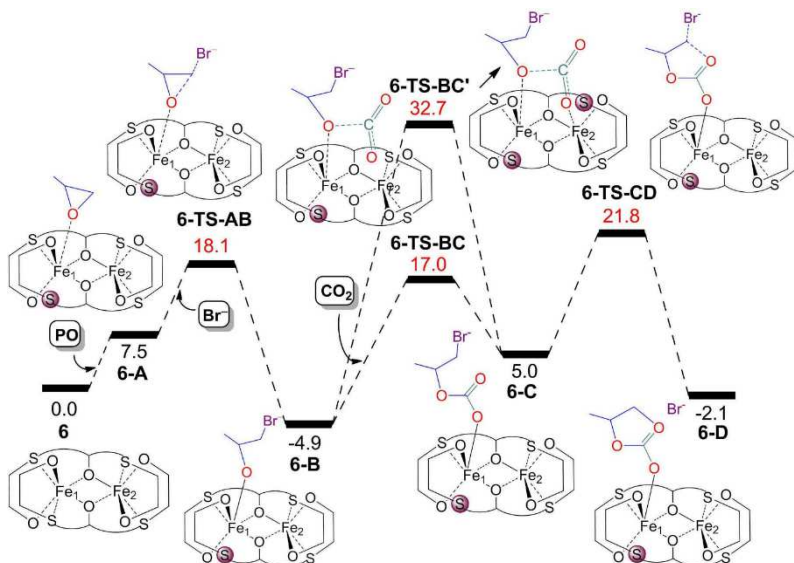


Figure 29 Computed free energy surface for the cycloaddition of CO₂ to PO catalysed by **6**/TBAB. The free energies in solution (PO as the solvent) are given in kcal/mol relative to the starting complex **6**. The energy values in red represent the energies of the transition states. ● indicates decoordination of a hemilabile S atom.

The coordination of PO to the Fe₁ centre in **6** is possible only after the dissociation of one of the two hemilabile S atoms ($r(\text{Fe}_1\text{-S})$ 2.704 Å). PO coordination is calculated to be endergonic and leads to intermediate **6-A**, which lies 7.5 kcal/mol above **6**. From a structural point of view, in **6-A**, PO coordinates to the Fe₁ center ($r(\text{Fe}_1\text{-O})$ = 2.412 Å) in the coordination position previously occupied by the dissociated S atom. PO coordination results in a slight decrease in the Fe₁-Fe₂ distance in **6-A** when compared to the catalyst species **6** (3.271 vs 3.364 Å, respectively; see Figure 30). To explore the eventual dissociation of one of the two Fe₁-S bonds prior to PO coordination in the starting complex **6**, we removed PO from the optimized geometry of intermediate **6-A** and we re-optimized the

complex. The resulting complex with Fe₁-S bond being dissociated is lying only 5.8 kcal/mol above species **6**, in line with the expected lability of the S binding.

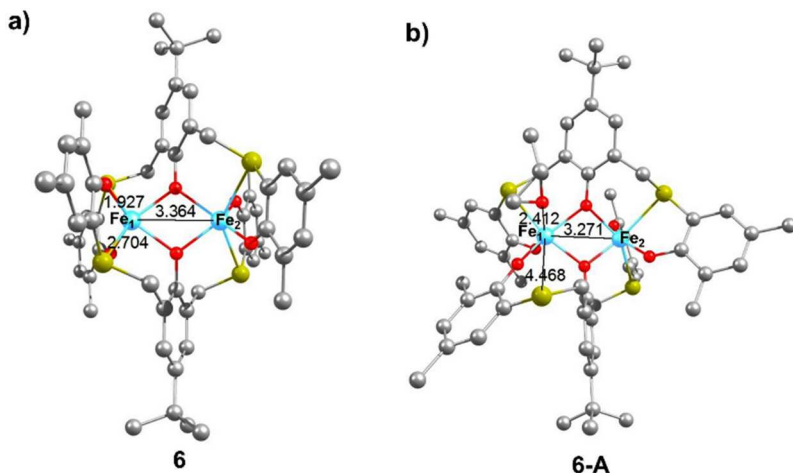


Figure 30 Geometry of the starting complex **6** (a) and of the PO coordinated intermediate **6-A** (b). Hydrogen atoms omitted for clarity, selected distances in Å.

The experimental evidence that the introduction of the electron withdrawing chlorine atoms on the lateral phenol rings (complex **4**) results in a lowering of the catalytic activity supports this scenario. As a matter of fact, the coordinating ability of the phenoxide O atoms should be reduced in **4** due to the presence of the *ortho* Cl atom.

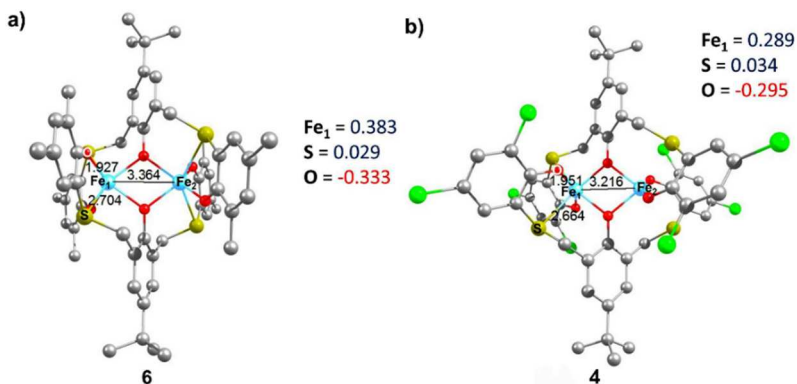


Figure 31 Geometry of the starting catalyst species **6** (a) and **4** (b). Hydrogen atoms omitted for clarity, Mulliken charges (e⁻) are presented, selected distances in Å.

This should result in increased Lewis acidity at the metal center and should reduce the lability of the sulfur atoms, rendering substitution of one sulphur moiety by PO less favorable. This scenario is supported by calculations on complex **4**, which presents slightly shorter Fe₁-S distances when compared to complex **6** (2.66 Å vs 2.70 Å, Figure 31). Consistently, dissociation of one Fe₁-S bond from complex **4** requires 8.6 kcal/mol versus 5.8 kcal/mol in **6**, and the PO coordinated intermediate **4-A**, is slightly less stable than **6-A** (8.7 vs 7.5 kcal/mol). Back to the main mechanism catalysed by **6**, the next step from the PO coordinated specie **6-A** corresponds to the opening of the PO ring by a Br anion, leading to the formation of the more stable intermediate **6-B**, 4.9 kcal/mol below **6**. This step proceeds through transition state **6-TS-AB** and requires overcoming an overall barrier of 18.1 kcal/mol above **6**. Then, we studied insertion of CO₂ into the Fe-O bond in the intermediate **6-B** to give the hemicarbonate intermediate **6-C**, which lies 10.0 kcal/mol above **6-B**. This CO₂ insertion step requires the overcoming of a barrier (**6-TS-BC**) of 21.9 kcal/mol from the most stable intermediate **6-B**. To our surprise, despite the relatively low calculated barrier we did not observe any cooperativity between the two Fe centres, since the CO₂ molecule is quite away from the Fe₂ center ($r(\text{Fe}_2\text{-CO}_2) = 3.772 \text{ \AA}$), see Figure 32a.

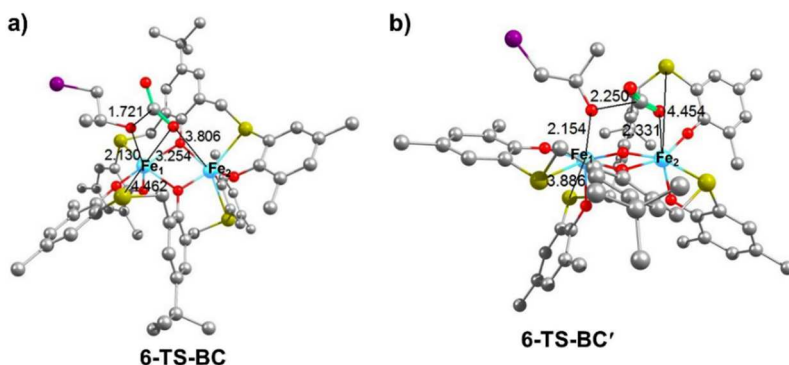


Figure 32 Geometry of transition states **6-TS-BC** (a) **6-TS-BC'** (b), for insertion of CO₂ into the Fe-O bond. Hydrogen atoms omitted for clarity, selected distances in Å.

As a further check on the possible cooperativity between the two Fe centers in the CO₂ insertion step, an alternative transition state for CO₂ insertion, **6-TS-BC'**, was calculated by forcing decoordination of

one of the two hemilabile S atoms from the Fe₂ centre. In this case a clear interaction between the Fe₂ centre and one of the O atoms of the CO₂ molecule ($r(\text{Fe}_2\text{-CO}_2) = 2.320 \text{ \AA}$) is observed, see Figure 32b. However, transition state **6-TS-BC'** is placed 15.7 kcal/mol higher in energy relative to transition state **6-TS-BC**. These observations suggest that though the catalyst species **6** under investigation is bimetallic, catalysis essentially occurs at a single Fe(III) centre without cooperation of the second Fe(III) centre. This is clearly different from the case of PO coupling with CO₂ to cyclic carbonate promoted by mono-metallic Nb complexes, where cooperativity between two Nb centres occurs both in the homogeneous phase as well as after grafting of the Nb complex on silica.⁴⁵ Next, starting from intermediate **6-C**, we studied the ring closing step leading to the formation of intermediate **6-D** with the desired cyclic carbonate product coordinated to the Fe metal centre. According to calculations, ring closing is predicted to be the rate determining step, with a barrier of 26.7 kcal/mol (**6-TS-CD**) relative to the most stable intermediate **6-B**. This is clearly a high barrier, which is however consistent with the remarkably high temperature of 120 °C needed experimentally to achieve a yield of at least 51% in 1 hour. Finally, intermediate **6-D** would release the carbonate product and a Br⁻ anion, regenerating intermediate **6-A** with recoordination of a free PO molecule, thus closing the catalytic cycle.

2.5 Conclusions

The synthesis and the complete characterization of five new thioether triphenolate ligands (**L2-6**), and of the corresponding bimetallic iron(III) complexes (**2-6**) have been described. When activated by TBAB, all the complexes resulted very efficient in the cycloaddition of CO₂ to epoxides, obtaining the highest initial activity reported so far for an iron based catalyst. In particular, complex **6** shows the best catalytic performance in terms of both activity and selectivity for several terminal epoxides with TOF values up to 5200 h⁻¹ and 7000 h⁻¹ for the conversion of PO and EPC respectively. Furthermore complex **6** also promotes the conversion to the corresponding cyclic carbonates of internal epoxides with a high degree of stereocontrol in the ring-closing reaction, leading to the retention of configuration of the starting epoxide ($\geq 97\%$) via a mechanism involving a double inversion of the initial epoxide

configuration. Finally the mechanistic studies conducted using DFT calculations show that, in spite of the dinuclear nature of the catalyst precursor, only one metal center is operative in the catalytic cycle and that coordination of the substrate and the subsequent reaction pathway can only take place by dissociation of a hemilabile S atom from one of the iron centers. These findings not only show that is possible to obtain highly active catalytic systems based on iron(III) for the CO₂/epoxides coupling but also highlight the fundamental role of this sulfur containing ligands in modulating the Lewis acidity of the iron center and thus the reactivity with CO₂ and oxiranes for this family of catalysts.

2.6 Experimental Part

General considerations

All manipulation involving air- and/or moisture-sensitive compounds were performed under nitrogen atmosphere using standard Schlenk technique and a MBraun glovebox. Toluene (99.5%; Sigma-Aldrich) and THF (99%; Sigma-Aldrich) were used as received or refluxed for 48 h over sodium or sodium ketyls and distilled before use for moisture- and oxygen-sensitive reactions. All other reagents were used as received (TCI or Sigma-Aldrich) or distilled under reduced pressure over calcium hydride. The ligand precursors: 2,6-[[3,5-di-tert-butyl-2-hydroxyphenyl]thio]-4-tert-butylphenol (**L1**), and the corresponding iron(III) complexe (Scheme 2) was synthesized according to the reported procedures.⁴¹ Deuterated solvents were purchased from Euriso-Top or Sigma-Aldrich and used as received. NMR spectra were collected on Bruker Avance spectrometers (600, 400, 300 or 250 MHz for ¹H): the chemical shifts were referenced to tetramethylsilane (TMS) as external reference using the residual protio signal of the deuterated solvents. Measurements of effective magnetic moments were performed on a Bruker Avance 600 MHz spectrometer at 25 °C in toluene-d8 using a 5 mm Wilmad coaxial insert NMR tube. Solutions of the iron complexes **2**, **3**, **4**, **5** and **6** in toluene-d8 with 1% (v/v) of TMS were prepared under nitrogen atmosphere. The effective magnetic moment (μ_{eff}) was calculated from $\mu_{\text{eff}} = 8\chi_{\text{g}}\text{MWT}$, where χ_{g} ($\text{cm}^3 \text{g}^{-1}$) is the corrected molar susceptibility derived from $\chi_{\text{g}} = 3\Delta f/4\pi f_0 \text{CMW} + \chi_0$. Δf is the shift in frequency (Hz) of the residual protio signal of the solvent in the presence of the complex from the value of the pure solvent, C and MW are respectively the concentration (mol cm^{-3}) and the molecular weight of the complex (g mol^{-1}), f_0 is the operating frequency of the spectrometer (Hz), and χ_0 is the mass susceptibility of the pure solvent ($-0.6179 \times 10^{-6} \text{ cm}^3 \text{g}^{-1}$ for toluene-d8). $4\pi/3$ is the shape factor for a cylindrical sample in a superconducting magnet. The magnetic susceptibilities of all the complexes **1-6** in the solid state were measured using a Sherwood Scientific MK 1 magnetic susceptibility balance by means of the Faraday method based on the following equation: $f_s / f_r = (\chi_s \cdot m_s) / (\chi_r \cdot m_r)$ where f_s , χ_s and m_s are the magnetic force, the specific susceptibility and the mass of the sample, while f_r , χ_r and m_r are the magnetic force, the specific

susceptibility and the mass of $\text{CuSO}_4 \cdot 5\text{H}_2\text{O}$ used as reference compound with a value of $\chi_r = 6.00 \cdot 10^{-6} \text{ cm}^3 \cdot \text{g}^{-1}$. Magnetic moments were calculated using the following equation: $\mu_{\text{eff}} = 2.828 \cdot (\text{T} \cdot \chi_m)^{1/2}$, where μ_{eff} is the effective magnetic moment, T is the absolute temperature and χ_m is the molar susceptibility. Elemental analysis was performed on a CHNS Thermo Scientific Flash EA 1112 equipped with a thermal conductivity detector. ESI-MS spectra were acquired on a Quattro microTM API triple quadrupole mass spectrometer from Waters equipped with electrospray ion source, using anhydrous acetonitrile as solvent. FT-IR measurements were carried out on a Bruker Vertex 70 spectrometer equipped with DTGS detector and a Ge/KBr beam splitter. The samples were analyzed in chloroform solutions or in the solid state as KBr disks. UV-Vis spectra were collected on a PerkinElmer Lambda EZ 201 spectrophotometer.

Synthesis of the pro-ligand 2,2'-(((5-(tert-butyl)-2-hydroxy-1,3-phenylene)bis(methylene))bis (sulfanediyl))-bis(2,4-di-(α,α' -dimethylbenzyl)phenol) L2 (Scheme 2)

A 50 mL two-neck round-bottom flask equipped with a condenser and a magnetic stirring bar was charged, under nitrogen atmosphere, with 2.02 g of 2-mercapto-4,6-bis-(α,α' -dimethylbenzyl)-2-phenol (5.56 mmol) dissolved in 25 mL of ethanol, 0.30 g of NaOH (22.2 mmol) and the mixture was refluxed about 1 hour until complete dissolution of the hydroxide. 0.94 g of 2,6-dibromomethyl-4-*t*-butylphenol (2.8 mmol) dissolved in 10 mL of ethanol were slowly added at 0 °C and the mixture heated to the reflux of the solvent that was kept overnight. The solvent was distilled off, water was added until dissolution of NaBr by-product and the aqueous phase extracted twice with methylene chloride. The combined organic phases were dried with MgSO_4 and, after evaporation of the solvent, the resulting crude solid was purified by column chromatography (light petroleum/ethyl acetate = 95/5). Yield: 0.81 g, 33%. EA for $\text{C}_{60}\text{H}_{66}\text{O}_3\text{S}_2$ calc.: C, 80.13; H, 7.40; S 7.13; found: C, 79.94; H, 7.27; S, 7.03. Mass spectrum: 899.2 m/z (M^+), 922.2 m/z (MNa^+).

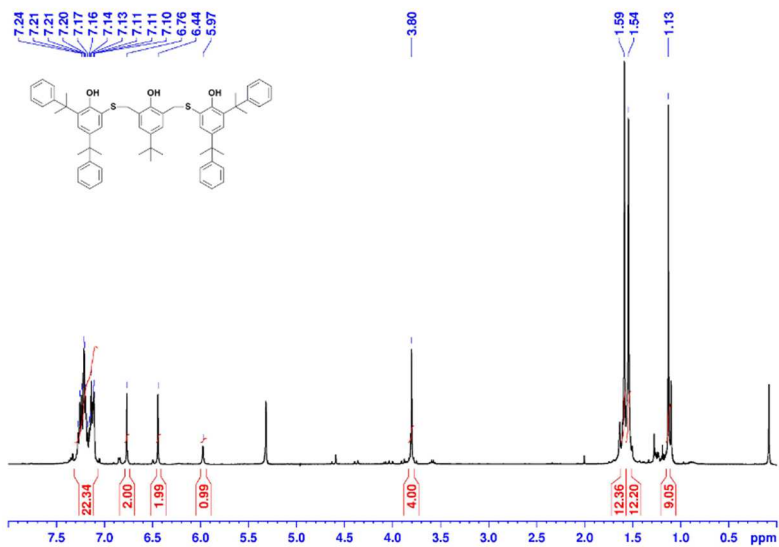


Figure S 1 ¹H NMR spectrum of the pro-ligand **L2** (CD₂Cl₂, 400 MHz, 25 °C).

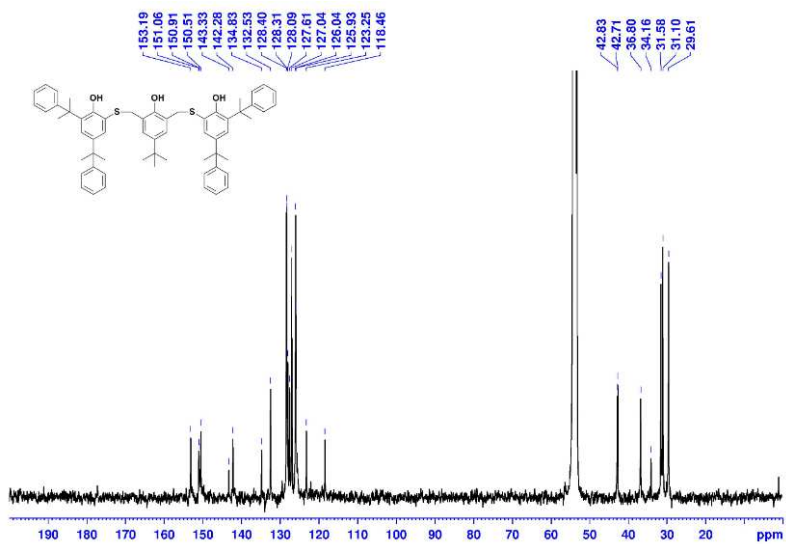


Figure S 2 ¹³C NMR spectrum of the pro-ligand **L2** (CD₂Cl₂, 400 MHz, 25 °C).

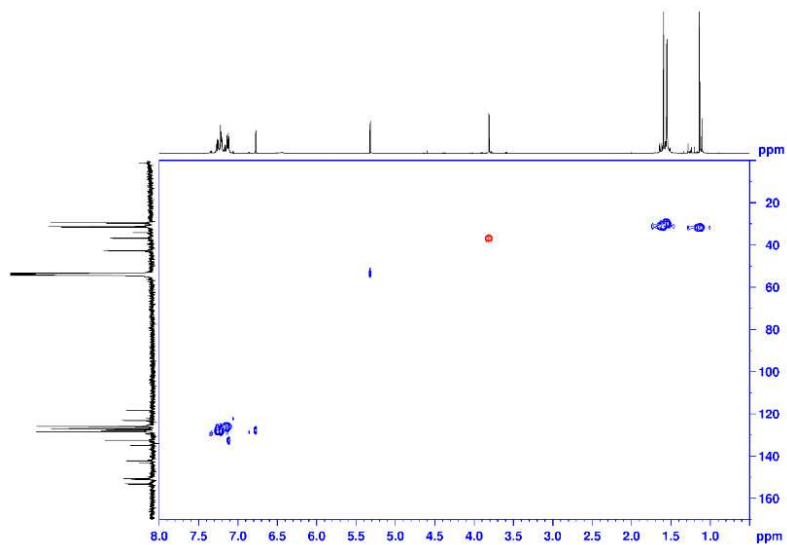


Figure S 3 ^1H - ^{13}C HSQC NMR spectrum of pro-ligand **L2** (CD_2Cl_2 , 600MHz).

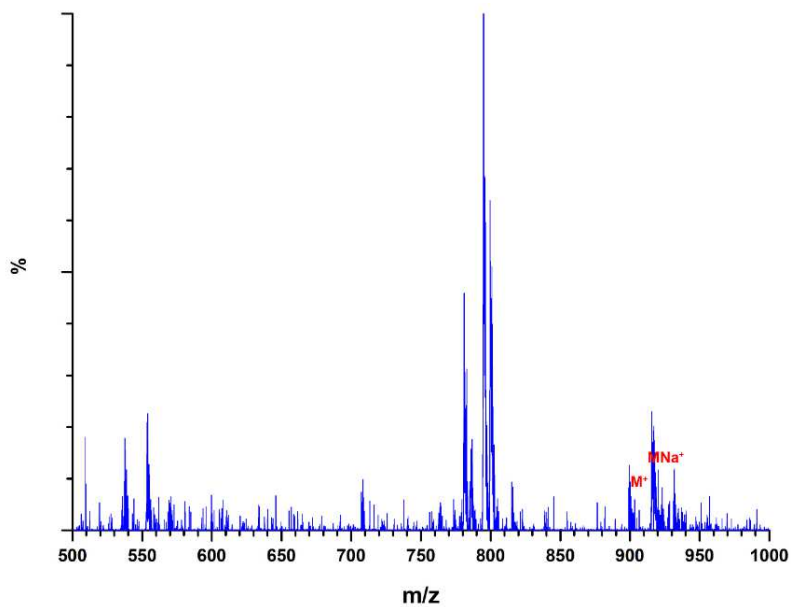


Figure S 4 ESI-MS spectrum of the pro-ligand **L2** (acetonitrile as solvent).

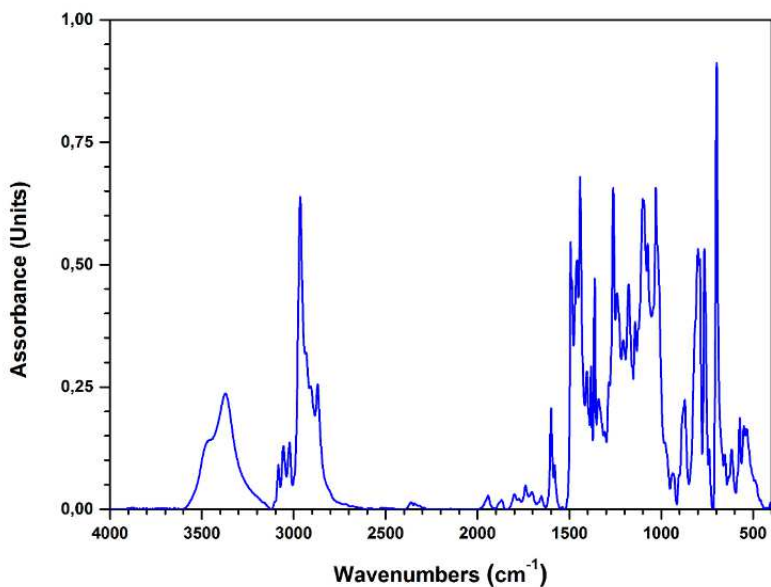


Figure S 5 FT-IR spectrum of the pro-ligand **L2** (KBr disk).

Synthesis of the pro-ligand 2,2'-(((5-(tert-butyl)-2-hydroxy-1,3-phenylene)bis(methylene))bis (sulfanediyl))-bisphenol **L3 (Scheme 2)**

A 500 mL two-neck round-bottom flask equipped with condenser and magnetic stirring bar was charged, under nitrogen atmosphere, with 5.00 g of 2-mercaptophenol (35.7 mmol) dissolved in 160 mL of ethanol, 1.43 g of NaOH (35.7 mmol) and the mixture was refluxed about 1 hour until complete dissolution of the hydroxide. 6.00 g of 2,6-dibromomethyl-4-t-butylphenol (17.83 mmol) dissolved in 50 mL of ethanol were slowly added at 0 °C and the mixture heated to the reflux of the solvent that was kept overnight. The solvent was distilled off, water was added until dissolution of NaBr by-product and the aqueous phase extracted twice with methylene chloride. The combined organic phases were dried with MgSO₄ and, after evaporation of the solvent, the product was recovered as a white solid. Yield: 7.36 g, 96.8 %. EA for C₂₄H₂₆O₃S₂ calc.: C, 67.57; H, 6.14; S 15.03; found: C, 67.27; H, 6.07; S, 14.93. Mass spectrum: 449.3 m/z (MNa⁺).

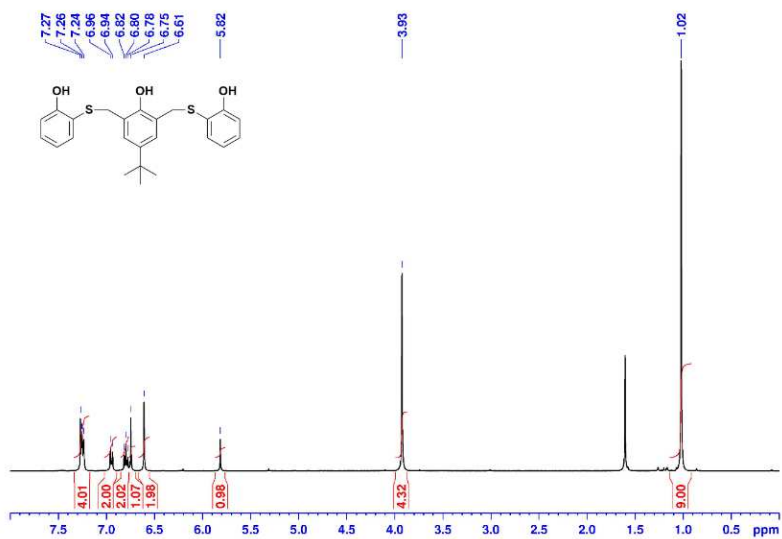


Figure S 6 ¹H NMR spectrum of the pro-ligand **L3** (CD₂Cl₂, 400 MHz, 25 °C).

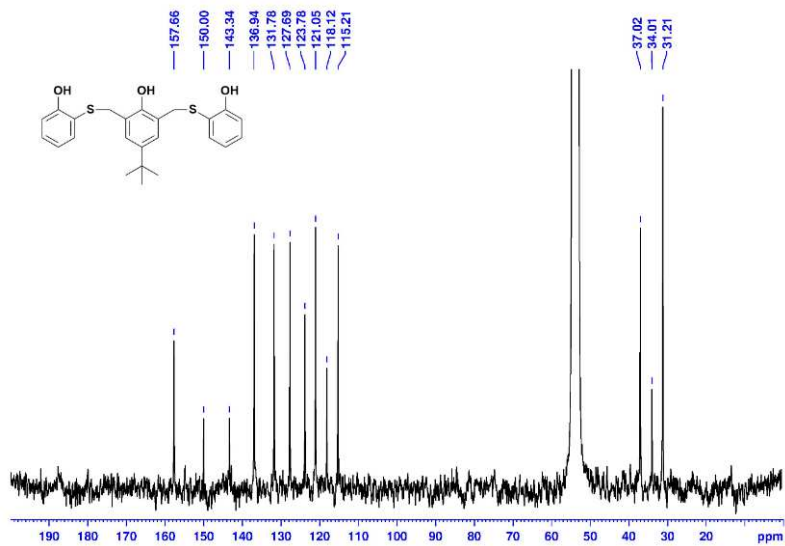


Figure S 7 ¹³C NMR spectrum of the pro-ligand **L3** (CD₂Cl₂, 400 MHz, 25 °C).

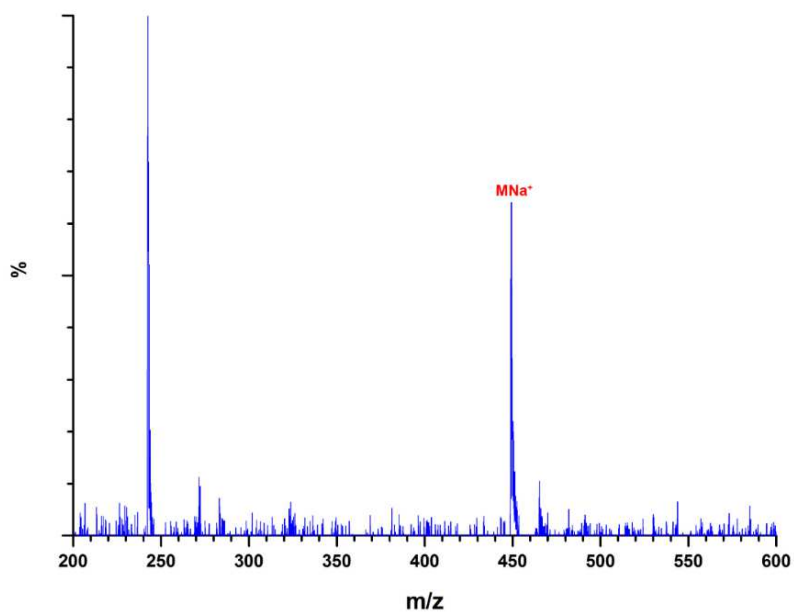


Figure S 8 ESI-MS spectrum of the pro-ligand **L3** (acetonitrile as solvent).

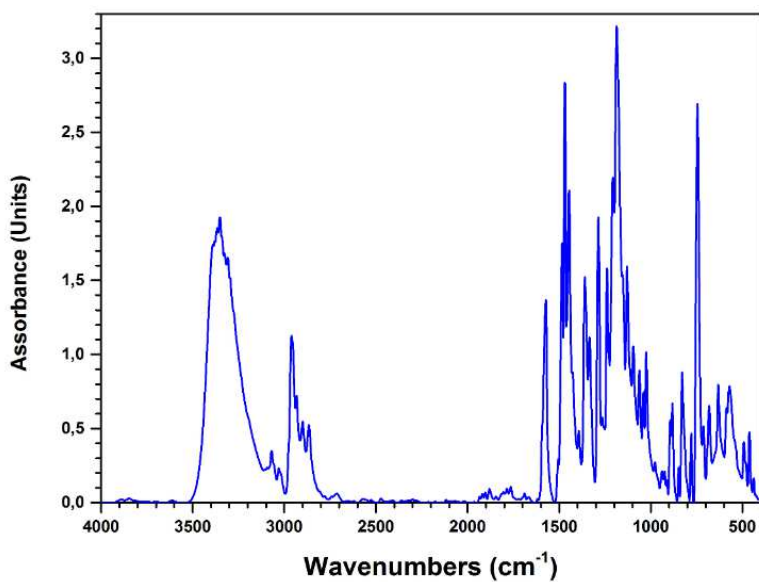


Figure S 9 FT-IR spectrum of the pro-ligand **L3** (KBr disk).

Synthesis of the pro-ligand 2,6-[(3,5-Dichloro-2-hydroxyphenyl)thio]-4-tert-butylphenol **L4** (Scheme 2)

The pro-ligand **L4** was synthesized using a modification of the previously reported procedure for **L1**.^[11] A 100-mL two neck round-bottom flask equipped with condenser and magnetic stirring bar was charged with 0.76 g of 2-mercapto-4,6-dichlorophenol (3.9 mmol) dissolved in 4 mL of ethanol, 1.4 g of Cs_2CO_3 (4.3 mmol) and the mixture was refluxed for 2 h until complete dissolution of Cs_2CO_3 . 0.66 g of 2,6-dibromomethyl-4-tert-butylphenol (1.96 mmol) dissolved in 2 mL of ethanol were slowly added at 0 °C and the mixture was refluxed overnight. The solvent was distilled off, water was added until dissolution of the residue and the aqueous phase extracted twice with CH_2Cl_2 . The combined organic phases were dried with MgSO_4 and, after evaporation of the solvent, the product was purified by column chromatography (eluent: CH_2Cl_2) and recovered as a white solid; yield: 0.94 g (85%). ^1H NMR (600 MHz, CD_2Cl_2 , 25 °C): δ =1.12 (9H, s), 4.04 (4H, s), 6.80 (2H, s, Ar-H), 7.19 (2H, d, Ar-H), 7.32 (2H, d, Ar-H); ^{13}C NMR (600 MHz, CD_2Cl_2 , 25 °C): δ =31.36, 34.21, 36.55, 121.08, 121.98, 123.05, 124.99, 127.99, 130.83, 134.07, 143.75, 150.61, 152.14; elemental analysis: calcd. for $\text{C}_{24}\text{H}_{22}\text{Cl}_4\text{O}_3\text{S}_2$: C 51.08, H 3.93, S 11.36; found: C 51.02, H 3.82, S 11.25; MS: m/z = 586.7 (MNa^+).

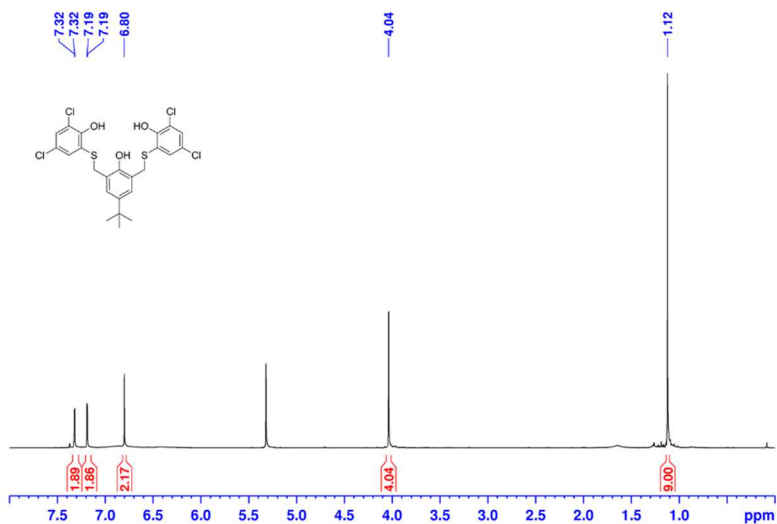


Figure S 10 ^1H NMR spectrum of the pro-ligand **L4** (CD_2Cl_2 , 600 MHz, 25 °C).

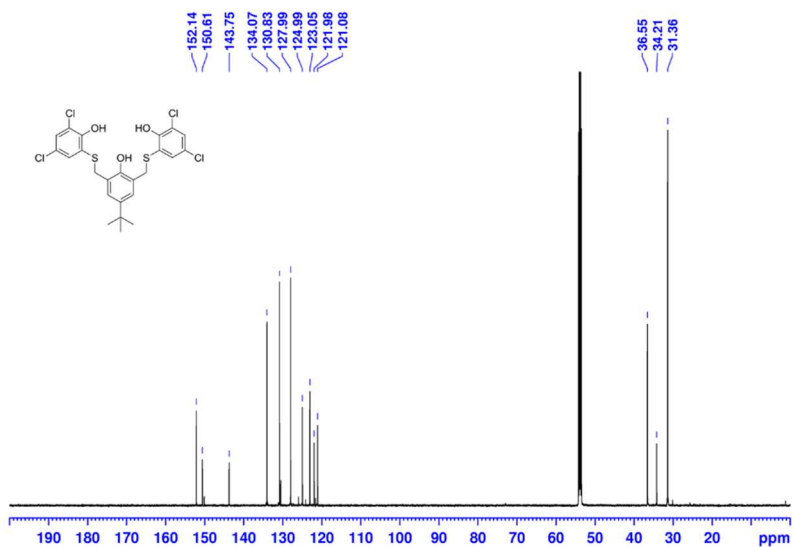


Figure S 11 ^{13}C NMR spectrum of the pro-ligand **L4** (CD_2Cl_2 , 600 MHz, 25 °C).

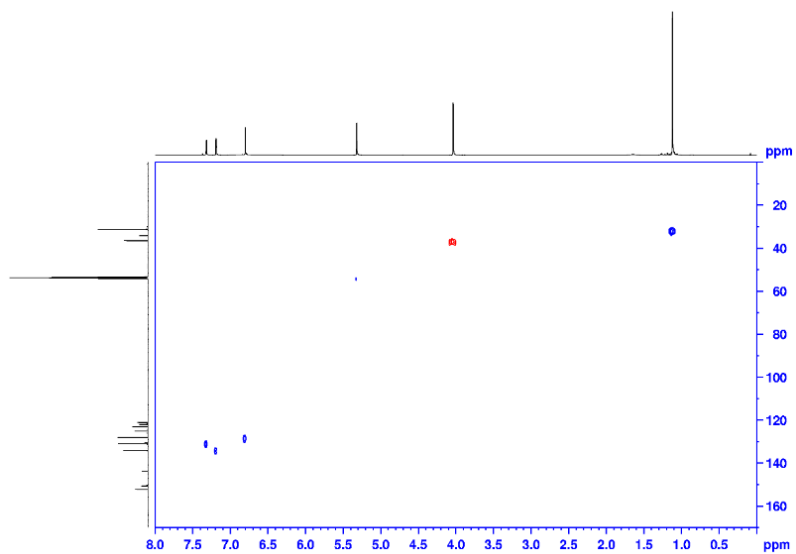


Figure S 12 ^1H - ^{13}C HSQC NMR spectrum of pro-ligand **L4** (CD_2Cl_2 , 600MHz).

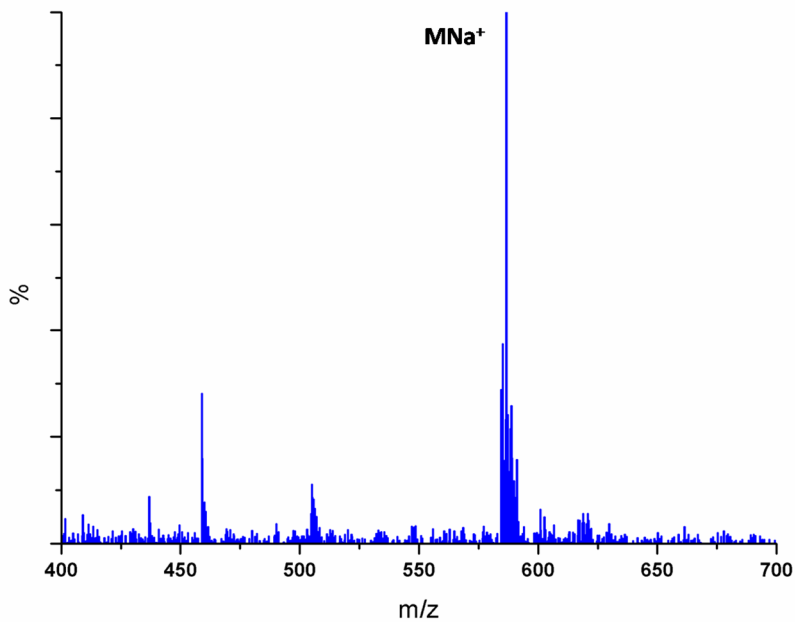


Figure S 13 ESI-MS spectrum of the pro-ligand **L4** (acetonitrile as solvent).

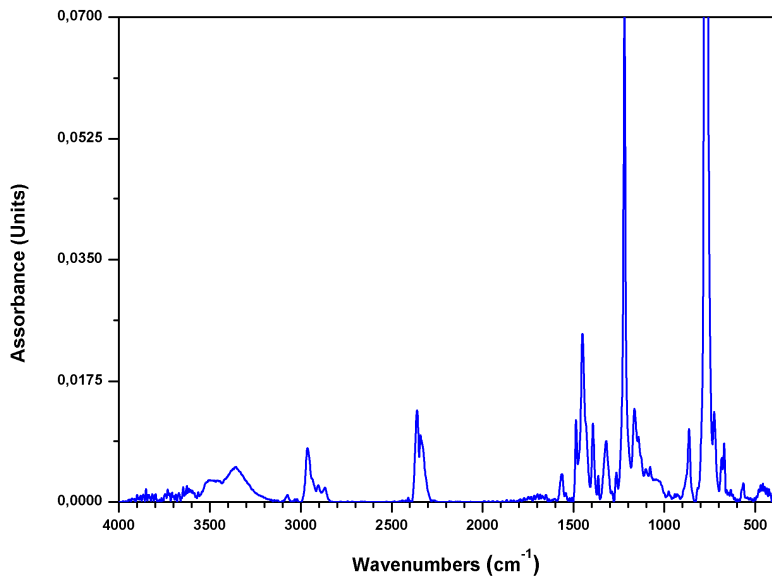


Figure S 14 FT-IR spectrum of the pro-ligand **L4** (KBr disk).

Synthesis of the pro-ligand 2,6-[[[3,5-dimethyl-2-hydroxyphenyl]thio]-4-chlorophenol L5 (Scheme 2)

The pro-ligand **L5** was synthesized using a modification of the previously reported procedure for **L1**.¹¹ A 100 mL two-neck round-bottom flask equipped with condenser and magnetic stirring bar was charged with 0.80 g of 2-mercapto-4,6-dimethylphenol (5.2 mmol) dissolved in 13 mL of DMF, 0.90 g of K_2CO_3 (6.5 mmol) and the resulting mixture was refluxed for 2 hours. 0.82 g of 2,6-dibromomethyl-4-chlorophenol (2.6 mmol) dissolved in 7 mL of DMF were slowly added at 0 °C and was refluxed overnight. The solvent was distilled off, water was added and the aqueous phase extracted twice with CH_2Cl_2 . The combined organic phases were dried with $MgSO_4$ and, the product was recovered after evaporation of the solvent as a white solid. Yield: 0.97 g, 81 %. 1H -NMR (400 MHz, CD_2Cl_2 , 25 °C): 2.17 (6H, s); 2.23 (6H,s); 3.86 (4H, s); 6.11 (1H, s broad, -OH); 6.54 (2H, s broad, -OH); 6.76 (2H, s, Ar-H); 6.92 (2H, s, Ar-H); 6.95 (2H,s, Ar-H). ^{13}C -NMR (400 MHz, CD_2Cl_2 , 25 °C): δ 16.48; 20.36; 36.52; 116.53; 124.38; 125.27; 126.23; 129.69; 129.89; 133.83; 134.03; 151.25; 153.23. EA for $C_{24}H_{25}Cl_2O_3S_2$ calc.: C, 62.52; H, 5.47; S 13.91; found: C, 62.49; H, 5.42; S, 13.87. Mass spectrum: 483.6 m/z (MNa^+).

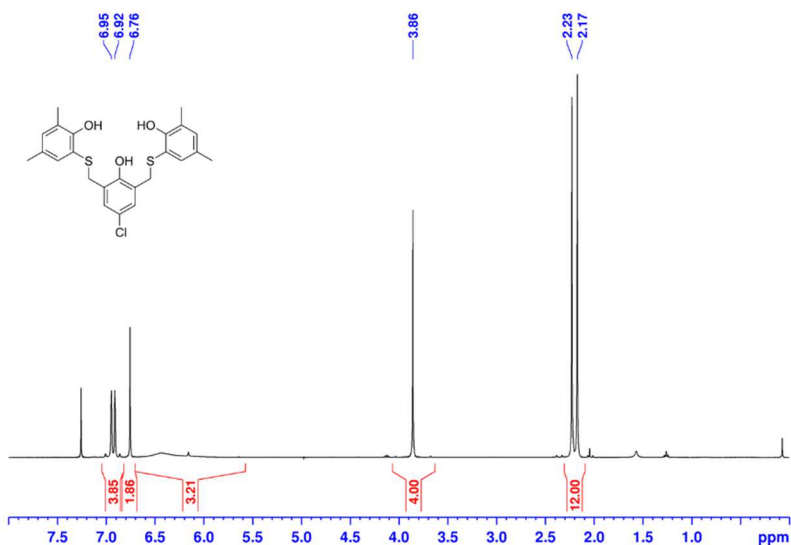


Figure S 15 1H NMR spectrum of the pro-ligand **L5** ($CDCl_3$, 400 MHz, 25 °C).

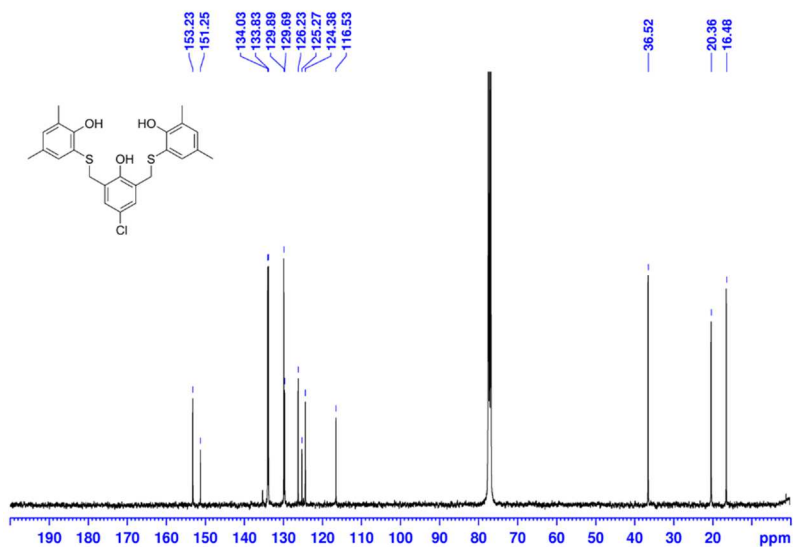


Figure S 16 ^{13}C NMR spectrum of the pro-ligand **L5** (CDCl₃, 400 MHz, 25 °C).

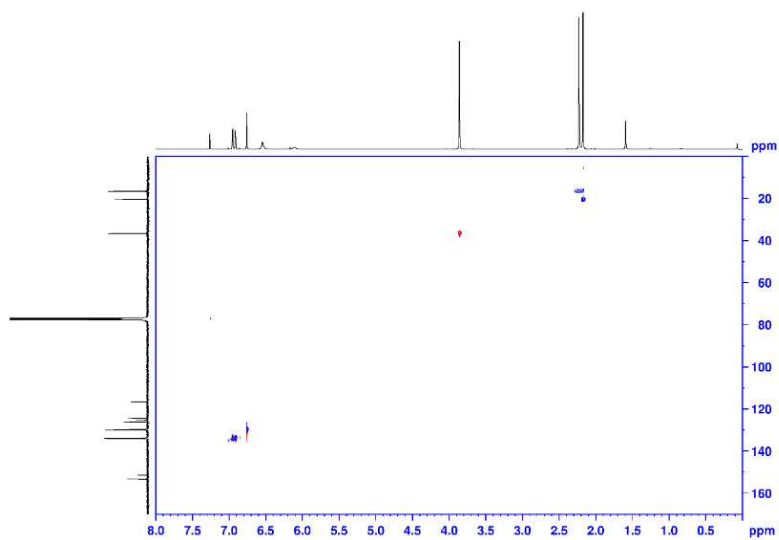


Figure S 17 ^1H - ^{13}C HSQC NMR spectrum of pro-ligand **L5** (CDCl₃, 400 MHz).

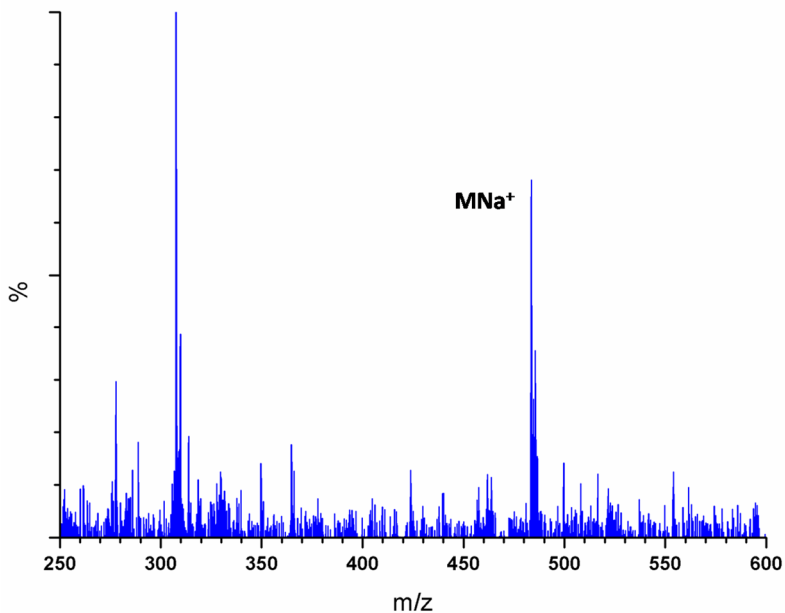


Figure S 18 ESI-MS spectrum of the pro-ligand **L5** (acetonitrile as solvent).

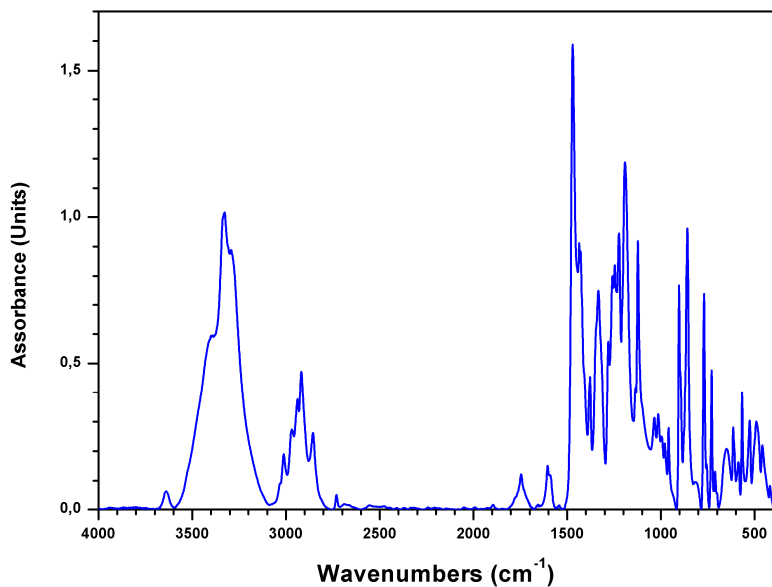


Figure S 19 FT-IR spectrum of the pro-ligand **L5** (KBr disk).

Synthesis of the pro-ligand 2,6-[[3,5-dimethyl-2-hydroxyphenyl]thio]-4-tert-butylphenol **L6** (Scheme 2)

The pro-ligand **L6** was synthesized using the previously reported procedure for **L1**.¹¹ A 100 mL two-neck round-bottom flask equipped with condenser and magnetic stirring bar was charged with 3.14 g of 2-mercapto-4,6-dimethylphenol (20.4 mmol) dissolved in 20 mL of ethanol, 0.90 g of NaOH (22.4 mmol) and the mixture was refluxed about 1 hour until complete dissolution of the hydroxide. 3.42 g of 2,6-dibromomethyl-4-*tert*-butylphenol (10.2 mmol) dissolved in 15 mL of ethanol were slowly added at 0 °C and the mixture heated to the reflux of the solvent that was kept overnight. The solvent was distilled off, water was added until dissolution of NaBr by-product and the aqueous phase extracted twice with CH₂Cl₂. The combined organic phases were dried with MgSO₄, after evaporation of the solvent the product was purified by column chromatography (petroleum ether : ethyl acetate = 95:5) and recovered as a white solid. Yield: 2.82 g, 57.3 %. ¹H-NMR (400 MHz, CD₂Cl₂, 25 °C): δ 1.05 (9H, s); 2.14 (6H, s); 2.17 (6H, s); 3.91 (4H, s); 5.79 (1H, s, -OH); 6.60 (2H, s, -OH); 6.69 (2H, s, Ar-H); 6.91 (4H, s, Ar-H). ¹³C-NMR (400 MHz, CD₂Cl₂, 25 °C): δ 16.47; 20.34; 31.27; 34.08; 37.17; 117.18; 124.04; 124.20; 127.55; 129.60; 133.75; 134.12; 143.46; 150.09; 153.56. EA for C₂₈H₃₄O₃S₂ calc.: C, 69.67; H, 7.10; S 13.29; found: C, 69.55; H, 7.09; S, 13.18. Mass spectrum: 505.0 m/z (MNa⁺).

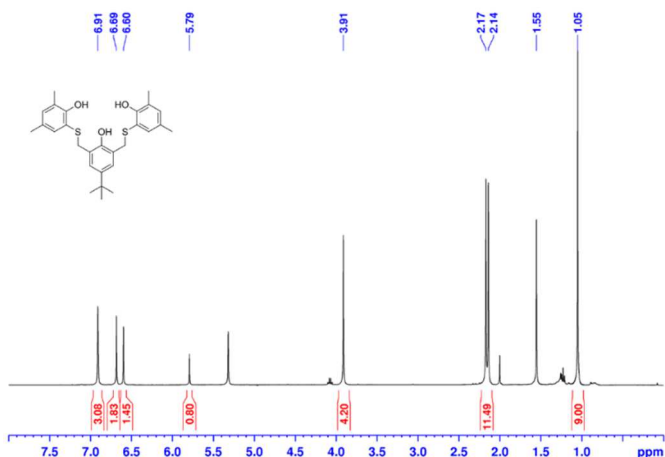


Figure S 20 ¹H NMR spectrum of the pro-ligand **L6** (CD₂Cl₂, 400 MHz, 25 °C).

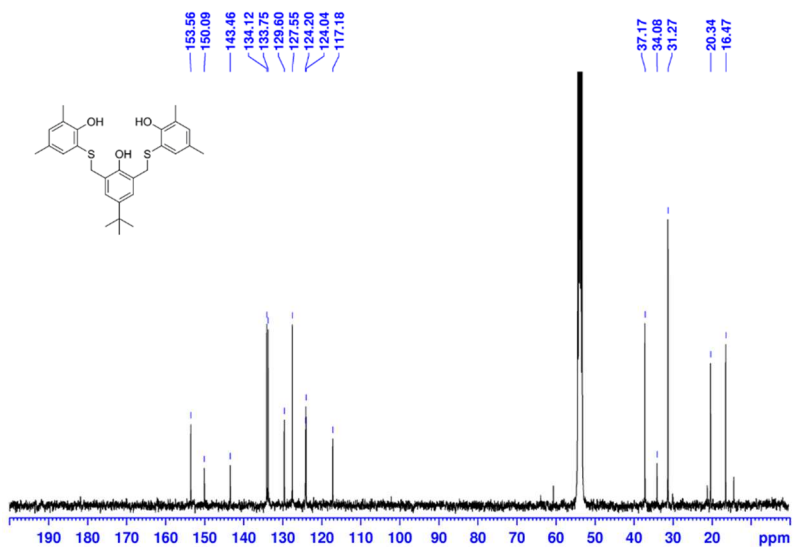


Figure S 21 ^{13}C NMR spectrum of the pro-ligand **L6** (CD_2Cl_2 , 400 MHz, 25 °C).

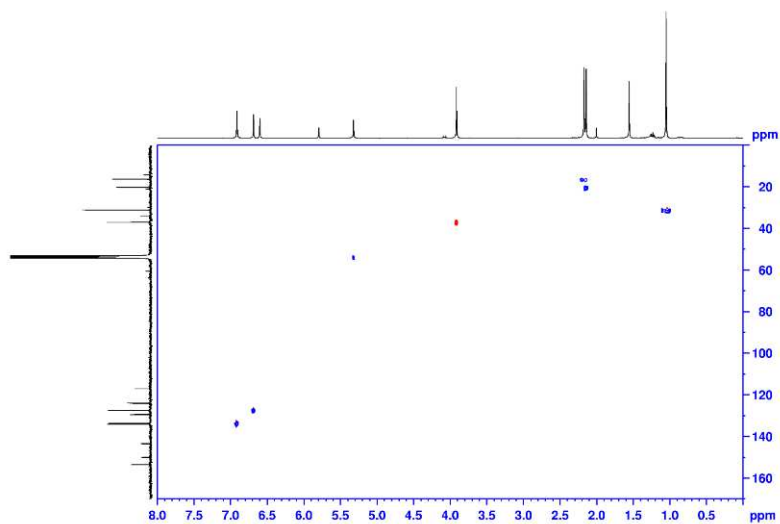


Figure S 22 ^1H - ^{13}C HSQC NMR spectrum of pro-ligand **L6** (CD_2Cl_2 , 400MHz).

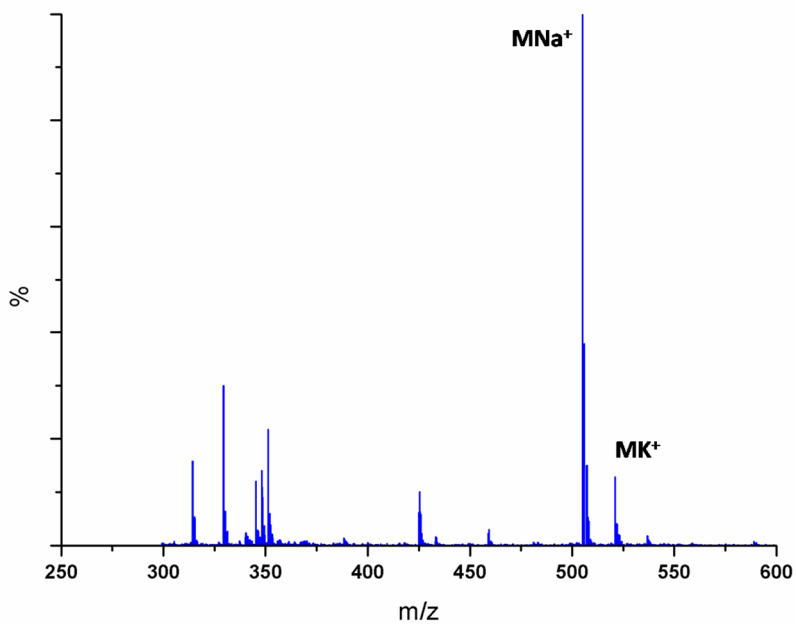


Figure S 23 ESI-MS spectrum of the pro-ligand **L6** (acetonitrile as solvent).

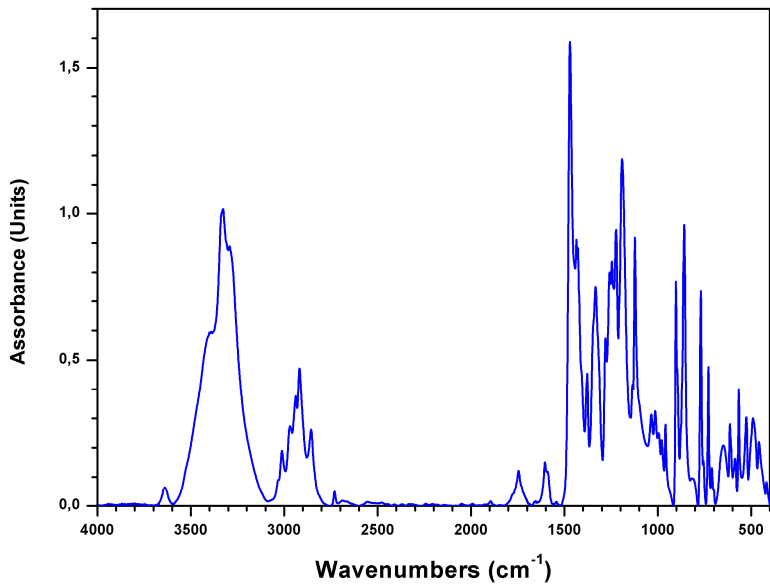


Figure S 24 FT-IR spectrum of the pro-ligand **L6** (KBr disk).

Synthesis of the iron(III) complex 2 (Scheme 2)

A 50 mL two-neck round-bottom flask, equipped with a magnetic stirring bar was charged with 0.073 g of sodium hydride (2.60 mmol) suspended in 20 mL of THF and a solution of 0.78 g of the ligand precursor **L2** (0.87 mmol) dissolved in 25 mL of THF was slowly added at room temperature under protective nitrogen atmosphere, thus allowed to react overnight. The resulting suspension was filtered through celite and slowly added at room temperature to 0.138 g of anhydrous iron(III) chloride (0.85 mmol) dissolved in 20 mL of THF. The rapid change of the colour to the deep blue was observed and the reaction kept overnight. The mixture was then filtered through celite and the solvent removed under reduced pressure affording a deep blue crystalline solid. Yield: 0.79 g, 97.7 %. EA for $C_{120}H_{126}Fe_2O_6S_4$ calc.: C, 75.69; H, 6.67; S, 6.74; found: C, 75.42; H, 6.58; S, 6.67. Mass spectrum: 1904 m/z (M^+), 1927 m/z (MNa^+). UV-Vis: $\epsilon_{585} = 7188 \text{ L mol}^{-1} \text{ cm}^{-1}$.

Synthesis of the iron(III) complex 3 (Scheme 2)

A 500 mL two-neck round-bottom flask, equipped with a magnetic stirring bar was charged with 0.51 g of sodium hydride (21.0 mmol) suspended in 130 mL of THF and a solution of 2.72 g of the ligand precursor **L3** (6.37 mmol) dissolved in 180 mL of THF was slowly added at room temperature under protective nitrogen atmosphere, thus allowed to react overnight. The resulting suspension was filtered through celite and slowly added at room temperature to 1.00 g of anhydrous iron(III) chloride (6.24 mmol) dissolved in 100 mL of THF. The rapid change of the colour to the deep purple was observed and the reaction kept overnight. The mixture was then filtered through celite and the solvent removed under reduced pressure affording a deep purple crystalline solid. Yield: 2.80 g, 94 %. EA for $C_{48}H_{46}Fe_2O_6S_4$ calc.: C, 60.13; H, 4.84; S, 13.38; found: C, 60.33 H, 4.47; S, 13.28. Mass spectrum: 981.2 m/z (MNa^+). UV-Vis: $\epsilon_{470} = 2804 \text{ L mol}^{-1} \text{ cm}^{-1}$.

Synthesis of the iron(III) complex 4 (Scheme 2)

The complex **4** was synthesized using the same procedure previously reported for complex **1**.¹¹ Pro-ligand **L4** (0.54 g; 0.96 mmol) was dissolved in THF (30mL). The solution was added to a suspension of sodium hydride (0.082 g; 3.4 mmol) in THF (20 mL)

and the mixture stirred at room temperature overnight. The resulting suspension was filtered through celite and slowly added at room temperature to 0.148 g of anhydrous iron(III) chloride (0.91 mmol) dissolved in 15 mL of THF. The rapid change of the color to blue was observed and the reaction kept overnight at room temperature. The mixture was then filtered through a celite path and the solvent removed under reduced pressure affording a deep purple crystalline solid. Yield: 0.44 g, 78 %. EA for $C_{48}H_{38}Fe_2Cl_8O_6S_4$ calc.: C, 46.70; H, 3.10; S, 10.39; found: C, 46.61; H, 3.03; S, 10.35. Mass spectrum: 981.2 m/z (MNa⁺); 1354.8 m/z (M(CH₃CN)₂K⁺). UV-Vis: $\epsilon_{585} = 5441 \text{ L mol}^{-1} \text{ cm}^{-1}$.

Synthesis of the iron(III) complex 5 (Scheme 2)

The complex **5** was synthesized using the same procedure previously reported for complex **1**.¹¹ Pro-ligand **L5** (0.94 g; 2.04 mmol) was dissolved in THF (70mL). The solution was added to a suspension of sodium hydride (0.17 g; 7.08 mmol) in THF (30 mL) and the mixture stirred at room temperature overnight. The resulting suspension was filtered through celite and slowly added at room temperature to 0.325 g of anhydrous iron(III) chloride (2.0 mmol) dissolved in 30 mL of THF. The rapid change of the color to the blue was observed and the reaction kept overnight. The mixture was then filtered through celite and the solvent removed under reduced pressure affording a deep purple crystalline solid. Yield: 0.83 g, 80 %. EA for $C_{48}H_{44}Fe_2Cl_2O_6S_4$ calc.: C, 56.10; H, 4.32; S, 12.48; found: C, 56.02; H, 4.28; S, 12.39. Mass spectrum: 981.2 m/z (MNa⁺). UV-Vis: $\epsilon_{596} = 4757 \text{ L mol}^{-1} \text{ cm}^{-1}$.

Synthesis of the iron(III) complex 6 (Scheme 2)

The complex **6** was synthesized using the same procedure previously reported for complex **1**.¹¹ Pro-ligand **L6** (1.62 g; 3.56 mmol) was dissolved in THF (100mL). The solution was added to a suspension of sodium hydride (0.30 g; 12.5 mmol) in THF (70 mL) and the mixture stirred at room temperature overnight. The resulting suspension was filtered through celite and slowly added at room temperature to 0.567 g of anhydrous iron(III) chloride (3.50 mmol) dissolved in 100 mL of THF. The rapid change of the color to the deep purple was observed and the reaction kept overnight. The mixture was then filtered through celite and the solvent removed

under reduced pressure affording a deep purple crystalline solid. Yield: 1.60 g, 85 %. EA for $C_{56}H_{62}Fe_2O_6S_4$ calc.: C, 62.30; H, 5.83; S, 11.98; found: C, 62.20; H, 5.78; S, 11.89. Mass spectrum: 1072.1 m/z (MH⁺). UV-Vis: $\epsilon_{586} = 4962 \text{ L mol}^{-1} \text{ cm}^{-1}$.

ESI-MS Characterization

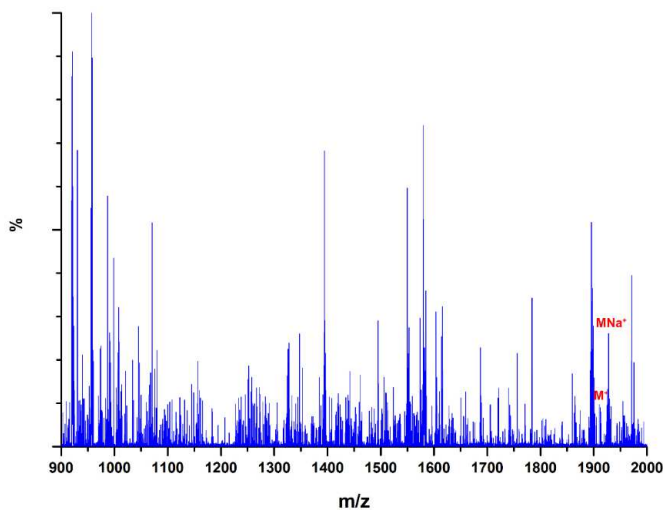


Figure S 25 ESI-MS spectrum of the complex **2** (acetonitrile as solvent).

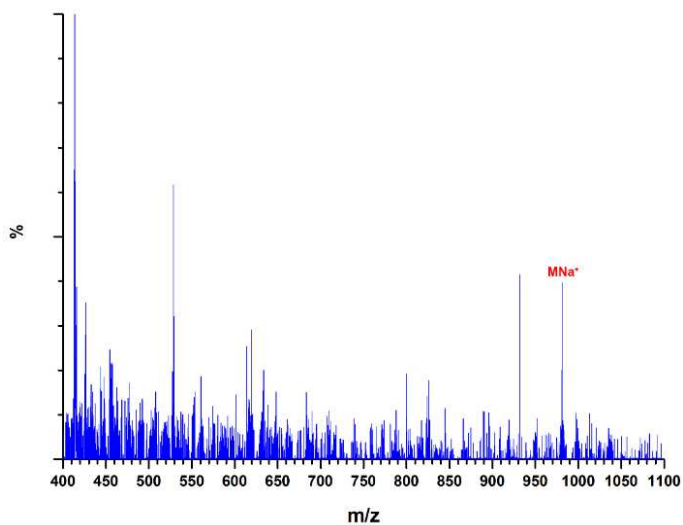


Figure S 26 ESI-MS spectrum of the complex **3** (acetonitrile as solvent).

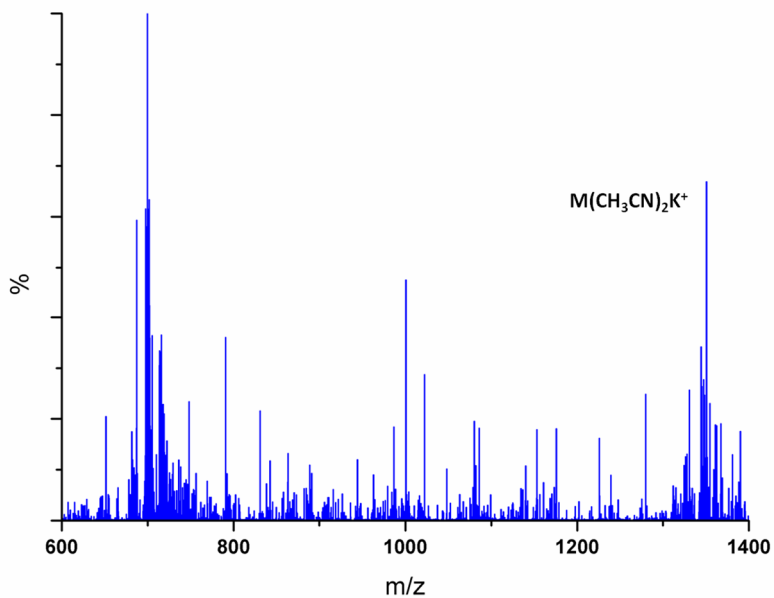


Figure S 27 ESI-MS spectrum of the complex 4 (acetonitrile as solvent).

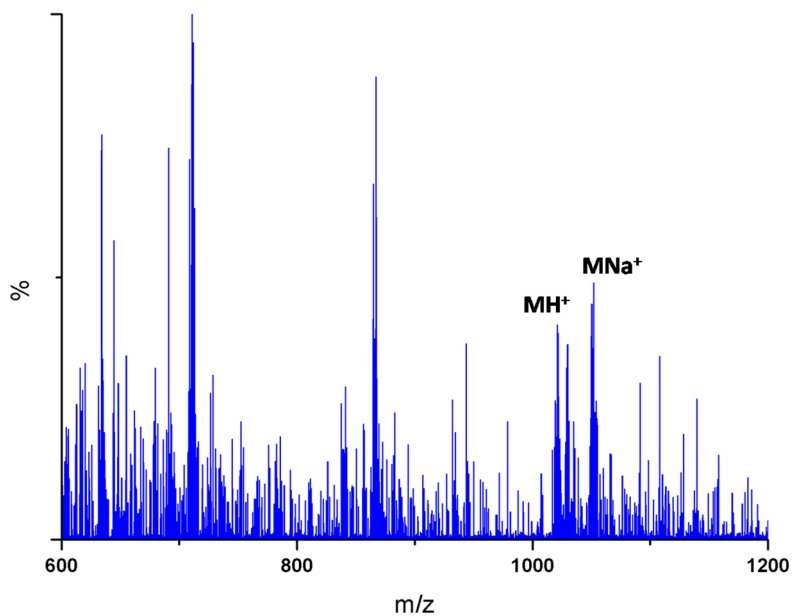


Figure S 28 ESI-MS spectrum of the complex 5 (acetonitrile as solvent).

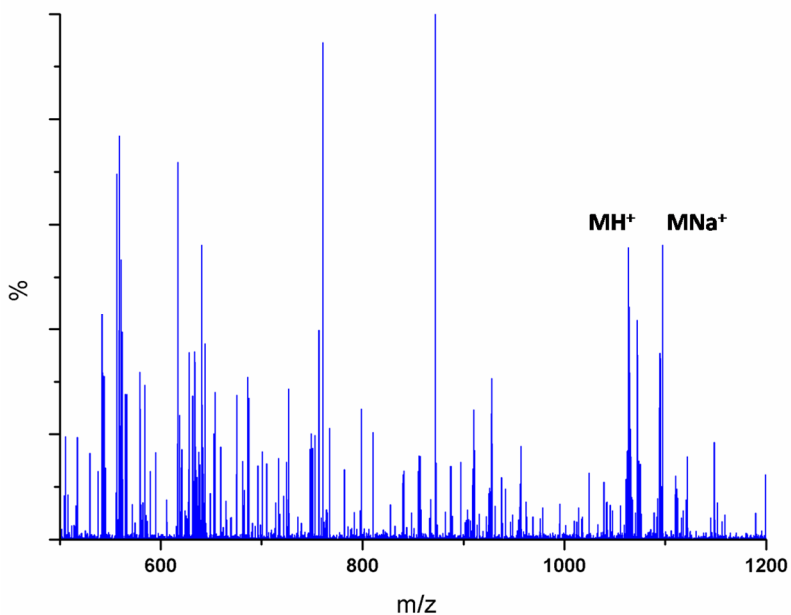


Figure S 29 ESI-MS spectrum of the complex **6** (acetonitrile as solvent).

FT-IR characterization

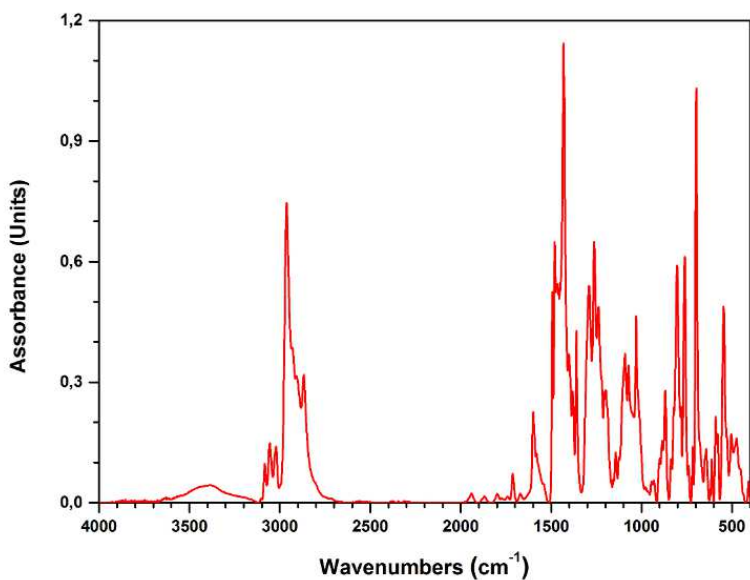


Figure S 30 FT-IR spectrum of the complex **2** (KBr disk).

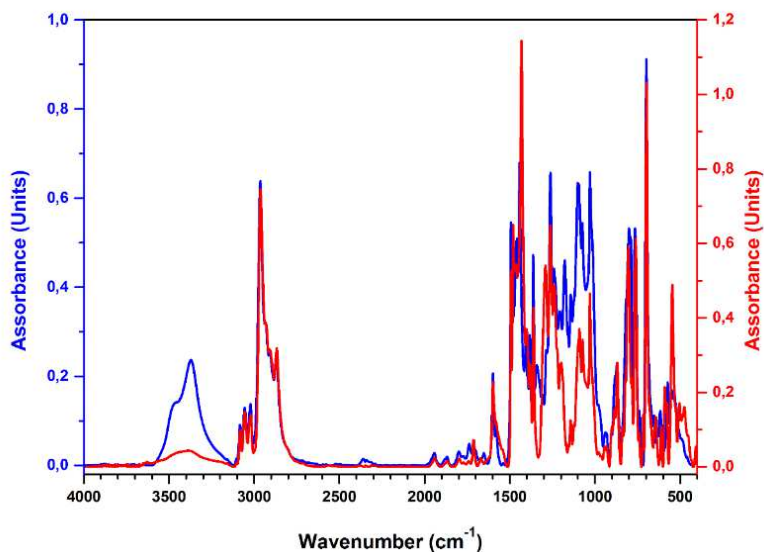


Figure S 31 Comparison of the FT-IR spectra of the pro-ligand **L2** (blue curve) and of the iron(III) complex **2** (red curve).

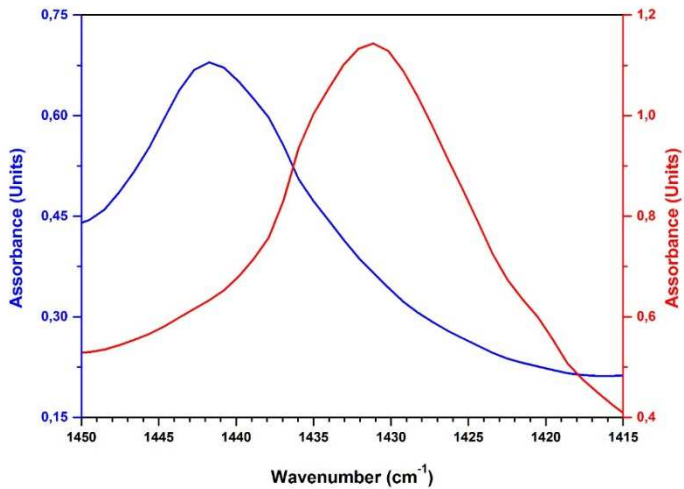


Figure S 32 Magnification of the region $1450\text{-}1415\text{ cm}^{-1}$ (for the $\text{CH}_2\text{-S-C}$ deformation)⁴⁶ of the FT-IR spectra of the pro-ligand **L2** (blue curve) and of the iron(III) complex **2** (red curve).

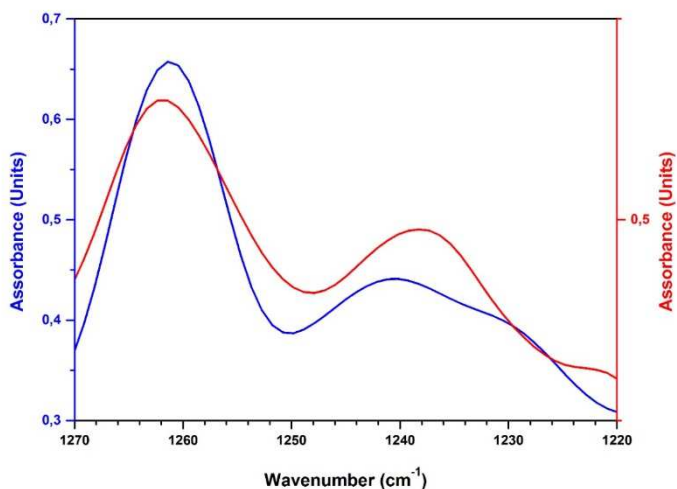


Figure S 33 Magnification of the region 1270-1220 cm^{-1} (for the $\text{CH}_2\text{-S-C}$ wagging)⁴⁶ of the FT-IR spectra of the pro-ligand **L2** (blue curve) and of the iron(III) complex **2** (red curve).

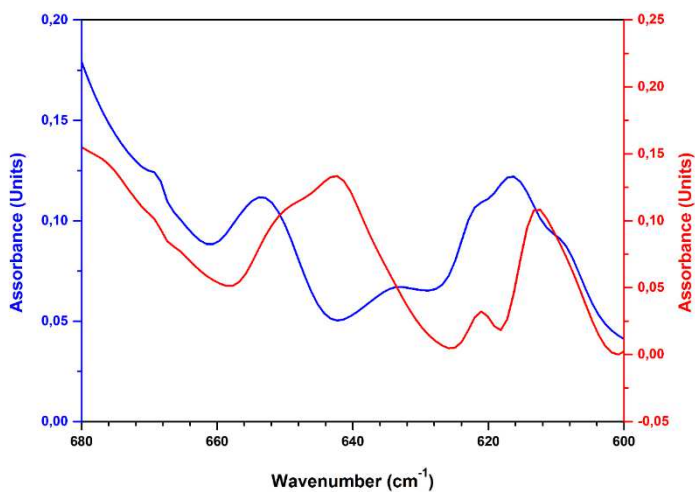


Figure S 34 Magnification of the region 680-600 cm^{-1} (for the C-S stretching vibration)⁴⁶ of the FT-IR spectra of the pro-ligand **L2** (blue curve) and of the iron(III) complex **2** (red curve).

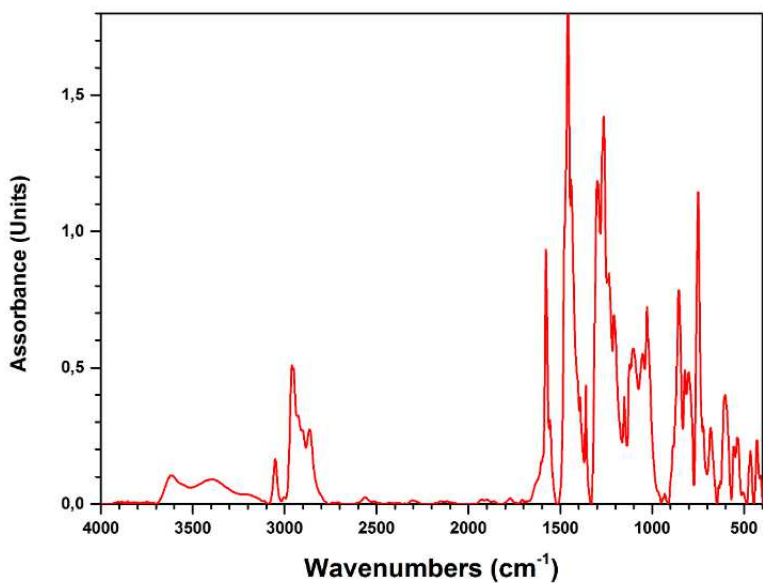


Figure S 35 FT-IR spectrum of the complex **3** (KBr disk).

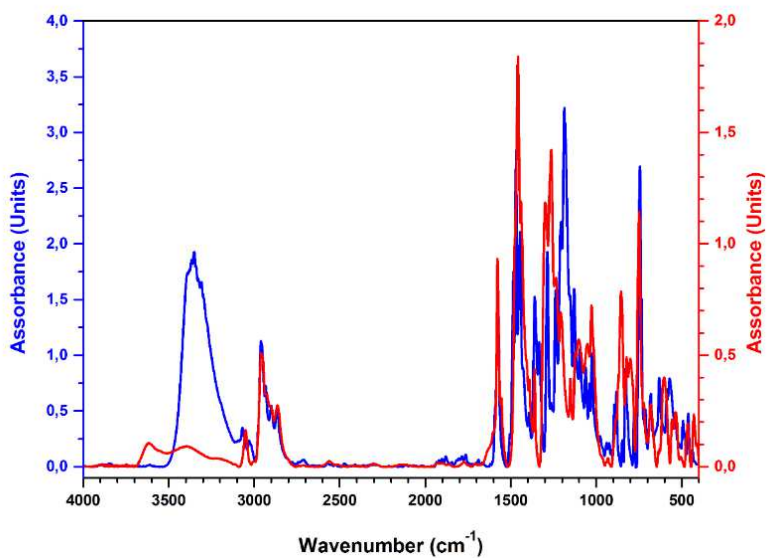


Figure S 36 Comparison of the FT-IR spectra of the pro-ligand **L3** (blue curve) and of the iron(III) complex **3** (red curve).

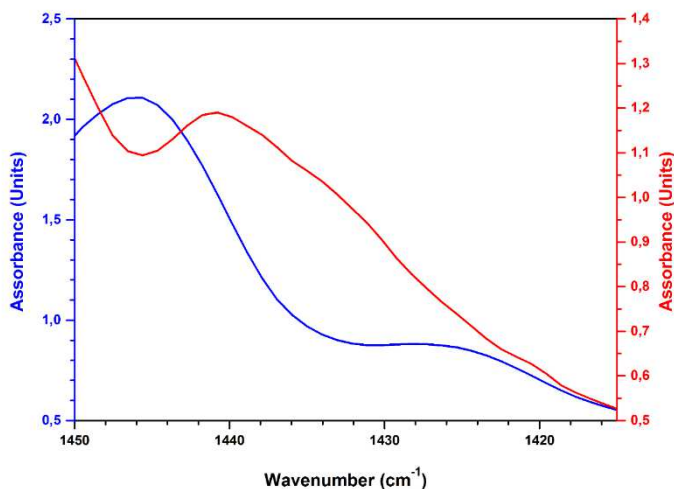


Figure S 37 Magnification of the region 1450-1415 cm^{-1} (for the $\text{CH}_2\text{-S-C}$ deformation)⁴⁶ of the FT-IR spectra of the pro-ligand **L3** (blue curve) and of the iron(III) complex **3** (red curve).

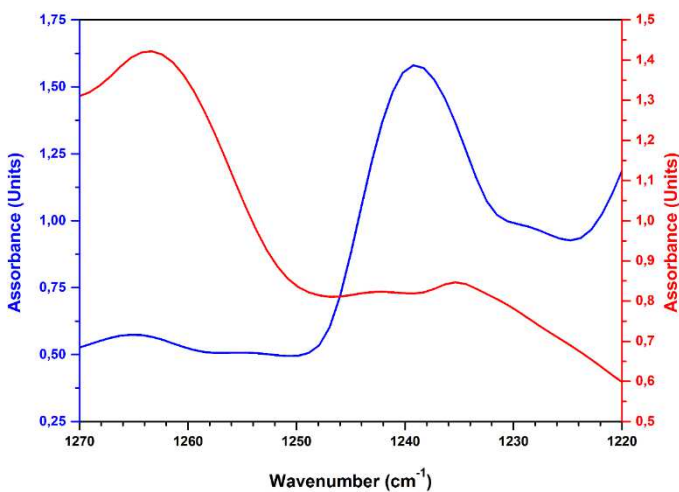


Figure S 38 Magnification of the region 1270-1220 cm^{-1} (for the $\text{CH}_2\text{-S-C}$ wagging)⁴⁶ of the FT-IR spectra of the pro-ligand **L3** (blue curve) and of the iron(III) complex **3** (red curve).

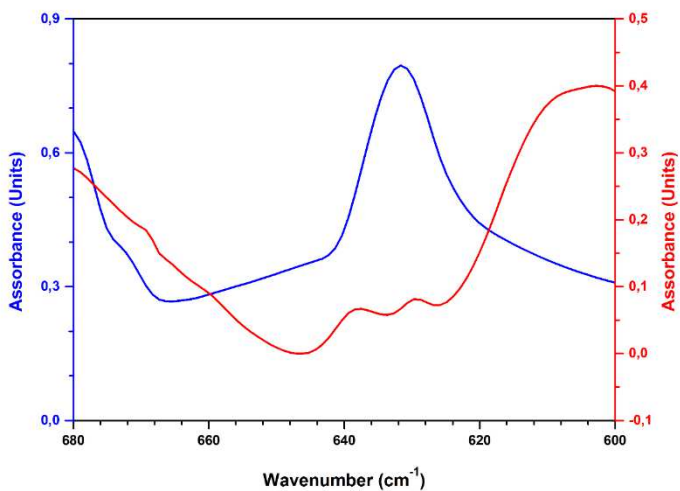


Figure S 39 Magnification of the region 680-600 cm⁻¹ (for the C-S stretching vibration)⁴⁶ of the FT-IR spectra of the pro-ligand **L3** (blue curve) and of the iron(III) complex **3** (red curve).

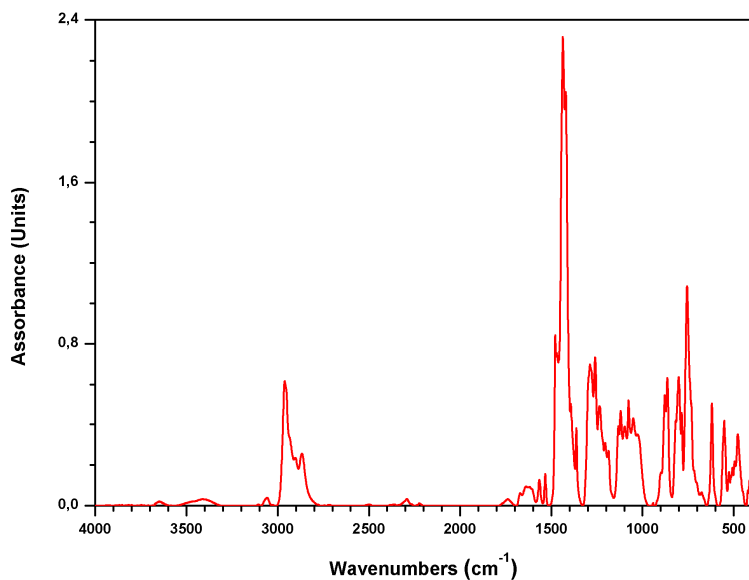


Figure S 40 FT-IR spectrum of the complex **4** (KBr disk).

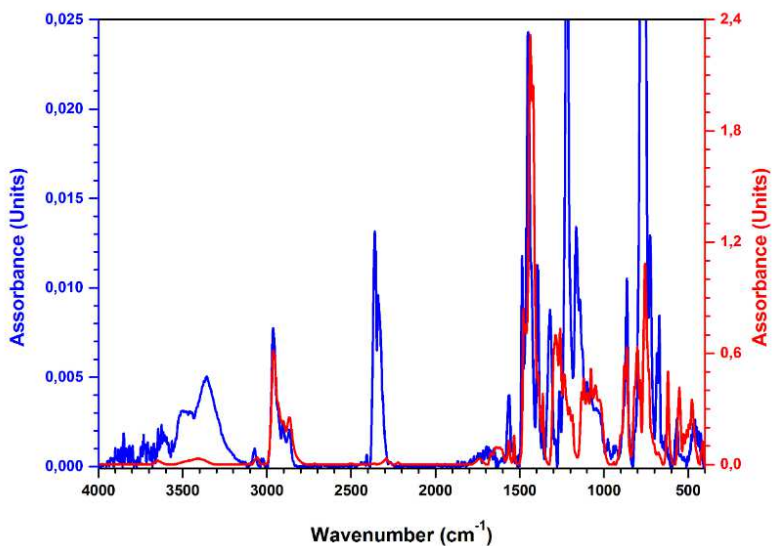


Figure S 41 Comparison of the FT-IR spectra of the pro-ligand **L4** (blue curve) and of the iron(III) complex **4** (red curve).

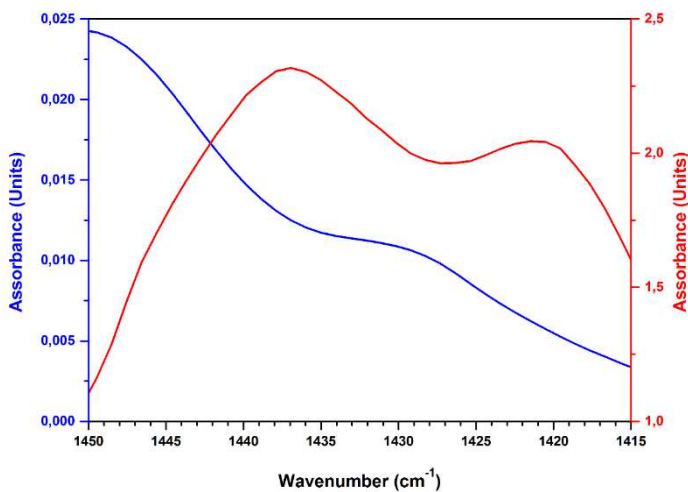


Figure S 42 Magnification of the region 1450-1415 cm^{-1} (for the $\text{CH}_2\text{-S-C}$ deformation)⁴⁶ of the FT-IR spectra of the pro-ligand **L4** (blue curve) and of the iron(III) complex **4** (red curve).

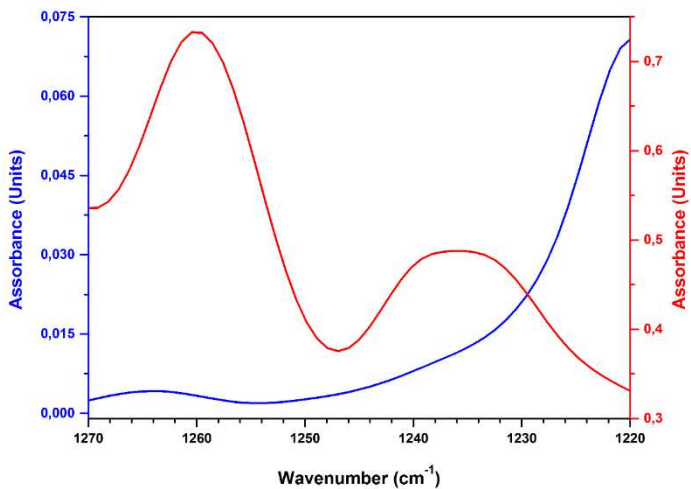


Figure S 43 Magnification of the region $1270\text{-}1220\text{ cm}^{-1}$ (for the $\text{CH}_2\text{-S-C}$ wagging)⁴⁶ of the FT-IR spectra of the pro-ligand **L4** (blue curve) and of the iron(III) complex **4** (red curve).

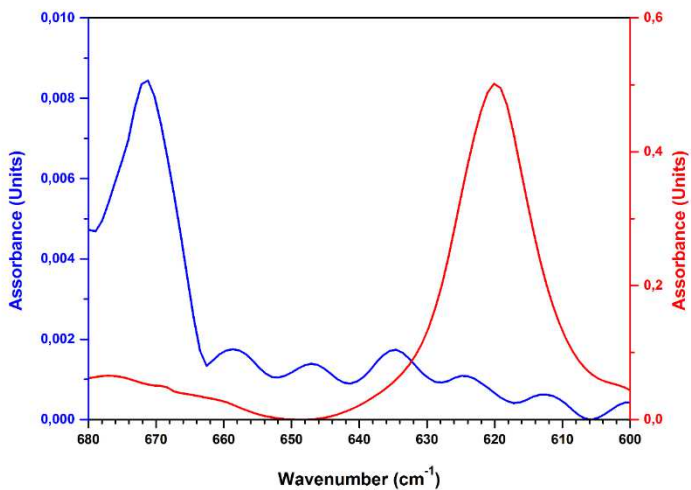


Figure S 44 Magnification of the region $680\text{-}600\text{ cm}^{-1}$ (for the C-S stretching vibration)⁴⁶ of the FT-IR spectra of the pro-ligand **L4** (blue curve) and of the iron(III) complex **4** (red curve).

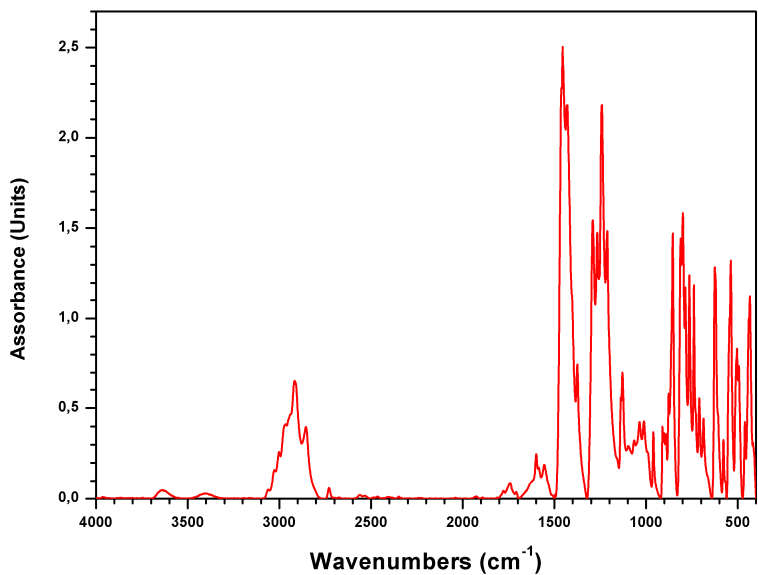


Figure S 45 FT-IR spectrum of the complex **5** (KBr disk).

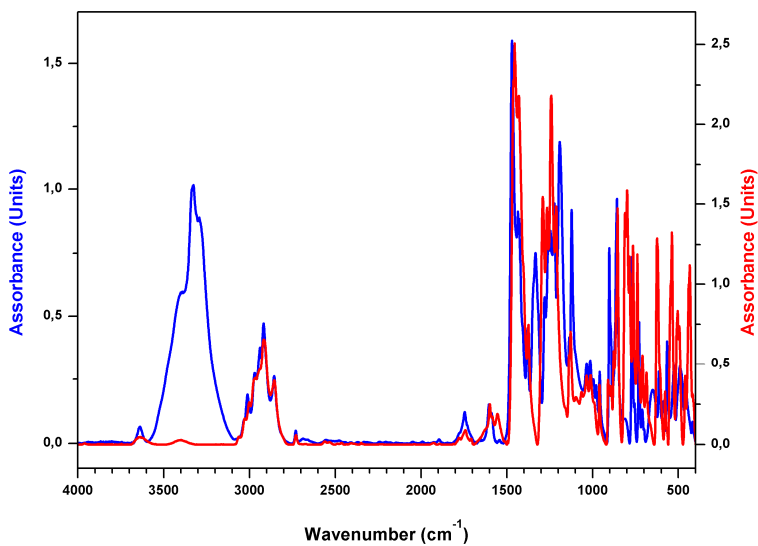


Figure S 46 Comparison of the FT-IR spectra of the pro-ligand **L5** (blue curve) and of the iron(III) complex **5** (red curve).

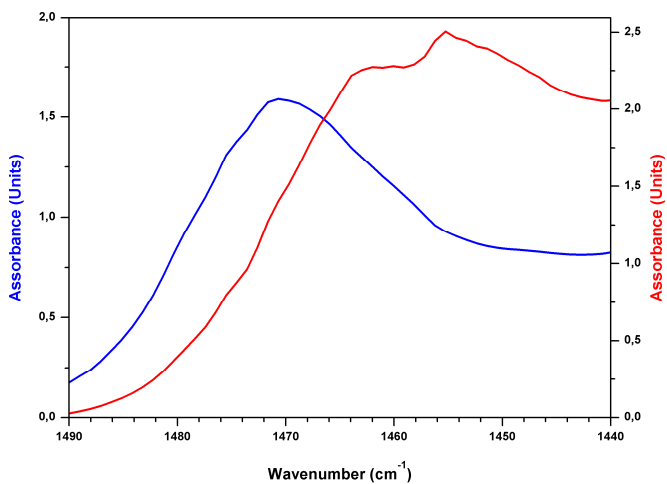


Figure S 47 Magnification of the region 1490-1440 cm^{-1} (for the $\text{CH}_2\text{-S-C}$ deformation)⁴⁶ of the FT-IR spectra of the pro-ligand **L5** (blue curve) and of the iron(III) complex **5** (red curve).

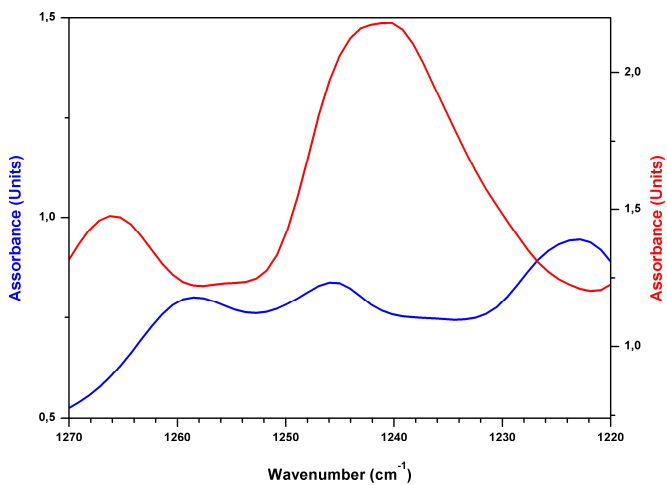


Figure S 48 Magnification of the region 1270-1220 cm^{-1} (for the $\text{CH}_2\text{-S-C}$ wagging)⁴⁶ of the FT-IR spectra of the pro-ligand **L5** (blue curve) and of the iron(III) complex **5** (red curve).

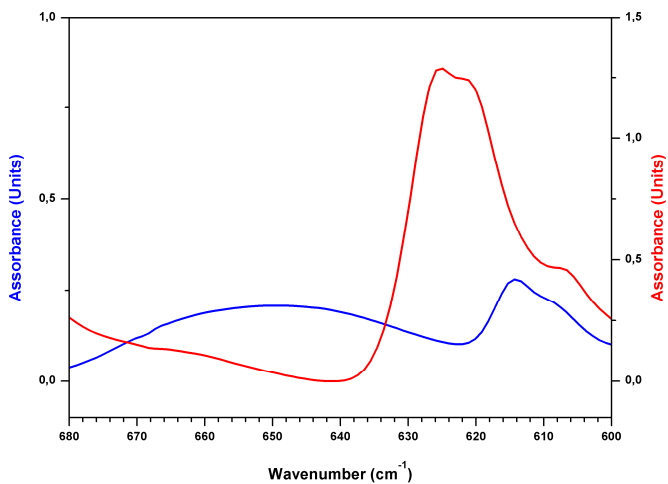


Figure S 49 Magnification of the region 680-600 cm⁻¹ (for the C-S stretching vibration)⁴⁶ of the FT-IR spectra of the pro-ligand **L5** (blue curve) and of the iron(III) complex **5** (red curve).

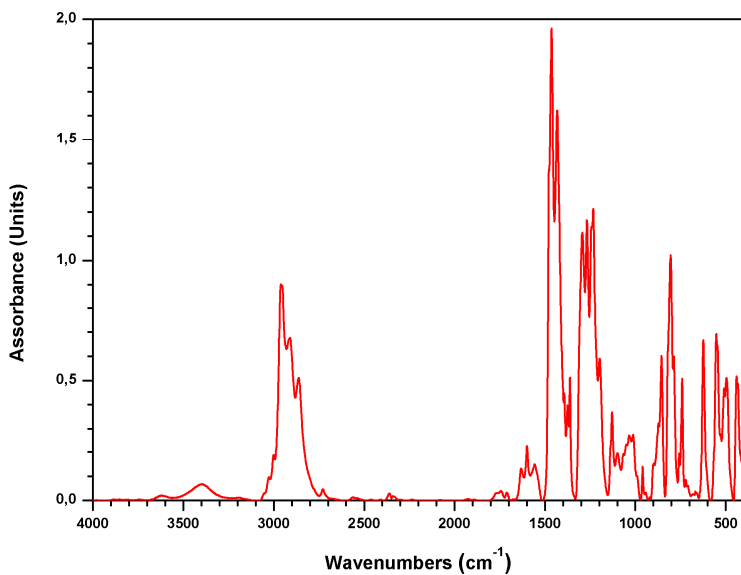


Figure S 50 FT-IR spectrum of the complex **6** (KBr disk).

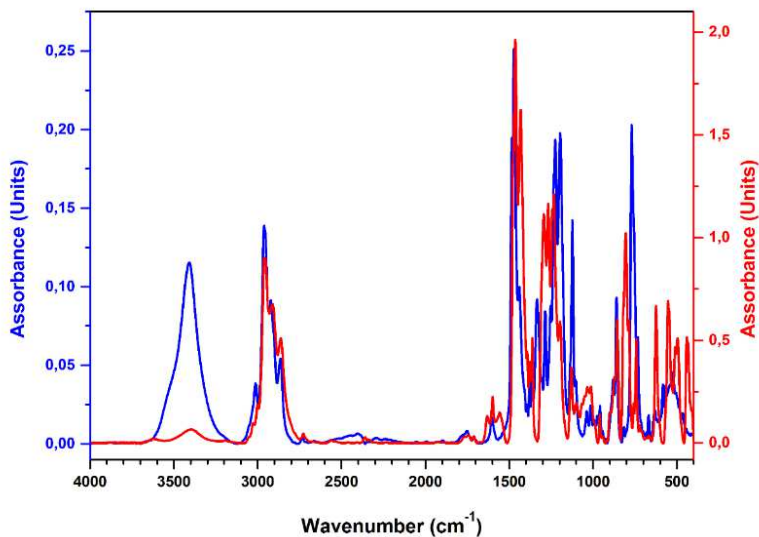


Figure S 51 Comparison of the FT-IR spectra of the pro-ligand **L6** (blue curve) and of the iron(III) complex **6** (red curve).

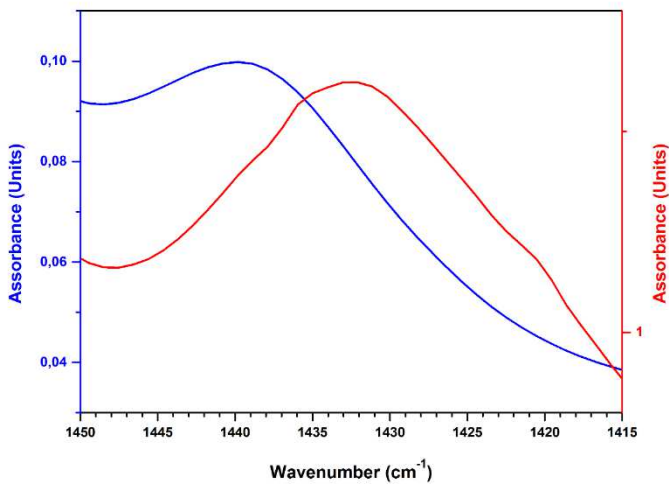


Figure S 52 Magnification of the region $1450\text{-}1415\text{ cm}^{-1}$ (for the $\text{CH}_2\text{-S-C}$ deformation)⁴⁶ of the FT-IR spectra of the pro-ligand **L6** (blue curve) and of the iron(III) complex **6** (red curve).

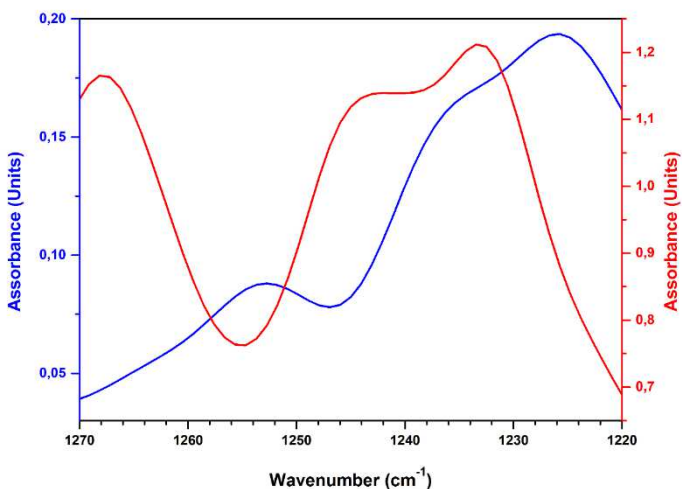


Figure S 53 Magnification of the region 1270-1220 cm^{-1} (for the $\text{CH}_2\text{-S-C}$ wagging)⁴⁶ of the FT-IR spectra of the pro-ligand **L6** (blue curve) and of the iron(III) complex **6** (red curve).

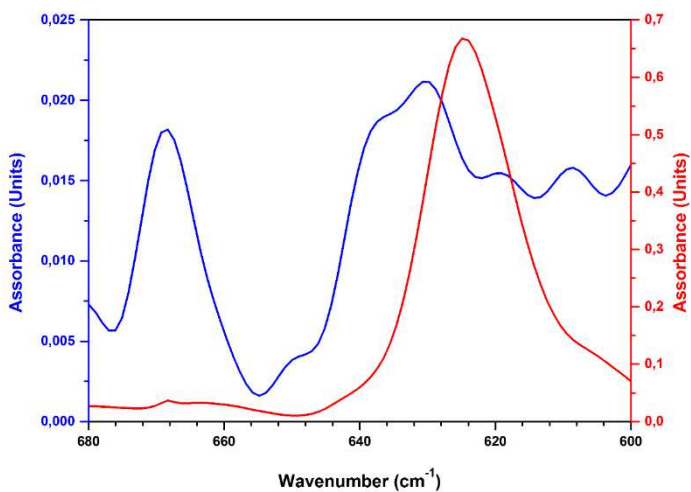


Figure S 54 Magnification of the region 680-600 cm^{-1} (for the C-S stretching vibration)⁴⁶ of the FT-IR spectra of the pro-ligand **L6** (blue curve) and of the iron(III) complex **6** (red curve).

UV-Vis characterization

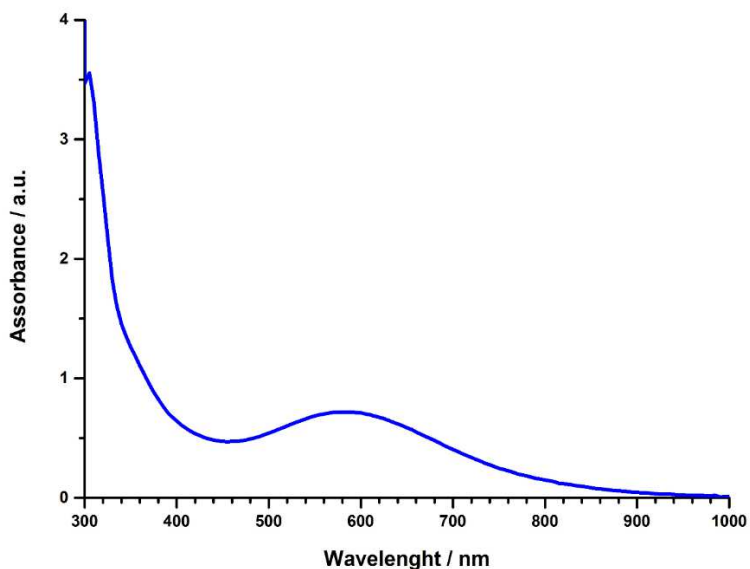


Figure S 55 UV-Vis spectrum of the complex **2** (1.07×10^{-4} M in toluene; $\epsilon_{585} = 7188$ L mol⁻¹ cm⁻¹).

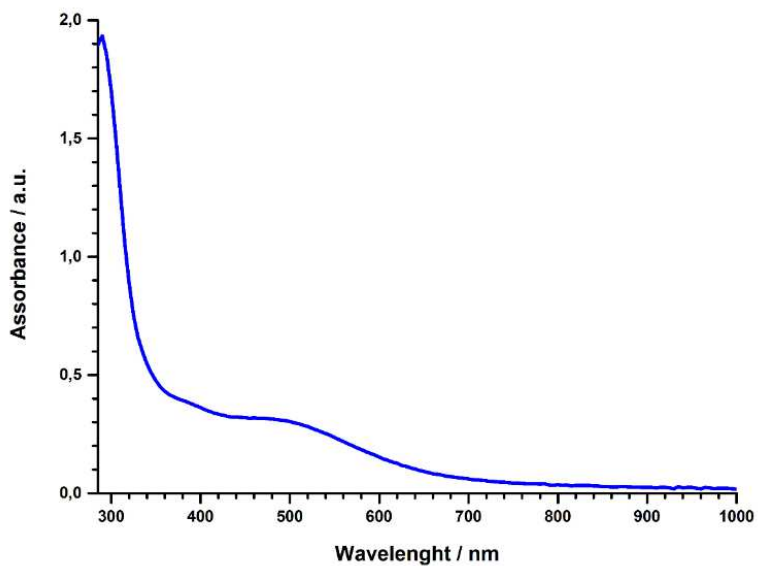


Figure S 56 UV-Vis spectrum of the complex **3** (1.07×10^{-4} M in toluene; $\epsilon_{470} = 2804$ L mol⁻¹ cm⁻¹).

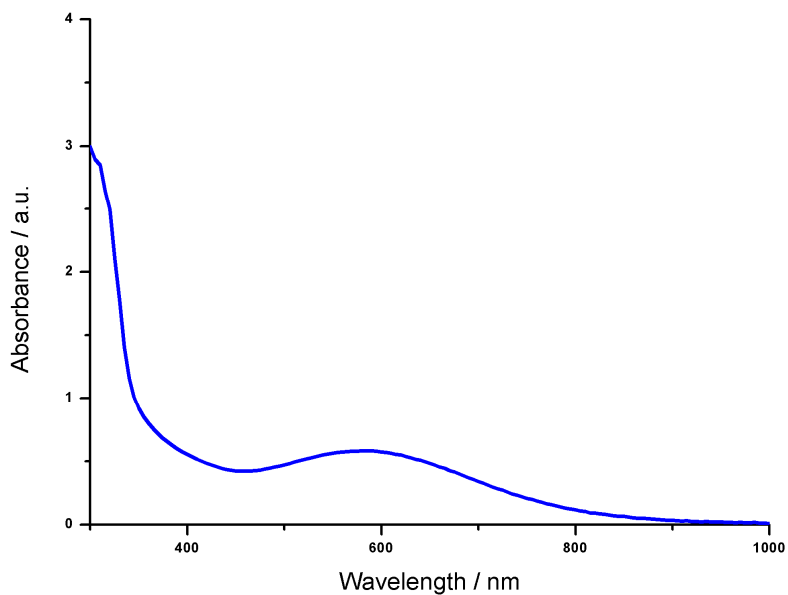


Figure S 57 UV-Vis spectrum of the complex **4** (1.07×10^{-4} M in toluene; $\epsilon_{585} = 5441$ L mol⁻¹ cm⁻¹).

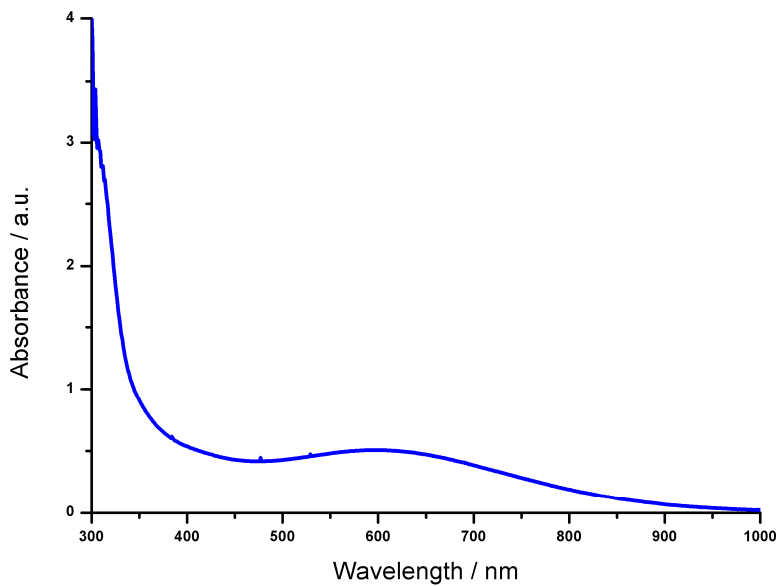


Figure S 58 UV-Vis spectrum of the complex **5** (1.07×10^{-4} M in toluene; $\epsilon_{596} = 4757$ L mol⁻¹ cm⁻¹).

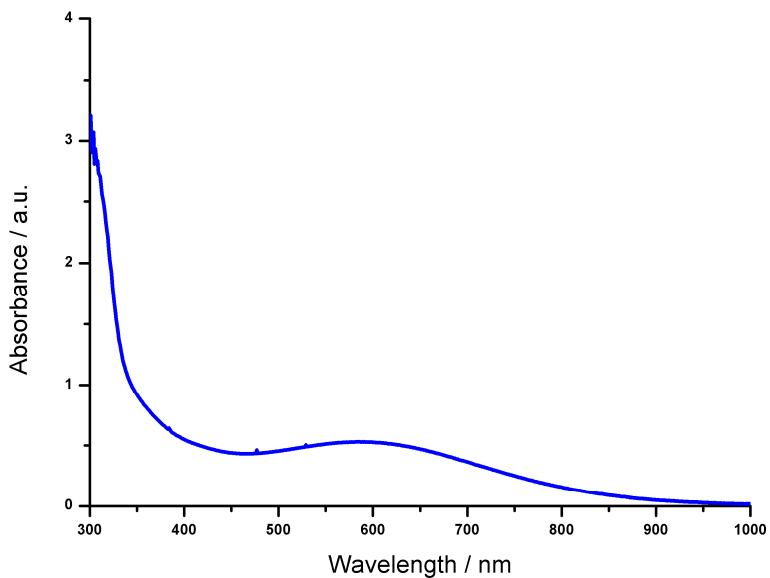


Figure S 59 UV-Vis spectrum of the complex **6** (1.07×10^{-4} M in toluene; $\epsilon_{586} = 4962$ L mol $^{-1}$ cm $^{-1}$).

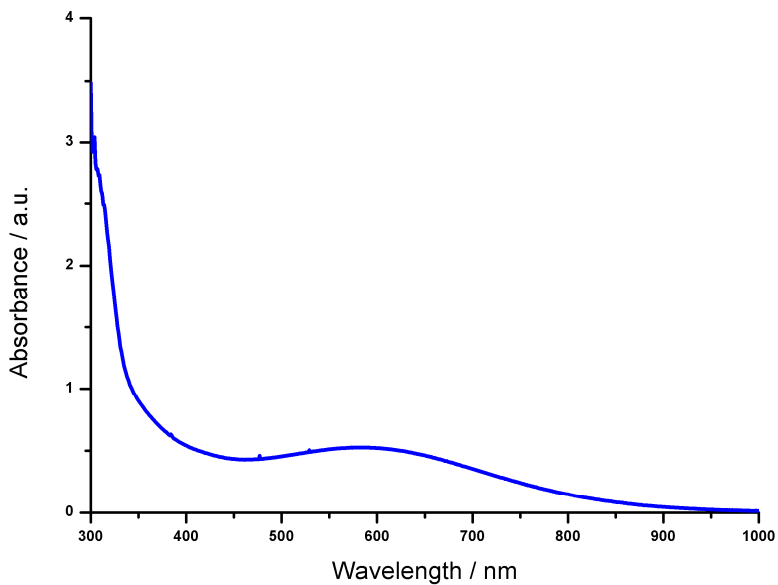


Figure S 60 UV-Vis spectrum of the complex **6** in the presence of 50 equivalents of Pyridine-d5 (1.07×10^{-4} M in toluene; $\epsilon_{586} = 4935$ L mol $^{-1}$ cm $^{-1}$).

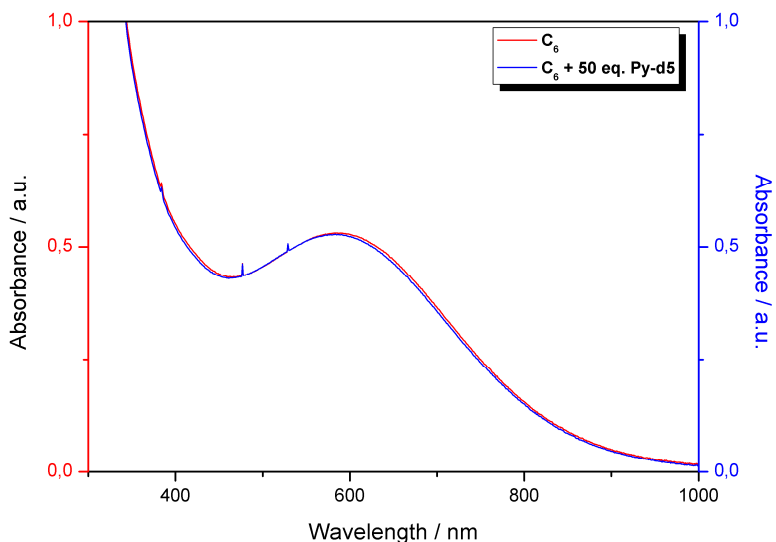


Figure S 61 Comparison of the UV-Vis spectra of the complex **6** before (red curve) and after the addition of 50 equivalents of Pyridine-d5 (blue curve)

Crystallographic data of the Iron(III) complex **6**

CCDC 1477580 contains the supplementary crystallographic data for this paper. These data can be obtained free of charge from the Cambridge Crystallographic Data Centre via <https://www.ccdc.cam.ac.uk/structures/>

Table S 1 Selected bond lengths [Å] for complex **6**

Fe(1)-O(1)	1.8894(14)	Fe(2)-O(6)	1.8943(14)
Fe(1)-O(4)	1.9030(13)	Fe(2)-O(3)	1.8994(15)
Fe(1)-O(5)	2.0314(13)	Fe(2)-O(5)	2.0345(13)
Fe(1)-O(2)	2.0384(14)	Fe(2)-O(2)	2.0514(14)
Fe(1)-S(1)	2.6102(5)	Fe(2)-S(2)	2.5914(5)
Fe(1)-S(3)	2.6466(5)	Fe(2)-S(4)	2.6585(5)

Table S 2 Crystal data and structure refinement for complex **6**

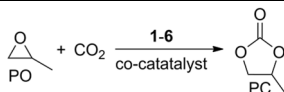
6	
Empirical formula	C ₅₆ H ₆₂ Fe ₂ O ₆ S ₄
Formula weight	1070.99
Temperature/K	100(2)
Crystal system	monoclinic
Space group	C2
<i>a</i> , Å	22.4656(6)
<i>b</i> , Å	15.5142(6)
<i>c</i> , Å	18.8242(6)
α , °	90
β , °	126.399(2)
γ , °	90
Cell volume, Å ³	2121(5)
Z	4
ρ_c , mg m ⁻³	1.347
μ (Mo-K α), mm ⁻¹	0.756
F(000)	2248
Crystal size mm	0.51 x 0.45 x 0.40
θ limits, °	1.344 to 27.993
Refl. collected, unique (<i>R</i> _{int})	47143 / 12667 [<i>R</i> (int) = 0.0229]
Goodness-of-fit-on F ²	1.042
<i>R</i> ₁ (F) ^a , w <i>R</i> ₂ (F ²) [<i>I</i> > 2 σ (<i>I</i>)] ^b	<i>R</i> ₁ = 0.0204, w <i>R</i> ₂ = 0.0537
Largest diff. peak and hole, e. Å ⁻³	0.302 and -0.236

^a $R_1 = \sum ||F_o| - |F_c|| / \sum |F_o|$. ^b $wR_2 = [\sum w(F_o^2 - F_c^2)^2 / \sum w(F_o^2)^2]^{1/2}$ where $w = 1 / [\sigma^2(F_o^2) + (aP)^2 + bP]$ where $P = (F_o^2 + F_c^2) / 3$.

Typical procedure for CO₂/epoxide coupling to cyclic carbonates catalyzed by 6/TBAB (referred to entry 6, Table 3). A 60 mL stainless steel pressure reactor equipped with a magnetic stirring bar was charged, under CO₂ atmosphere, with 7.7 mg of catalyst **6** ($7.15 \cdot 10^{-6}$ mol) and 23.0 mg of TBAB ($7.15 \cdot 10^{-5}$ mol) dissolved in 5.0 mL of PO ($7.15 \cdot 10^{-2}$ mol). The reaction mixture was pressurized with CO₂ at 2.0 MPa and stirred at 120 °C for 1 h. The reactor was cooled with ice, the CO₂ released, 1.0 mL of mesitylene ($7.15 \cdot 10^{-3}$ mol) was added as an internal standard and the mixture was analyzed by ¹H NMR spectroscopy using CDCl₃ as solvent. Yield 52.0 %.

Catalytic tests

Table S 3 Propylene carbonate formation promoted by Fe(III) complexes 1-6.



Entry ^a	Catalyst	Co-Catalyst	PO/Co-cat/Cat	T	P _{CO₂}	Conversion ^{b,c}	TOF ^d		
	mol%	mol%	molar ratio	°C	bar	mol%	h ⁻¹		
S1	1	0.025	TBAB	0.05	4000/2/1	80	20	4.6	185
S2	1	0.025	TBAB	0.05	4000/2/1	100	20	16.8	675
S3	1	0.025	TBAB	0.05	4000/2/1	120	20	39.8	1595
S4	1	0.025	TBAB	0.05	4000/2/1	140	20	57.4	2300
S5	2	0.025	TBAB	0.05	4000/2/1	80	20	4.6	185
S6	2	0.025	TBAB	0.05	4000/2/1	100	20	20.1	805
S7	2	0.025	TBAB	0.05	4000/2/1	120	20	29.4	1175
S8	2	0.025	TBAB	0.05	4000/2/1	140	20	47.5	1900
S9	3	0.025	TBAB	0.05	4000/2/1	80	20	2.4	96
S10	3	0.025	TBAB	0.05	4000/2/1	100	20	16.9	680
S11	3	0.025	TBAB	0.05	4000/2/1	120	20	49.2	1970
S12	3	0.025	TBAB	0.05	4000/2/1	140	20	60.5	2420
S13	6	0.025	TBAB	0.05	4000/2/1	80	20	28.3	1132
S14	6	0.025	TBAB	0.05	4000/2/1	100	20	46	1840
S15	6	0.025	TBAB	0.05	4000/2/1	120	20	57.6	2304
S16	6	0.025	TBAB	0.05	4000/2/1	140	20	67.0	2680
S17	6	0.025	DMAP	0.05	4000/2/1	120	20	0.5	20
S18	6	0.025	[PPN]Cl	0.05	4000/2/1	120	20	34.2	1368
S19	6	0.025	TBAC	0.05	4000/2/1	120	20	31.5	1260
S20	6	0.025	TBAI	0.05	4000/2/1	120	20	34.3	1372
S21	6	0.025	TBAB	0.10	4000/4/1	120	20	76.1	3044
S22	6	0.025	TBAB	0.25	4000/10/1	120	20	82.6	3304
S23	-	-	TBAB	0.25	4000/10/0	120	20	10.0	-
S24	6	0.025	TBAB	0.25	4000/10/1	120	5	80.6	3224
S25	6	0.025	TBAB	0.25	4000/10/1	120	40	>99	4000

a) Reaction conditions: PO = 5 mL, 7.15×10^{-2} mol; reaction time = 1 h. b) Determined by ¹H-NMR using mesitylene as internal standard. c) The selectivity toward the formation of propylene carbonate was always found to be >99%. d) Turnover Frequency (mol_{PC} · mol_{Catalyst}⁻¹ · reaction time⁻¹).

2.7 References

- ⁴¹ Buonerba A., De Nisi A., Grassi A., Milione S., Capacchione C.,* Vagin S. and Rieger B., *Catal. Sci. Technol.*, **2015**, *5*, 118-123.
- ⁴² Metzinger R., Limber C. Z., *Z. Anorg. Allg. Chem.*, **2012**, *638*, 2225–2234.
- ⁴³ Whiteoak C. J., Martin E., Escudero-Adán E., Kleij A. W., *Adv. Synth. Catal.*, **2013**, *355*, 2233–2239
- ⁴⁴ Martín C., Fiorani G., Kleij A. W., *ACS Catal.*, **2015**, *5*, 1353-1370.
- ⁴⁵ D’Elia V., Ghani A. A., Monassier A., Sofack-Kreutzer J., Pelletier J. D. A., Drees M., Vummaleti S. V. C., Poater A., Cavallo L., Cokoja M., Basset J.-M., Kghn F. E., *Chem. Eur. J.*, **2014**, *20*, 11870-11882;
b) D’Elia V., Dong H., Rossini A. J., Widdifield C. M., Vummaleti S. V. C., Minenkov Y., Poater A., Abou-Hamad E., Pelletier J. D. A., Cavallo L., Emsley L., Basset J.-M., *J. Am. Chem. Soc.*, **2015**, *137*, 7728-7739.
- ⁴⁶ a) *The Sadtler handbook of infrared spectra*, ed. W. W. Simons, Sadtler Research Laboratories, Philadelphia, **1978**. b) *Interpreting Infrared, Raman, and Nuclear Magnetic Resonance Spectra*, ed. R. A. Nyquist, Academic Press, San Diego, **2001**, pp. 65-83.

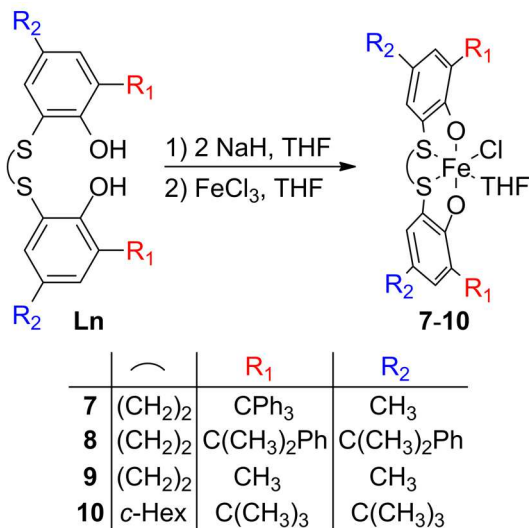
3 [OSSO]-type Iron(III) complexes

The investigation of the reaction mechanism conducted for the bimetallic thioether-triphenolate Fe(III) complexes, described in the paragraph 2.4, suggests that only one metal centre is involved in the the reaction between CO₂ and PO. Moreover the role of the soft neutral S donor in the coordination sphere of the catalytic site was highlighted. Indeed, the decoordination of one sulphur atom from one of the iron centres is crucial for the coordination, and subsequently activation, of the epoxide. Taking into account these mechanistic features, and driven by the excellent results obtained in catalysis, we decided to design mononuclear Fe(III) complexes presenting a similar coordination sphere, in order to study their behaviour as catalyst for the coupling of CO₂ with epoxides. At this purpose, we chose the dianionic tetradentate [OSSO]-type ligands to synthesize new compounds with the desired properties. Indeed, the use of this class of ligands for the preparation of monometallic complexes, *i.e.* of Group 3 and Group 4 metals, and their use in catalysis, is well documented, especially for polymerization reactions.⁴⁷ Moreover, a series of Cr(III) complexes bearing [OSSO]-type ligands, have been recently reported and their use for the co-polymerization of CO₂ with vinyl-cyclohexene oxide was described.⁴⁸ In this chapter the synthesis and complete characterization of four new thioether-phenolate [OSSO]-type Fe(III) complexes is described. The application of these compounds as catalyst for chemo- and stereo-selective production of cyclic organic carbonates (COCs) from carbon dioxide and epoxides is reported. The chemoselectivity divergence of the reaction toward the formation of the polymer product was observed in the case of CHO and the selective copolymerization of CO₂ and CHO is also described. Insights on the role of the metal centre in the reaction mechanism, for formation of both PC and PCC, are given on the basis of kinetic investigations conducted by means of ATR-IR measurements.

3.1 Synthesis and characterization

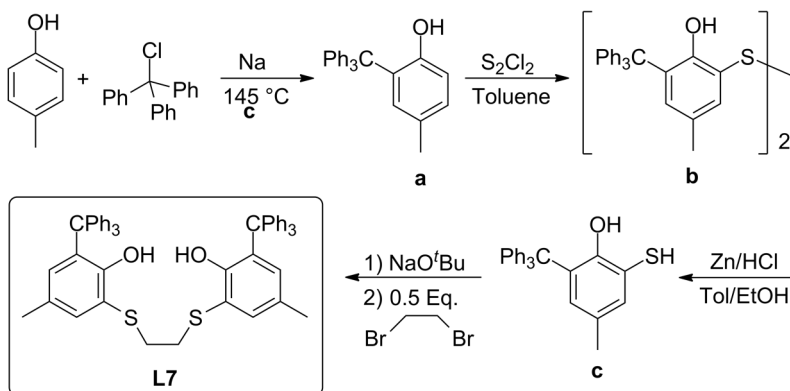
Since the bulkiness of the substituents at the *orto* positions of the phenol rings showed to play a major role in the determination of the catalytic activity in the case of complexes **1-6**, we decided to prepare

four new [OSSO]-type Fe(III) complexes with different substitution at the R₁ positions (Scheme 4).



Scheme 4 Synthesis of the [OSSO]-Fe(III) complex **7-10**.

The [OSSO]-type ligands **L8-10** were prepared following the procedures reported in the literature.⁴⁹ The new ligand **L7**, with trityl substituents, was prepared for the first time following the synthesis shown in Scheme 5.



Scheme 5 Synthesis of the trityl substituted [OSSO] ligand **L7**.

The synthesis starts from the preparation of the 2-trityl-4-methylphenol **a**. The mercapto-phenol **c** was obtained with the same

procedure adopted for the reported ligands **L8-10**. Finally, the S_N2 reaction of the thiol with 1,2-dibromoethane led to the formation of the desired product **L7**, that was isolated in good yields by crystallization and fully characterized by NMR and HR-MS analysis. All the complexes **8-10**, were obtained by reaction of an equimolar amount of $FeCl_3$ with the sodium salt of the corresponding pro-ligand in THF, obtained from the reaction of the ligand precursor with 2 equivalents of sodium hydride (Scheme 4). All the products were recovered in high yield as deep-blue powders. The formation of the desired products was confirmed by elemental analysis. In addition, in the FT-IR spectra of the complexes, the disappearance of the hydroxyl group vibration at about 3300 cm^{-1} is evident. The formation of a monomeric structure was supported by the HR-ESI-MS analysis from DCM/MeOH solutions (see ESI-MS Characterization). Indeed the effective magnetic moments (μ_{eff}), determined by means of the Evans method in deuterated toluene in the range from 30 to 90 °C, are comparable with the calculated value for one isolated high spin (HS) iron(III) centre.

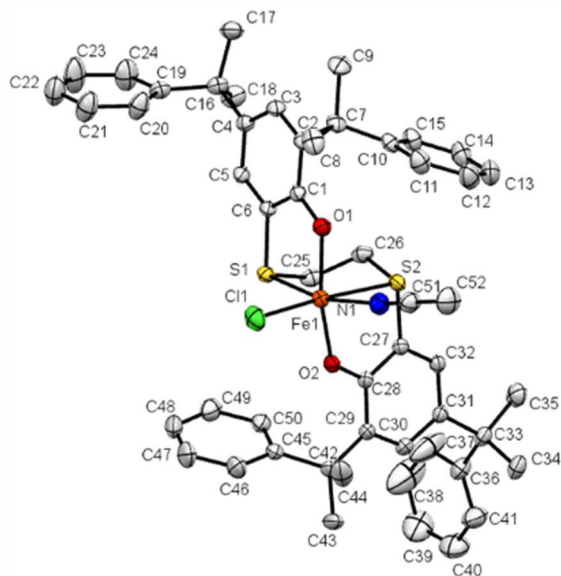


Figure 33 Molecular structure of compound **8**. Hydrogen atoms have been omitted for the sake of clarity (thermal ellipsoids are drawn at 30% of the probability level). Selected bond lengths (Å) and angles (°): Fe_1-O_1 1.908(2), Fe_1-O_2 1.900(2), Fe_1-S_1 2.5642(8), Fe_1-S_2 2.6936(9), Fe_1-Cl_1 2.2497(9), Fe_1-N_1 2.124(2), $S_1-Fe_1-S_2$ 83.20(2).

Single crystals of **8** were grown from a saturated acetonitrile solution. The crystal structure of complex **8** (Figure 33) shows the Fe atom in a distorted octahedral geometry coordinated by one tetradentate [OSSO] ligand adopting a *fac-fac* coordination, one chloride and one N atom of acetonitrile ligand. The Fe atom is involved in a puckered five-membered ring (Fe1-S1-C25-C26-S2) with a S1-Fe1-S2 bite angle of 83.20(2)°, smaller than that found for example in the complex [Fe(CO)₂(tbu₄-dtted)].⁵⁰

3.2 Cyclic organic carbonate formation

The complexes **7-10** were tested in the coupling of carbon dioxide with 1,2-epoxyhexane (HO) under very mild reaction conditions, namely 35 °C, 1 bar of CO₂ pressure and 0.1 mol% of complex with respect to the epoxide. In the absence of co-catalyst, no conversion was observed in 24 hours. On the basis of the results obtained using the complexes **1-6**, the reactions were repeated in the presence of 0.1 mol% of TBAB, under the same conditions.

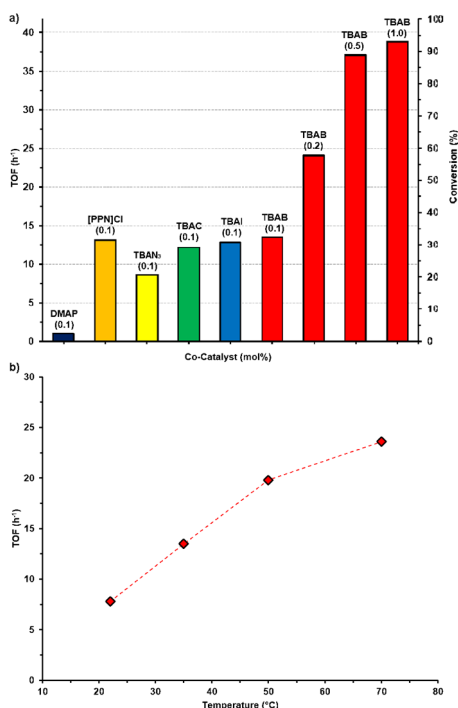


Figure 34 Effect of the co-catalyst type and loading (a) and temperature (b) on the catalytic activity of **10** in HO/CO₂ coupling (entries S4-15 Table S 5).

As expected, the presence of the co-catalyst activates the catalysts, leading to the selective formation of the cyclic product 4-butyl-1,3-dioxolan-2-one (hexene carbonate, HC) (entries S1-4 Table S 5). The best result was obtained in the case of the complex **10** with a TOF of 13.5 h⁻¹. In addition to TBAB, the screening of the following co-catalysts, in the presence of **10** under the same conditions, was performed: DMAP, [PPN]Cl, TBAN₃, TABC and TBAI (entries S5-9, Table S 5 Figure 34 a). Excluding DMAP, the catalytic activity does not change remarkably by varying the nature of the co-catalyst. Notably, a very positive effect was observed increasing TBAB from 0.1 to 0.5 mol%, increasing the conversion from 32 to 89% (entries S4 and S11 Table S 5). A further increase of the TBAB amount to 1.0 mol% poorly affects the progress of the reaction, reaching a conversion of 93% (entry S12 Table S 5). The effect of the reaction temperature on the catalytic activity of **10**, was monitored in the range from 20 to 70 °C (entries S13-15 Table S 5, Figure 34 b). A linear increase of the activity was observed until 50 °C, while a deviation was observed at 70 °C.

Table 4 Hexene carbonate formation promoted by Fe(III) complex **7-10**.

The reaction scheme shows 1-butylene oxide (a three-membered epoxide ring with an nBu group) reacting with CO₂ in the presence of catalysts **7-10** and TBAB to form 4-butyl-1,3-dioxolan-2-one (a five-membered cyclic carbonate ring with an nBu group).

Entry ^a	Catalyst	Conversion ^{b,c} mol%	TOF ^d h ⁻¹
1	7	33	55
2	8	27	45
3	9	32	53
4	10	38	63
5 ^e	-	2	-

^aReaction conditions: HO = 4.15 × 10⁻² mol; Catalyst = 4.15 × 10⁻⁵ mol (0.1 mol%); TBAB = 2.07 × 10⁻⁴ mol (0.5 mol%); T = 35 °C; P(CO₂) = 1 bar; reaction time = 6 h, neat. ^bDetermined by ¹H NMR using mesitylene as internal standard. The selectivity toward the formation of carbonate was always found to be >99%. ^cTurnover frequency (mol_{Carbonate} · mol_{Catalyst}⁻¹ · reaction time⁻¹). ^dControl experiment in the absence of the iron catalyst.

The catalytic performances of **7-10** were compared determining the conversion of HO to the corresponding cyclic carbonate HC after 6 hours, in the presence of 5 equivalents of TBAB at 35 °C and 1 bar of CO₂ pressure (Table 4). From the results it appears that the steric hindrance of the ligand does not have an essential effect on the reaction, since all the complexes show high and comparable activity. However the catalyst **10** resulted the most efficient with a TOF of 63 h⁻¹. Although the values of turnover frequencies listed in Table 4 are actually much lower than those observed in the case of the system **6**/TBAB, it is worth noting that the reactions are conducted under very mild reaction conditions. Indeed it is difficult to obtain high efficiency at low temperature and CO₂ pressure. For example the obtained results can be compared to those recently reported by North *et al.* in the case of a chromium(III) salophen system, where the conversion of several epoxide to the corresponding cyclic carbonate was investigated at 25 °C and 1 bar of CO₂ pressure, using a 2.5 mol% loading of the chromium catalyst and 2.5 mol% loading of TBAB.⁵¹ Under this conditions the highest activity was reported to be 6 h⁻¹ in the case of styrene oxide as the substrate and similar activity observed in the case of HO. In the case of the [OSSO]-type iron(III) complex **10** reported in this study the catalytic activity is about ten times higher, with a catalyst loading of only 0.1 mol%. In order to support the significance of the results described above, we performed a number of experiments under the same reaction conditions reported in a recent study by Rintjema and Kleij.⁵² In such study, the authors investigated the catalytic activity of a series of highly active binary catalytic systems, and determined three different reaction conditions under which the cycloaddition of CO₂ to HO could be conducted, with the aim to compare the results with those reported in literature. Even though this study takes into account aluminium based catalysts (**A-D** Figure 35),^{53a,53c-d} the concept of the comparison of catalytic activity measured under the same reaction conditions is of general application, giving a clear method for the classification of a catalytic system. For these reasons the coupling of CO₂ to HO promoted by the system **10**/TBAB was performed under three reaction conditions (entries 1, 6 and 11 Table S 6). The obtained results are compared in Figure 36 with those reported in the study for the Al based systems.

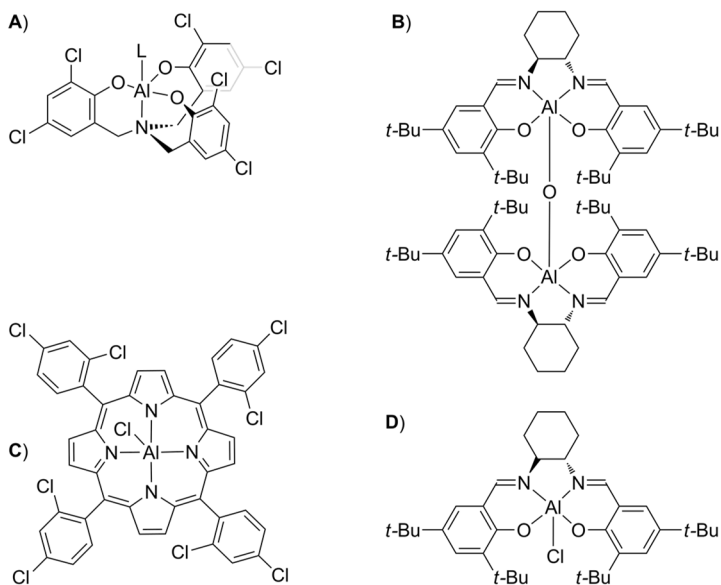


Figure 35 Aluminium complexes reported for comparison of catalytic activities in reference 52.

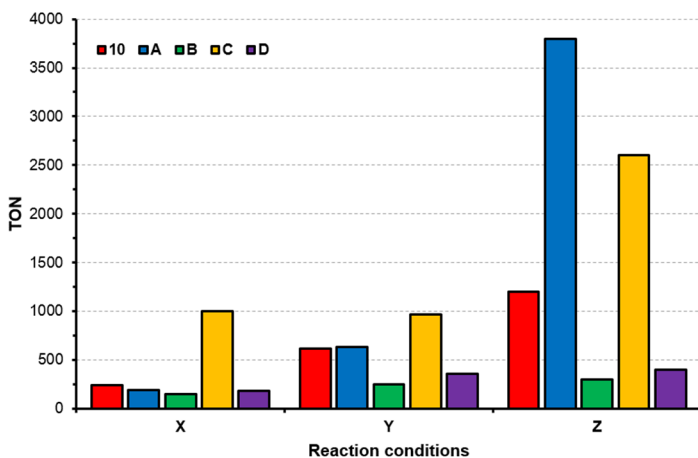
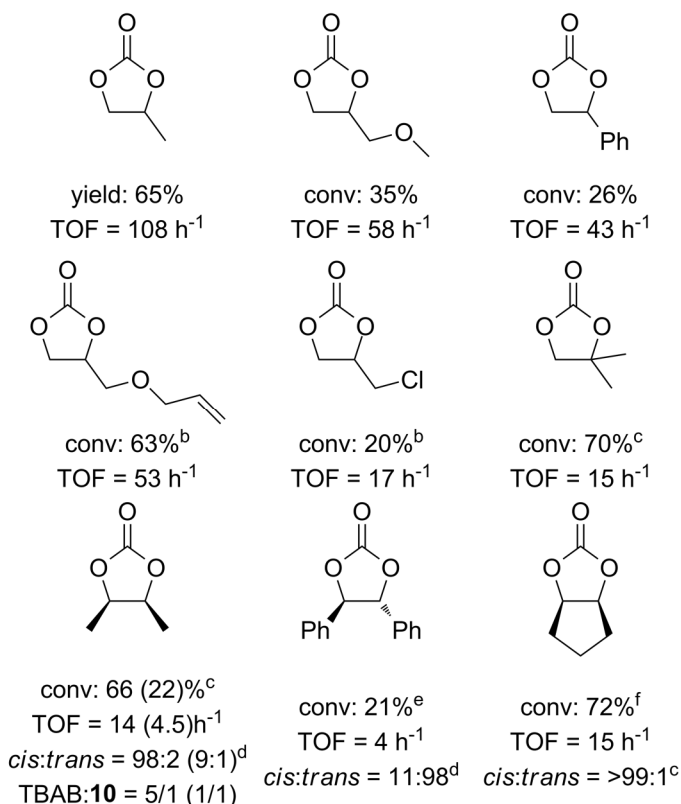


Figure 36 Comparison of the catalytic activity of the Fe(III) complex **10** and Al based complexes **A**, **B**, **C** and **D** in the reaction of HO with CO₂ under the same reaction conditions. **X**: Catalyst = 0.1 mol%, TBAB = 0.5 mol%, P(CO₂) = 10 bar, T = 25 °C, time = 8 h. **Y**: Catalyst = 0.1 mol%, TBAB = 0.5 mol%, P(CO₂) = 10 bar, T = 50 °C, time = 3 h. **Z**: Catalyst = 0.02 mol%, TBAB = 1.0 mol%, P(CO₂) = 10 bar, T = 105 °C, time = 2 h. Data of Al catalyts **A**, **B**, **C** and **D** from reference 52 (Table S 6).

At 25 °C, the observed TON of 240 is higher than those of complexes **A**, **B** and **D**. The porphyrin based catalyst **C** is the only one capable to reach complete conversion. At 50 °C **10** and **A** show approximately the same TON around 600, that is about two times those recorded with salen bimetallic and monometallic systems **B** and **D**, while **C** shows a TON of 970. At high temperature and lower catalyst loading, namely 105 °C and 0.02 mol%, **10** reaches a TON of 1200 in 2 hours. This value is one third and one half the TONs observed with **A** and **C** respectively, while it is three times more active than **B** and **D**. From this analysis it emerges that the catalytic system **10**/TBAB gives the best results under very mild reaction conditions. This is exactly what have to be done to render the reaction of carbon dioxide with oxiranes a CO₂ consumer (or neutral) process. The reaction of CO₂ with a series of differently substituted epoxides was than conducted using complex **10** in the presence of TBAB as the catalytic system (Chart 2). As it was expected, the reaction with the less encumbered propylene oxide proceeds faster, with a TOF higher than 100 h⁻¹. A small attenuation in the catalytic activity was observed in the case of methoxy and phenyl substituted epoxides. For the reaction of allyloxy and chloride substituted epoxides, the use of 0.2 mol% of **10** was required to obtain significant conversion. A similar behaviour was already reported for other catalytic systems.⁵⁴ The reaction with di-substituted oxiranes was also accomplished. Since these epoxides are known to be less reactive, the reaction temperature and pressure of CO₂ were fixed at 50 °C and 10 bar respectively. In all cases good activity were obtained. In particular, the reaction of *cis*-butene oxide proceeds with high degree of stereoretention, even in the case in which the TBAB/**10** molar ratio was reduced from 5/1 to 1/1. The reaction of cyclopentene oxide proceeds as well, with the selective formation of the corresponding cyclic carbonate. Intriguingly, the reaction of cyclohexene oxide (CHO) under the same reaction conditions, leads to the exclusive formation of almost perfect poly(cyclohexene carbonate) (PCHC) (entry S1 Table S 7). Such divergence in the selectivity was already reported in literature, however a mixture of the cyclic and polymeric products is often obtained. Moreover, the iron based catalytic systems capable to promote the selective alternate co-polymerization of CHO with CO₂ are rather scarce.⁵⁵

Chart 2 Cyclic organic carbonates formation promoted by Fe(III) complex **10**.^a



a) Reaction conditions: epoxide = 4.15×10^{-2} mol; **10** = 0.1 mol%; TBAB = 0.5 mol%; T = 35 °C; P(CO₂) = 1 bar; reaction time = 6 h, neat. Conversion determined by ¹H NMR using mesitylene as internal standard. The selectivity toward the formation of cyclic carbonate was always found >99%. b) **10** = 0.1 mol%; TBAB = 0.5 mol%. c) Epoxide = 1.0 mL; T = 50 °C; P(CO₂) = 10 bar; reaction time = 24 h. d) Stereoselectivity determined by ¹H NMR. e) Epoxide = 1.0 g; T = 90 °C; P(CO₂) = 10 bar; reaction time = 24 h. f) T = 50 °C; P(CO₂) = 10 bar; reaction time = 24 h.

3.3 Co-polymerization of CO₂ with cyclohexene oxide

Aiming to better understand the behaviour of the catalytic system in the co-polymerization process, the complexes **7-10** were tested in the reaction of carbon dioxide with CHO at 80 °C, 10 bar of CO₂ pressure using 0.1 mol% of the complex and 0.1 mol% of TBAB (entries S2-5 Table S 7). At a first glance it is evident that in this case the nature of the substituents on the ligand has an important effect

on the reaction, differently from the case of the cycloaddition reaction. Actually, while the methyl substituted complex **9** produces only traces of polymer in 2 hours, 40% of conversion was obtained in the case of the more sterically demanding complex **8**, with a TOF of 200 h⁻¹ (entries S3 and S4 Table S 7). A further increase of the steric demand introducing trityl groups in the R₁ positions, or reducing the flexibility of the ligand, changing the ethyl bridge with a cyclohexyl moiety, negatively affects the catalytic performance respect to the catalyst **8** (entries S2 and S5, Table S 7). The influence of the co-catalyst type and loading on the co-polymerization reaction promoted by the complex **8** was investigated (entries S6-17, Table S 7). Interestingly, the catalyst is able to give the desired product also in the absence of co-catalyst, even if lower activity and a lower content of carbonate linkages are obtained (entry S7 Table S 7). Furthermore, TBAC was found to be the most effective co-catalyst, with a TOF of 340 h⁻¹ (entry S15 Table S 7). On one hand, reducing the TBAC/**8** ratio from 1/1 to 0.5/1 almost halves the catalytic activity, with no variation in the co-polymer composition (entry S14 Table S 7). On the other, increasing TBAC/**8** ratio to 2/1 only a small enhancement of the catalytic activity was observed, with a TOF of 400 h⁻¹ (entry S16 Table S 7). The variation of the catalytic activity of **8** with respect to the temperature, in the range from 40 to 100 °C, was also monitored (entries S18-20 Table S 7). When temperature is lower than 60 °C, the conversion is negligible. Raising the temperature to 100 °C increases the catalytic activity of about 20%, reaching a TOF of 420 h⁻¹. To the best of our knowledge, this is the highest activity reported so far for an iron based catalyst for the co-polymerization of CO₂ with CHO. The influence of the pressure of CO₂ on the co-polymerization reaction was also investigated. When the pressure was fixed at 5 bar, the catalytic activity was slightly lower than that observed at 10 bar. Notably, good catalytic activity was observed even at only 1 bar of CO₂ pressure (TOF = 170 h⁻¹, entry S21 Table S 7), without modification in the polymer composition. Curiously the TOF observed at 20 bar was comparable to that of the experiment conducted at 1 bar (entry S23 Table S 7), however in this case significantly lower molecular weight were obtained. The catalytic performances of the complexes **7-10** were compared again, determining the conversion of CHO in PCHO after

1 hour, at 80 °C, 10 bar of CO₂ pressure using 0.1 mol% of the catalyst and 0.1 mol% of TBAC (entries 1-4 Table 5).

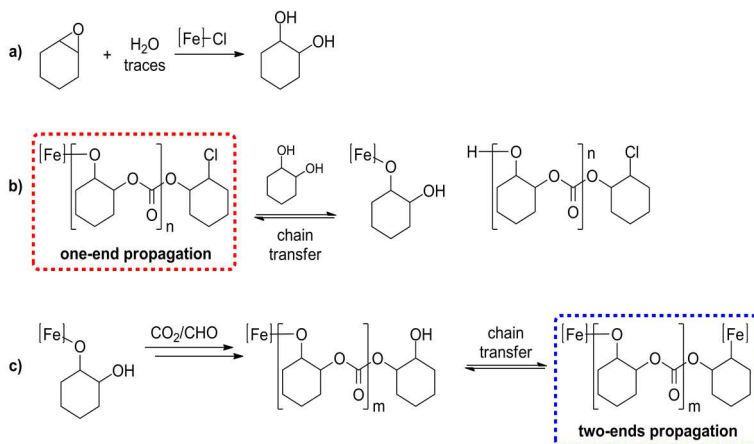
Table 5 Poly(cyclohexene carbonate) formation promoted by Fe(III) complex **7-10**.

Entry	Catalyst	Yield ^b	TOF ^c	Mn ^d	Đ ^d	Mn(1)
		%	h ⁻¹	kDa		Mn(2) ^d
1	7	14	140	9.8	1.01	7
				4.6		1.04
2	8	34	340	23.2	1.01	30
				11.0		1.03
3 ^e	9	25	42	20.0	1.01	15
				10.4		1.02
4	10	17	170	17.8	1.01	24
				8.3		1.04
5 ^f	8	29	290	14.3	1.01	28
				6.7		1.03
6 ^g	8	40	400	27.8	1.01	7
				12.8		1.06

a) Reaction conditions: CHO = $5.93 \cdot 10^{-2}$ mol; catalyst = 0.1 mol%; TBAC = 0.1 mol%; T = 80 °C; P(CO₂) = 10 bar; reaction time = 1 h; neat. b) Gravimetric. Carbonate linkages always >99%. c) Turnover Frequency (yield · 0.01 · mol_{Catalyst}⁻¹ · reaction time⁻¹). d) Determined by Gel Permeation Chromatography at 25 °C in THF respect to polystyrene standards. e) reaction time = 6 h. f) H₂O = 0.1 mol%. g) CHO was distilled twice over CaH₂ prior to use.

Only in the case of the complex **9**, the reaction time was fixed at 6 hours in order to obtain a suitable polymer sample for further analysis and to verify the selectivity of the reaction (entry 3, Table 5). Using the optimized reaction conditions, the catalytic activities follow the same trend previously observed using TBAB, finding that the catalyst **8** is the most efficient of the series. A bimodal distribution of the molecular weights was obtained in each case. In the GPC profile two peaks were observed: the prevalent one exhibits M_n value that is almost twice that of the lower, and both presents a very narrow polydispersity index (Đ). The same behaviour have been already

observed in the CO₂/CHO co-polymerization, in particular by Sugimoto *et al.*, using an aluminum Schiff base,⁵⁶ and by Williams *et al.* using a dizinc complex supported by a macrocyclic ligand.⁵⁷ In the first case, the bimodal distribution was attributed to the ability of the catalyst to promote the co-polymerization on both the sides of a rigid, planar catalytic species. In the latter, the *in situ* formation of 1,2-cyclohexene diol (CHD), due to the hydrolysis of the oxirane ring in presence of water residue, leads to the immortal polymerization process, where CHD acts as a chain transfer agent. Considering that the complex **8** lacks of two opposite coordination sites, the first mechanism seems unreasonable. Therefore, to verify if water is effectively influencing the course of the reaction, the co-polymerization of CO₂ with CHO in the presence of **8**/TBAC was performed using two reaction conditions: in the first case one equivalent of water with respect to iron was added to the reaction mixture, in the second the water residue was minimized by distilling the CHO two times from CaH₂ (entry 5 and 6 Table 5). Notably, the catalyst is able to promote the co-polymerization even in the presence of exogenous water, however lower molecular weights were obtained. The minimization of the water content in the system positively affects catalytic activity and molecular weights distribution. In fact, the TOF increases from 340 to 400 h⁻¹ and a narrow and nearly unimodal distribution was obtained.



Scheme 6 Proposed mechanism for the bimodal molecular weights distribution.

These observation supports the mechanism based on the CHD formation, and the bimodal distribution can be explained on the basis of the reactions reported in the Scheme 6. When the reaction was conducted in the presence of traces of water, the hydrolysis of CHO occurs, with formation of CHD (Scheme 6a). The CO₂/CHO copolymerization starts with the formal insertion of the epoxide into the Fe-Cl bond, and consecutive insertions of the monomers leads to the formation of a polymer chain that is able to grow only from one end (Scheme 6b), corresponding to the distribution with the lower M_n. In the presence of CHD, two chain transfer reactions can occur on the same diol molecule, with the formation of a polymer chain that is able to grow from both the sides (Scheme 6c), corresponding to the distribution with the higher M_n. Since the chain transfer reaction is much faster than the propagation reaction, all the chains grow at the same rate, explaining both the narrow polydispersity and the relative ratio of M_n values of 2:1. The beneficial effect is also evident in terms of the thermal properties of the polymer. Indeed, the glass transition temperature (T_g) increases from 91 to 118 °C, probably as a consequence of the higher molecular weight (Figure S 87).

3.4 Kinetic study

Despite the coupling reaction of CO₂ with epoxides is known since the early 1930s,⁵⁸ and numerous homogeneous catalytic systems have been developed in last decades, to date an univocal reaction mechanism was not assessed. While several investigations focusing on the stereochemistry of the process have been reported,⁵⁹ the chemoselectivity toward the cyclic or the polymeric product is not definitively understood, even if some seminal investigation have been made by Darensbourg,⁶⁰ Coates,⁶¹ and Williams.⁵⁷ To better understand the reaction mechanism, a detailed kinetic investigation was performed for the formation of propylene carbonate using the system **10**/TBAB and for the poly(cyclohexene carbonate) formation using the system **8**/TBAC, by means of online attenuated total reflection infrared (ATR-IR) measurements.

3.4.1 Propylene carbonate formation

The propylene carbonate formation in the presence of **10**/TBAB as the catalytic system was investigated, using a PO/DCM mixture as the reaction medium to guarantee the homogeneity of the system

during the experiments. The general kinetic equation for the reaction of CO₂ with PO can be written as follow:

$$v = k \cdot [\text{PO}]^a \cdot [\text{CO}_2]^b \cdot [\mathbf{10}]^c \cdot [\text{TBAB}]^d \quad (\text{eq. 3.1})$$

First, the reaction order with respect to **10** was determined by performing a series of experiments varying the concentration of **10** in the range from 4.8 to 28.6 mM, keeping the concentration of TBAB constant at 28.6 mM (Figure S 88). The log-log plot of the initial rate versus the concentration of the catalyst is shown in Figure 37a.

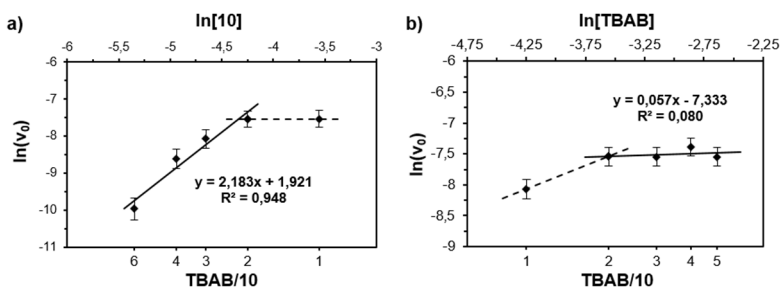


Figure 37 Plot of $\ln(v_0)$ versus $\ln[10]$ (a) and $\ln[\text{TBAB}]$ (b). The TBAB/10 molar ratio is reported on the bottom axes.

It emerges that the rate of the reaction follows a second-order dependence in **10**. However the dependence on the catalyst concentration is valid only in the presence of an excess of the co-catalyst, namely when the TBAB/10 molar ratio is equal or major than 2. This finding is in accordance with the observation that the presence of the co-catalyst is essential for observing catalytic activity. An analogous set of experiments was performed to study the dependence with respect to TBAB, varying the concentration of TBAB in the range from 14.3 to 71.5 mM, keeping the concentration of **10** constant at 14.3 mM (Figure S 89). The log-log plot of the initial rate versus the concentration of the co-catalyst is shown in Figure 37b. Compared with **10**, a specular behaviour was observed in this case. Indeed the reaction rate increases until the TBAB is in excess with respect to iron, while a zero-order dependence was observed when the TBAB/10 molar ratio is equal or higher than 2. The results described above suggest that complex **10** reacts with TBAB forming a new species that is involved in the reaction mechanism. A similar behaviour was recently described by North *et al.* in the case of chromium(III) salophen complexes.⁵¹ In that case the reaction order

with respect to the concentration of the chromium catalyst was found to be zero in the case that the concentration of Cr(III) was higher than that of TBAB, and one in the case that it was lower. Such behaviour was explained showing that the Cr(salophen) complex reacts with TBAB generating a new $[\text{Cr}(\text{salophen})\text{Br}_2]^-$ species that was claimed to be the real catalyst (Figure 38).

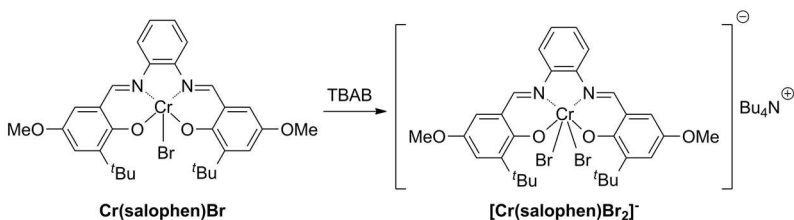


Figure 38 Formation of the $[\text{Cr}(\text{salophen})\text{Br}_2]^-$ in the presence of TBAB as reported in reference 51.

To verify the occurrence of a similar reaction, the UV-Vis spectra of DCM solutions of **10** in the presence of different amount of TBAB have been recorded (Figure 39).

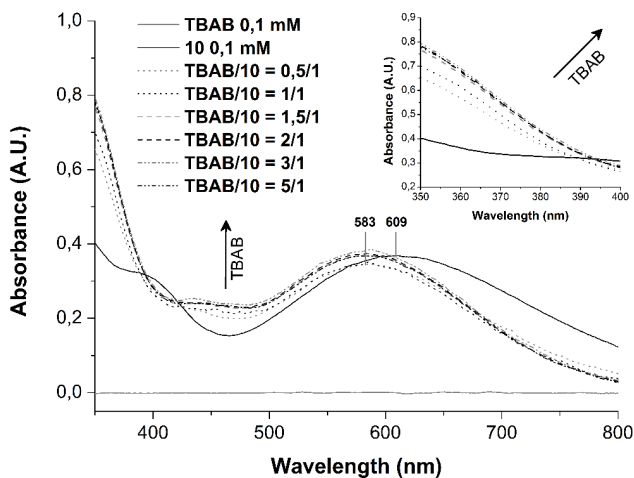


Figure 39 UV-Vis spectra of complex **10** in DCM solution before and after the addition of TBAB (from 0.5 to 5 equivalents with respect to iron). The TBAB spectrum is reported on the bottom for comparison.

After the addition of only 0.5 equivalent of TBAB, the spectrum profile completely changes. For example the maximum of absorbance at 610 nm undergoes a blue-shift to 583 nm. It is worth noting that the

absorbance intensity raises by adding more TBAB, until the TBAB/**10** molar ratio is equal to 2. At this value the intensity does not change anymore, even in the presence of 5 equivalents of TBAB. From this results, it appears that the complex **10** reacts with TBAB, reasonably leading to the formation of a new iron containing anionic species [**10-Br**]⁻ (Figure 40).

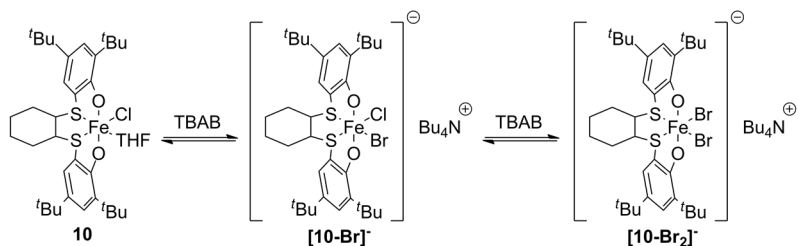


Figure 40 Formation of the anionic species [**10-Br₂**]⁻ in the presence of TBAB.

The reaction seems to proceed until 2 equivalent of TBAB with respect to iron are added to the solution. This can be explained with the formation a new complex [**10-Br₂**]⁻ in which the chlorine atom is substituted with the bromine coming from TBAB, and consequently further reaction is not possible.

The reaction order with respect to PO was determined performing a series of experiments with different concentration of PO (Figure S 90). The log-log plot of the initial rate v_0 with respect of the concentration of the epoxide gives a first-order dependence with respect to PO (Figure 41a).

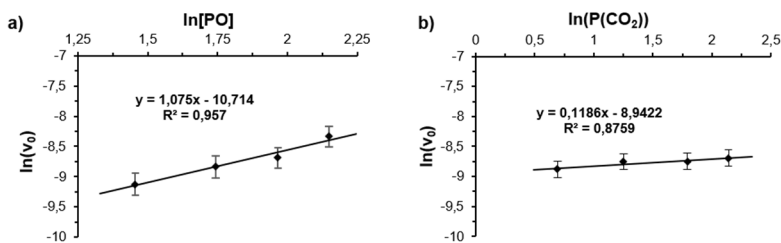


Figure 41 Plot of $\ln(v_0)$ versus $\ln[\text{PO}]$ (a) and $\ln(\text{P}(\text{CO}_2))$ (b).

Keeping constant the epoxide concentration, the carbon dioxide pressure was changed in the range from 2 to 8.5 bar (Figure S 92), and the reaction order with respect to CO_2 was found to be zero (Figure 41b).

On the basis of the Eyring equation, the thermodynamic parameters for the reaction can be determined plotting the $\ln(v_0/T)$ versus $1/T$. The reaction of PO with CO_2 was conducted, under the same reaction conditions, at different temperature in the range from 30 to 70 °C (Figure S 92). The Eyring plot is shown in Figure 42.

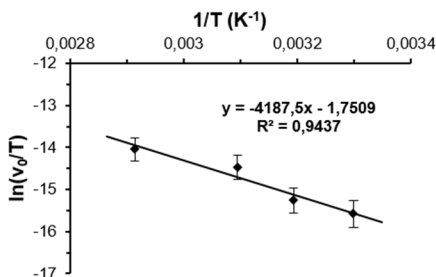


Figure 42 Plot of $\ln(v_0/T)$ versus $\ln(1/T)$ (Eyring plot) in the range from 30 to 70 °C.

Using this data we found the following results: $\Delta H^\ddagger = 34.7$ kJ/mol, $\Delta S^\ddagger = -213$ J/(mol · K) and $\Delta G^\ddagger_{323} = 103.4$ kJ/mol.

Finally we can conclude that, in the presence of an excess of the co-catalyst, the kinetic equation for the formation of propylene carbonate can be written as follow:

$$v = k \cdot [\text{PO}] \cdot [\mathbf{10}]^2 \text{ (eq. 3.2)}$$

From all the data described above it is possible to conclude that the ring opening of PO is the rate limiting step of the reaction. Since the mononuclear nature of the [OSSO]-type Fe(III) complexes have been confirmed with different analysis, the second order dependence with respect to the concentration of **10** could be surprisingly, especially taking into account the monometallic mechanism supposed for the dinuclear thioether-triphenolate system **6**/TBAB discussed in a previous chapter. Nevertheless, a bimetallic reaction pathway is claimed in many cases. In particular the bimetallic mechanism for the propylene carbonate formation in the presence of an Fe(II) complex have been previously demonstrated by Rieger *et al.*⁶² However in such case the carbon dioxide insertion into the Fe-O bond was found to be the rate limiting step.

3.4.2 Poly(cyclohexene carbonate) formation

The poly(cyclohexene carbonate) formation in the presence of **8**/TBAC as the catalytic system was investigated, using a CHO/toluene mixture as the reaction medium to guarantee the homogeneity of the system during the experiments. The general kinetic equation for the reaction of CO₂ with CHO can be written as follow:

$$v = k \cdot [\text{CHO}]^a \cdot [\text{CO}_2]^b \cdot [\mathbf{8}]^c \cdot [\text{TBAC}]^d \quad (\text{eq. 3.3})$$

At first, the reaction order with respect to **8** was determined by performing a series of experiments varying the concentration of **8** in the range from 3.6 to 18.2 mM, keeping the concentration of TBAC constant at 9.1 mM (Figure S 93). The log-log plot of the initial rate versus the concentration of the catalyst is shown in Figure 43a.

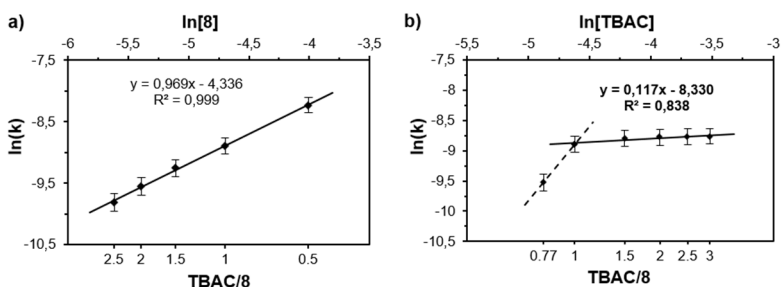


Figure 43 Plot of ln(k) versus ln[**8**] (a) and ln[TBAC] (b). The TBAC/**8** molar ratio is reported on the bottom axes.

Differently from the case of PO, the reaction order with respect to the complex **8** was found to be one. Moreover, the slope of the line does not change by varying the TBAC/**8** ratio, even in the case in which the co-catalyst is substoichiometric with respect to **8**. This is in agreement with the observation that the catalyst is able to promote the reaction even in the absence of any co-catalyst. An analogous set of experiments was performed to study the dependence with respect to TBAC, varying the concentration of TBAC in the range from 7.6 to 29.7 mM, keeping the concentration of **8** constant at 9.8 mM (Figure S 94). The log-log plot of the initial rate versus the concentration of the co-catalyst is shown in Figure 43b. A zero order dependence was found in this case. However, as it was expected, the reaction rate depends on the [TBAC] when the iron catalyst is in

excess. That dependence indicates that the addition of TBAC results in a better activation of the complex, with the concentration of the activated catalyst increasing until the 1/1 molar ratio. The reaction order with respect to CHO was determined performing a series of experiments with different concentration of CHO (Figure S 95). The double logarithmic plot of the initial rate v_0 with respect to the concentration of the epoxide gives a first-order dependence with respect to CHO (Figure 44a).

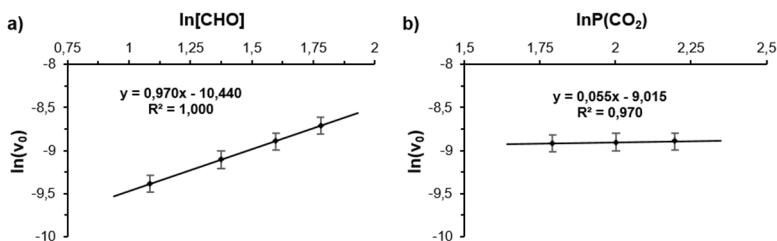


Figure 44 Plot of $\ln(v_0)$ versus $\ln[\text{CHO}]$ (a) and $\ln(P(\text{CO}_2))$ (b).

With constant epoxide concentration, the carbon dioxide pressure was changed in the range from 6 to 9 bar (Figure S 96), and the reaction order with respect to CO_2 was found to be zero (Figure 44b). The co-polymerization reaction of CHO with CO_2 was conducted, under the same reaction conditions, at different temperature in the range from 60 to 90 °C (Figure S 97). The Eyring plot is shown in Figure 45. Using this data we found the following results: $\Delta H^\ddagger = 49.6$ kJ/mol, $\Delta S^\ddagger = -180$ J/(mol · K) and $\Delta G^\ddagger_{353} = 113.0$ kJ/mol.

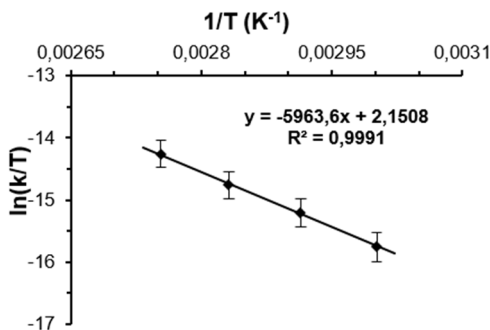


Figure 45 Plot of $\ln(k/T)$ versus $\ln(1/T)$ (Eyring plot) in the range from 60 to 90 °C.

Finally we can conclude that the kinetic equation for the co-polymerization of CHO with CO₂ can be written as follow:

$$v = k \cdot [\text{CHO}] \cdot [\mathbf{8}] \text{ (eq. 3.4)}$$

Even in this case the ring opening of the epoxide was found to be the rate limiting step. Differently from the case of the propylene carbonate formation, an excess of co-catalyst is not needed to obtain the maximum catalytic activity. The reason can be in the fact that, in the case of the co-polymerization, the TBAC is involved only during the initiation step, i.e. the ring opening of the first epoxy ring. Indeed, during the propagation reaction, the insertion of the CHO happens in the Fe-carbonate bond.

The divergence in the cyclic carbonate or the polycarbonate product formation on the basis of the reaction conditions has been reported for different catalytic systems. In particular, the temperature dependence of the product mixture composition in the case of PO and CHO was investigated by Coates,⁶³ Darensburg,⁶⁴ and Williams.⁶⁵ In all these cases, both the products were claimed to derive from the same reaction mechanism, in which the polycarbonate was identified as the kinetic product, favored at low temperature, and the cyclic carbonate as the thermodynamic product, favored at high temperature. The key for the selective formation of the polycarbonate at low temperature was thus identified in the different activation energies between the propagation and the backbiting reaction.

In the case of the [OSSO]-Fe(III) complexes **7-10** discussed in this study, a direct comparison of the activation energies for a given epoxide between the cyclic and polymeric product it is not possible, due to the selective formation of only one product regardless the reaction conditions employed. However the ΔG^\ddagger values for both the PC and PCHC formation are 103.4 and 113.0 kJ/mol respectively evidencing that the difference between these two values is too low to be responsible for the different product selectivity. Indeed, the different behavior of PO and CHO in the coupling with CO₂ is rather the consequence of the existence of two distinct reaction mechanisms. As a matter of fact, the kinetic measurements revealed a different role of the catalyst precursor in the reaction pathways, that is the keystone for the observed product divergence. In the case of

the PC formation, a second order with respect to the Fe(III) concentration was found, while in the case of the PCHC a first order was observed, even though the ring opening of the epoxy-ring was always found to be the rate limiting step. The selective obtaining of the polymeric product without the concomitant production of the *trans*-CHC, that is obtained in the case of the backbiting reaction, regardless the reaction temperature in the case of CHO/CO₂ coupling reaction is a further confirm of the depicted scenario for this new class of catalysts.

3.5 Conclusions

We have described the synthesis and the complete characterization of four new [OSSO]-type ligand based mononuclear Fe(III) complexes (**7-10**). When activated by tetrabutylammonium bromide, all the complexes resulted very efficient in the cycloaddition of CO₂ to epoxides under very mild reaction conditions. In particular, the complex **10** shows the best catalytic performance, with a TOF of 108 h⁻¹ for the PC formation at 35 °C and 1 bar CO₂ pressure. Moreover the TON of complex **10** in the formation of HC, well compares with that of the most active catalysts reported in the literature. The conversion of different internal epoxides to the corresponding cyclic carbonate, was accomplished with an high degree of stereoritention of the starting configuration. Only in the case of CHO, the selective production of perfectly alternate PCHC was obtained with the highest TOF of 420 h⁻¹ in the case of the cumyl substituted complex **8**, activated by TBAC. To the best of our knowledge, it is the one of the very few examples of iron-based catalytic systems capable to promote the co-polymerization reaction, with the highest activity reported so far. A complete kinetic investigation was conducted for the formation of both PC and PCHC, by means of an ATR-FT-IR apparatus, using complex **10** and **8** respectively. In the first, the rate limiting step was found to involve two metal centres, in spite of the mononuclear nature of the starting Fe(III) specie. The explanation was found in the formation of a new catalytic active species from the reaction of **10** with the co-catalyst. In the second case, the co-catalyst only participates in the initiation process, and the reaction proceeds *via* a monometallic mechanism.

3.6 Experimental Part

General considerations

All manipulation involving air- and/or moisture-sensitive compounds were performed under nitrogen atmosphere using standard Schlenk technique and a MBraun glovebox. Toluene (99.5%; Sigma-Aldrich) and THF (99%; Sigma-Aldrich) were used as received or refluxed for 48 h over sodium or sodium ketyls and distilled before use for moisture- and oxygen-sensitive reactions. All other reagents were used as received (TCI or Sigma-Aldrich) or distilled under reduced pressure over calcium hydride. Deuterated solvents were purchased from Euriso-Top or Sigma-Aldrich and used as received. NMR spectra were collected on Bruker Avance spectrometers (600, 400, 300 or 250 MHz for ^1H): the chemical shifts were referenced to tetramethylsilane (TMS) as external reference using the residual protio signal of the deuterated solvents. Measurements of effective magnetic moments were performed on a Bruker Avance 400 MHz spectrometer in toluene- d_8 using a 5 mm Wilmad coaxial insert NMR tube. The effective magnetic moment (μ_{eff}) was calculated from $\mu_{\text{eff}} = 8\chi_g\text{MwT}$, where χ_g ($\text{cm}^3 \text{g}^{-1}$) is the corrected molar susceptibility derived from $\chi_g = 3\Delta f/4\pi f_0\text{CMw} + \chi_o$. Δf is the shift in frequency (Hz) of the residual protio signal of the solvent in the presence of the complex from the value of the pure solvent, C and Mw are respectively the concentration (mol cm^{-3}) and the molecular weight of the complex (g mol^{-1}), f_0 is the operating frequency of the spectrometer (Hz), and χ_o is the mass susceptibility of the pure solvent ($-0.6179 \times 10^{-6} \text{ cm}^3 \text{g}^{-1}$ for toluene- d_8). $4\pi/3$ is the shape factor for a cylindrical sample in a superconducting magnet. Elemental analysis was performed on a CHNS Thermo Scientific Flash EA 1112 equipped with a thermal conductivity detector. FT-IR measurements were carried out on a Bruker Vertex 70 spectrometer equipped with DTGS detector and a Ge/KBr beam splitter. The samples were analyzed in chloroform solutions or in the solid state as KBr disks. UV-Vis spectra were collected on a PerkinElmer Lambda EZ 201 spectrophotometer.

Synthesis of the [OSSO]-type ligand L7 (Scheme 5)

A 100 mL two-neck round-bottom flask equipped with condenser and magnetic stirring bar was charged with 6.32 g of 2-mercapto-4-methyl-

6-triethylphenol (16.5 mmol) dissolved in 15 mL of ethanol, 0.67 g of NaOH (16.8 mmol) and the mixture was refluxed about 1 hour until complete dissolution of the hydroxide. 1.56 g of 1,2-dibromomethane (8.3 mmol) were slowly added at 0 °C and the mixture heated to the reflux of the solvent that was kept overnight. The solvent was distilled off, water was added until dissolution of NaBr by-product and the aqueous phase extracted twice with CH₂Cl₂. The combined organic phases were dried with MgSO₄, after evaporation of the solvent the product was purified by crystallization from acetonitrile and recovered as a pale yellow solid. Yield: 5.16 g, 79%. ¹H-NMR (400 MHz, CD₂Cl₂, 25 °C): δ 2.15 (6H, s); 2.51 (4H, s); 6.37 (2H, s, -OH); 7.01-7.23 (32H, overlapped signals, Ar-H). ¹³C-NMR (400 MHz, CD₂Cl₂, 25 °C): δ 16.47; 20.34; 31.27; 34.08; 37.17; 117.18; 124.04; 124.20; 127.55; 129.60; 133.75; 134.12; 143.46; 150.09; 153.56. EA for C₂₈H₃₄O₃S₂ calc.: C, 69.67; H, 7.10; S 13.29; found: C, 69.55; H, 7.09; S, 13.18. Mass spectrum: 505.0 m/z (MNa⁺).

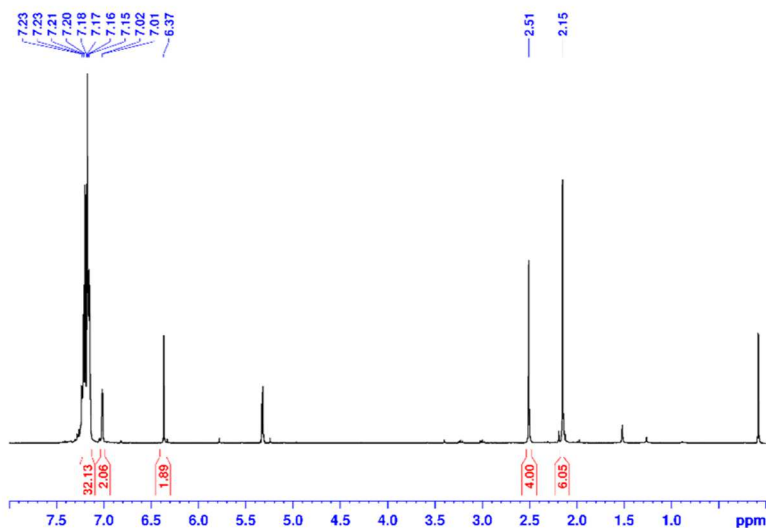


Figure S 62 ¹H NMR spectra of pro-ligand L7 (CD₂Cl₂, 400 MHz).

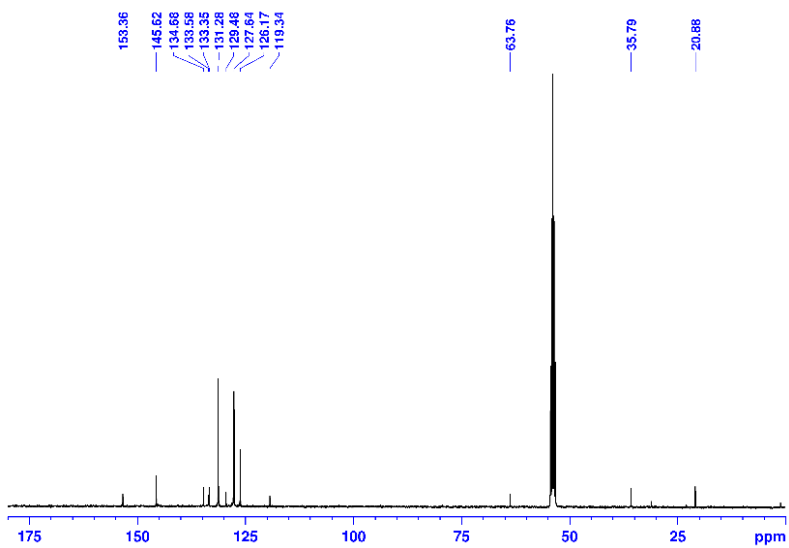


Figure S 63 ^{13}C NMR spectra of pro-ligand L7 (CD_2Cl_2 , 400 MHz).

Synthesis of the iron(III) complex 7 (Scheme 4)

Pro-ligand **L7** (0.530 g; 0.67 mmol) was dissolved in THF (20 mL). The solution was added to a suspension of sodium hydride (0.035 g; 1.47 mmol) in THF (10 mL) and the mixture stirred at room temperature overnight. The resulting suspension was filtered through celite and slowly added at room temperature to 0.106 g of anhydrous iron(III) chloride (0.66 mmol) dissolved in 20 mL of THF. The rapid change of the color to the deep purple was observed and the reaction kept overnight. The mixture was then filtered through celite and the solvent removed under reduced pressure affording a deep purple crystalline solid. Yield: 0.566 g, 90.0 %. Mass spectrum: 844.2146 m/z (LFe⁺, calc: 844.21267).

Synthesis of the iron(III) complex 8 (Scheme 4)

Pro-ligand **L8** (7.170 g; 9.55 mmol) was dissolved in THF (150 mL). The solution was added to a suspension of sodium hydride (0.50 g; 21.0 mmol) in THF (50 mL) and the mixture stirred at room temperature overnight. The resulting suspension was filtered through celite and slowly added at room temperature to 1.117 g of anhydrous iron(III) chloride (9.36 mmol) dissolved in 150 mL of THF. The rapid change of the color to the deep purple was observed and the reaction kept overnight. The mixture was then filtered through celite and the solvent removed under reduced pressure affording a deep purple crystalline solid. Yield: 7.76 g, 90.9 %. Mass spectrum: 804.2775 m/z (LFe⁺, calc: 844.27527).

Synthesis of the iron(III) complex 9 (Scheme 4)

Pro-ligand **L9** (1.256 g; 3.75 mmol) was dissolved in THF (100 mL). The solution was added to a suspension of sodium hydride (0.198 g; 8.26 mmol) in THF (45 mL) and the mixture stirred at room temperature overnight. The resulting suspension was filtered through celite and slowly added at room temperature to 0.597 g of anhydrous iron(III) chloride (3.68 mmol) dissolved in 100 mL of THF. The rapid change of the color to the deep purple was observed and the reaction kept overnight. The mixture was then filtered through celite and the solvent removed under reduced pressure affording a deep purple crystalline solid. Yield: 1.70 g, 93.2 %. Mass spectrum: 610.26009 m/z (LFe⁺, calc: 610.25962).

Synthesis of the iron(III) complex 10 (Scheme 4)

Pro-ligand **L10** (2.000 g; 3.59 mmol) was dissolved in THF (100 mL). The solution was added to a suspension of sodium hydride (0.190 g; 7.92 mmol) in THF (45 mL) and the mixture stirred at room temperature overnight. The resulting suspension was filtered through celite and slowly added at room temperature to 0.571 g of anhydrous iron(III) chloride (3.52 mmol) dissolved in 100 mL of THF. The rapid change of the color to the deep purple was observed and the reaction kept overnight. The mixture was then filtered through celite and the solvent removed under reduced pressure affording a deep purple crystalline solid. Yield: 2.45 g, 96.9 %. Mass spectrum: 388.02484 m/z (LFe^+ , calc: 388.02486).

ESI-MS Characterization

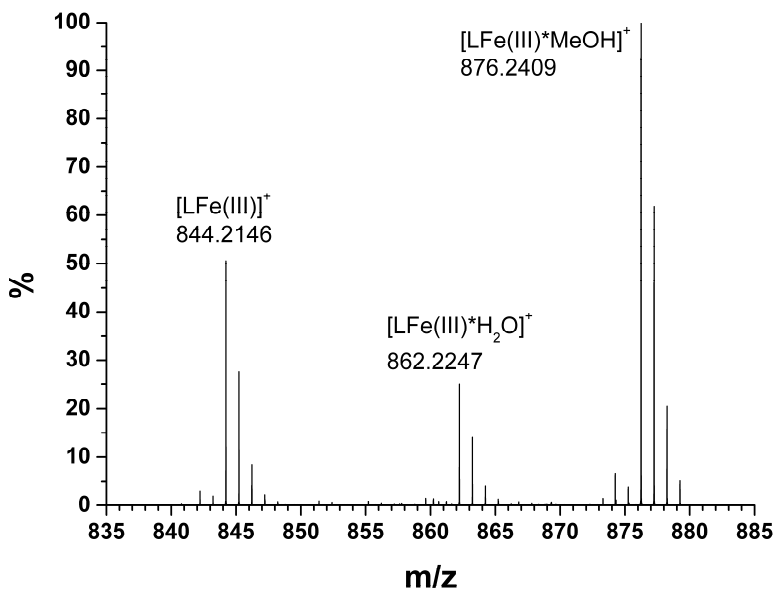


Figure S 64 HR ESI-MS spectrum of the complex 7 (DCM/MeOH 50/50 as solvent).

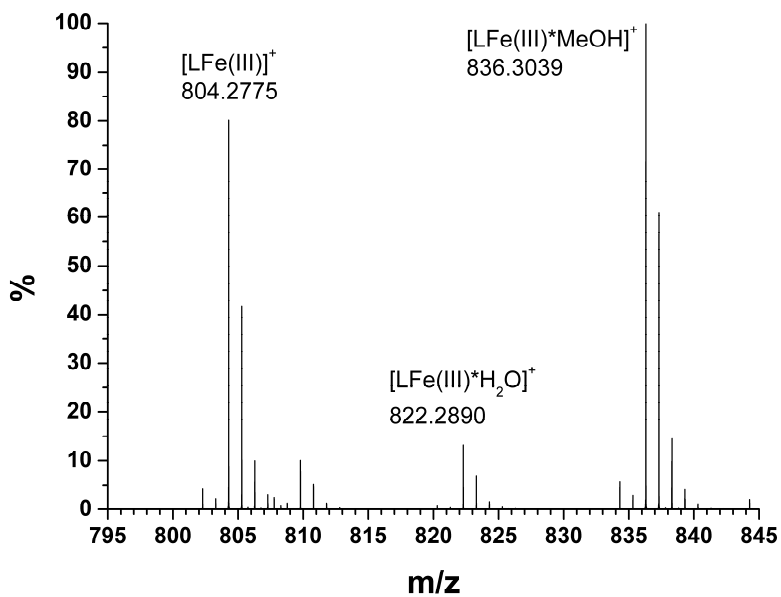


Figure S 65 HR ESI-MS spectrum of the complex 8 (DCM/MeOH 50/50 as solvent).

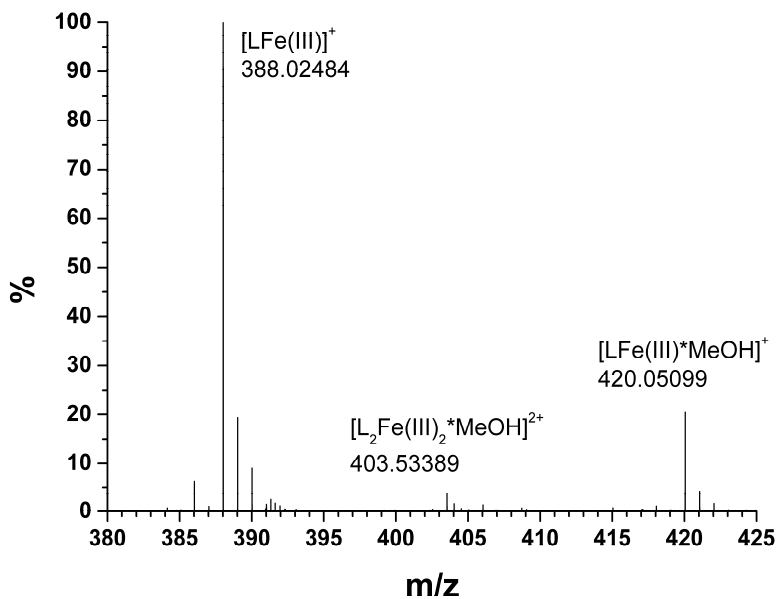


Figure S 66 HR ESI-MS spectrum of the complex 9 (DCM/MeOH 50/50 as solvent).

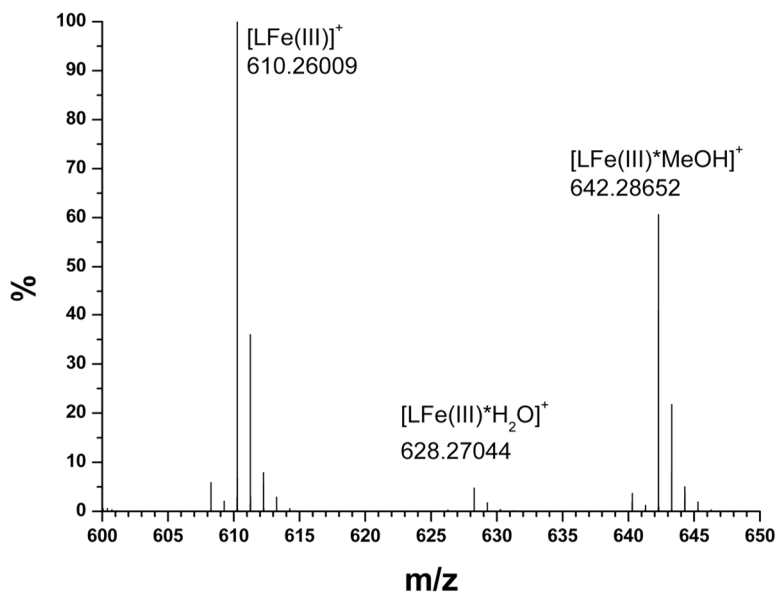


Figure S 67 HR ESI-MS spectrum of the complex 10 (DCM/MeOH 50/50 as solvent).

Effective magnetic moment measurements in solution

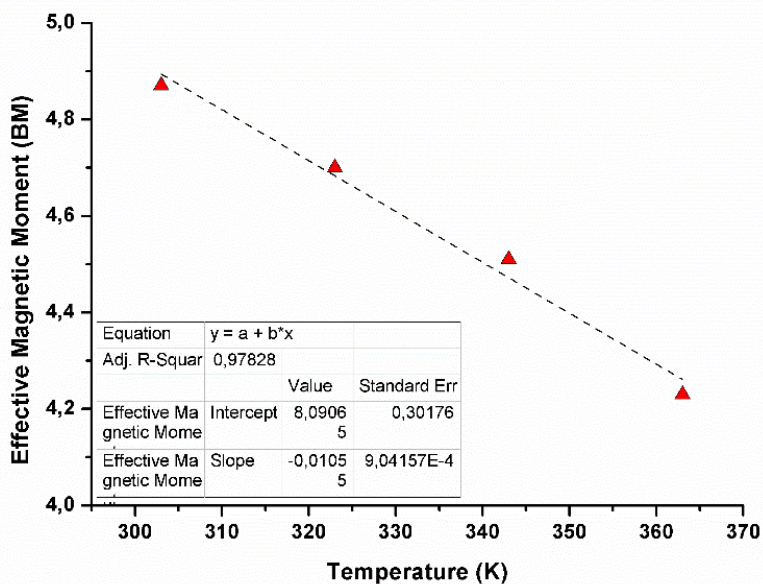


Figure S 68 Effective magnetic moment of 7 with respect to temperature.

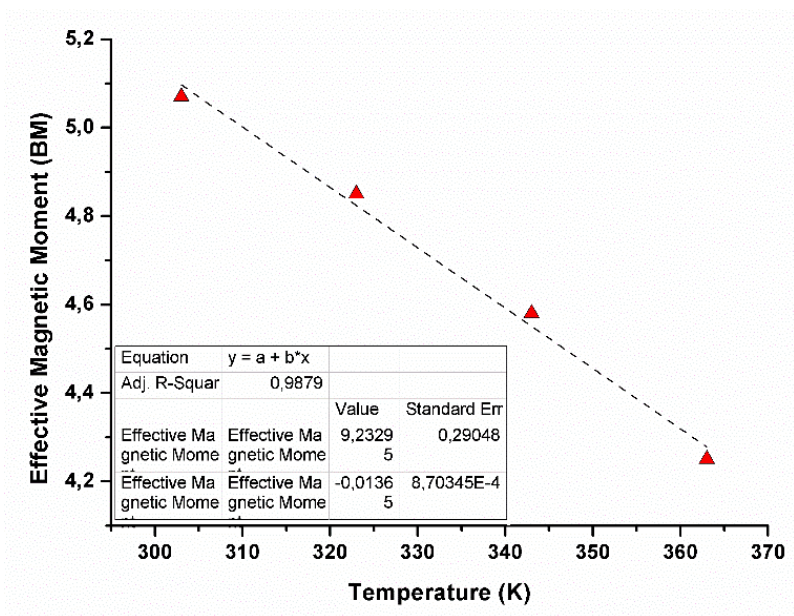


Figure S 69 Effective magnetic moment of **8** with respect to temperature.

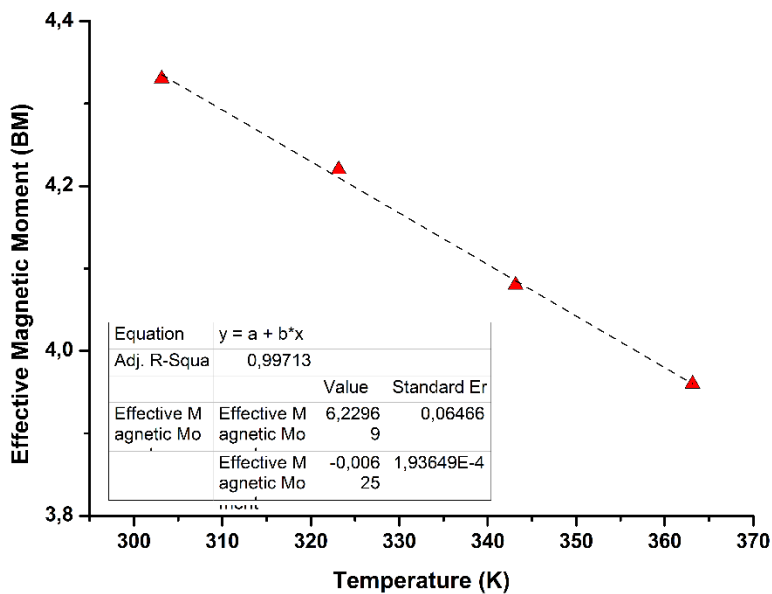


Figure S 70 Effective magnetic moment of **9** with respect to temperature.

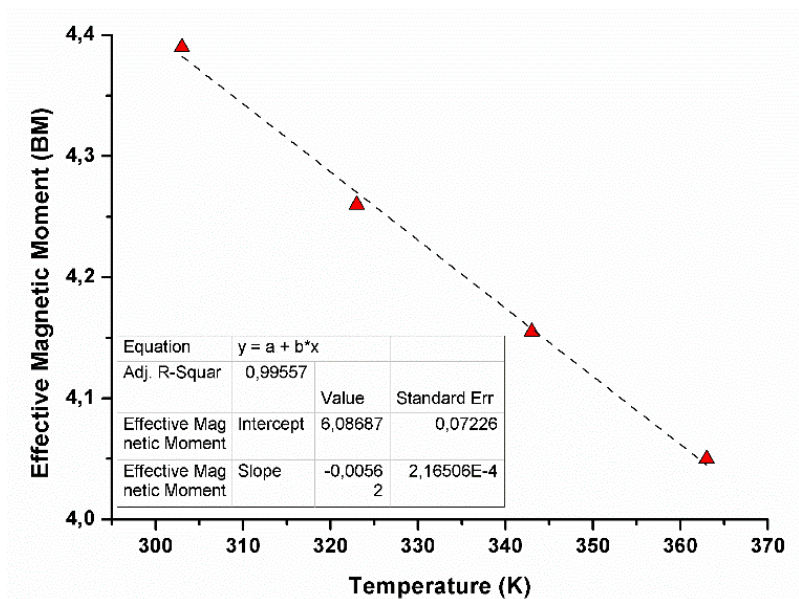


Figure S 71 Effective magnetic moment of **10** with respect to temperature.

FT-IR analysis

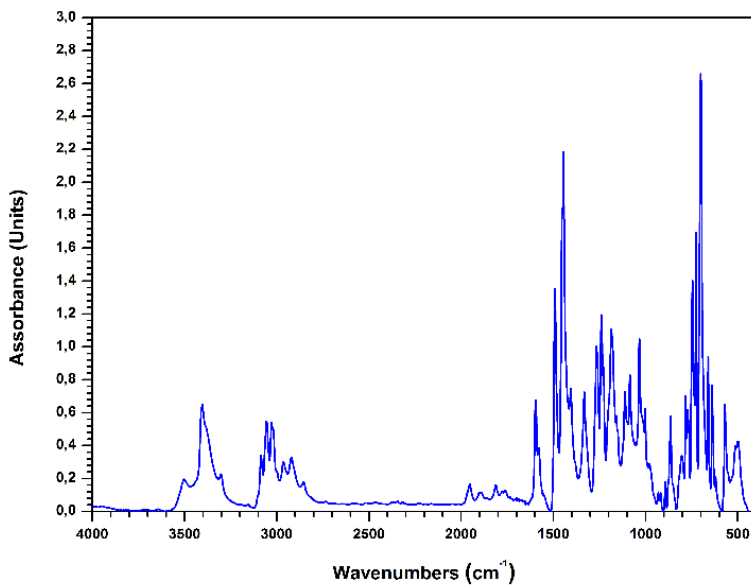


Figure S 72 FT-IR spectrum of the pro-ligand **L7** (KBr disk).

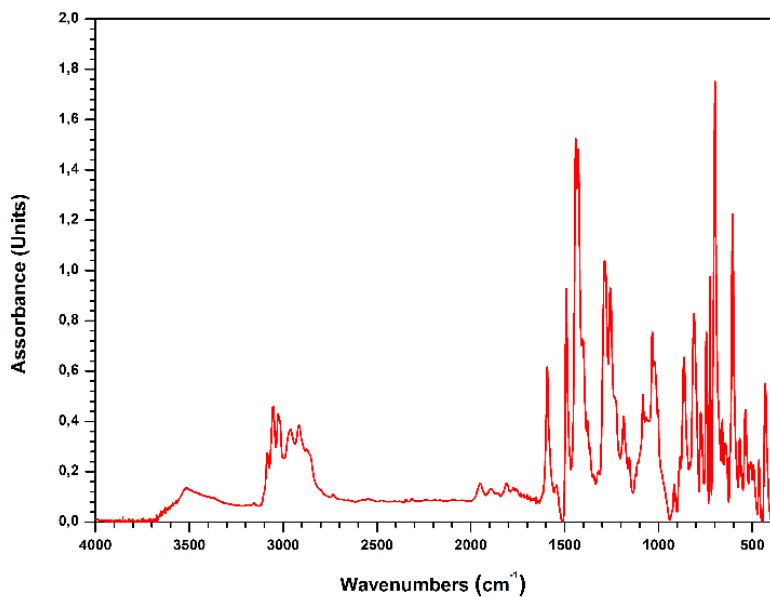


Figure S 73 FT-IR spectrum of the iron(III) complex **7** (KBr disk).

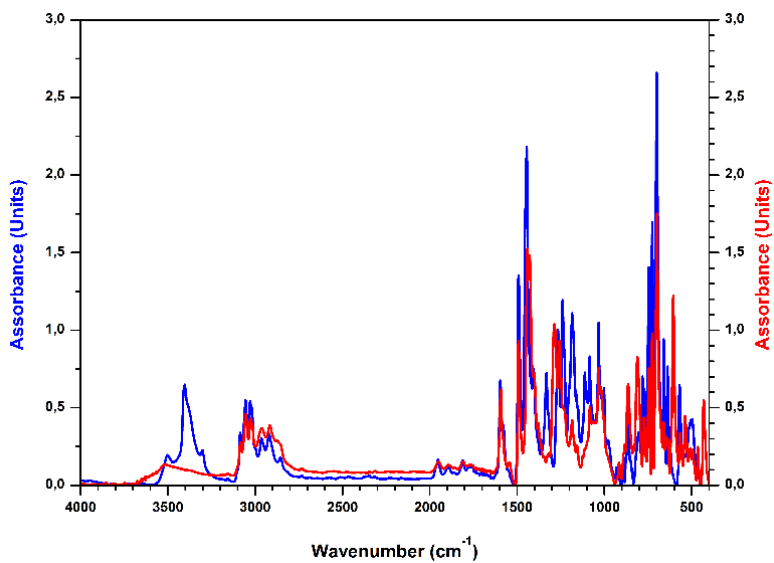


Figure S 74 Comparison of the FT-IR spectra of the pro-ligand **L7** (blue curve) and of the iron(III) complex **7** (red curve)

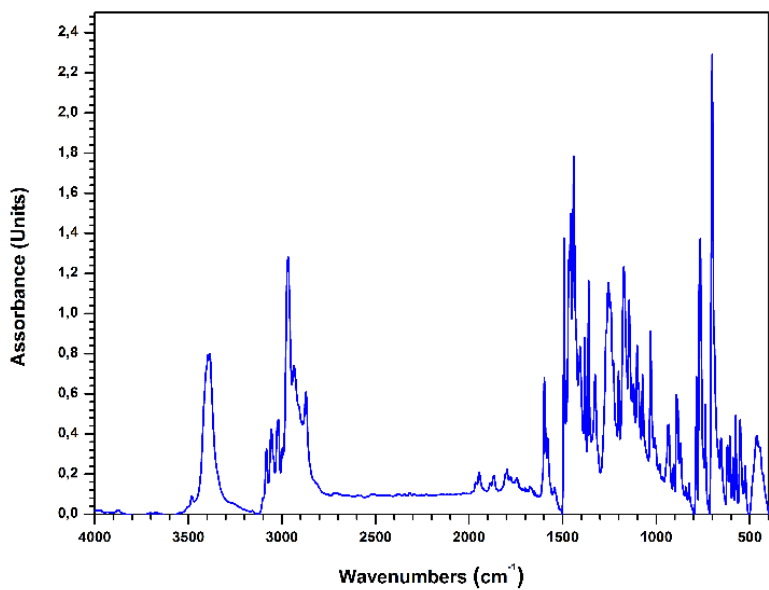


Figure S 75 FT-IR spectrum of the pro-ligand **L8** (KBr disk).

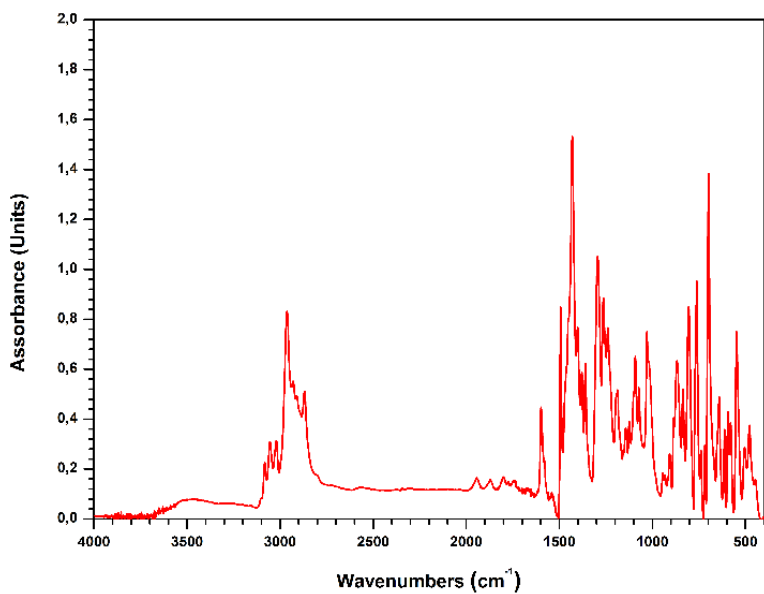


Figure S 76 FT-IR spectrum of the iron(III) complex **8** (KBr disk).

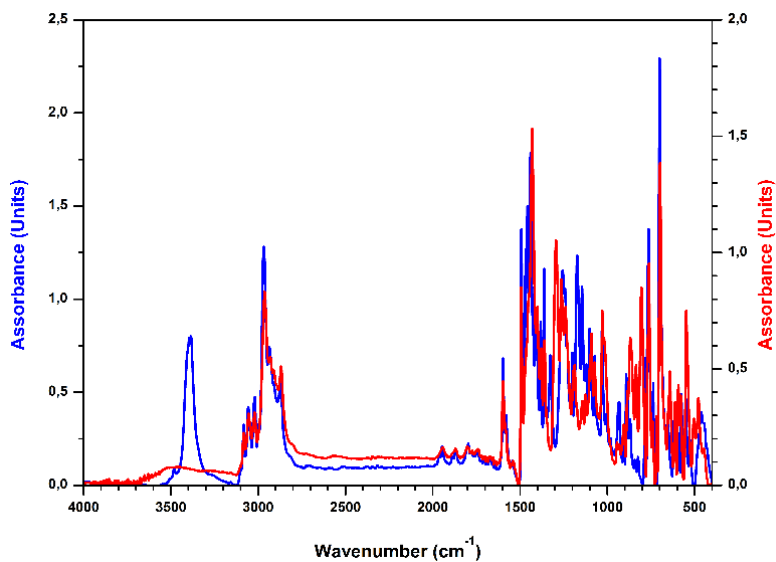


Figure S 77 Comparison of the FT-IR spectra of the pro-ligand **L8** (blue curve) and of the iron(III) complex **8** (red curve)

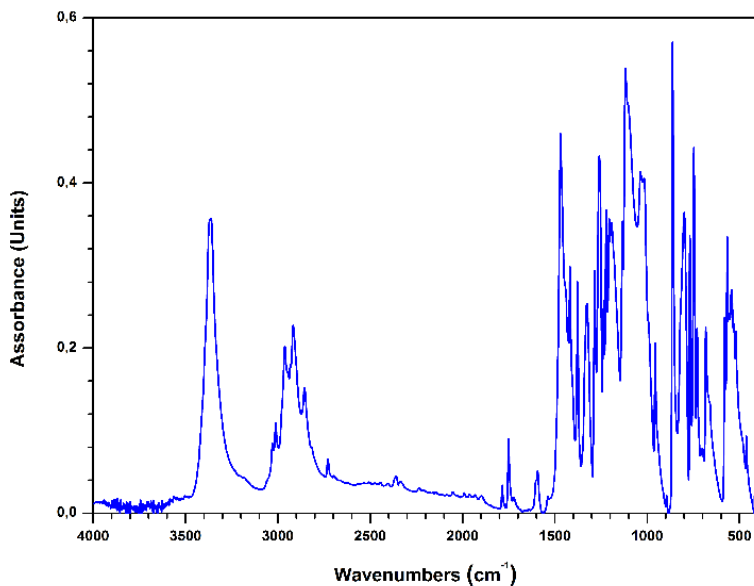


Figure S 78 FT-IR spectrum of the pro-ligand **L9** (KBr disk).

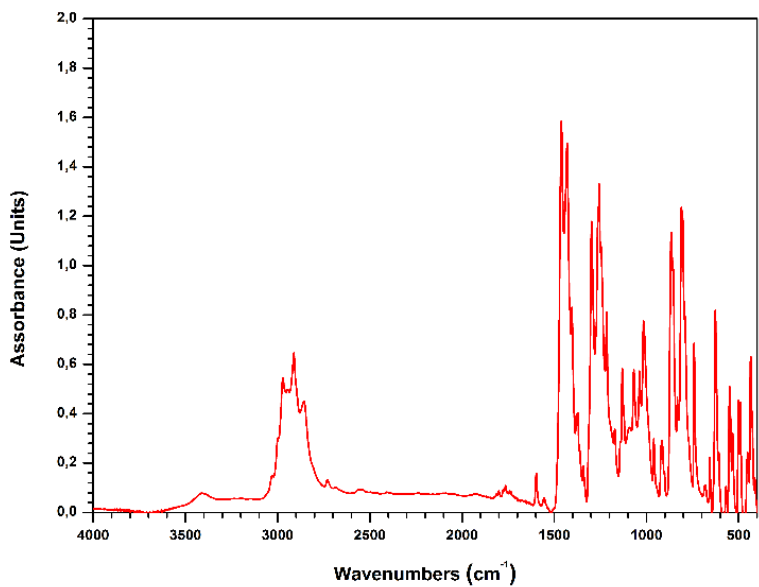


Figure S 79 FT-IR spectrum of the iron(III) complex **9** (KBr disk).

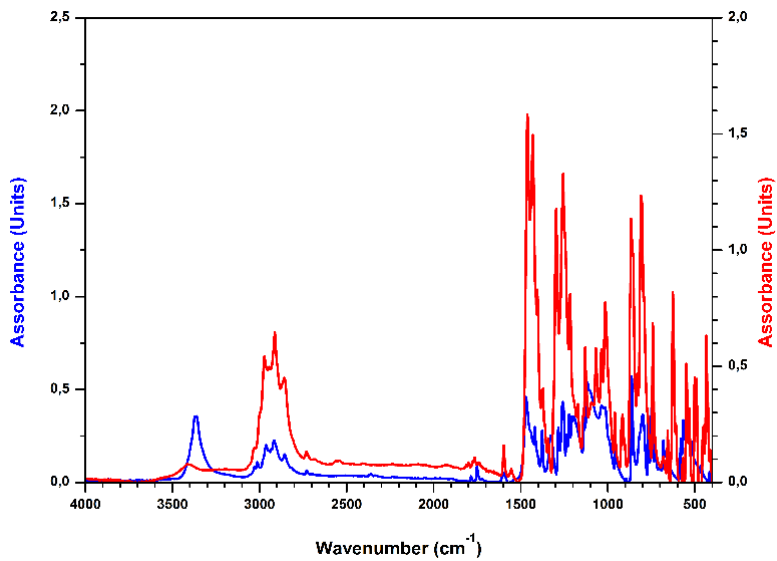


Figure S 80 Comparison of the FT-IR spectra of the pro-ligand **L9** (blue curve) and of the iron(III) complex **9** (red curve)

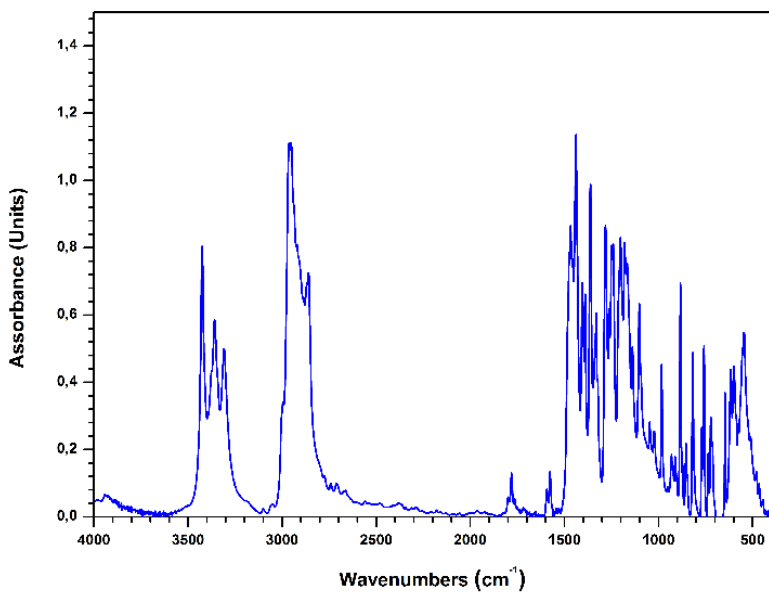


Figure S 81 FT-IR spectrum of the pro-ligand **L10** (KBr disk).

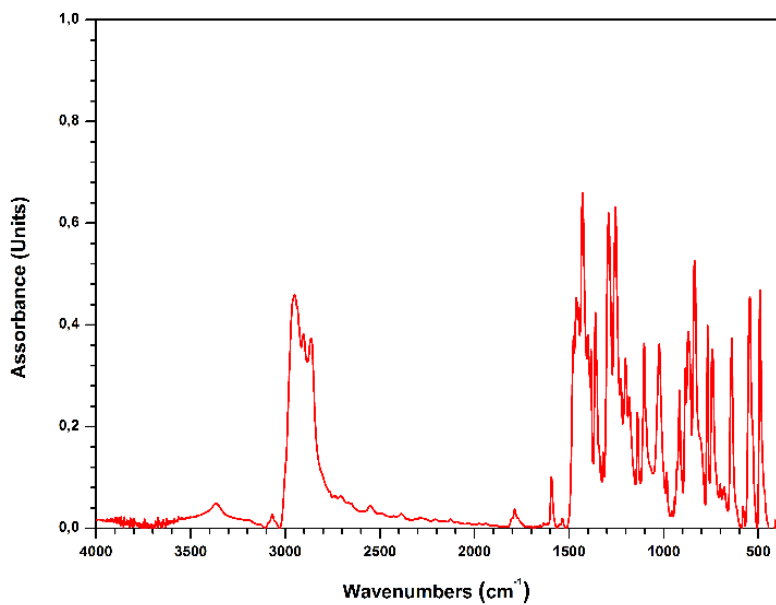


Figure S 82 FT-IR spectrum of the iron(III) complex **10** (KBr disk).

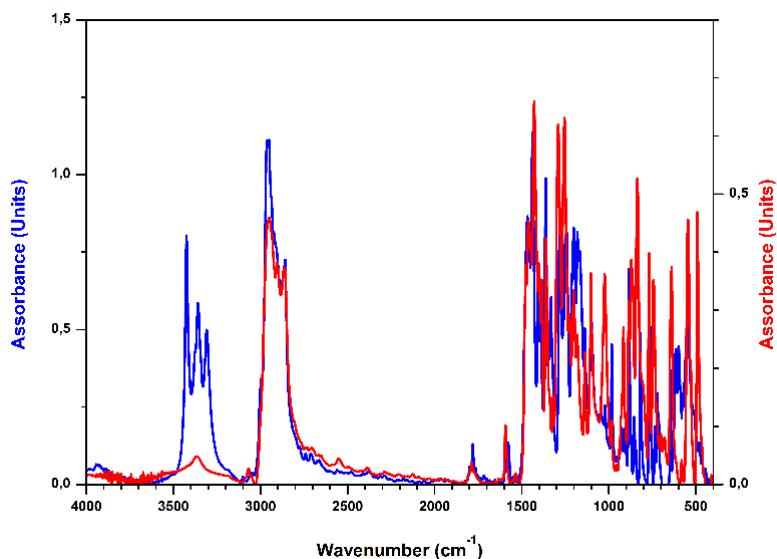


Figure S 83 Comparison of the FT-IR spectra of the pro-ligand **L10** (blue curve) and of the iron(III) complex **10** (red curve)

Crystallographic data of the Iron(III) complex **8**

The X-ray intensity data for **8** were measured on a Bruker X8 Apex four-circle diffractometer. The Bruker-Nonius X8 APEX package was used for collecting frames of data, indexing reflections, and determining lattice parameters. The collected frames were then processed for integration by the SAINT program, and an empirical absorption correction was applied using SADABS. The structure was solved by direct methods (SIR 97) and subsequent Fourier syntheses and refined by full-matrix least squares on F^2 (SHELXL), using anisotropic thermal parameters for all non-hydrogen atoms. All hydrogen atoms were added in calculated positions, included in the final stage of refinement with isotropic thermal parameters, $U(H) = 1.2[U_{eq}(C)]$ ($U(H) = 1.5[U_{eq}(C-Me)]$), and allowed to ride on their carrier carbons. In the asymmetric unit of compound **8** one CH_3CN solvent molecule is present. Crystal data and details of the data collection for **8** are reported in Table S1.

CCDC 1564256 contains supplementary crystallographic data for this paper. These data can be obtained free of charge from the

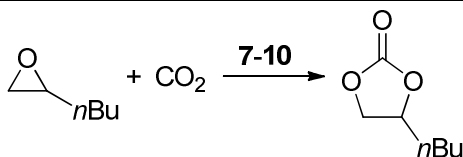
Table S 4 Crystal data and structure refinement for complex **8**

Compound	8
Formula	C ₅₂ H ₅₅ ClFeN O ₂ S ₂ ·CH ₃ CN
Fw	922.44
T, K	293
λ, Å	0.71073
Crystal symmetry	Monoclinic
Space group	<i>P</i> 2 ₁ / <i>c</i>
<i>a</i> , Å	17.208(4)
<i>b</i> , Å	10.880(3)
<i>c</i> , Å	27.059(6)
α	90
β	101.257(7)
γ	90
Cell volume, Å ³	4969(2)
<i>Z</i>	4
D _c , Mg m ⁻³	1.233
μ(Mo-Kα), mm ⁻¹	0.482
F(000)	1948
Crystal size/ mm	0.44 x 0.37 x 0.31
θ limits, °	1.535 to 26.000
Reflections collected	45659
Unique obs. Reflections [F _o > 4σ(F _o)]	9749 [R(int) = 0.0309]
Goodness-of-fit-on F ²	1.141
R ₁ (F) ^a , wR ₂ (F ²) [I > 2σ(I)]	0.0412, 0.1251
Largest diff. peak and hole, e. Å ⁻³	0.750 and -0.796

^a) $R_1 = \sum ||F_o| - |F_c|| / \sum |F_o|$. ^b) $wR_2 = [\sum w(F_o^2 - F_c^2)^2 / \sum w(F_o^2)^2]^{1/2}$ where $w = 1/[\sigma^2(F_o^2) + (aP)^2 + bP]$ where $P = (F_o^2 + F_c^2)/3$.

Catalytic tests

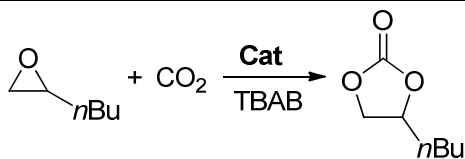
Table S 5 Hexene carbonate formation promoted by Fe(III) complexes **7-10**.



Entry	Catalyst	Co-catalyst	Temp.	Conv. ^b	TON ^c	TOF ^d	
		mol%	°C	mol%		h ⁻¹	
S1	7	TBAB	0.1	35	15.2	152	6.3
S2	8	TBAB	0.1	35	16.5	165	6.9
S3	9	TBAB	0.1	35	8.2	82	3.4
S4	10	TBAB	0.1	35	32.3	323	13.5
S5	10	DMAP	0.1	35	2.5	25	1
S6	10	[PPN]Cl	0.1	35	31.5	315	13.1
S7	10	TABN ₃	0.1	35	20.6	206	8.6
S8	10	TBAC	0.1	35	29.1	291	12.1
S9	10	TBAI	0.1	35	30.8	308	12.8
S10	10	TBAB	0.2	35	57.7	577	24
S11	10	TBAB	0.5	35	88.9	889	37
S12	10	TBAB	1.0	35	93	930	38.8
S13	10	TBAB	0.1	22	18.7	187	7.8
S14	10	TBAB	0.1	50	47.4	474	19.8
S15	10	TBAB	0.1	70	56.6	566	23.6

^aReaction conditions: HO = 5.0 mL, 4.15 × 10⁻² mol; P(CO₂) = 1 bar; reaction time = 24 h, neat. ^bDetermined by ¹H NMR using mesitylene as internal standard. The selectivity toward the formation of cyclic carbonate was always found to be >99%. ^cTurnover number (mol_{carbonate} · mol_{Catalyst}⁻¹). ^dTurnover frequency (mol_{carbonate} · mol_{Catalyst}⁻¹ · reaction time⁻¹).

Table S 6 Comparison of the activity of catalytic system **10**/TBAB with the activities of binary systems reported in reference 52



Entry ^a	Catalyst	Temperature °C	Conversion ^b %	TON ^c	TOF ^d h ⁻¹
1	10	25	24	240	30
2 ^e	A	25	19	190	24
3 ^e	B	25	30	150	19
4 ^e	C	25	>99	1000	125
5 ^e	D	25	18	180	23
6	10	50	62	620	207
7 ^e	A	50	63	630	210
8 ^e	B	50	49	245	82
9 ^e	C	50	97	970	323
10 ^e	D	50	36	360	120
11	10	105	24	1200	600
12 ^e	A	105	76	3800	1900
13 ^e	B	105	12	300	150
14 ^e	C	105	52	2600	1300
15 ^e	D	105	8	400	200

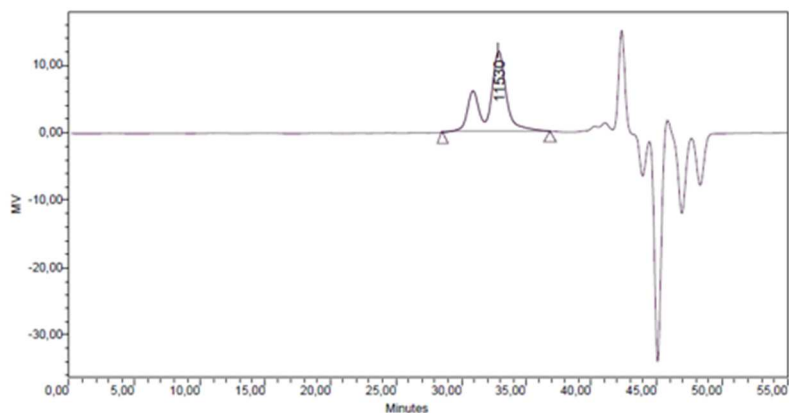
a) Reaction conditions at 25 °C and 50 °C: HO = 4.15×10^{-2} mol; **10** = 4.15×10^{-5} mol (0.1 mol%); TBAB = 2.07×10^{-4} mol (0.5 mol%); P(CO₂) = 10 bar; reaction time = 8 h (25 °C) and 3 h (50 °C), neat. Reaction conditions at 105 °C: HO = 4.15×10^{-2} mol; **10** = 8.3×10^{-6} mol (0.02 mol%); TBAB = 4.15×10^{-5} mol (0.1 mol%); P(CO₂) = 10 bar; reaction time = 2 h, neat. b) Determined by ¹H NMR using mesitylene as internal standard. The selectivity toward the formation of cyclic carbonate was always found to be >99%. c) Turnover number (mol_{Carbonate} · mol_{Catalyst}⁻¹). d) Turnover frequency (mol_{Carbonate} · mol_{Catalyst}⁻¹ · reaction time⁻¹). e) Data from reference 52.

Table S 7 Co-polymerization of CHO with CO₂ in the promoted by the [OSSO]-Fe(III) complexes **7-10**

Entry	Catalyst mol%	Co-Catalyst mol%	T °C	P(CO ₂) bar	Time h	Conv. %	TOF h ⁻¹	Carbonate %	Mn(1) kDa	Đ(1)	Mn(2) kDa	Đ(2)	Mn(1)/Mn(2) %
S1	10 (0.2)	TBAB (1.0)	50	10	24	70	15	98	24.3	1.01	11.2	1.04	6/94
S2	7 (0.1)	TBAB (0.1)	80	10	2	22	110	98	21.1	1.01	10.1	1.03	12/88
S3	8 (0.1)	TBAB (0.1)	80	10	2	41	205	98	32.8	1.01	15.8	1.03	11/89
S4	9 (0.1)	TBAB (0.1)	80	10	2	traces	-	-	-	-	-	-	-
S5	10 (0.1)	TBAB (0.1)	80	10	2	20.5	103	98	19.1	1.01	8.9	1.03	15/85
S6	8 (0.1)	-	80	10	1	traces	-	-	-	-	-	-	-
S7	8 (0.1)	-	80	10	6	16	27	7	63.4	1.4	-	-	-
S8	8 (0.1)	DMAP (0.1)	80	10	6	47	78	98	12.2	1.21	-	-	-
S9	8 (0.1)	DMAP (0.1)	80	10	1	4.5	45	98	-	-	-	-	-
S10	8 (0.1)	[PPN]Cl (0.1)	80	10	1	30.3	300	98	17.5	1.01	8.5	1.04	19/81
S11	8 (0.1)	TBAB (0.1)	80	10	1	19.3	190	98	11.8	1.01	5.2	1.03	38/62
S12	8 (0.1)	TBAI (0.1)	80	10	1	21.2	210	98	14.4	1.01	6.2	1.04	23/77
S13	8 (0.1)	TBAN ₃ (0.1)	80	10	1	29.4	290	98	19.6	1.01	9.4	1.03	23/77
S14	8 (0.1)	TBAC (0.05)	80	10	1	14.5	145	98	10.5	1.01	4.1	1.03	42/68
S15	8 (0.1)	TBAC (0.1)	80	10	1	34.0	340	98	23.2	1.01	11.0	1.03	31/69
S16	8 (0.1)	TBAC (0.2)	80	10	1	40.4	400	98	22.3	1.01	10.9	1.03	24/76
S17	8 (0.1)	TBAC (0.5)	80	10	1	26.6	265	98	7.7	1.01	3.4	1.05	9/91
S18	8 (0.1)	TBAC (0.1)	40	10	1	2	20	98	-	-	-	-	-
S19	8 (0.1)	TBAC (0.1)	60	10	1	7.6	75	98	5.5	1.01	4.5	1.04	23/77
S20	8 (0.1)	TBAC (0.1)	100	10	1	42.1	420	98	24.0	1.01	11.1	1.04	23/77
S21	8 (0.1)	TBAC (0.1)	80	1	1	16.9	170	98	13.4	1.01	6.1	1.04	23/77
S22	8 (0.1)	TBAC (0.1)	80	5	1	29.7	300	98	22.5	1.01	10.5	1.04	25/75
S23	8 (0.1)	TBAC (0.1)	80	20	1	16.5	165	98	7.5	1.02	3.6	1.02	63/37

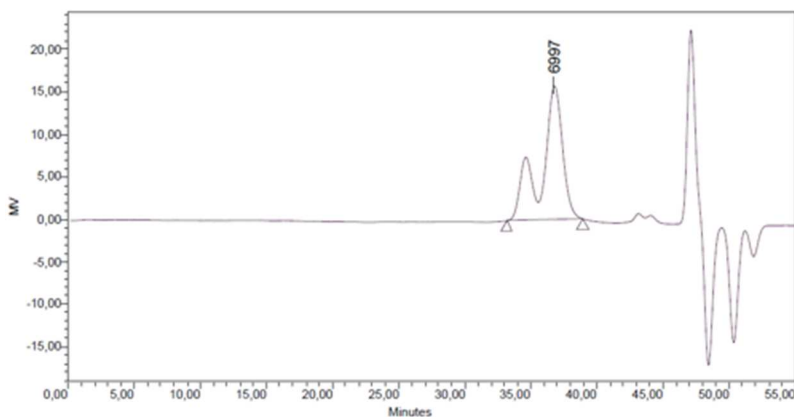
^aReaction conditions: CHO = 5.93 × 10⁻² mol, ^bGravimetric, ^cTurnover Frequency (yield × 0.01 × molCatalyst⁻¹ × reaction time⁻¹), ^dDetermined by ¹H NMR, ^eDetermined by Gel Permeation Chromatography at 25 °C in THF respect to polystyrene standards

Gel permeation chromatography characterization



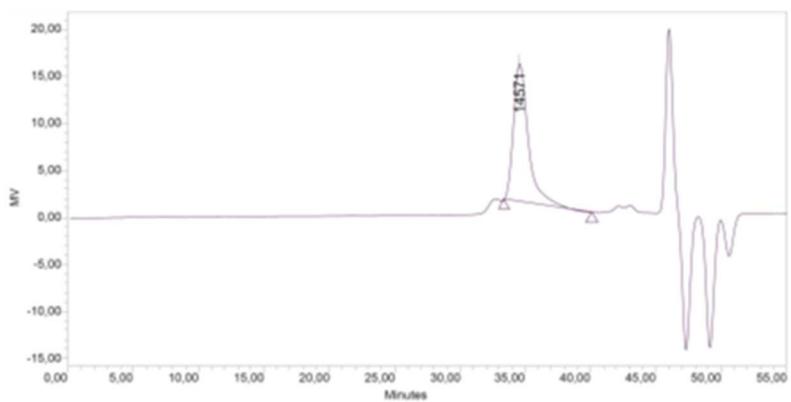
	Distribution Name	Mn (Daltons)	Mw (Daltons)	MP (Daltons)	Mz (Daltons)	Mz+1 (Daltons)	Polydispersity	Mz/Mw	Mz+1/Mw
1		23194	23511	23271	23833	24158	1,013638	1,013690	1,027546
1		11056	11334	11530	11593	11837	1,025084	1,022842	1,044384

Figure S 84 GPC trace of sample obtained as in entry 2 Table 5.



	Distribution Name	Mn (Daltons)	Mw (Daltons)	MP (Daltons)	Mz (Daltons)	Mz+1 (Daltons)	Polydispersity	Mz/Mw	Mz+1/Mw
1		14308	14489	14347	14671	14853	1,012640	1,012563	1,025125
1		6713	6897	6958	7076	7250	1,027425	1,026003	1,051176

Figure S 85 GPC trace of sample obtained as in entry 5 Table 5.



Broad Unknown Relative Peak Table

Distribution Name	Mn (Daltons)	Mw (Daltons)	MP (Daltons)	Mz (Daltons)	Mz+1 (Daltons)	Polydispersity	Mz/Mw	Mz+1/Mw
1	12866	13684	14571	14298	14785	1,063576	1,044883	1,080451
1	27833	27987	27900	28142	28296	1,505538	1,005618	1,011023

Figure S 86 GPC trace of sample obtained as in entry 6 Table 5.

Thermal analysis

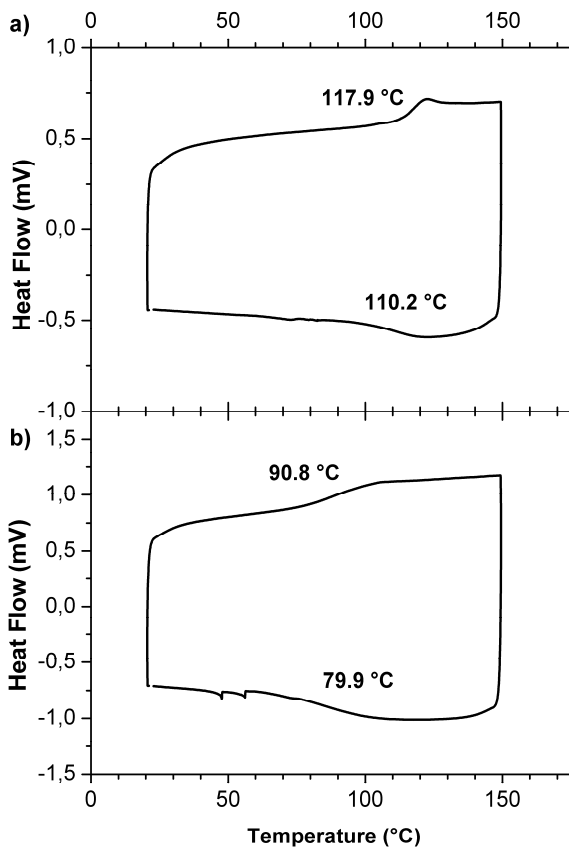


Figure S 87 DSC analysis of poly-(cyclohexene carbonate) a) sample reported in entry 6 Table 5, b) sample reported in entry 5 Table 5.

Kinetic experiments for PC formation promoted by 10/TBAB

Reaction order with respect to [10]

Table S 8 Summary of the PO/CO₂ experiments for reaction order with respect to 10

Entry	PO/TBAB/10	[10] mM	v ₀ l/s·10 ⁴
S1	500/1/1	28.6	5.33
S2	1000/2/1	14.3	5.30
S3	1500/3/1	9.5	3.10
S4	2000/4/1	7.2	1.81
S5	3000/6/1	4.8	0.47

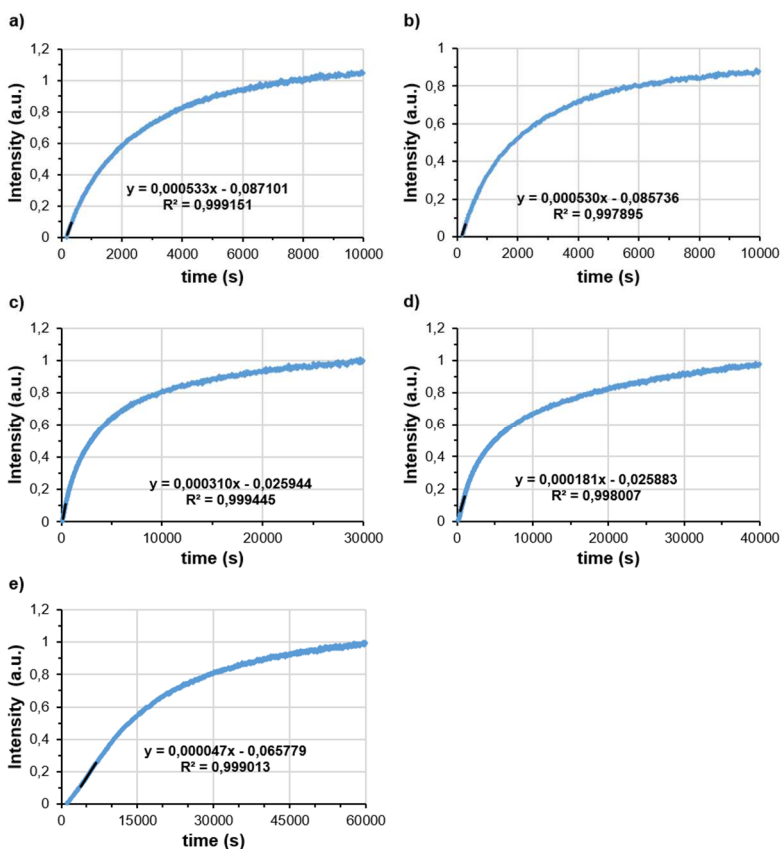


Figure S 88 Variation of the intensity of the PC C=O stretching band with respect to time for experiments in Table S 8. a) [10] = 28.6 mM, b) [10] = 14.3 mM, c) [10] = 9.5 mM, d) [10] = 7.2 mM, e) [10] = 4.8 mM.

Reaction order with respect to [TBAB]

Table S 9 Summary of the PO/CO₂ experiments for reaction order with respect to TBAB

Entry	PO/TBAB/10	[TBAB] mM	v ₀ l/s·10 ⁴
S1	1000/1/1	14.3	3.12
S2	1000/2/1	28.6	5.30
S3	1000/3/1	42.9	5.28
S4	1000/4/1	57.2	6.19
S5	1000/5/1	71.5	5.26

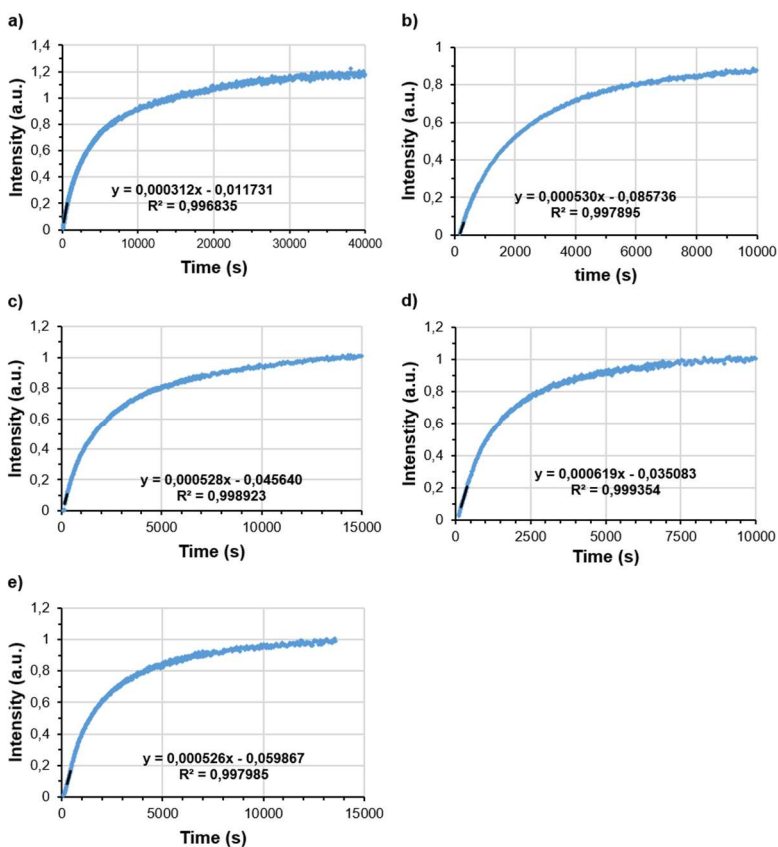


Figure S 89 Variation of the intensity of the PC C=O stretching band with respect to time for experiments in Table S 9. a) [TBAB] = 14.3 mM, b) [TBAB] = 28.6 mM, c) [TBAB] = 42.9 mM, d) [TBAB] = 57.2 mM, e) [TBAB] = 71.5 mM.

Reaction order with respect to [PO]

Table S 10 Summary of the PO/CO₂ experiments for reaction order with respect to PO

Entry	[PO] mol/L	K l/s·10 ⁴
S1	4.29	1.09
S2	5.72	1.45
S3	7.15	1.68
S4	8.57	2.40

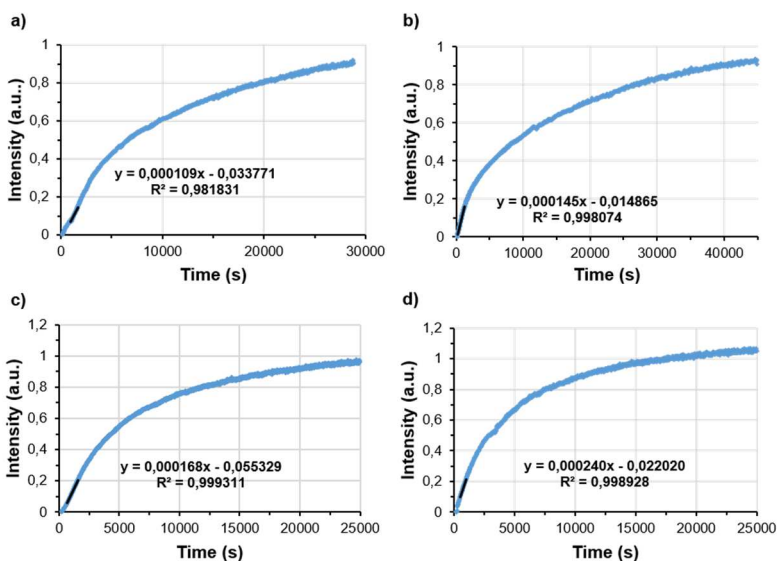


Figure S 90 Variation of the intensity of the PC C=O stretching band with respect to time for experiments in Table S 10. a) [PO] = 4.29 M, b) [PO] = 5.72 M, c) [PO] = 7.15 M, d) [PO] = 8.57 M.

Reaction order with respect to P(CO₂)

Table S 11 Summary of the PO/CO₂ experiments for reaction order with respect to CO₂

Entry	P(CO ₂) bar	K l/s·10 ⁴
S1	2	1.39
S2	3.5	1.58
S3	6	1.59
S4	8.5	1.68

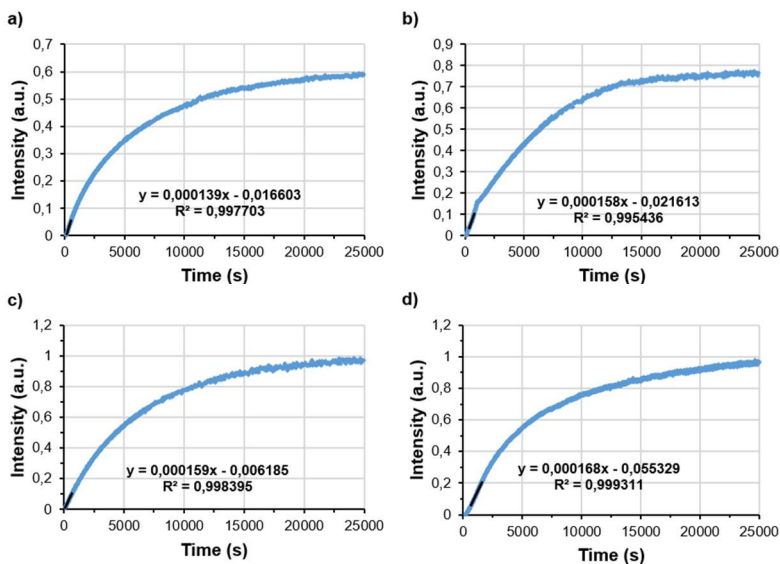


Figure S 91 Variation of the intensity of the PC C=O stretching band with respect to time for experiments in Table S 11. a) P(CO₂) = 2.0 bar, b) P(CO₂) = 3.5 bar, c) P(CO₂) = 6.0 bar, d) P(CO₂) = 8.5 bar.

Eyring plot

Table S 12 Summary of the PO/CO₂ experiments at different temperatures for the determination of the activation parameters.

Entry	PO/TBAB/10	Temperature °C	K l/s·10 ⁴
S1	1666/5/1	30	0.52
S2	1666/5/1	40	0.74
S3	1666/5/1	50	1.68
S4	1666/5/1	70	2.73

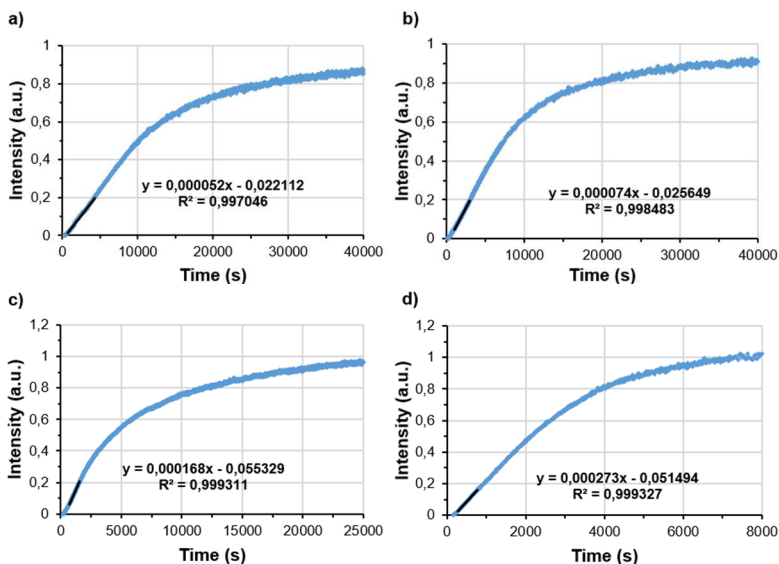


Figure S 92 Variation of the intensity of the PC C=O stretching band with respect to time for experiments in Table S 12. a) T = 30°C, b) T = 40°C, c) T = 50°C, d) T = 70°C.

Kinetic experiments for PCHC formation promoted by 8/TBAC

Reaction order with respect to [8]

Table S 13 Summary of the CHO/CO₂ experiments for reaction order with respect to 10

Entry	CHO/TBAC/8	[8] mM	v ₀ l/s·10 ⁴
S1	2500/2.5/1	3.6	0.55
S2	2000/2/1	4.6	0.71
S3	1500/1.5/1	6.1	0.96
S4	1000/1/1	9.1	1.37
S5	500/0.5/1	18.2	2.67

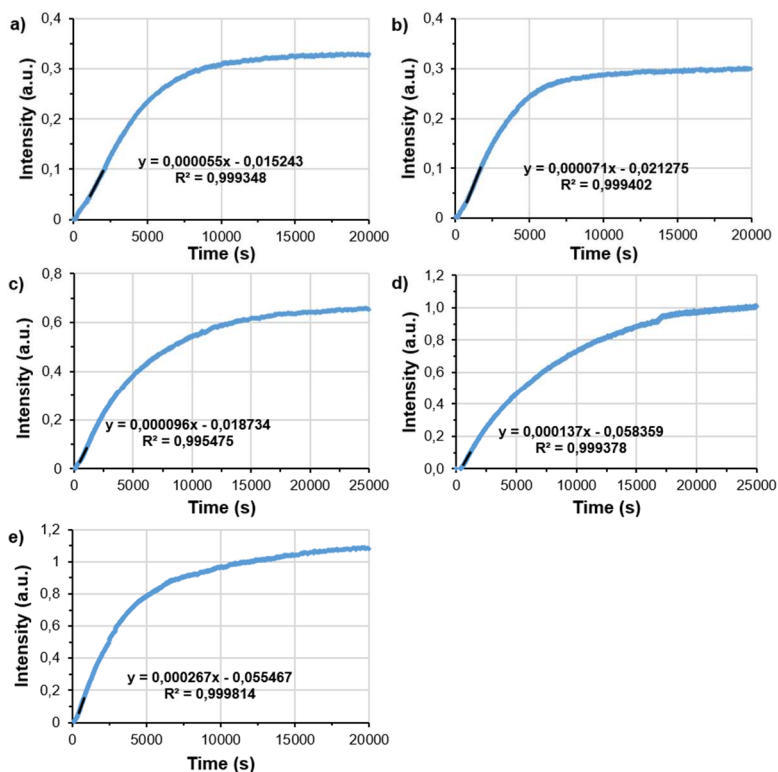


Figure S 93 Variation of the intensity of the PCHC C=O stretching band with respect to time for experiments in Table S 13. a) [8] = 3.6 mM, b) [8] = 4.6 mM, c) [8] = 6.1 mM, d) [8] = 9.1 mM, e) [8] = 18.2 mM.

Reaction order with respect to [TBAC]

Table S 14 Summary of the CHO/CO₂ experiments for reaction order with respect to TBAC

Entry	CHO/TBAC/8	[TBAC] mM	v ₀ l/s·10 ⁴
S1	1000/0.77/1	7.6	0.73
S2	1000/1/1	9.8	1.37
S3	1000/1.5/1	14.8	1.52
S4	1000/2/1	19.8	1.54
S5	1000/2.5/1	24.8	1.56
S6	1000/3/1	29.7	1.57

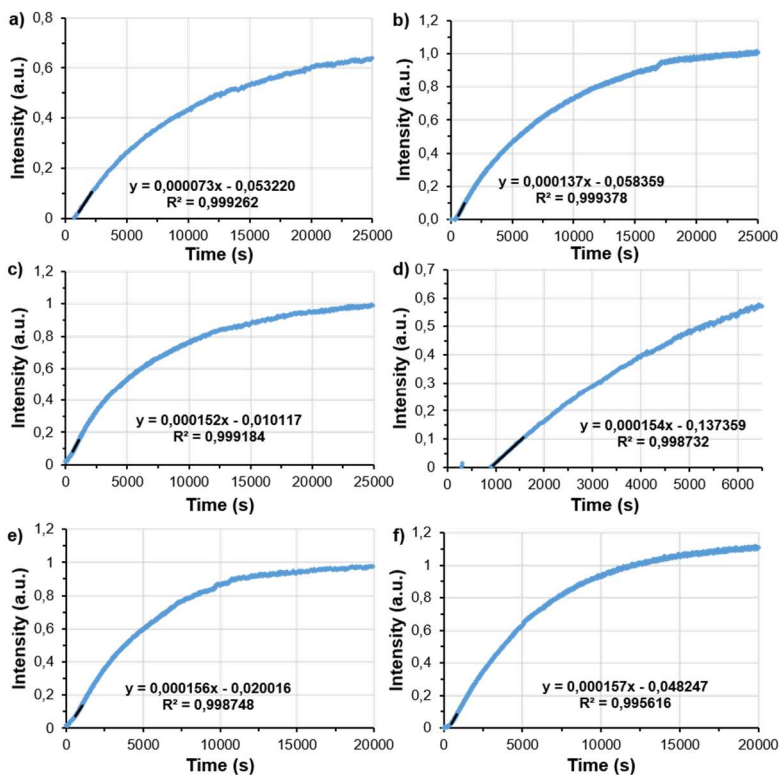


Figure S 94 Variation of the intensity of the PCHC C=O stretching band with respect to time for experiments in Table S 14. a) [TBAC] = 7.6 mM, b) [TBAC] = 9.8 mM, c) [TBAC] = 14.8 mM, d) [TBAC] = 19.8 mM, e) [TBAC] = 24.8 mM, f) [TBAC] = 29.7 mM.

Reaction order with respect to [CHO]

Table S 15 Summary of the CHO/CO₂ experiments for reaction order with respect to CHO

Entry	CHO/TBAC/8	[CHO]	v ₀
		M	l/s·10 ⁴
S1	600/1/1	2.97	0.85
S2	800/1/1	3.95	1.11
S3	1000/1/1	4.94	1.37
S4	1200/1/1	5.93	1.65

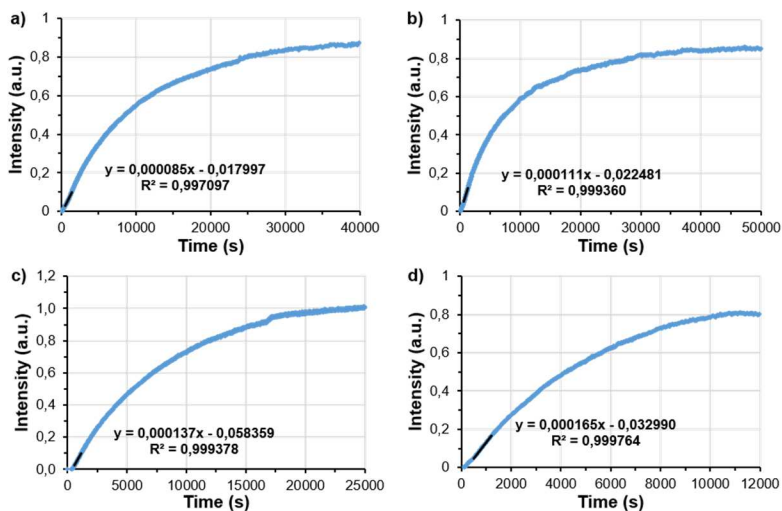


Figure S 95 Variation of the intensity of the PCHC C=O stretching band with respect to time for experiments in Table S 15. a) [CHO] = 2.97 M, b) [CHO] = 3.95 M, c) [CHO] = 4.94 M, d) [CHO] = 5.93 mM.

Reaction order with respect to P(CO₂)

Table S 16 Summary of the CHO/CO₂ experiments for reaction order with respect to CO₂

Entry	P(CO ₂) bar	K l/s·10 ⁴
S1	6	1.33
S2	7.4	1.58
S3	9	1.59

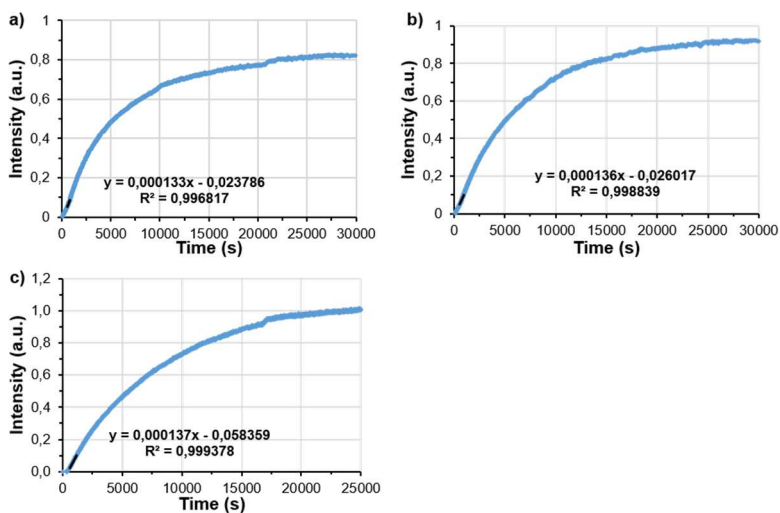


Figure S 96 Variation of the intensity of the PCHC C=O stretching band with respect to time for experiments in Table S 16. a) P(CO₂) = 6.0 bar, b) P(CO₂) = 7.4 bar, c) P(CO₂) = 9.0 bar.

Eyring plot

Table S 17 Summary of the CHO/CO₂ experiments at different temperatures for the determination of the activation parameters.

Entry	CHO/TBAC/8	Temperature °C	K l/s·10 ⁴
S1	1000/1/1	60	0.48
S2	1000/1/1	70	0.85
S3	1000/1/1	80	1.37
S4	1000/1/1	90	2.33

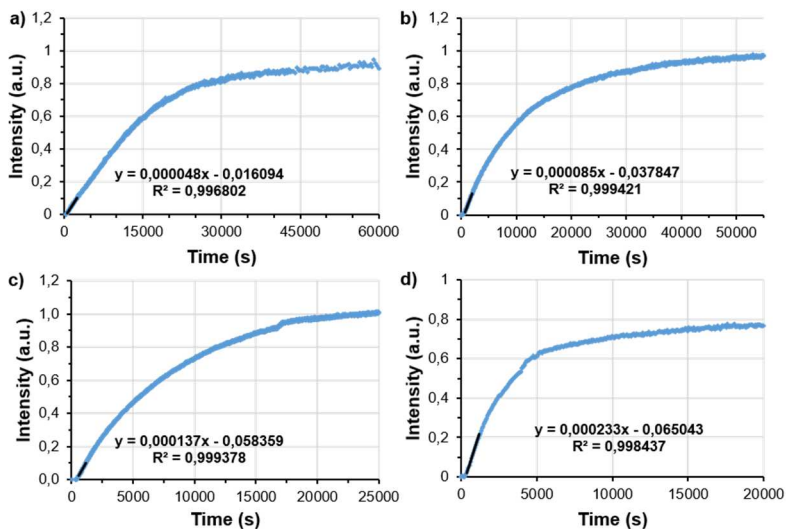


Figure S 97 Variation of the intensity of the PCHC C=O stretching band with respect to time for experiments in Table S 12. a) T = 30°C, b) T = 40°C, c) T = 50°C, d) T = 70°C.

3.7 References

- ⁴⁷ a) Capacchione C., Proto A., Ebeling H., Mülhaupt R., Möller K., Spaniol T. P., Okuda J., *J. Am. Chem. Soc.*, **2003**, *125*, 4964-4965. b) Ishii A., Toda T., Nakata N., Matsuo T., *J. Am. Chem. Soc.*, **2009**, *131*, 13566-13567. c) Kapelski A., Buffet J.-C., Spaniol T. P., Okuda J., *Chem. Asian J.*, **2012**, *7*, 1320-1330.
- ⁴⁸ Si G., Zhang L., Han B., Zhang H., Li X., Liu B., *RSC Adv.*, **2016**, *6*, 22821-22826.
- ⁴⁹ Capacchione C., Manivannan R., Barone M., Beckerle K., Centore R., Oliva L., Proto A., Tuzi A., Spaniol T. P., Okuda J., *Organometallics*, **2005**, *24*, 2971-2982.
- ⁵⁰ Sellmann D., Freyberger G., Eberlein R., Bohlen E., Huttner G., Zsolnai L., *J. Organomet. Chem.*, **1987**, *323*, 21-35.
- ⁵¹ Castro-Osma J. A., Lamb K. J., North M., *ACS Catal.* **2016**, *6*, 5012-5025.
- ⁵² Rintjema J., Kleij A. W., *ChemSusChem* **2017**, *10*, 1274-1282.
- ⁵³ (a) Clegg, W.; Harrington, R. W.; North, M.; Pasquale, R., *Chem. Eur. J.* **2010**, *16*, 6828-6843 (b) Tian, D.; Liu, B.; Gan, Q.; Li, H.; Darensbourg, D. J.; *ACS Catalysis* **2012**, *2*, 2029-2035. (c) Whiteoak, C. J.; Kielland, N.; Laserna, V.; Escudero-Adán, E. C.; Martin, E.; Kleij, A. W.; *J. Am. Chem. Soc.* **2013**, *135*, 1228-1231. (d) Qin, Y.; Guo, H.; Sheng, X.; Wang, X.; Wang, F.; *Green Chem.* **2015**, *17*, 2853-2858. (e) North, M.; Quek, S. C. Z.; Pridmore, N. E.; Whitwood, A. C.; Wu X.; *ACS Catal.* **2015**, *5*, 3398-3402.
- ⁵⁴ Wu, X.; North, M.; *ChemSusChem* **2017**, *10*, 74-78.
- ⁵⁵ a) Buchard A., Kember M. R., Sandeman K. G., Williams C. K., *Chem. Commun.*, **2011**, *47*, 212-214. b) Taherimehr M., Al-Amsyar S. M., Whiteoak C. J., Kleij A. W., Pescarmona P. P., *Green Chem.*, **2013**, *15*, 3083-3090. c) Nakano K., Kobayashi K., Ohkawara T., Imoto H., Nozaki K., *J. Am. Chem. Soc.*, **2013**, *135*, 8456-8459.
- ⁵⁶ Sugimoto, H.; Ohtsuka, H.; Inoue, S. *J. Polym. Sci., Part A: Polym. Chem.*, **2005**, *43*, 4172-4186.
- ⁵⁷ Jutz F., Buchard A., Kember M. R., Fredriksen S. B., Williams C. K., *J. Am. Chem. Soc.*, **2011**, *133*, 17395-17405.
- ⁵⁸ a) Carothers W.H., Hill J.W., *J. Am. Chem. Soc.*, **1933**, *55*, 5043. b) Spanagel E.W., Carothers W.H., *J. Am. Chem. Soc.*, **1935**, *5*, 929.
- ⁵⁹ a) Wu X., Castro-Osma J. A., North M., *Symmetry*, **2016**, *8*, 4. b) Gomez J. E., Kleij A. W., *Current Opinion in Green and Sustainable Chemistry*, **2017**, *3*, 55-60.

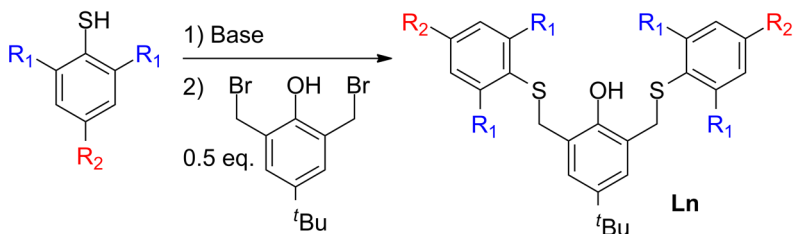
- ⁶⁰ Darensbourg D. J., Yarbrough J. C., Ortiz C., Fang C. C., *J. Am. Chem. Soc.*, **2003**, *125*, 7586-7591.
- ⁶¹ Moore D. R., Cheng M., Lobkovsky E. B., Coates G. W., *J. Am. Chem. Soc.*, **2003**, *125*, 11911-11924.
- ⁶² Dengler J. E., Lehenmeier M. W., Klaus S., Anderson C. E., Herdtweck E., Rieger B., *Eur. J. Inorg. Chem.*, **2011**, 336-343.
- ⁶³ Allen S. D., Moore D. R., Lobkovsky E. B., Coates G. W.; *J. Am. Chem. Soc.* **2002**, *124*, 14284-14285.
- ⁶⁴ Darensbourg D. J., Yarbrough J. C., Ortiz C., C. C. Fang; *J. Am. Chem. Soc.* **2003**, *125*, 7586-7591.
- ⁶⁵ Jutz F., Buchard A., Kember M. R., Fredriksen S. B., Williams C. K.; *J. Am. Chem. Soc.* **2011**, *133*, 17395-17405.

4 Thioether-phenolate Fe(II) and Fe(III) complexes

The reaction mechanism investigations conducted for the cyclic carbonate formation using the bimetallic and monometallic Fe(III) complexes reported in the previous chapters gave opposite results. In the first case, a monometallic mechanism was proposed on the bases of DFT investigations. In the second, a bimetallic rate limiting step was found by kinetic measurements. However, for the [OSSO]-Fe(III) catalysts, the co-polymerization mechanism of CHO with CO₂ was found to involve only one metal centre. Therefore it seems that not only the nuclearity of the system plays a role, but also the presence of a labile monoanionic ligand (i.e. an halide) plays a key role in the determination of the reaction mechanism. Here we report the synthesis and characterization of three new bis-thioether phenolate monoanionic tridentate ligands, and the synthesis of the corresponding Fe(II) and Fe(III) complexes. Their application as catalyst for the reaction of carbon dioxide with epoxides was investigated, with the aim to obtain further information about the catalyst structure-activity relationship and the reaction mechanism.

4.1 Synthesis and characterization

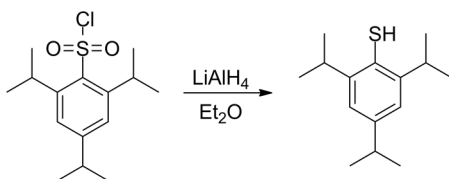
The three new thioether-phenolate monoanionic tridentate ligands **L11-13** have been synthesised with a procedure similar to that used in the case of thioether-triphenolate trianionic pentadentate ligands **L1-6** (Scheme 7).



n	11	12	13
R_1	-CH ₃	-Cl	-CH(CH ₃) ₂
R_2	-H	-H	-CH(CH ₃) ₂

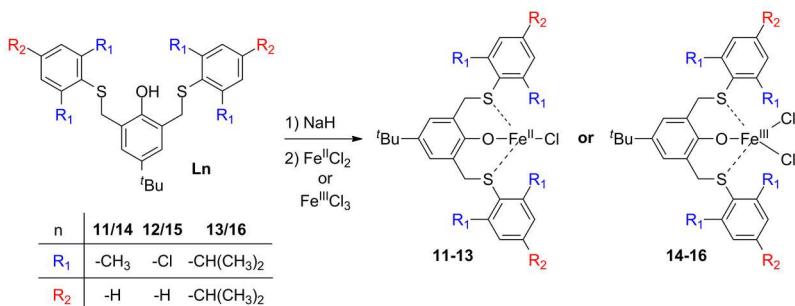
Scheme 7 Synthesis of bis-thioether-phenolate ligands **L11-13**

While the methyl and chloride substituted thiophenols are commercially available, the 2,4,6-tri-isopropyl-thiophenol was prepared according to a previously reported procedure by reduction of the corresponding sulfonyl chloride with lithium aluminium hydride (Scheme 8).⁶⁶



Scheme 8 Synthesis of tri-isopropyl-thiophenol.

All the ligands have been isolated in good yield (from 65 to 80%) by crystallization from acetonitrile or pentane solutions, and characterised by NMR and HR-ESI-MS. For each of the ligands, the corresponding Fe(II) (**11-13**) and Fe(III) (**14-16**) complexes were prepared reacting the sodium salt of the ligand with Fe(II)Cl₂ or Fe(III)Cl₃ in THF solution (Scheme 9). All the complexes decompose if exposed to air or moisture, and both IR and ESI-MS were not suitable for the characterization of these compounds.



Scheme 9 Synthesis of the bis-thioether phenolate complexes **11-16**.

Attempts to record the ¹H NMR spectra of the Fe(II) complexes **11-13** in the spectral window from -200 to 200 ppm were not successful. The effective magnetic moments μ_{eff} of all the Fe(II) and Fe(III) complexes, in CD₂Cl₂ solutions at 30 °C, were determined by means of the Evans method using TMS as internal standard. In order to obtain more information about the nature of the species in solution, the ¹H NMR experiment was repeated for each complex before and

after the addition of a large excess (50 equivalents) of deuterated pyridine (Pyr- d_5). The results are listed in Table 6.

Table 6 Effective magnetic moments μ_{eff} for the Fe(II) **11-13** and Fe(II) **14-16** complexes.

Complex	μ_{eff} (μ_{B}) ^a	
	Complex	Complex + Pyridine
11	5.60	5.70
12	2.60	4.65
13	4.95	5.48
14	2.49	4.72
15	4.85	4.89
16	4.54	4.61

a) Determined in CD_2Cl_2 solution at 30 °C using using TMS as internal standard. The value are calculated for a single metal centre.

Typical values of HS Fe(II) centres were observed for complexes **11** and **13**, explaining the ineffectiveness of the NMR experiments. A lower value was obtained in the case of the chlorine substituted **12**. However after the addition of pyridine, the magnetic moment increased up to 4.65 μ_{B} . This behaviour can be explained with the formation of a dimeric structure in the native form of **12**, in which an antiferromagnetic coupling of the two HS Fe(II) centres is responsible of the low observed value. It is worth noting that, as a consequence of the addition of pyridine to the solutions, the signals of free THF (at 1.90 and 3.80 ppm) appeared in all cases, indicating that THF is part of the coordination sphere of the complexes (see experimental section). Exactly the same observations were made for the Fe(III) complexes **14-16**, with the only difference that the variation of the magnetic moment was observed not in the case of the chlorine containing complex **15**, but for the methyl substituted complex **14**. Therefore, one can conclude that for complexes **12** and **14** the presence of pyridine induces the breaking of the dimeric structure formed in THF during the synthesis, while for all the others it just replace THF in the coordination sphere of the metal centre. On the basis of these considerations, the structure showed in Figure 46 are proposed. A similar dimeric-monomeric structure conversion was reported by Kleij *et al.* for a group of Fe(III) complexes bearing amino-triphenolate ligands. Even in that case a variation of the magnetic

moments in solution was observed, after the addition of pyridine, due to the breaking of the dimeric structure.⁶⁷

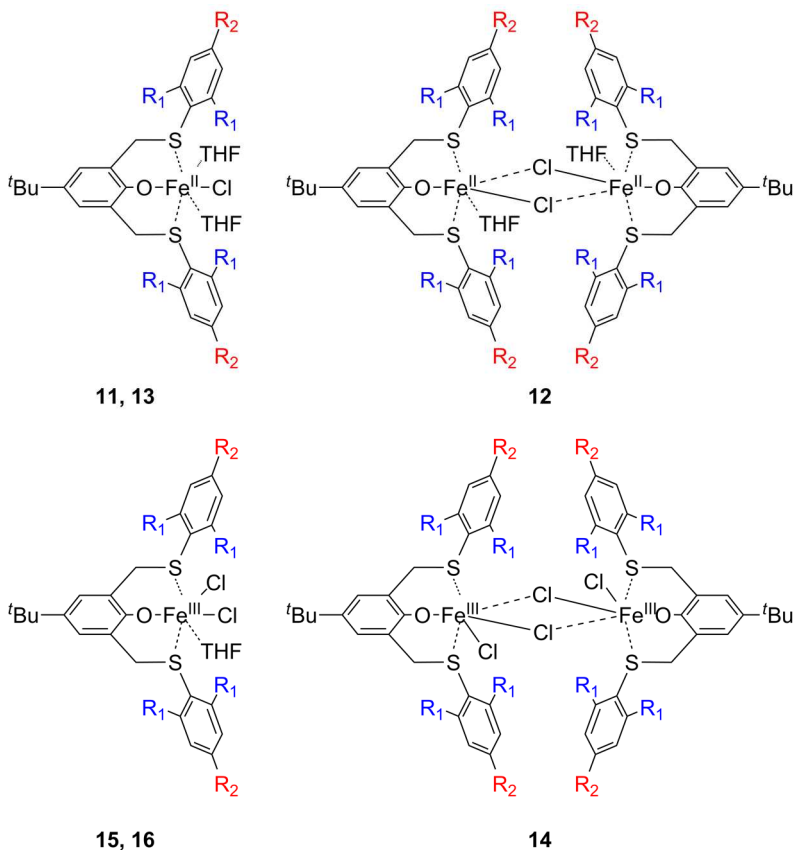


Figure 46 Proposed structure for the Fe(II) and Fe(III) complexes **11-16**.

4.2 Catalytic activity

The cycloaddition reaction of CO₂ to HO, without solvent, in the presence of **11** was selected as benchmark to find the best reaction conditions. As first, the reaction was performed, at 50 °C, 10 bar of CO₂ pressure and 0.1 mol% of **11**, using 0.1 mol% of different co-catalysts: DMAP, [PPN]Cl, TBAN₃, TBAC, TBAI and TBAB. The catalytic activity was determined on the basis of the conversion to the corresponding cyclic carbonate HC after 24 hours, and the results are shown in Figure 47a. The best performance was obtained in the presence of TBAB, with a TON of 110. An

enhancement of the TON at 185 was obtained increasing the amount of TBA up to 0.5 mol%. Further increasing the TBAB concentration to 1 mol% does not affect the course of the reaction.

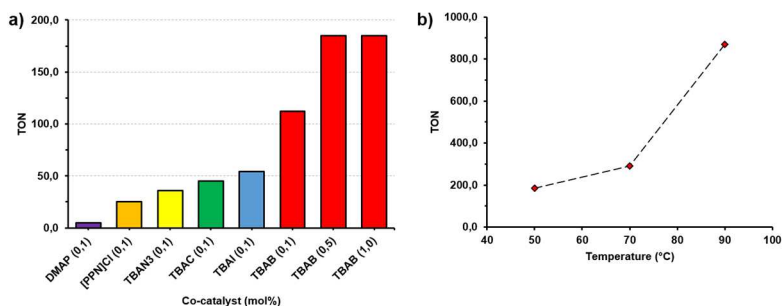


Figure 47 Effect of the co-catalyst type and loading (a) and temperature (b) on the catalytic activity of **11** in HO/CO₂ coupling (Table S 18).

The TON moderately increases passing from 50 to 70 °C, while at 90 °C a strong effect on the catalytic activity was observed, reaching a TON of 870 (Figure 47b). All the complexes **11-16** were finally tested under the same reaction conditions, namely at 90 °C, 10 bar CO₂ pressure, 0.1 mol% of catalyst and 0.5 mol% of TBAB (Table 7).

Table 7 Reaction of CO₂ with HO promoted by Fe(II) complexes **11-13** and Fe(III) complexes **14-16**.^a

Entry	Complex	Conversion ^b	TON ^c
1	11	87	870
2	12	35	350
3	13	41	410
4	14	77	770
5	15	76	760
6	16	77	770
7	-	10	-

a) Reaction conditions: HO = 3.0 mL, 24.9 mmol; catalyst = $2.5 \cdot 10^{-5}$ mol (0.1 mol%); TBAB = $1.25 \cdot 10^{-4}$ mol (0.5 mol%); P(CO₂) = 10 bar; reaction time = 24 h, neat. b) Determined by ¹H NMR using mesitylene as internal standard. The selectivity toward the formation of cyclic carbonate was always found to be >99%. c) Turnover number (mol_{carbonate} · mol_{Catalyst}⁻¹). d) Control experiment in the absence of the iron complex.

At a first glance, it appears evident that on the basis of the oxidation state of the iron centre the catalytic activity is differently influenced by the nature of the ligand structure. More into details, the most active of the Fe(II) species was the methyl substituted complex **11** (entry 1 Table 7). The presence of the bulkier iso-propyl groups, in the complex **12**, has a detrimental effect on the TON (entry 2 Table 7) probably rendering the coordination of the epoxide to the metal centre less favourable. The chlorine substituted complex **13** shows a TON near the that of **12** (entry 3 Table 7). This is reasonably due to the dimeric nature of the species in solution, as previously demonstrated by NMR Evans experiments. The same structure-reactivity correlation have been describe for the Fe(III) amino-triphenolate complexes, in which the dimeric catalyst was found to be less reactive that the one in the monomeric form.^{67b} Differently, for the Fe(III) complexes **14-16**, no dependence of the catalytic activity from the ligand structure was observed, with all of them showing almost the same TON (entries 4-6 Table 7). Notably the catalytic activity was the same even in the case of the complex **14**, that was found to exist in solution as a dimer.

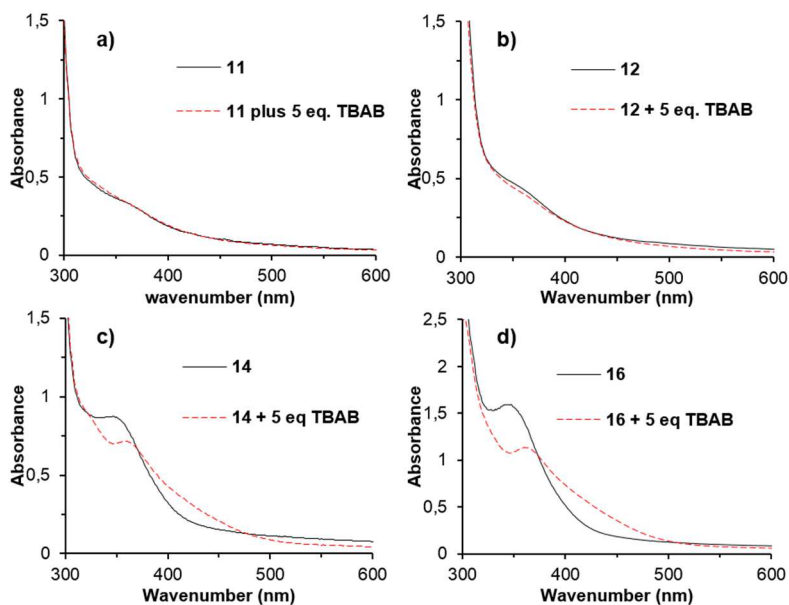


Figure 48 UV-Vis spectra of complexes **11**, **12**, **14** and **16** before and after the addition of TBAB.

With the aim to obtain further information on the catalytic active species, the UV-Visible spectrum of complexes were recorded before and after the addition of 5 equivalents of TBAB with respect to iron (Figure 48). Observing the spectrum profile for the Fe(II) complexes, no variation in the absorbance was detected after the addition of TBAB. Notably, for the dimeric complex **12**, the spectrum was not affected by the presence of the salt (Figure 48 **a** and **b**), indicating that the dimer remains stable in solution even in an excess of bromide anion. On the contrary, the interaction between TBAB and the Fe(III) complexes, was observed for both the dimeric and monomeric complexes **14** and **16** (Figure 48 **c** and **d**). As reported in chapter 3, describing the catalytic activity of [OSSO]-type Fe(III) complexes, this interaction can be ascribed to the formation of an anionic compound, deriving from the reaction of the complex with TBAB, that is actually the true catalytic species (Figure 49). It is worth noting that even in that case the catalytic activity was poorly influenced by the structure of the ligand.

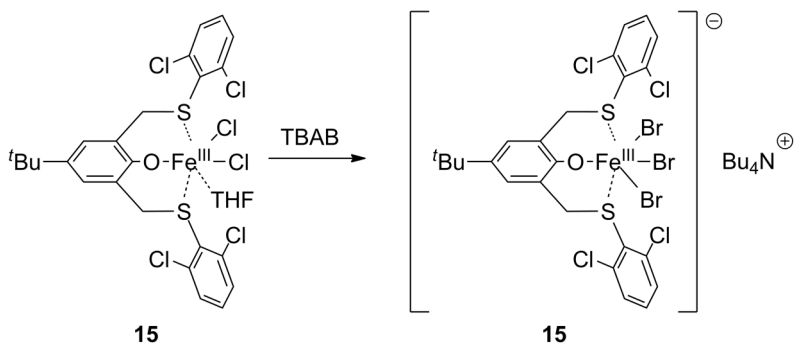
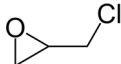
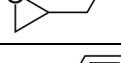
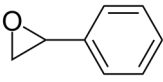
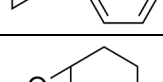
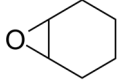
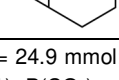


Figure 49 Formation of the anionic species [**15-Br₃**][⊖] in the presence of TBAB.

On the basis of the results described above, it appears that a prominent role in the determination of the catalytic activity is played by the steric encumbrance around the catalytic site, instead of the oxidation state of the iron centre. Indeed, in the case of the Fe(II) complexes **11-13**, the highest activity was observed for the less encumbered catalyst **11**, while sterically encumbered **12** and the stable dimeric complex **13** was found to be much less reactive. In the case of the Fe(III) based complexes **14-16**, TONs near to that of recorded for **11** were observed in all cases, because the bromide anion of TBAB was transferred to the metal centres with the *in situ*

formation of the monomeric catalytic species, even in the case of the dimeric complex **14**. Therefore, under the same conditions and similar coordination sphere, the catalytic activity does not convey the oxidation state of the iron centre. Since the catalytic system **11**/TBAB resulted the most active in the formation of HC, it was tested in the reaction of carbon dioxide with other epoxides. The same reactions were also conducted using the Fe(III) complex **14**, bearing the same methyl substituted ligand, for comparison. The results are listed in Table 8.

Table 8 Cyclic organic carbonates formation promoted by complexes **11** and **14**.^a

Entry	Complex	Epoxide	Conversion ^b	TON ^c
1	11		>99	1000
2	14		>99	1000
3	11		65	650
4	14		69	690
5	11		35	760
6	14		37	770

a) Reaction conditions: Epoxyde = 24.9 mmol; catalyst = $2.5 \cdot 10^{-5}$ mol (0.1 mol%); TBAB = $1.25 \cdot 10^{-4}$ mol (0.5 mol%); $P(\text{CO}_2)$ = 10 bar; reaction time = 24 h, neat. b) Determined by ^1H NMR using mesitylene as internal standard. The selectivity toward the formation of cyclic carbonate was always found to be >99%. c) Turnover number ($\text{mol}_{\text{carbonate}} \cdot \text{mol}_{\text{Catalyst}}^{-1}$).

The complete conversion of epichlorohydrin was obtained in both cases (entries 1 and 2 Table 8). Comparable activities were observed in the formation of styrene carbonate (entries 3 and 4 Table 8) and cyclohexene carbonate (entries 5 and 6 Table 8). In the last case, a total selectivity toward the formation of *cis*-CHC was achieved.

4.3 Conclusions

We have described the synthesis and the complete characterization of three new bis-thioether phenolate ligands (**L11-13**), and of the corresponding Fe(II) and complexes Fe(III) (**11-16**). The formation of monomeric or dimeric structures depending on the ligand was confirmed by magnetic moments measurements. When activated by TBAB, all the complexes resulted active in the cycloaddition of CO_2 to HO. Insights on the factors influencing the reaction were obtained

by UV-Vis experiments, and comparison of the catalytic activity. The obtained results suggest the oxidation state of the metal centre does play a prominent role into the modulation of the catalytic activity.

4.4 Experimental section

General considerations

All manipulation involving air- and/or moisture-sensitive compounds were performed under nitrogen atmosphere using standard Schlenk technique and a MBraun glovebox. Toluene (99.5%; Sigma-Aldrich) and THF (99%; Sigma-Aldrich) were used as received or refluxed for 48 h over sodium or sodium ketyls and distilled before use for moisture- and oxygen-sensitive reactions. All other reagents were used as received (TCI or Sigma-Aldrich) or distilled under reduced pressure over calcium hydride. Deuterated solvents were purchased from Euriso-Top or Sigma-Aldrich and used as received. NMR spectra were collected on Bruker Avance spectrometers (600, 400, 300 or 250 MHz for ^1H): the chemical shifts were referenced to tetramethylsilane (TMS) as external reference using the residual protio signal of the deuterated solvents. Measurements of effective magnetic moments were performed on a Bruker Avance 400 MHz spectrometer at 25 °C in toluene-d8 using a 5 mm Wilmad coaxial insert NMR tube. Solutions of the iron complexes **11**, **12**, **13**, **14**, **15** and **16** in toluene-d8 with 1% (v/v) of TMS were prepared under nitrogen atmosphere. The effective magnetic moment (μ_{eff}) was calculated from $\mu_{\text{eff}} = 8\chi_{\text{g}}\text{MWT}$, where χ_{g} ($\text{cm}^3 \text{g}^{-1}$) is the corrected molar susceptibility derived from $\chi_{\text{g}} = 3\Delta f/4\pi f_0\text{CMW} + \chi_0$. Δf is the shift in frequency (Hz) of the residual protio signal of the solvent in the presence of the complex from the value of the pure solvent, C and MW are respectively the concentration (mol cm^{-3}) and the molecular weight of the complex (g mol^{-1}), f_0 is the operating frequency of the spectrometer (Hz), and χ_0 is the mass susceptibility of the pure solvent ($-0.6179 \times 10^{-6} \text{cm}^3 \text{g}^{-1}$ for toluene-d8). $4\pi/3$ is the shape factor for a cylindrical sample in a superconducting magnet. Elemental analysis was performed on a CHNS Thermo Scientific Flash EA 1112 equipped with a thermal conductivity detector. ESI-MS spectra were acquired on a Quattro microTM API triple quadrupole mass spectrometer from Waters equipped with electrospray ion source, using anhydrous acetonitrile as solvent. UV-

Vis spectra were collected on a PerkinElmer Lambda EZ 201 spectrophotometer.

Synthesis of the pro-ligand 4-*tert*-butyl-2,6-((2,6-dimethylthiophenyl)-phenol) L11 (Scheme 7)

A 100 mL flask equipped with a magnetic stirring bar was charged, under nitrogen atmosphere, with 2.46 g (18.0 mmol) of 2,6-dimethylbenzenthiole and THF (30 mL). A solution of *t*BuONa (1.72 g, 18.0 mmol) in THF (15 mL) was added to the flask dropwise. After 15 minutes, A solution of 2,6-bis-bromomethyl-4-*tert*-butyl-phenol (3.05 g, 9.0 mmol) in THF (30 mL) was added dropwise and the reaction was kept at room temperature overnight. The solvent was distilled off, water was added until dissolution of NaBr by-product and the aqueous phase extracted twice with methylene chloride. The combined organic phases were dried with Na₂SO₄. After evaporation of the solvent, the pure product was obtained by crystallization from acetonitrile solution at -20 °C. Yield: 2.80 g, 69%. Mass spectrum: 473.1949 m/z (MNa⁺, calc: 473.1943), 923.4006 m/z (M₂Na⁺, calc. 923.3994).

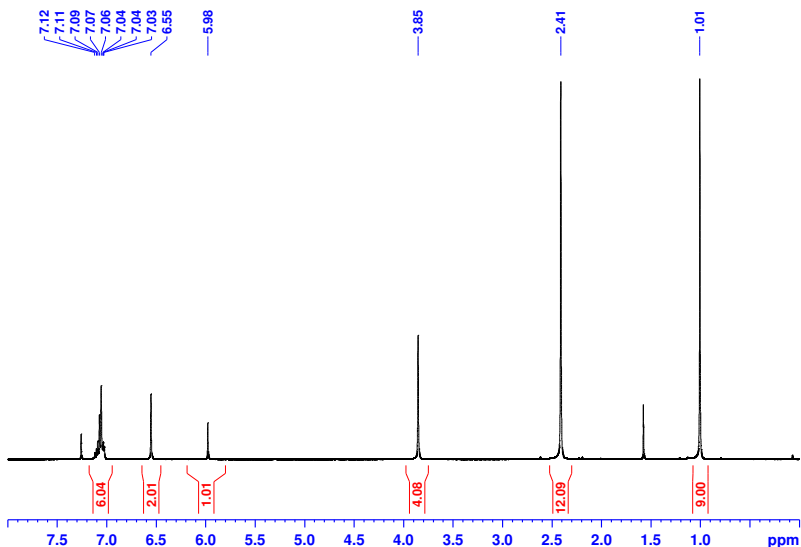


Figure S 98 ¹H NMR of pro-ligand L11 (CDCl₃, 300 MHz).

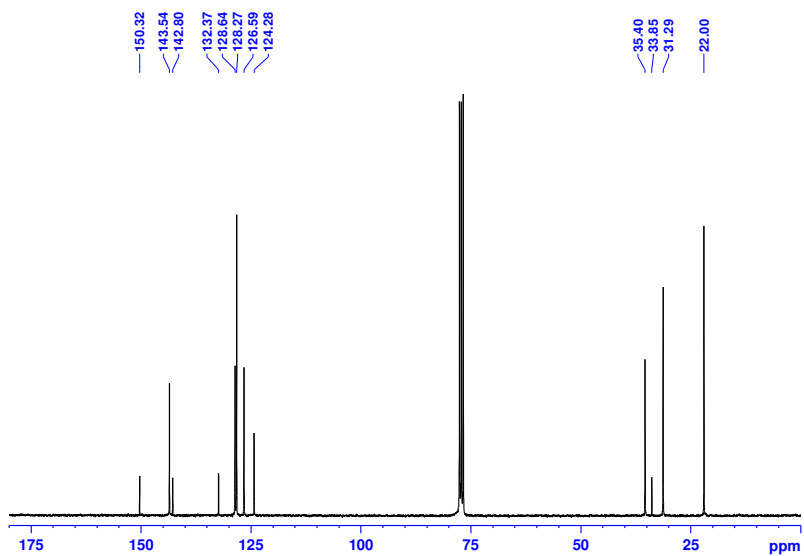


Figure S 99 ^{13}C NMR of pro-ligand **L11** (CDCl_3 , 300 MHz).

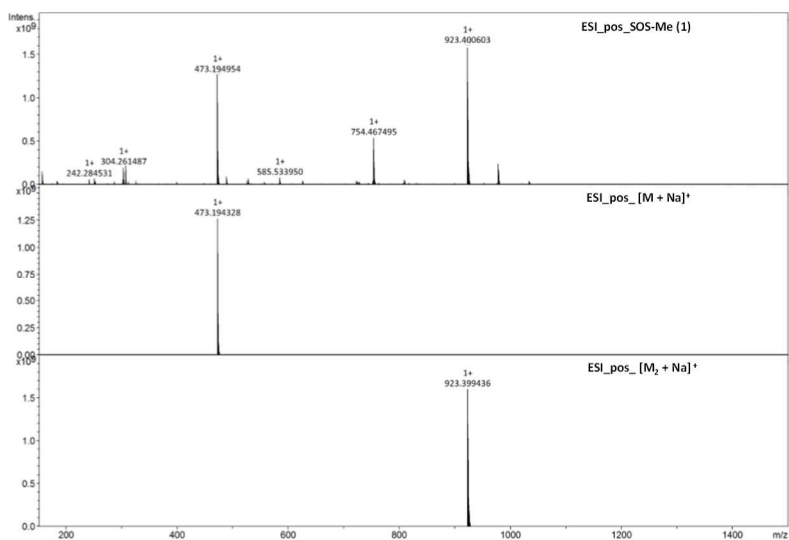


Figure S 100 HR ESI-MS of pro-ligand **L11**.

Synthesis of the pro-ligand 4-*tert*-butyl-2,6-((2,6-dichloro)thiophenyl)-phenol **L12** (Scheme 7)

A 100 mL flask equipped with a magnetic stirring bar was charged, under nitrogen atmosphere, with 2.00 g (11.2 mmol) of 2,6-dichlorobenzenthiol and THF (20 mL). A solution of *t*BuONa (1.08 g, 11.2 mmol) in THF (10 mL) was added to the flask dropwise. After 15 minutes, A solution of 2,6-bis-bromomethyl-4-*tert*-butyl-phenol (1.90 g, 5.6 mmol) in THF (20 mL) was added dropwise and the reaction was kept at room temperature overnight. The solvent was distilled off, water was added until dissolution of NaBr by-product and the aqueous phase extracted twice with methylene chloride. The combined organic phases were dried with Na₂SO₄. After evaporation of the solvent, the pure product was obtained by crystallization from pentane solution. Yield: 2.34 g, 80%. Mass spectrum: 554.9744 m/z (MNa⁺, calc: 554.9728), 1086.9610 m/z (M₂Na⁺, calc. 1086.9574).

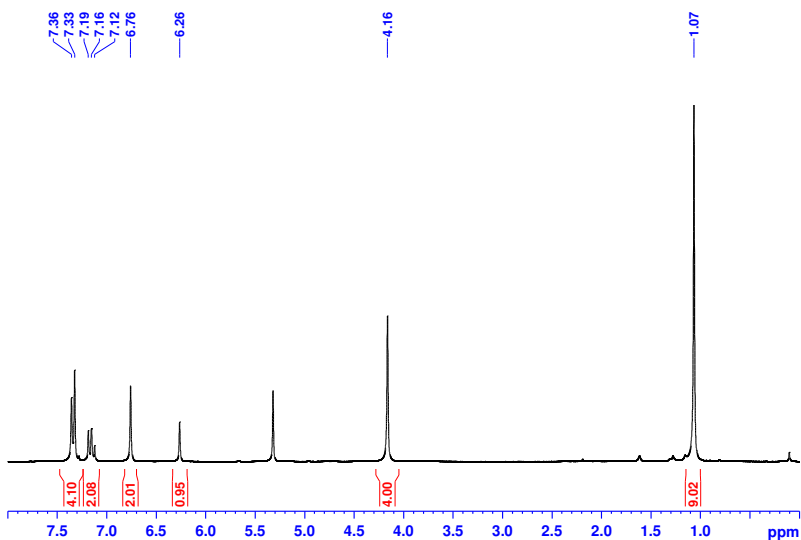


Figure S 101 ¹H NMR of pro-ligand **L12** (CD₂Cl₂, 300 MHz).

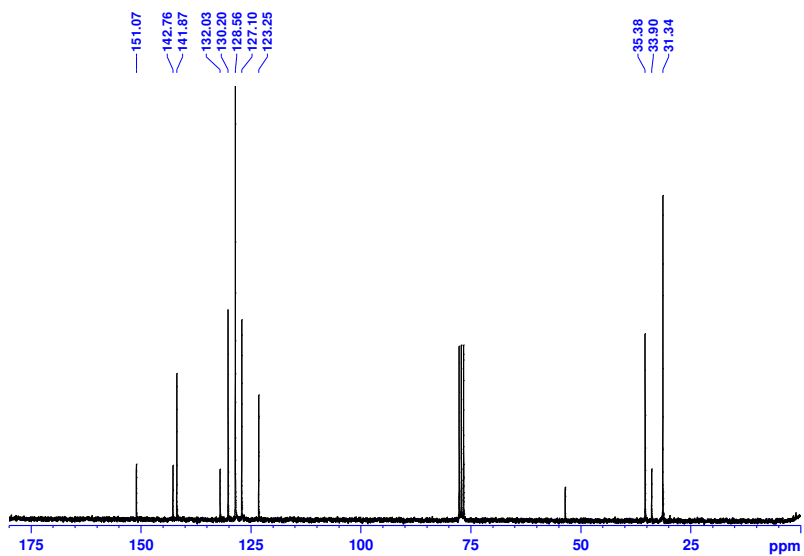


Figure S 102 ^{13}C NMR of pro-ligand **L12** (CDCl_3 , 300 MHz).

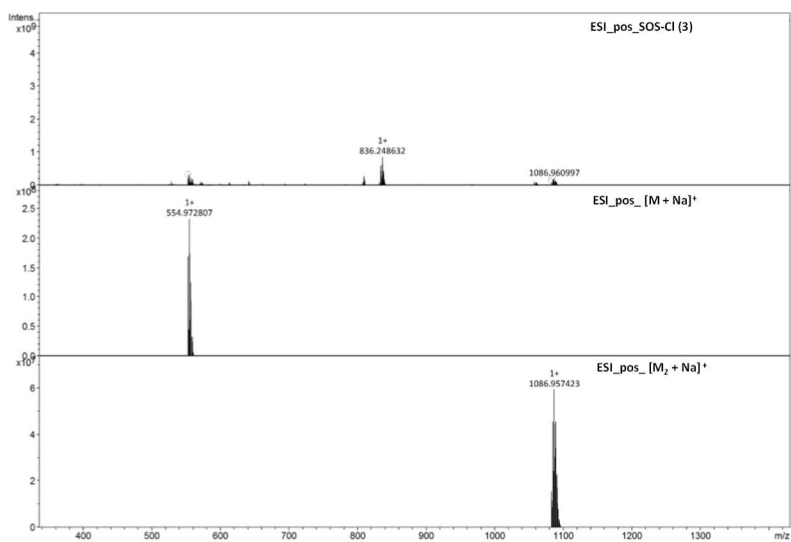


Figure S 103 HR ESI-MS of pro-ligand **L12**.

Synthesis of the pro-ligand 4-*tetr*-butyl-2,6-((2,4,6-tri-*iso*-propyl)thiophenyl)-phenol **L13** (Scheme 7)

A 100 mL flask equipped with a magnetic stirring bar was charged, under nitrogen atmosphere, with 4.03 g (17.0 mmol) of 2,4,6-tri-*iso*-propylbenzenthiole and THF (30 mL). A solution of *t*BuONa (1.64 g, 17.0 mmol) in THF (15 mL) was added to the flask dropwise. After 15 minutes, A solution of 2,6-bis-bromomethyl-4-*tert*-butyl-phenol (2.86 g, 8.5 mmol) in THF (30 mL) was added dropwise and the reaction was kept at room temperature overnight. The solvent was distilled off, water was added until dissolution of NaBr by-product and the aqueous phase extracted twice with methylene chloride. The combined organic phases were dried with Na₂SO₄. After evaporation of the solvent, the pure product was obtained by crystallization from pentane solution. Yield: 3.52 g, 65%. Mass spectrum: 669.4148 m/z (MNa⁺, calc: 669.4134), 1315.8441 m/z (M₂Na⁺, calc. 1315.8376).

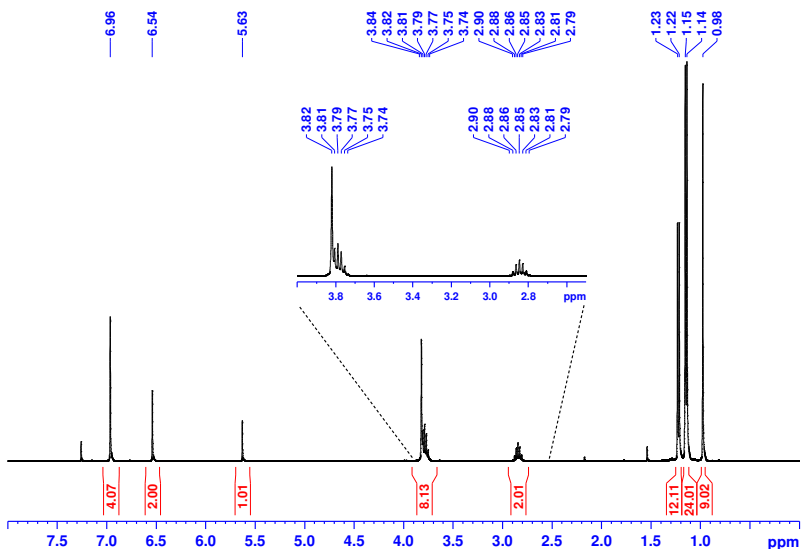


Figure S ¹⁰⁴H NMR of pro-ligand **L13** (CDCl₃, 400 MHz).

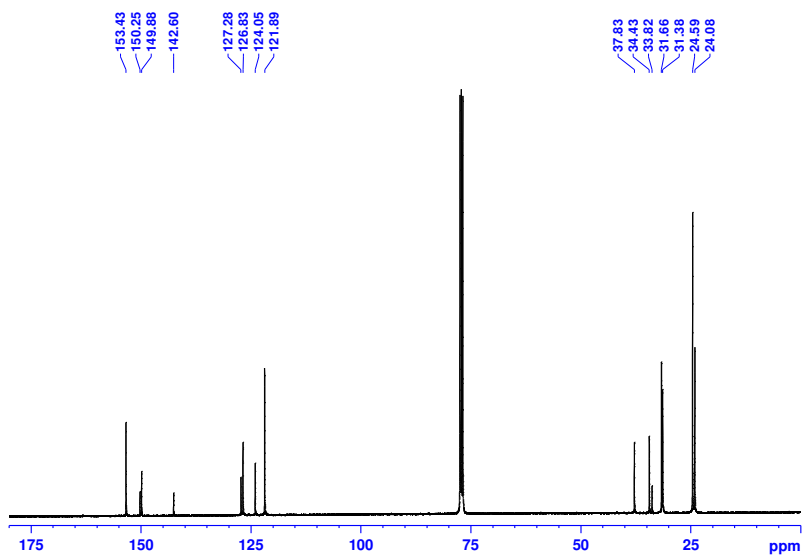


Figure S 105 ^{13}C NMR of pro-ligand **L13** (CDCl_3 , 400 MHz).

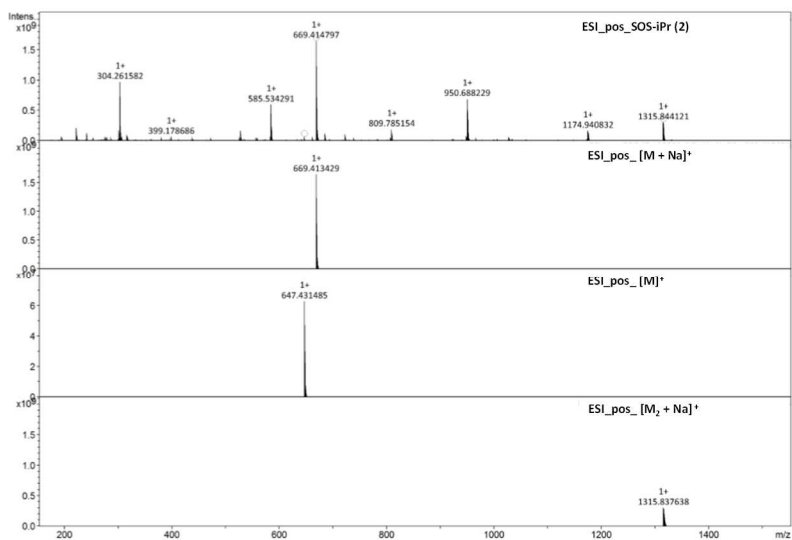


Figure S 106 HR ESI-MS of pro-ligand **L13**.

Synthesis of the iron(II) complex 11 (Scheme 9)

Pro-ligand **L11** (0.5026 g; 1.11 mmol) was dissolved in THF (40 mL). The solution was added to a suspension of sodium hydride (47.6 mg; 1.89 mmol) in THF (10 mL) and the mixture stirred at room temperature overnight. The resulting suspension was filtered through celite and slowly added at room temperature to 0.1372 g of anhydrous iron(II) chloride (1.08 mmol) dissolved in 40 mL of THF. The reaction was kept overnight. The mixture was then filtered through celite and the solvent removed under reduced pressure. The solid was washed with hexane and dried in vacuum, affording a gray solid. Yield: 0.41 g, 65 %.

Synthesis of the iron(II) complex 12 (Scheme 9)

Pro-ligand **L12** (0.5012 g; 0.94 mmol) was dissolved in THF (35 mL). The solution was added to a suspension of sodium hydride (40.1 mg; 1.59 mmol) in THF (10 mL) and the mixture stirred at room temperature overnight. The resulting suspension was filtered through celite and slowly added at room temperature to 0.1162 g of anhydrous iron(II) chloride (0.92 mmol) dissolved in 35 mL of THF. The reaction was kept overnight. The mixture was then filtered through celite and the solvent removed under reduced pressure. The solid was washed with hexane and dried in vacuum, affording a gray solid. Yield: 0.43 g, 75 %.

Synthesis of the iron(II) complex 13 (Scheme 9)

Pro-ligand **L13** (0.5002 g; 0.77 mmol) was dissolved in THF (30 mL). The solution was added to a suspension of sodium hydride (36.9 mg; 1.54 mmol) in THF (5 mL) and the mixture stirred at room temperature overnight. The resulting suspension was filtered through celite and slowly added at room temperature to 97.0 mg of anhydrous iron(II) chloride (0.76 mmol) dissolved in 30 mL of THF. The reaction was kept overnight. The mixture was then filtered through celite and the solvent removed under reduced pressure. The solid was washed with hexane and dried in vacuum, affording a dark-gray solid. Yield: 0.36 g, 64 %.

Synthesis of the iron(III) complex 14 (Scheme 9)

Pro-ligand **L11** (0.5052 g; 1.12 mmol) was dissolved in THF (40 mL). The solution was added to a suspension of sodium hydride (54.6 mg;

2.16 mmol) in THF (10 mL) and the mixture stirred at room temperature overnight. The resulting suspension was filtered through celite and slowly added at room temperature to 0.1772 g of anhydrous iron(III) chloride (1.09 mmol) dissolved in 40 mL of THF. The reaction was kept overnight. The mixture was then filtered through celite and the solvent removed under reduced pressure. The solid was washed with hexane and dried in vacuum, affording a dark solid. Yield: 0.47 g, 75 %.

Synthesis of the iron(III) complex 15 (Scheme 9)

Pro-ligand **L12** (0.5016 g; 0.94 mmol) was dissolved in THF (30 mL). The solution was added to a suspension of sodium hydride (41.4 mg; 1.64 mmol) in THF (10 mL) and the mixture stirred at room temperature overnight. The resulting suspension was filtered through celite and slowly added at room temperature to 0.1485 g of anhydrous iron(III) chloride (0.91 mmol) dissolved in 30 mL of THF. The reaction was kept overnight. The mixture was then filtered through celite and the solvent removed under reduced pressure. The solid was washed with hexane and dried in vacuum, affording a dark solid. Yield: 0.52 g, 85 %.

Synthesis of the iron(III) complex 16 (Scheme 9)

Pro-ligand **L13** (0.5062 g; 0.78 mmol) was dissolved in THF (25 mL). The solution was added to a suspension of sodium hydride (34.1 mg; 1.41 mmol) in THF (5 mL) and the mixture stirred at room temperature overnight. The resulting suspension was filtered through celite and slowly added at room temperature to 0.1233 g of anhydrous iron(III) chloride (0.76 mmol) dissolved in 25 mL of THF. The reaction was kept overnight. The mixture was then filtered through celite and the solvent removed under reduced pressure. The solid was washed with hexane and dried in vacuum, affording a dark solid. Yield: 0.44 g, 75 %.

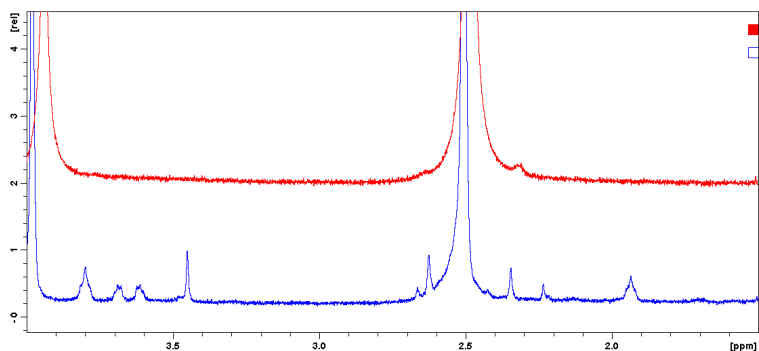


Figure S 107 ^1H NMR spectra of Fe(II) complex **11**, in the region from 1.5 to 4.0 ppm, before (red) and after (blue) the addition of 50 eq of deuterated pyridine (CD_2Cl_2 , 30 $^\circ\text{C}$, 400 MHz).

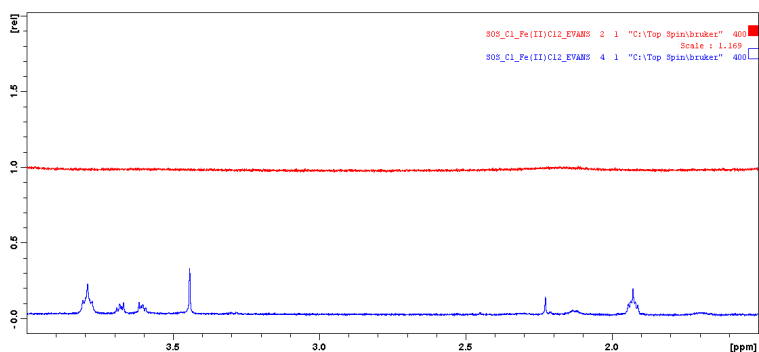


Figure S 108 ^1H NMR spectra of Fe(II) complex **12**, in the region from 1.5 to 4.0 ppm, before (red) and after (blue) the addition of 50 eq of deuterated pyridine (CD_2Cl_2 , 30 $^\circ\text{C}$, 400 MHz).

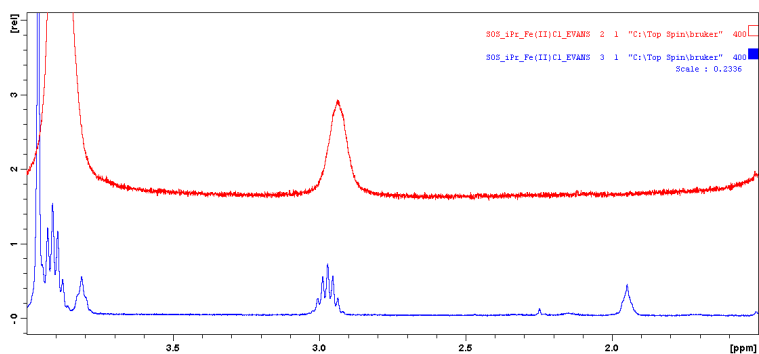


Figure S 109 ^1H NMR spectra of Fe(II) complex **13**, in the region from 1.5 to 4.0 ppm, before (red) and after (blue) the addition of 50 eq of deuterated pyridine (CD_2Cl_2 , 30 $^\circ\text{C}$, 400 MHz).

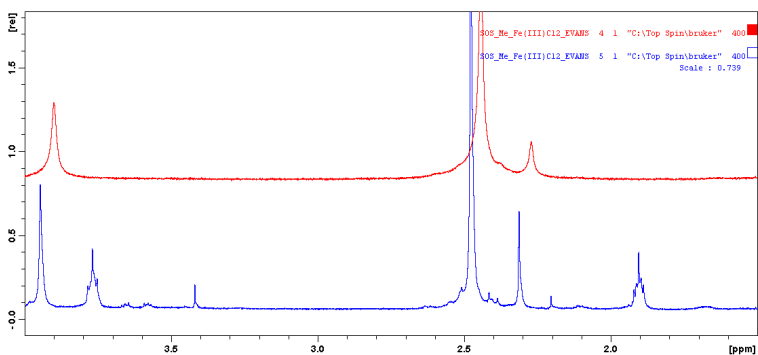


Figure S 110 ^1H NMR spectra of Fe(III) complex **14**, in the region from 1.5 to 4.0 ppm, before (red) and after (blue) the addition of 50 eq of deuterated pyridine (CD_2Cl_2 , 30 $^\circ\text{C}$, 400 MHz).

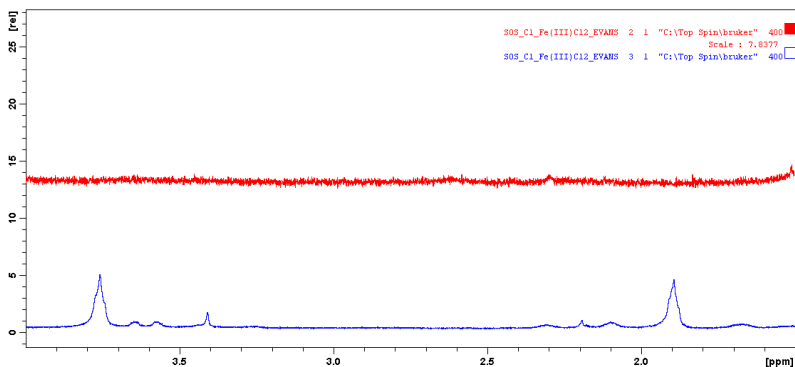


Figure S 111 ^1H NMR spectra of Fe(III) complex **15**, in the region from 1.5 to 4.0 ppm, before (red) and after (blue) the addition of 50 eq of deuterated pyridine (CD_2Cl_2 , 30 $^\circ\text{C}$, 400 MHz).

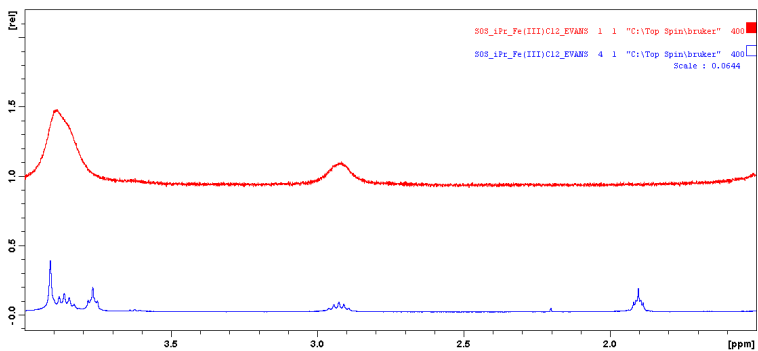
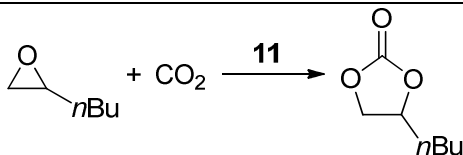


Figure S 112 ^1H NMR spectra of Fe(III) complex **16**, in the region from 1.5 to 4.0 ppm, before (red) and after (blue) the addition of 50 eq of deuterated pyridine (CD_2Cl_2 , 30 $^\circ\text{C}$, 400 MHz).

Catalytic tests

Table S 18 Hexene carbonate formation promoted by the Fe(II) complex **11**.^a



Entry	Co-catalyst	Temperature		Conversion ^b	TON ^c	TOF ^d
		mol%	°C			
S1	DMAP	0.1	50	0.5	5	0.2
S2	[PPN]Cl	0.1	50	2.5	25	1.0
S3	TBAN ₃	0.1	50	3.6	36	1.5
S4	TBAC	0.1	50	4.5	45	1.9
S5	TBAI	0.1	50	5.4	54	2.3
S6	TBAB	0.1	50	11.2	112	4.7
S7	TBAB	0.5	50	18.5	185	7.7
S8	TBAB	1.0	50	18.5	185	7.7
S9	TBAB	0.5	70	29	290	12.1
S10	TBAB	0.5	90	87	870	36.3
S11 ^e	TBAB	0.1	50	0.5	-	-
S12 ^e	TBAB	1.0	50	3.0	-	-
S13 ^e	TBAB	0.5	90	10	-	-

^aReaction conditions: HO = 3.0 mL, 24.9 mmol; **11** = 2.5 · 10⁻⁵ mol (0.1 mol%); P(CO₂) = 10 bar; reaction time = 24 h, neat. ^bDetermined by ¹H NMR using mesitylene as internal standard. The selectivity toward the formation of cyclic carbonate was always found to be >99%. ^cTurnover number (mol_{carbonate} · mol_{catalyst}⁻¹). ^dTurnover frequency (mol_{carbonate} · mol_{catalyst}⁻¹ · reaction time⁻¹). ^eControl experiment in the absence of the Fe(II) complex.

4.5 References

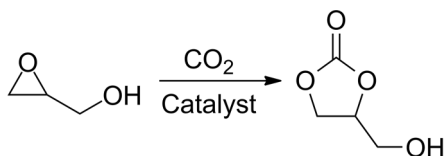
⁶⁶ Wurster J., Liotta D. C., Wang, J., Wilson, L. J., Patent No: 5602245, 11/1997; Appl. No: 970691.

⁶⁷ a) Whiteoak C. J., Martin E., Martínez Belmonte M., Benet-Buchholz J., Kleij A. W., *Adv. Synth. Catal.*, **2012**, *354*, 469-476. b) Whiteoak C. J., Gjoka B., Martin E., Martínez Belmonte M., Escudero-Adán E. C., Zonta C., Licini G., Kleij A. W., *Inorg. Chem.* **2012**, *51*, 10639-10649.

5 The particular case of glycidol in the coupling reaction with CO₂

5.1 Glycerol carbonate

In the last decade, parallel to the development of CO₂ chemistry, the increasing production of biodiesel from vegetable oils has offered to the market a new cheap raw material: glycerol. The decrease of the glycerol price has triggered a growing interest not only in the new possible use of this product, but also in the development of processes for the efficient conversion of this molecule to valuable commodity chemicals in both academic and industrial environments.⁶⁸ Among the possible glycerol derivatives, glycerol carbonate (GC) is a particularly interesting target because, owing to its physical properties, GC has potential application as low volatile organic compounds (VOCs), a bio-based alternative to organic solvents from a non-renewable resource. Furthermore, the presence in the GC skeleton of both a hydroxyl group and a 2-oxo-1,3-dioxolane group renders this molecule a major candidate as chemical intermediate for the synthesis of other value added products.⁶⁹ Actually, the most covered routes from glycerol to GC involve the reaction of glycerol with phosgene or its transesterification with alkyl carbonates.⁷⁰ More recently, the direct carboxylation of glycerol⁷¹ and the glycerolysis of urea⁷² in the presence of heterogeneous catalysts were also achieved. Nevertheless these synthetic approaches often require the use of highly toxic (COCl₂) or highly inflammable reactants (CO), harsh reaction conditions and in many cases present a low selectivity to the desired product. A 100% atom economical and environmental friendly way to produce GC is the cycloaddition of CO₂ to glycidol (Scheme 10).



Scheme 10 Synthesis of glycerol carbonate (GC) from glycidol and CO₂.

This reaction has been reported to be promoted by several catalytic systems based on transition metal complexes⁷³ and in some case on

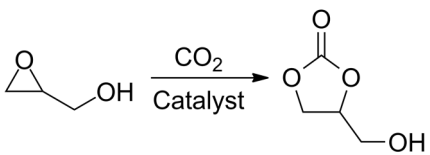
polyphenols as organocatalysts.⁷⁴ Very recently a new and high efficient route for the production of glycidol from 2-chloro-1,3-propanediol, a by-product in the epichlorohydrin production plant, was reported offering an economical and feasible way to obtain glycidol.⁷⁵ It is worth noting that differently to other epoxides, glycidol, owing to the presence of an hydroxyl functionality, can also act as hydrogen-bond donor. In other words, glycidol seems to be a non-innocent substrate with the possibility of playing the double role of reagent and catalyst.

5.2 Cycloaddition of CO₂ to glycidol

In our ongoing search for active catalysts for the coupling of CO₂ with epoxides [17g–i] we have noticed that glycidol is sensibly more reactive than other epoxides [e.g., propylene oxide (PO)]. To get deeper insights into the reaction of glycidol with CO₂, we decided to investigate the reaction in the presence of bis-(triphenylphosphine)-iminium chloride and various ammonium salts. The main results, reported in Table 9, clearly show the efficient conversion (70–85%) of this substrate to the desired product under mild, solventless conditions (T = 80 °C, P(CO₂) = 10 bar). Among the promoters investigated (entry 1-4, Table 9), tetrabutylammonium bromide (TBAB) resulted the most efficient. Noteworthy, the low TBAB loading (1 mol% of TBAB, entry 4, Table 9) and the reaction time required (t = 1 h) for the high conversion (85%) of the substrate are by far more favourable than those reported for other ammonium salts with conventional epoxides, such as PO and cyclohexene oxide (CHO).⁷⁶ When the reaction temperature was decreased below 60 °C, the epoxide conversion was negligible under the same reaction conditions (entries 6 and 7, Table 9). On the other hand, by increasing the TBAB loading to 5%, it is possible to reach the complete conversion (>99%) in only 3 h at 60 °C. Notably a good conversion to GC is still possible under very mild reaction conditions (40 °C, P(CO₂) = 1 bar, entry 12, Table 9). For comparison, methylglycidyl ether (entry 13, Table 9) and PO (entry 14, Table 9) yielded a much lower conversion. With the aim to shed more light on the mechanism underlying the facile conversion of glycidol to GC, the reaction path was investigated by density functional theory (DFT) calculations. According to the previous DFT studies on the cycloaddition reaction of CO₂ to epoxides in presence of quaternary

ammonium salts, the reaction route was assumed to be composed by three consecutive elementary steps: 1) epoxide ring opening; 2) CO₂ insertion; 3) ring closure of cyclic carbonate.

Table 9 Cycloaddition of CO₂ to glycidol.



Entry ^a	Catalyst	Temperature		Conversion ^b
		mol %	°C	
1	[PPN]Cl	1.0	80	70
2	TBAC	1.0	80	80
3	TBAI	1.0	80	82
4	TBAB	1.0	80	85
5	TBAB	1.0	60	51
6	TBAB	1.0	40	12
7 ^e	TBAB	1.0	20	2
8	TBAB	3.0	40	30
9	TBAB	5.0	40	40
10 ^c	TBAB	5.0	40	87
11 ^c	TBAB	5.0	60	>99
12 ^d	TBAB	5.0	40	52
13 ^{c,e}	TBAB	5.0	60	12
14 ^{c,f}	TBAB	5.0	60	4

a) Reaction conditions: glycidol=75.4 mmol, P(CO₂) = 10 bar, t = 1 h, neat. b) Determined by ¹H NMR using tetrachloroethane as internal standard; the observed selectivity was always >99%. c) t = 3 h. d) P(CO₂) = balloon, t =24 h. e) Methyl glycidyl ether as substrate. f) Propylene oxide as substrate.

The free energy profile along the reaction coordinate is depicted in Figure 50. The contribution of the tetrabutylammonium (TBA) cation was neglected in analogy to previous calculations on the CO₂

coupling promoted by TBAB in presence of a hydrogen-bond activator.⁷⁷ The reaction starts with the nucleophilic attack of bromide anion to the C₃ atom of glycidol, leading to the opening of the oxirane ring through the transition state **AB** (**TS-AB**) with a barrier of 12.4 kcal/mol. The reaction is not regioselective because the nucleophilic attack of bromide anion to the C₂ atom proceeds with a slight higher activation barrier (13.7 kcal/mol, see Figure S 113). In the following step, the nucleophilic attack of the alkoxy intermediate **B** to CO₂ leads to the hemicarboxylate intermediate **C** through a barrier-less reaction pathway in agreement with a previous DFT investigation on similar systems.^{76d}

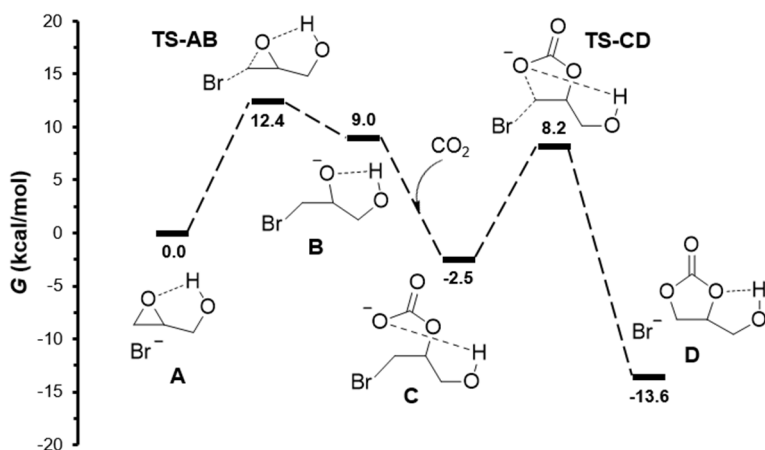


Figure 50 Computed free energy surface for the cycloaddition of CO₂ to glycidol promoted by TBAB. Free energies are given in kcal/mol.

The scan of the energy surface corresponding to the approach of the CO₂ to the oxy anion of intermediate **B** revealed that the energy continues to decrease as the O_{oxy}-C_{CO2} distance is shortened without any saddle point, supporting that the binding of the CO₂ to intermediate **B** is a barrier-less process (see Figure S 114). Finally, intermediate **C** converts into GC through an intramolecular ring-closure reaction that occurs via **TS-CD** with a barrier of 8.2 kcal/mol. The total reaction is exergonic by 13.6 kcal/mol as compared to the reactants. In this reaction path all intermediates and TSs are involved in an intramolecular hydrogen bond formed between the oxygen atom of the oxirane ring or the oxygen atom of the carboxy group and hydrogen atom of hydroxyl group.

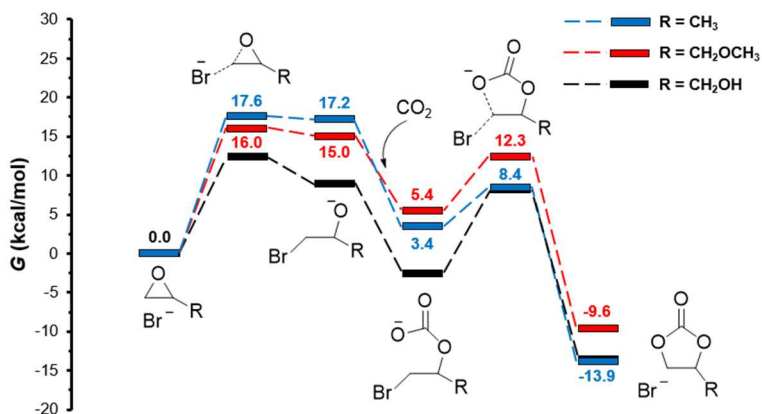


Figure 51 Relative free energy profiles for the cycloaddition of CO_2 to methyl glycidyl ether (red path) and propylene oxide (blue path). The reaction profile for glycidol (black path) is also reported for comparative purposes. Free energies are given in kcal/mol.

To address the importance of the intramolecular hydrogen bonds, we evaluated the Gibbs free energy profile for the same reaction path for PO and methyl glycidyl ether (Figure 51). In all cases, the rate-determining step was the nucleophilic attack of the bromide anion to the epoxide ring, the relative activation energy increases in the order glycidol (12.4 kcal/mol) < methyl glycidyl ether (16.0 kcal/mol) < PO (17.6 kcal/mol). Moreover the formation of the first and second intermediates in the case of the methyl glycidyl ether and PO is thermodynamically less favoured compared to the case of glycidol. Thus the hydroxyl group is involved in the activation of the epoxide opening and in the stabilization of the two negatively charged intermediates. The trend emerging from our calculations is fully in agreement with the activities experimentally observed for these substrates. Subsequently we explored the influence of the hydrogen bond between the hydroxyl group of a second non-reactive molecule of glycidol and the bromide anion. In this case we found that the epoxide ring opening steps requires overcoming a barrier of 16.2 kcal/mol (see Figure S 115). This result suggests that the kinetics of the reaction do not overcome the stabilization effect of the second hydrogen bond involving the bromide anion. With its two hydrogen bond contacts, the oxygen acceptor and hydroxy donor/acceptor, glycidol is capable of forming both intra and intermolecular hydrogen

bonds. In the latter case, the mutual hydrogen interactions lead to the formation of dimeric, trimeric, or larger cluster structures.

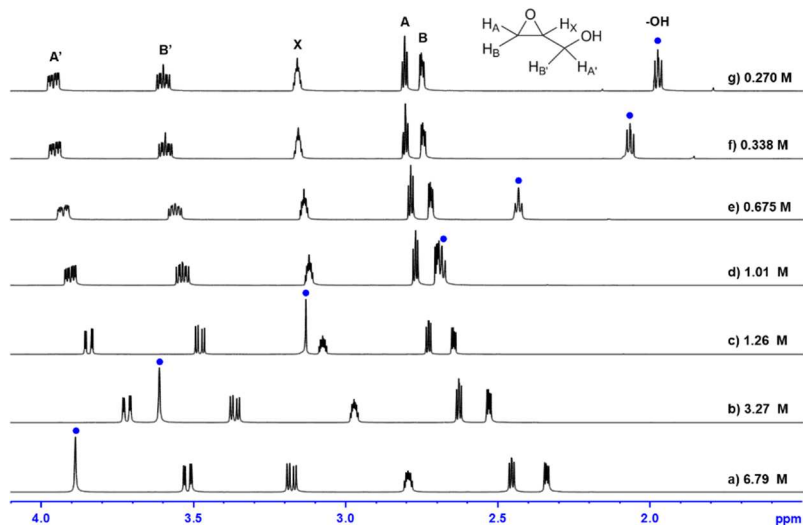
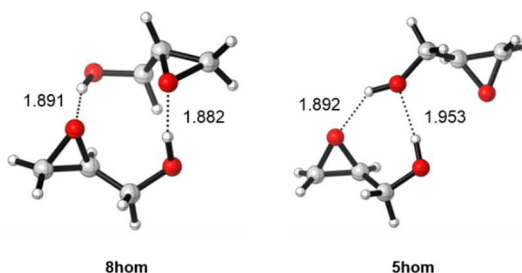


Figure 52 ^1H NMR spectra of glycidol at different concentrations (CDCl_3 ; 600 MHz). The symbol “•” indicates the hydroxyl signal.

Both theoretical and experimental studies highlighted the peculiar capability of glycidol in chiral self-recognition, that is, the ability of discriminating the same or the opposite enantiomer in the formation of aggregates via intermolecular interactions. Through vibrational circular dichroism and optical rotation measurements, it was established that at low concentration (0.2 M), the equilibrium reaction between the monomer and homochiral dimer is shifted toward the monomer, whereas at higher concentration (3.5 M), the predominant species is the homochiral dimer.⁷⁸ To get more information on the species present in neat liquid, we investigated the concentration dependence of the NMR proton resonances of glycidol. The drift of the chemical shifts is reported in Figure 52. In very dilute solution, the chemical shift of the hydroxyl proton (δ) in CDCl_3 is 1.57 ppm. As the concentration of glycidol increases, the resonance is significantly shifted upfield until 3.93 ppm in neat liquid. The δ of the alcoholic proton of glycidol at 3.27 M is very close to that of neat glycidol (3.61 vs. 3.93 ppm) suggesting that the dimer is the predominant species under the latter condition. Moreover nonlinear least-square analysis of the changes of the proton resonance signal of the hydroxyl group

shows a good fit to the monomer-dimer model ($R^2=0.983$) with a dimerization constant K_2 of about $0.54 \pm 0.10 \text{ M}^{-1}$ (see Figure S 116). Although not elevated, this values reflects the free energy gain when the system switches from an intra- to an inter-molecular hydrogen bond. Theoretical studies shed light on the structure of such a dimer; among the different conformations, the more stable ones are those in which the two monomers form reciprocal hydroxyl-ether hydrogen bonds, leading to eight-membered rings of heavy atoms (**8hom**, Scheme 11).⁷⁹



Scheme 11 Hydrogen-bond topology of eight-membered (**8hom**) and five-membered (**5hom**) ring structures of glycidol dimers.

Because the hydroxyl group can also act simultaneously as a hydrogen-bond donor and acceptor, stable conformers were also obtained in five-membered heavy atom ring structure and a dangling oxirane ring (**5hom**, Scheme 11). We used the structures reported in Scheme 11 to remodel the reaction path for the conversion of glycidol to GC, the free energy profiles along the reaction coordinate are reported in Figure 53. By comparing the different profiles, it results that the ring opening step is particularly affected by these strong intermolecular hydrogen bonds. As a matter of fact, for both dimers, the nucleophilic attack of the bromide anion to the C3 atom is predicted to occur with a lower activation barrier compared to that found for the monomeric glycidol. In particular, in the case of monomeric glycidol, the ring-opening step requires overcoming a barrier of 12.4 kcal/mol, whereas in the case of dimeric glycidol featuring the eight-membered heavy atom ring, the activation energy is determined to be 9.8 kcal/mol and in the case of the dimeric glycidol with the five-membered heavy atom ring, the activation energy is determined to be 8.1 kcal/mol.

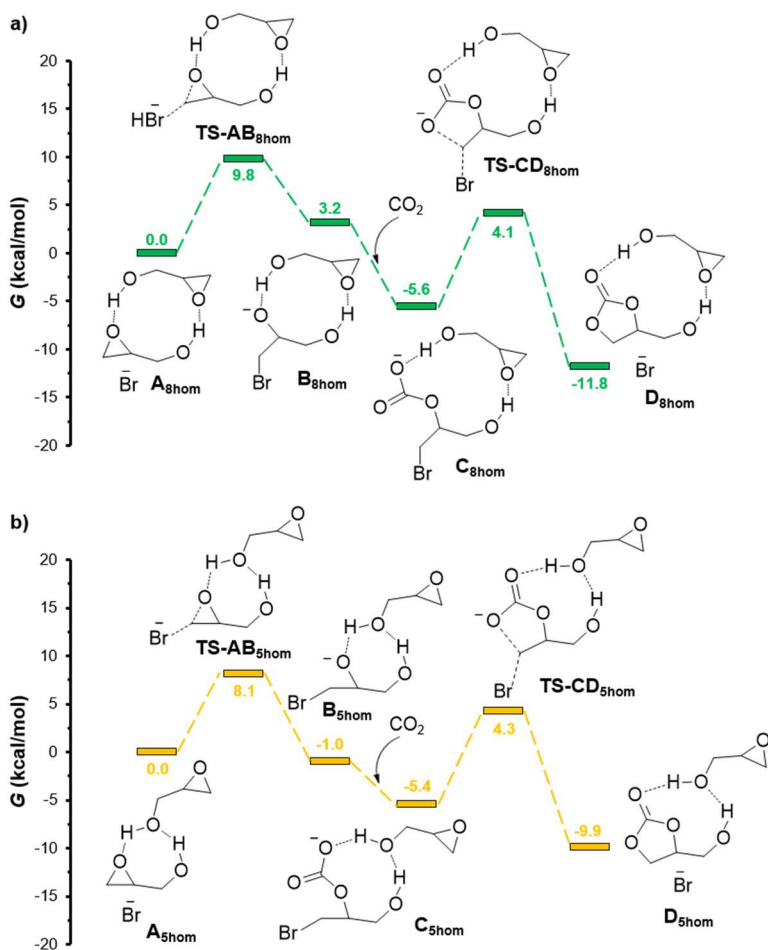


Figure 53 Relative free energy profiles for the cycloaddition of CO₂ to glycidol computed for the dimers of glycidol featuring the (a) eight-membered heavy atom ring (**8hom**) and (b) five-membered heavy atom ring (**5hom**). Free energies are given in kcal/mol.

It is worth noting that linear correlations between the height of these barriers and the geometric characteristics of the corresponding transition state structures (**TS-AB**, **TS-AB_{8hom}**, and **TS-AB_{5hom}**, Figure 54) can be found. In particular, the hydrogen bond distance between the oxy anion and the hydrogen of the hydroxyl group (d_{O-H} , Figure 54) becomes shorter (and stronger) in the series **TS-AB**, **TS-AB_{8hom}**, and **TS-AB_{5hom}**, with a corresponding decrease in the activation barrier. As d_{O-H} decreases, the distance between the oxy

anion and C₃ atom of the oxirane ring (d_{O-C} , Figure 54) decreases, and the distance between the C₃ atom of the oxirane ring and the bromide anion (d_{Br-C} , Figure 54) increases.

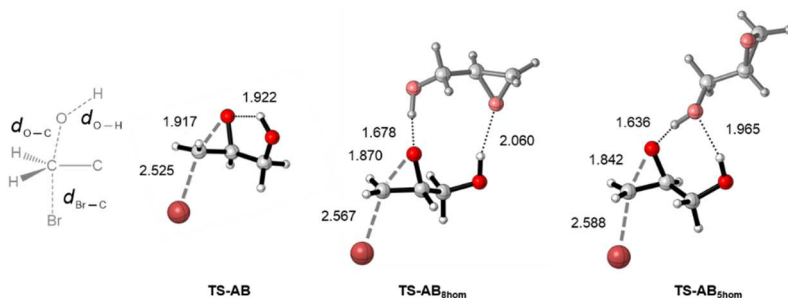


Figure 54 Transition state structures for the ring-opening step for monomer (**TS-AB**) and dimer of glycidol (**TS-AB_{5hom}** and **TS-AB_{8hom}**). Distances are given in Å.

Moreover, the alcoholate intermediate **B**, resulting from this step, is efficiently stabilized by the intermolecular hydrogen present in the dimeric structures. The relative energy of this intermediate follows the same order observed for the activation energies: decreasing from 9.0 kcal/mol obtained for the intermediate **B** of monomeric glycerol (Figure 50) to 3.2 kcal/mol for the same intermediate obtained in the dimer with the eight-membered heavy atom ring (**B_{8hom}**, Figure 53a) until reaching the value of -1.0 kcal/mol in the case of the dimer with the five-membered heavy atom ring (**B_{5hom}**, Figure 53b). In the last case, the formation of the intermediate is thermodynamically favoured. The ring-closure step is only slightly affected by these intermolecular hydrogen bonds. As a matter of fact, the hemicarboxylate intermediate formed after the CO₂ addition has to overcome a barrier of 10.7 kcal/mol when only an intramolecular hydrogen bond is present (Figure 50), and a barrier of 9.7 kcal/mol in the case where intermolecular hydrogen bonds are formed (Figure 53). By comparing the energetics of paths a and b in Figure 53, it can be observed that the barrier of the ring-opening of epoxide in path a is higher than that in path b by 1.7 kcal/mol, and the barrier of the ring closure of cyclic carbonate is the same for both the paths, which implies that the two intermolecular hydrogen-bond networks in the dimers of glycidol are equally effective in reducing the barriers for nucleophilic attack of the bromide anion to the epoxide ring.

Table 10 Cycloaddition of CO₂ to propylene oxide in the presence of glycidol and TBAB as catalytic system.

Entry ^a	Glycidol mol %	TBAB mol %	Temperature °C	Yield ^b %
1	1	1	50	15
2	1	1	60	40
3	1	1	70	66
4	1	1	80	83
5	-	1	80	30
6	3	3	60	63
7	5	5	60	84
8	-	5	60	16
9 ^c	5	5	60	85

a) Reaction conditions: PO = 71.5 mmol, P(CO₂) = 10 bar, t = 24 h, neat. b) Isolated yield, the observed selectivity was always >99%. c) GC in the place of glycidol.

Owing to the unique behaviour of glycidol in forming intermolecular hydrogen bonds, we envisaged the possibility to use this hydrogen-bond donor molecule as catalyst component, in combination with a nucleophile, for the conversion of other epoxides into the corresponding cyclic carbonates. Accordingly we used the binary system glycidol/TBAB as organocatalyst, for the conversion of PO to propylene carbonate (PC) as benchmark. The results reported in Table 10 clearly show that under the same reaction conditions the binary system is sensibly more active (entry 4, Table 10) compared to the use of TBAB alone (entry 5, Table 10). It is worth noting that under very mild conditions (T = 60 °C, P(CO₂) = 10 bar) PO can be converted to PC in very good yield (entry 7, Table 10).

Table 11 Cycloaddition of CO₂ to various epoxides in the presence of glycidol and TBAB as catalytic system.

Entry ^a	Epoxide	Conversion ^b %
1 ^c		26
2		31
3 ^d		83
4 ^e		85
5		57
6 ^f		76
7 ^{e,f}		19

a) Reaction conditions: epoxide = 71.5 mmol, glycidol = 1 mol%, TBAB = 1 mol%, P(CO₂) = 10 bar, T = 60 °C, t = 24 h, neat. b) Determined by ¹H NMR using mesitylene as internal standard, the observed selectivity was always >99%. The values in brackets are the conversions in the absence of glycidol. c) P(CO₂) = balloon. d) Glycidol = 5 mol%, TBAB = 5 mol%, t = 3 h. e) Glycidol = 5 mol%, TBAB = 5 mol%. f) Methyl ethyl ketone (MEK) = 10 mL.

Thus, under these reaction conditions, glycidol activates the PO towards the nucleophilic attack of the bromide and convert itself to GC, playing the double role of organocatalyst and substrate and rendering the recovery of the catalyst superfluous owing to the low catalyst loading and to the close chemical and physical properties of

the main product and GC. Indeed, under these reaction conditions one can expect that glycidol is firstly converted to GC and thus the true organocatalyst is the latter compound that also can act as hydrogen bond donor. As a matter of fact, the binary system GC/TBAB give the same results in term of conversion and selectivity than the binary system glycidol/TBAB supporting this hypothesis (compare entries 7 and 9, Table 10).

Finally, to test the activity of this new binary catalytic system to a wider family of substrates, we performed, under mild reaction conditions, the cycloaddition of CO₂ to a series of oxiranes (Table 11). All the substrates are converted into the corresponding carbonates in high to excellent yields. In particular, in the case of epichlorohydrin the presence of the electron withdrawing chlorine atom on the epoxy ring is beneficial giving the highest conversion observed. In addition the more challenging internal epoxide cyclohexene oxide is also converted in moderate yield that well compare with the most active organocatalysts.⁸⁰

5.3 Conclusions

A simple and efficient route to obtain glycerol carbonate (GC) was developed by coupling of glycidol with CO₂. Owing to the formation of hydrogen bonds between the glycidol molecules, this substrate behaves uniquely, playing the double role of substrate and catalyst in this reaction, allowing the synthesis of GC under metal-free, solvent-free, and rather mild reaction conditions (T = 60-80 °C, P(CO₂) = 1-10 bar) and short times (t = 1-3 h). The mechanism of the reaction was studied using density functional theory (DFT). The nucleophilic attack by the bromide anion was revealed to be the rate determining step. The hydroxyl group of glycerol, acting as a hydrogen-bond donor, serves to activate the epoxide for the ring opening and to stabilize the two negatively charged intermediates, and is thus essential for reaction rate. Analysis of the hydrogen-bond network revealed that the intermolecular hydrogen-bond interactions are particularly effective in facilitating the reaction pathway for the conversion of glycerol to GC. To extend the applicability of this substrate in the field of the CO₂ fixation reaction, we explored the possibility of using glycerol as a co-catalyst for the TBAB-catalysed cycloaddition. Actually, the binary system glycidol/TBAB can act as efficient organocatalyst for the conversion of diverse epoxides into

the corresponding cyclic carbonates in high-to-excellent yields under very mild conditions ($T = 60\text{-}80\text{ }^{\circ}\text{C}$, $P(\text{CO}_2) = 1\text{-}10\text{ bar}$). Finally the low catalyst loading and the fact that the glycidol is also converted to the corresponding carbonate render the recovery of the catalyst superfluous for most applications making this catalytic system sustainable from both the environmental and economical point of views.

5.4 Experimenta section

Computational details

All computations were carried out using the Becke's threeparameter hybrid exchange functional in combination with the gradient-corrected correlation functional of Lee, Yang, and Parr (B3LYP) by using the GAUSSIAN 09 program packages.⁸¹ The basis set employed was 6-31+g(d) for all atoms. Stationary point geometries were characterized as local minimum on the potential energy surfaces. The absence of imaginary frequency verified that structures were true minima at their respective levels of theory. The structure of transition state were located by applying Schlegel's synchronous-transit-guided quasi-Newton (QST2) method as implemented in GAUSSIAN 09. The transition states were verified with frequency calculations to ensure they were first-order saddle points with only one negative eigenvalue. The free energy differences reported in Figure 50, Figure 51, and Figure 53 are in gas phase, the sum of the free energies of the CO₂ and the adduct between the bromide anion and epoxide is taken as zero energy. Cartesian coordinates of all DFT-optimized structures are available on request. Structures were visualized by the CYLview program.⁸²

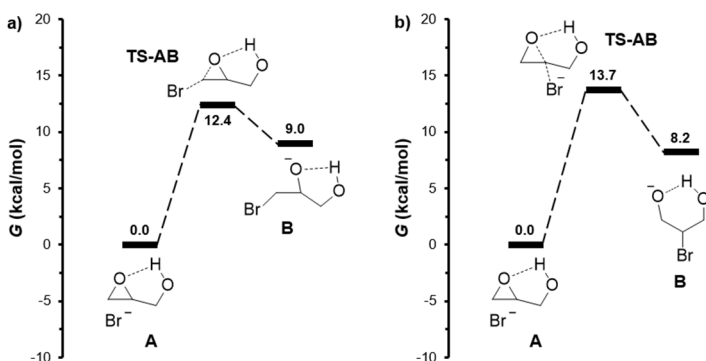


Figure S 113 Free energy profile for the cycloaddition of CO₂ to glycidol in the presence of OH-Br hydrogen bond. The free energies are given in kcal/mol.

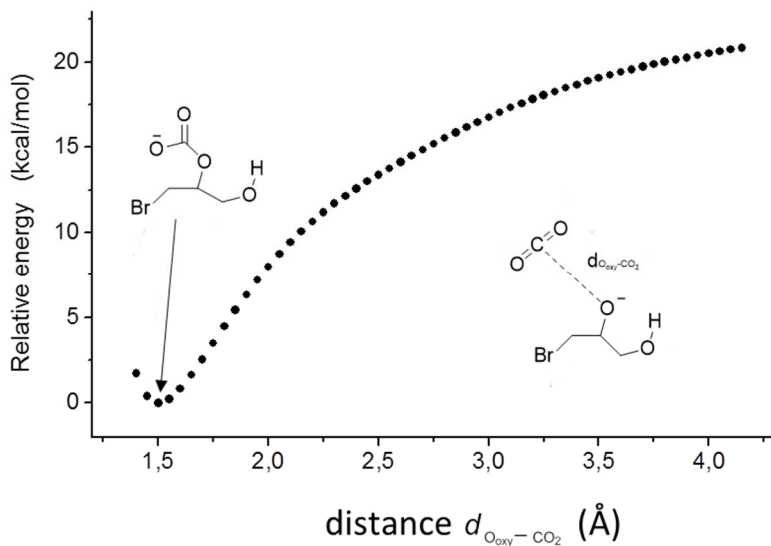


Figure S 114 The potential energy surface scan for the $O_{(\text{glycidol})}-C_{(\text{CO}_2)}$ bond formation at the B3LYP/6-31G+(d) level of theory.

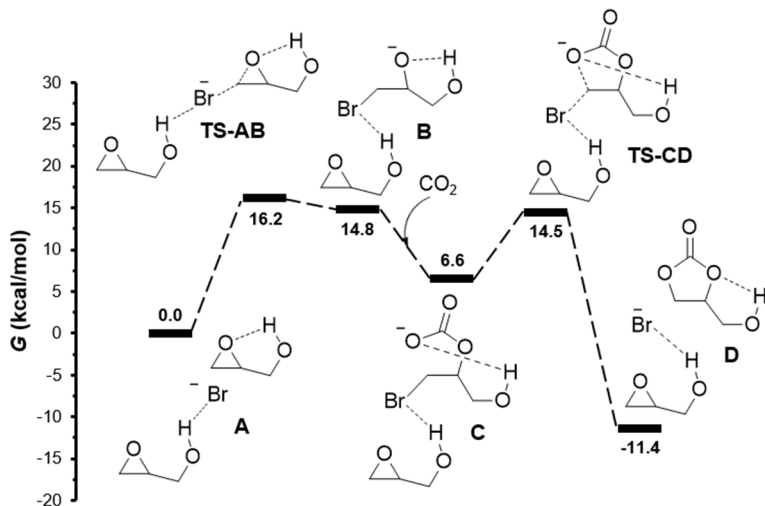


Figure S 115 Free energy profile for the cycloaddition of CO_2 to glycidol in the presence of $\text{OH}-\text{Br}$ hydrogen bond. The free energies are given in kcal/mol.

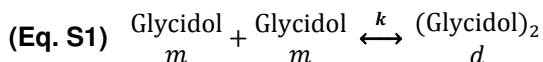
Chemical shift versus glycidol concentration analysis

The chemical shift variation of the alcoholic hydrogen ^1H NMR signal of glycidol in CDCl_3 solution as function of the molar concentration of glycidol was investigated. Different solutions of glycidol in CDCl_3 were prepared by volumetric dilution of stock solutions prepared by weighing solute. The ^1H NMR spectra were recorded on a 600 MHz Bruker Avance spectrometer. Collected data are listed below:

Table S 19 Chemical Shift of OH ^1H NMR signal of Glycidol in CDCl_3 solution with respect to molar concentration.

Entry	[Glycidol] mol/L	OH Chemical Shift ppm
S1	15.07	3.928
S2	11.31	3.928
S3	6.79	3.886
S4	4.52	3.751
S5	3.27	3.611
S6	2.26	3.438
S7	1.76	3.262
S8	1.26	3.131
S9	1.01	2.686
S10	0.675	2.435
S11	0.338	2.068
S12	0.270	1.978
S13	0.225	1.944
S14	0.180	1.877
S15	0.158	1.838
S16	0.135	1.799
S17	0.113	1.760
S18	0.068	1.685
S19	0.045	1.627
S20	0.023	1.588
S21	0.012	1.572

The results can be described mathematically, on the base of a model involving the formation of a dimeric species, using the following equations:⁸³



$$\text{(Eq. S2)} \quad \delta = \delta_m + (\delta_d - \delta_m) \cdot \left(1 + \frac{1 - \sqrt{1 + 8 \cdot k \cdot C_{tot}}}{4 \cdot k \cdot C_{tot}} \right)$$

where m is the monomer, d is the dimer, δ_m is the chemical shift of the monomer, δ_d is the chemical shift of the dimer, k is the dimerization equilibrium constant and C_{tot} is the total concentration of Glycidol in the solution.

In order to find the value of the dimerization equilibrium constant, a nonlinear fitting was performed using equation S2. A value of $k = 0.54 \pm 0.10$ was obtained with an $R^2 = 0.983$ ().

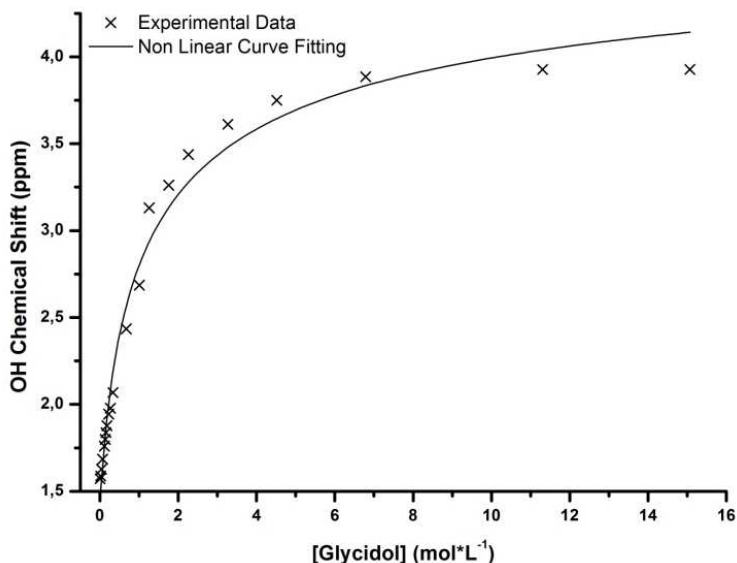


Figure S 116 ¹H NMR chemical shift of glycidol OH signal in CDCl₃ solution as function of molar concentration.

General procedure for CO₂/glycidol coupling to glycerol carbonate

A 60 mL stainless steel pressure reactor equipped with a magnetic stirring bar was charged with TBAB (0.754 mmol, 0.2430 g). Three cycles of pressurization-depressurization were carried out and glycidol (5.0 mL, 75.4 mmol) was introduced in the reactor. The reaction mixture was pressurized with CO₂ at 10 bar and stirred at 80 °C for 1 h. The reactor was cooled with ice, the CO₂ released, tetrachloroethane (0.8 mL, 7.54 mmol) was added as an internal standard and the mixture was analysed by ¹H NMR spectroscopy using CDCl₃ as the solvent. Conversion: 85%.

General procedure for CO₂/propylene oxide coupling to propylene carbonate

A 60 mL stainless steel pressure reactor equipped with a magnetic stirring bar was charged with TBAB (0.715 mmol, 0.2303 g) and glycidol (47 μL, 0.715 mmol). Three cycles of pressurization-depressurization were carried out and propylene oxide (5.0 mL, 71.4 mmol) was introduced in the reactor. The reaction mixture was pressurized with CO₂ at 10 bar and stirred at 80 °C for 24 h. The reactor was cooled with ice, the CO₂ released. Unreacted epoxide was removed under vacuum. The residue was dissolved in methylene chloride, filtered over silica and the solvent removed under vacuum. Isolated yield: 85%.

Typical procedure for CO₂/epoxide coupling to the corresponding cyclic carbonate

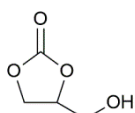
The procedure for 1,2-epoxyhexane is as reported: A 60 mL stainless steel pressure reactor equipped with a magnetic stirring bar was charged with TBAB (3.57 mmol, 1.15 g) and glycidol (237 μL, 3.57 mmol). Three cycles of pressurization-depressurization were carried out and 1,2-epoxyhexane (8.6 mL, 71.4 mmol) was introduced in the reactor. The reaction mixture was pressurized with CO₂ at 10 bar and stirred at 60 °C for 24 h. The reactor was cooled with ice, the CO₂ released, mesitylene (1.0 mL, 7.14 mmol) was added as an internal standard, and the mixture was analysed by ¹H NMR spectroscopy using CDCl₃ as the solvent. Conversion: 93%. For other epoxides a similar procedure was employed.

Typical procedure for CO₂/epoxide coupling to the corresponding cyclic carbonate at low pressure

The procedure for 1,2-epoxyhexane is as reported: A 50 mL three-neck round-bottom flask equipped with a magnetic stirring bar and a condenser was charged with TBAB (3.57 mmol, 1.15 g) and glycidol (237 μ L, 3.57 mmol). The flask was flushed with CO₂ and 1,2-epoxyhexane (8.6 mL, 71.4 mmol) was introduced in the reactor. The apparatus was connected to a balloon filled with CO₂ and the reaction mixture stirred at 60 °C for 24 h. The reactor was cooled with ice, the CO₂ released, mesitylene (1.0 mL, 7.14 mmol) was added as an internal standard and the mixture was analysed by ¹H NMR spectroscopy using CDCl₃ as the solvent. Conversion: 56%. For other epoxides a similar procedure was employed.

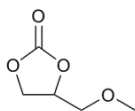
List of ^1H MNR data for the cyclic organic carbonate products

4-hydroxymethyl-1,3-dioxolan-2-one (CDCl_3 , 250MHz)



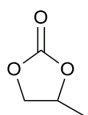
4.85-4.78 (m, 1H, ring CHCH_3), 4.55-4.45 (m, 2H, CHCH_2), 3.98 (dd, 1H, $J = 12.8$ Hz, $J = 3.1$ Hz, ring CHH), 3.73 (dd, 1H, $J = 12.8$ Hz, $J = 3.5$ Hz, ring CHH), 2.61 (s broad, 1H, OH).

4-methyloxymethyl-1,3-dioxolan-2-one (CDCl_3 , 300MHz)



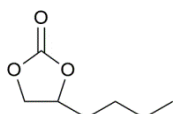
4.84-4.77 (m, 1H, ring CHCH_3), 4.49 (dd, $J = 8.4$, $J = 8.4$ Hz, 1H,), 4.38 (dd, 1H, $J = 8.3$ Hz, $J = 6.1$ Hz, ring CHH), 3.64 (dd, 1H, $J = 10.9$ Hz, $J = 3.8$ Hz, ring CHH), 3.57 (dd, 1H, $J = 10.9$ Hz, $J = 3.8$ Hz, ring CHH), 3.42 (s, 3H, CH_3).

4-methyl-1,3-dioxolan-2-one (CDCl_3 , 250MHz)



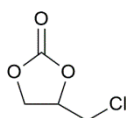
4.93-4.79 (m, 1H, ring CHCH_3), 4.56 (dd, 1H, $J = 8.3$ Hz, $J = 7.7$ Hz, ring CHH), 4.03 (dd, 1H, $J = 8.3$ Hz, $J = 7.2$ Hz, ring CHH), 1.50 (d, 3H, $J = 6.2$ Hz, CH_3).

4-butyl-1,3-dioxolan-2-one (CDCl_3 , 250MHz)



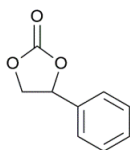
4.72-4.66 (m, 1H, ring CHCH_3), 4.52 (t, 1H, $J = 8.1$ Hz, ring CHH), 4.07 (dd, 1H, $J = 8.2$ Hz, $J = 7.3$ Hz, ring CHH), 1.85-1.77 (m, 1H, CHCH_2CH_2), 1.74-1.67 (m, 1H, CHCH_2CH_2), 1.52-1.33 (m, 4H, $\text{CH}_2\text{CH}_2\text{CH}_2$ and $\text{CH}_2\text{CH}_2\text{CH}_3$), 0.92 (t, 3H, $^3J = 6.9$ Hz, CH_3).

4-chloromethyl-1,3-dioxolan-2-one (CDCl_3 , 250MHz)



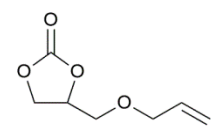
5.02-4.93 (m, 1H, ring CHCH_3), 4.60 (dd, 1H, $J = 8.8$ Hz, $J = 8.1$ Hz, ring CHH), 4.42 (dd, 1H, $J = 8.8$ Hz, $J = 5.8$ Hz, ring CHH), 3.76 (m, 2H, CH_2Cl).

4-phenyl-1,3-dioxolan-2-one (CDCl_3 , 250MHz)



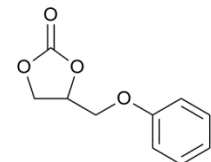
7.44-7.41 (m, 2H, Ar-H), 7.38-7.30 m, 2H, Ar-H), 5.68 (dd, 1H, $J = 8.1$ Hz, $J = 8.1$ Hz, ring CHCH_3), 4.81 (dd, 1H, $J = 8.1$, $J = 8.1$, ring CHH), 4.35 (dd, 1H, $J = 8.1$ Hz, $J = 8.1$ Hz, ring CHH).

4-allyloxymethyl-1,3-dioxolan-2-one (CDCl₃, 400MHz)



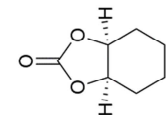
5.92-5.82 (m, 1H, CH=CH₂), 5.29 (dd, 1H, (E)-CH=CHH, *J* = 17.3 Hz, *J* = 1.4 Hz), 5.23 (dd, 1H, (Z)-CH=CHH, *J* = 10.4 Hz, *J* = 1.4 Hz), 4.85-4.79 (m, 1H, ring CHCH₂), 4.50 (dd, 1H, *J* = 8.3 Hz, *J* = 8.3 Hz), 4.41 (dd, 1H, *J* = 8.3 Hz, *J* = 6.3 Hz), 4.10- 4.02 (m, 2H, ring CHH), 3.71-3.60 (m, 2H,).

4-phenoxyethyl-1,3-dioxolan-2-one (CDCl₃, 400MHz)



7.32-7.23 (m, 2H), 7.03-6.94 (m, 1H), 6.91-6.85 (m, 2H), 5.05-4.99(m, 1H, ring CHCH₃), 4.64-4.57 (m, 1H), 4.56-4.47 (m, 1H), 4.25-4.19 (m, 1H), 4.17-4.10 (m, 1H).

(3aR,7aS)-hexahydrobenzo-1,3-dioxol-2-one (CDCl₃, 400MHz)



4.68 (m, 2H, ring CHCH₂), 1.99-1.77 (m, 4H), 1.67-1.57 (m, 2H), 1.47-1.37 (m, 2H).

5.5 References

- ⁶⁸ a) Pagliaro M., Ciriminna R., Kimura H., Rossi M., Pina C. D., *Angew. Chem. Int. Ed.*, **2007**, *46*, 4434-4440; *Angew. Chem.* **2007**, *119*, 4516-4522; b) Bozell J. J., Petersen G. R., *Green Chem.*, **2010**, *12*, 539-554; c) Simles C., Baranton S., Coutanceau C., *ChemSusChem*, **2012**, *5*, 2106-2124; d) García J. I., Garcia-Marín H., Pires E., *Green Chem.*, **2014**, *16*, 1007-1033; e) Sutter M., Da Silva E., Duguet N., Raoul Y., Métay E., M. Lemaire, *Chem. Rev.*, **2015**, *115*, 8609-8651.
- ⁶⁹ Sonnati M. O., Amigoni S., de Givenchy E. P. T., Darmanin T., Choulet O., Guittard F., *Green Chem.*, **2013**, *15*, 283-306.
- ⁷⁰ a) Ochoa-Gómez J. R., Gómez-Jiménez-Aberasturi O., Ramírez-López C., Belsué M., *Org. Process Res. Dev.*, **2012**, *16*, 389-399; b) W. Jacquemin in *Encyclopedia of Chemical Processing and Design*, eds. McKetta J. J., Cunningham W. A., Marcel Decker, New York, **1984**, vol. 20, pp. 177-201; c) Vieville C., Yoo J. W., Pelet S., Mouloungui Z., *Catal. Lett.*, **1998**, *56*, 245; d) Patel Y., George J., Pillai S. M., Munshi P., *Green Chem.*, **2009**, *11*, 1056; e) Takagaki A., Iwatami K., Nishimura S., Ebitani K., *Green Chem.*, **2010**, *12*, 578-581.
- ⁷¹ a) Aresta M., Di Benedetto A., Nocito F., Pastore C., *J. Mol. Catal. A*, **2006**, *257*, 149-153; b) George J., Patel Y., Pillai S. M., Munshi P., *J. Mol. Catal. A*, **2009**, *304*, 1-7.
- ⁷² a) Li Q., Zhang W., Zhao N., Wei W., Sun Y., *Catal. Today*, **2006**, *115*, 111-116; b) Aresta M., Dibenedetto A., Nocito F., Ferragina C., *J. Catal.*, **2009**, *268*, 106-114; c) Dibenedetto A., Angelini A., Aresta M., Ethiraj J., Fragale C., Nocito F., *Tetrahedron*, **2011**, *67*, 1308-1313.
- ⁷³ a) North M., Young C., *Catal. Sci. Technol.*, **2011**, *1*, 93-99; b) Whiteoak C. J., Martin E., Belmonte M. M., Benet-Buchholz J., Kleij A. W., *Adv. Synth. Catal.*, **2012**, *354*, 469-476; c) Whiteoak C. J., Kielland N., Laserna V., Escudero-Adán E. C., Martin E., Kleij A. W., *J. Am. Chem. Soc.*, **2013**, *135*, 1228-1231; d) Whiteoak C. J., Kielland N., Laserna V., Castro-Gómez F., E. Martin, Escudero-Adán E. C., Bo C., Kleij A. W., *Chem. Eur. J.*, **2014**, *20*, 2264-2275; e) Castro-Osma J. A., North M., Wu X., *Chem. Eur. J.*, **2014**, *20*, 15005-15008; f) Martínez J., Castro-Osma J. A., Earlam A., Alonso-Moreno C., Otero A., Lara-Sánchez A., North M., Rodríguez-Diéguez A., *Chem. Eur. J.*, **2015**, *21*, 9850-9862; g) Buonerba A., De Nisi A., Grassi A., Milione S., Capacchione C., Vagin S., Rieger B., *Catal. Sci. Technol.*, **2015**, *5*, 118-112; h) Buonerba A., Della Monica F., De Nisi A., Luciano E., Milione S., Grassi A., Capacchione C., Rieger B., *Faraday Discuss.*, **2015**, *183*, 83-95; j) Rintjema J., Epping R., Fiorani G., Martín E., Escudero-Adán E. C., Kleij A. W., *Angew.*

Chem. Int. Ed., **2016**, *55*, 3972-3976; *Angew. Chem.* **2016**, *128*, 4040-4044.

⁷⁴ a) Whiteoak C. J., Nova A., Maseras E., Kleij A. W., *ChemSusChem*, **2012**, *5*, 2032-2038; b) Sopeça S., Fiorani G., Martin C., Kleij A. W., *ChemSusChem*, **2015**, *8*, 3248-3254; c) Alves M., Grignard B., Gennen S., Mereau R., Detrembleur C., Jerome C., Tassaing T., *Catal. Sci. Technol.*, **2015**, *5*, 4636-4643.

⁷⁵ Cespi D., Cucciniello R., Ricciardi M., Capacchione C., Vassura I., Passarini F., Proto A., *Green Chem.*, **2016**, *18*, 4559-4570.

⁷⁶ a) V. Calò, A. Nacci, A. Monopoli, A. Fanizzi, *Org. Lett.* **2002**, *4*, 2561-2563; b) J.-Q. Wang, K. Dong, W.-G. Cheng, J. Sun, S.-J. Zhang, *Catal. Sci. Technol.* **2012**, *2*, 1480-1484; c) T. Ema, K. Fukuhara, T. Sakai, M. Ohbo, F.-Q. Bai, J. Hasegawa, *Catal. Sci. Technol.* **2015**, *5*, 2314-2321; d) C. C. Rocha, T. Onfroy, J. Pilm8, A. Denicourt-Nowicki, A. Roucoux, F. Launay, *J. Catal.* **2016**, *333*, 29-39.

⁷⁷ Whiteoak C. J., Nova A., Maseras E., Kleij A. W., *ChemSusChem*, **2012**, *5*, 2032-2038.

⁷⁸ Yang G., Xu Y., *Phys. Chem. Chem. Phys.*, **2008**, *10*, 6787-6795.

⁷⁹ a) Borho N., Häber T., Suhm M. A., *Phys. Chem. Chem. Phys.*, **2001**, *3*, 1945-1948; b) Borho N., Suhm M. A., *Phys. Chem. Chem. Phys.*, **2002**, *4*, 2721-2732.

⁸⁰ a) X. F. Liu, Q. W. Song, S. Zhang, L. N. He, *Catal. Today* **2016**, *263*, 69-74; b) M. Cokoja, M. E. Wilhelm, M. H. Anthofer, W. A. Hermann, F. E. Kehn, *ChemSusChem* **2015**, *8*, 2436-2454; c) G. Fiorani, W. Guo, A. W. Kleij, *Green Chem.* **2015**, *17*, 1375-1389.

⁸¹ Gaussian 09 (Revision A.02), M. J. Frisch, G. W. Trucks, H. B. Schlegel, G. E. Scuseria, M. A. Robb, J. R. Cheeseman, G. Scalmani, V. Barone, B. Mennucci, G. A. Petersson, H. Nakatsuji, M. Caricato, X. Li, H. P. Hratchian, A. F. Izmaylov, J. Bloino, G. Zheng, J. L. Sonnenberg, M. Hada, M. Ehara, K. Toyota, R. Fukuda, J. Hasegawa, M. Ishida, T. Nakajima, Y. Honda, O. Kitao, H. Nakai, T. Vreven, J. A. Montgomery, Jr., J. E. Peralta, F. Ogliaro, M. Bearpark, J. J. Heyd, E. Brothers, K. N. Kudin, V. N. Staroverov, R. Kobayashi, J. Normand, K. Raghavachari, A. Rendell, J. C. Burant, S. S. Iyengar, J. Tomasi, M. Cossi, N. Rega, J. M. Millam, M. Klene, J. E. Knox, J. B. Cross, V. Bakken, C. Adamo, J. Jaramillo, R. Gomperts, R. E. Stratmann, O. Yazyev, A. J. Austin, R. Cammi, C. Pomelli, J. W. Ochterski, R. L. Martin, K. Morokuma, V. G. Zakrzewski, G. A. Voth, P. Salvador, J. J. Dannenberg, S. Dapprich, A. D. Daniels, O. Farkas, J. B. Foresman, J. V. Ortiz, J. Cioslowski, D. J. Fox, Gaussian, Inc.: Wallingford, CT, **2009**.

⁸² C. Y. Legault CYLview, v1.0b, Universit8 de Sherbrooke, **2009**; <http://www.cylview.org>.

⁸³ Martin R. B., *Chem. Rev.*, **1996**, *96*, 3043-3064.

Acknowledgements

I want to sincerely thank all the people that contributed in any extent to my PhD. The first thanks is for Prof Carmine Capacchione that beside to be my scientific tutor is a life mentor from the early period of my studies, to Prof Alfonso Grassi that always remembered me that rigor is the most important quality for a scientist, and to Dr Stefano Milione who gave his support every time and treat me more like a peer than like a student.

I have to appropriately thank Prof. Magda Monari and Assunta De Nisi, from the Università di Bologna, for the determination of the crystal structures by X-ray diffraction experiments.

Many thanks to Prof Luigi Cavallo and Dr Sai Vummaleti from the King Abdullah University of Science and Technology, to have supported our work with valuable quantum mechanical calculations.

A great acknowledgement is for Prof Dr Bernhard Rieger, who hosted me in his laboratories at the Technical University of Munich, for the first time, before my PhD, and for a short period later. From the same institution a heartfelt thanks is also deserved to Thomas Pehl, for the work spent in the FT-IR experiments, and to Dr Marco Giuman as a friend I will never forget.

To reach the end of the doctoral program has been both demanding and exciting at the same time, and I want to thank especially my great friends Vito Capaccio, Antonio Bounerba, Ermanno Luciano and Rosita Lapenta for their support and affection. It is not possible to mention all the students that passed through the laboratory, however I have to say thanks to Mattia Leone, Marco Naddeo and Salvatore Impemba because they left something more than chemical products.

I deeply feel I have to express my great gratitude to all the members of my family, because they never left me alone.

In the end, the most important person I want to thank is my wife Veronica, because she is the most precious treasure of my life.